DOKUZ EYLÜL UNIVERSITY

GRADUATE SCHOOL OF NATURAL AND APPLIED SCIENCES

DESIGN AND SETUP OF REGULAR/IRREGULAR WAVE GENERATOR AND EXPERIMENTAL AND NUMERICAL INVESTIGATION OF DIFFERENT TYPES OF WAVE ABSORBERS

by

Bassem NOUIOUI

September,2023

İZMİR

DESIGN AND SETUP OF REGULAR/IRREGULAR WAVE GENERATOR AND EXPERIMENTAL AND NUMERICAL INVESTIGATION OF DIFFERENT TYPES OF WAVE ABSORBERS

A Thesis Submitted to the
Graduate School of Natural and Applied Sciences of Dokuz Eylül University
In Partial Fulfillment of the Requirements for the Degree of Doctor of Philosophy in Civil Engineering, Hydraulic, Hydrology and Water Resources Program

Bassem NOUIOUI

September,2023

İZMİR

Ph.D. THESIS EXAMINATION RESULT FORM

We have read the thesis entitled "**DESIGN AND SETUP OF REGULAR/IRREGULAR WAVE GENERATOR AND EXPERIMENTAL AND NUMERICAL INVESTIGATION OF DIFFERENT TYPES OF WAVE ABSORBERS**" completed by **BASSEM NOUIOUI** under supervision of **PROF.DR. MUSTAFA DOĞAN** and we certify that in our opinion it is fully adequate, in scope and in quality, as a thesis for the degree of Doctor of Philosophy.

Prof. Dr. Mustafa DOĞAN

Supervisor

Assoc. Prof. Dr. Ayşegül ÖZGENÇ AKSOY

Thesis Committee Member

Prof. Dr. Hasan ÖZTÜRK

Thesis Committee Member

Prof. Dr. Mehmet SORGUN

Examining Committee Member

Prof. Dr. Abdullah Cem KOÇ

Examining Committee Member

Prof. Dr. Okan FISTIKOĞLU

Director

Graduate School of Natural and Applied Sciences

ACKNOWLEDGMENT

We express our deepest gratitude to my supervisor, Prof.Dr. Mustafa DOĞAN , whose unwavering support and guidance have been the cornerstone of this thesis. We are also thankful to Assoc.Prof.Dr. Ayşegül ÖZGENÇ AKSOY, Prof.Dr Hasan ÖZTÜRK , and Prof.Dr. Yalçın ARISOY for their expertise, encouragement, and mentorship , which have been invaluable in shaping the research direction and refining our methodologies.

Our sincere thanks go to Muhammed Ikbal TORTUMLUOĞLU, whose dedication and collaborative efforts have been instrumental in the successful execution of this study. His expertise in data analysis, software support, and experimental design significantly enriched our research outcomes.

We are also grateful to İsa ÜSTÜNDAĞ for his technical support and assistance in setting up the physical model experiments. His expertise in maintaining the wave tank and troubleshooting challenges ensured smooth and reliable experiments.

Furthermore, we would like to acknowledge the financial support provided by the Scientific and Technological Research Council of Turkey (TUBITAK) for supporting the study through the project 218M445.

Finally, I am deeply grateful to my family and friends for their unwavering support and understanding throughout this research journey. Their encouragement and patience have been a constant source of motivation.

Bassem NOUIOUI

DESIGN AND SETUP OF REGULAR/IRREGULAR WAVE GENERATOR AND EXPERIMENTAL AND NUMERICAL INVESTIGATION OF DIFFERENT TYPES OF WAVE ABSORBERS

ABSTRACT

Two primary tools for studying wave phenomena and solving coastal engineering problems are hydraulic physical model tests and numerical models. However, the high initial investment cost and limitations in laboratory infrastructure have hindered the widespread adoption of irregular wave generators.

This research addresses these challenges by proposing a cost-effective hybrid approach that combines numerical simulations and physical model experiments to develop a passive wave absorption system for coastal wave studies. The numerical simulations were performed using the FLOW3D computational fluid dynamics software, allowing for the investigation of various passive absorber designs under both regular and irregular wave conditions. Different wave heights and periods were considered to ensure experimental feasibility.

The study evaluated the effectiveness of passive wave absorbers in reducing reflection coefficients and assessed their efficiency, adaptability, ease of modification, and cost-effective manufacturability through numerical simulations. The results indicated that 2-slopes and 3-slopes designs were significantly more effective in reducing wave amplitudes for regular waves, with reflection coefficients ranging from 4% to 15%, while the parabolic design had coefficients within the range of 8% to 25%. However, no significant difference was observed in the reflection coefficient for irregular waves.

By combining numerical simulations and physical model experiments, this research aims to offer a reliable and economically feasible solution for coastal laboratories and engineering projects. By leveraging domestic capabilities and cost-effective passive

absorbers, the proposed hybrid approach seeks to enhance coastal infrastructure planning and contribute to sustainable coastal development worldwide.

Keywords: Physical model, Numerical model, FLOW3D, Regular/Irregular waves, Wave generator, Passive wave absorption.

DÜZENLI/DÜZENSIZ DALGA ÜRETECI TASARIMI VE KURULUMU İLE FARKLI TİP DALGA SÖNÜMLEYİCİLERİNİN DENEYSEL VE SAYISAL ARAŞTIRMASI

ÖZ

Dalga olgularını incelemek ve kıyı mühendisliği sorunlarını çözmek için kullanılan temel iki araç, hidrolik fiziksel modeller ve sayısal modellerdir. Ancak yüksek başlangıç yatırım maliyeti ve laboratuvar altyapısındaki sınırlamalar, düzensiz dalga üreteçlerinin yaygın kullanımını engellemektedir.

Bu araştırmada, pasif dalga sönümleme sistemi geliştirmek amacıyla sayısal simülasyonlar ile fiziksel model deneylerini birleştiren maliyet-etkin bir hibrit yaklaşım önerilmektedir. Sayısal simülasyonlar, FLOW3D hesaplamalı akışkanlar dinamiği yazılımı kullanılarak gerçekleştirilmiş olup, hem düzenli hem de düzensiz dalga koşulları altında çeşitli pasif sönümleyici tasarımların incelenmesine olanak tanınmıştır. Deneylerde ve sayısal simülasyonlarda farklı dalga yükseklikleri ve periyotları göz önünde bulundurulmuştur.

Bu çalışma kapsamında, sayısal simülasyonlar aracılığıyla pasif dalga sönümleyicilerin yansıma katsayılarını azaltma etkinliği ve verimliliği, uyum sağlama yeteneği, değiştirme kolaylığı ve maliyet-etkin üretilebilirliği değerlendirilmiştir. Sonuçlar, 2-eğim ve 3-eğim tasarımlarının düzenli dalgalar için dalga genliklerini azaltmada önemli ölçüde daha etkili olduğunu göstermiştir. Yansıma katsayıları %4 ila %15 arasında değişmekte iken, parabolik tasarımda katsayılar %8 ila %25 arasında değer almaktadır. Bununla birlikte, düzensiz dalgalar için yansıma katsayısında önemli bir fark gözlenmemiştir.

Gerçekleştirilen çalışma sonucunda, sayısal simülasyonlar ve fiziksel model deneyleri ışığında, kıyı laboratuvarları ve mühendislik projeleri için güvenilir ve ekonomik olarak uygulanabilir bir çözüm sunulmaktadır. Yerel olanaklar ile imal edilen maliyet-etkin pasif sönümleyiciler kullanılarak, önerilen hibrit yaklaşım kıyı yapılarının planlamasını geliştirmeyi hedeflemekte ve sürdürülebilir kıyı gelişimine dünya genelinde katkıda bulunmayı amaçlamaktadır.

Anahtar kelimeler: Fiziksel model, Sayısal model, FLOW3D, Düzenli/Düzensiz dalga, Dalga üreteci, Pasif dalga sönümleyici.

CONTENTS

Ph.D. THESIS EXAMINATION RESULT FORM ii

ACKNOWLEDGMENT iii

ABSTRACT iv

ÖZ vi

LIST OF FIGURES xi

LIST OF TABLES xxii

CHAPTER ONE INTRODUCTION 1

1.1 Wave Generation 1

1.2 Wave Absorber 2

CHAPTER TWO LITERATURE REVIEW 3

2.1 Wave Generation 3

2.2 Wave Absorber 5

CHAPTER THREE WAVE GENERATION AND ANALYSIS 13

3.1 Wave Analysis 13

3.1.1 Wave Spectral Analysis 13

3.1.2 Time-domain Analysis 14

3.1.3 Random Wave Generation 15

3.1.4 Random Phase Method Improvement 15

3.1.5 Wave Board Displacement Time Series 19

3.1.6 Preparation of Random Wave Generation Signal 21

3.2 Wave Maker Theory 22
3.2.1 Governing Equations 22
3.3 Wave Reflection Analysis 43
3.3.1 Regular Wave 45
3.3.2 Irregular Wave 46

CHAPTER FOUR DESIGN OF WAVE MAKER 48

4.1 Wave Flume Setup 48
4.2 Wavemaker Setup and Mechanical Construction 54
4.3 Wave Analysis and Measurement 58
4.4 The Control Software 59

CHAPTER FIVE DESIGN OF WAVE ABSORAPTER 62

5.1 Alternative proposals wave absorbers evaluation 62
5.2 Geometrical Characteristics of the Alternatives Passive Wave Absorbers 63
5.3 The Most Efficient Proposals Fabrication 67
5.3.1 The 2-slopes proposition 68
5.3.2 The 3-slopes proposition 68
5.3.3 The parabolic (curved) proposition 69

CHAPTER SIX NUMERICAL SIMULATION 73

6.1 Equations of Motion 73
6.2 Numerical simulation of wavemaker and wave absorbers 77
6.3 Geometry Creation and Model Setup 77
6.4 Meshing and Sensitivity Analysis 77
6.5 Boundary Conditions and Solution Initialization 78

CHAPTER SEVEN RESULTS AND DISCCUSIONS 81

7.1 Wave Generation 81
7.2 Wave Absorption 90
7.2.1 The Most Efficient Proposals Substantiation 97

CHAPTER EIGHT CONCLUSIONS 170

REFERENCES 172

APPENDIX A 177

APPENDIX B 199

LIST OF FIGURES

Page

Figure 2.1 The wave absorber designed by Le Méhauté (Le Méhauté, 1972).....6
Figure 2.2 The different wave absorbers systems investigated (Ouellet and Datta, 1986) 7
Figure 2.3 The permeable sloping absorber (Chegini, 1993). 8
Figure 2.4 Front view of the screen perforations (Chegini, 1995).....9
Figure 2.5 A view of the expanded metal sheet (Chegini, 1995).....9
Figure 2.6 Sketch diagram of an offshore breakwater of porous materials (Twu and Chieu, 2000).....10
Figure 2.7 Geometry of a few models tested by Hodaei (Hodaei, 2016).....12
Figure 3.1 Waves defined by zero-up crossing.....14
Figure 3.2 An irregular wave's surface elevation time series and its JONSWAP spectrum. 17
Figure 3.3 An irregular wave's adjusted surface elevation time series and its JONSWAP spectrum. 19
Figure 3.4 An example of the paddle control signal (H_s=0.144 m, T_s=1.56 s, duration=600 s, and Δt=0.002s).....20
Figure 3.5 Flow diagram of the preparation of the input signal to an irregular wave generator.....21
Figure 3.6 Definition sketch (Schäffer 2003). 22
Figure 3.7 Scetch of wave board with translatory motion (piston type) (Schäffer 2003). 24
Figure 3.8 Far field Biésel transfer function Equation (3. 48) for piston-type wave maker against kh.....30
Figure 3.9 The transfer function and the total evanescent-mode transfer function for a piston-type wavemaker, (water depth h=1 m).....31
Figure 3.10 The displacement of the second order wave board for a regular wave (H=0.20 m , T=2s). 35

Figure 3.11 The targeted spectrum of the irregular wave and its corresponding spectrum of first order wave paddle motion. 37
Figure 3.12 Dimensionless first-order frequencies vs real (top) and imaginary (bottom) parts of subharmonic complex transfer functions $F-/\delta nm$ for a piston type wavemaker. (Schäffer,2003). 41
Figure 3.13 Dimensionless first-order frequencies vs real (top) and imaginary (bottom) parts of superharmonic complex transfer functions $F+/\delta nm$ for a piston type wavemaker. (Schäffer,2003). 42
Figure 3.14 Wave measurement setup sketch for the analysis of reflection. 44
Figure 4.1 Schematic representation of the wave channel's cross-section and plan view. 49
Figure 4.2 Reinforced foundation. 50
Figure 4.3 The spider crane and the wave channel's steel columns. 51
Figure 4.4 The installation process of the last piece of the channel. 51
Figure 4.5 The two crane systems. 52
Figure 4.6 Dokuz Eylül University Hydraulic Laboratory wave flume.....53
Figure 4.7 Varying sizes of rocks fill with a slope of 1:7. 54
Figure 4.8 The motion control system. 55
Figure 4.9 The piston-type paddle 56
Figure 4.10 Side and top views of the piston-type wavemaker section design (Not to scale). 56
Figure 4.11 Top views of the servo motor and the ball-screwed shaft. 57
Figure 4.12 Over-travel boundaries sensors.....57
Figure 4.13 The piston-type wave generator system with the control unit. 58
Figure 4.14 The wave flume sketch with the measuring equipment (not to scale). 59
Figure 4.15 The ULS (Ultralab Level System) device and the USS20130 (Ultralab Sound Sensors). 59
Figure 4.16 The controller Personal Computer. 60
Figure 4.17 The user interface of the control software. 61
Figure 5.1 Side view of proposition 1. 63

Figure 5.2 Side view of proposition 2. 63
Figure 5.3 Side view of proposition 3. 64
Figure 5.4 Top view of proposition 4. 64
Figure 5.5 Side view of proposition 5. 65
Figure 5.6 Side view of proposition 6. 65
Figure 5.7 Side view of proposition 7. 66
Figure 5.8 Side view of proposition 8. 66
Figure 5.9 Side view of proposition 9. 67
Figure 5.10 Photograph and the scale model (right bottom) of the 2-slopes proposition. 68
Figure 5.11 Photograph and the scale model (right bottom) of the 3-slopes proposition 69
Figure 5.12 Photograph and the scale model (right bottom) of the Parabolic proposition. 70
Figure 5.13 Removing stages of the 3-slopes proposition design from the wave flume. 72
Figure 6.1 The models mesh system. 78
Figure 6.2 The Boundary conditions system for irregular wave simulations. 80
Figure 6.3 The Boundary conditions system for regular wave simulations. 80
Figure 7.1 Comparison of the experimental and numerical surface elevations. 83
Figure 7.2 Flow depth example of a simulated irregular wave profile. 83
Figure 7.3 An example of a simulated irregular wave profile. 84
Figure 7.4 Scatter diagram for experimental and numerical T_s. 84
Figure 7.5 Scatter diagram for experimental and numerical H_s. 85
Figure 7.6 Experimental, numerical, and the target JONSWAP spectrum of IRW_01 H_s =0.22 m T_s=2.3 s. 85
Figure 7.7 Experimental, numerical, and the target JONSWAP spectrum of IRW_02 H_s=0.20 m T_s=2.7 s. 86
Figure 7.8 Experimental, numerical, and the target JONSWAP spectrum of IRW_03 H_s=0.17 m T_s=3.1 s. 86

Figure 7.9 Experimental, numerical, and the target JONSWAP spectrum of IRW_04 H_s=0.13 m T_s =3.6 s. 87
Figure 7.10 Experimental, numerical, and the target JONSWAP spectrum IRW_05 H_s=0.144 m T_s=1.56 s 87
Figure 7.11 the reflection coefficient of the numerical simulations of the suggested propositions. 92
Figure 7.12 The flow depth of the numerical simulations at P1 and P2 of proposition 1 in case of SRW01 H=0.25 m, T=2.0 s. 92
Figure 7.13 The flow depth of the numerical simulations at P1 and P2 of proposition 2 in case of SRW01 H=0.25 m, T=2.0 s. 93
Figure 7.14 The flow depth of the numerical simulations at P1 and P2 of proposition 3 in case of SRW01 H=0.25 m, T=2.0 s. 93
Figure 7.15 The flow depth of the numerical simulations at P1 and P2 of proposition 4 in case of SRW01 H=0.25 m, T=2.0 s. 94
Figure 7.16 The flow depth of the numerical simulations at P1 and P2 of proposition 5 in case of SRW01 H=0.25 m, T=2.0 s. 94
Figure 7.17 The flow depth of the numerical simulations at P1 and P2 of proposition 6 in case of SRW01 H=0.25 m, T=2.0 s. 95
Figure 7.18 The flow depth of the numerical simulations at P1 and P2 of proposition 7 in case of SRW01 H=0.25 m, T=2.0 s. 95
Figure 7.19 The flow depth of the numerical simulations at P1 and P2 of proposition 8 in case of SRW01 H=0.25 m, T=2.0 s. 96
Figure 7.20 The flow depth of the numerical simulations at P1 and P2 of proposition 9 in case of SRW01 H=0.25 m, T=2.0 s. 96
Figure 7.21 Experimental and numerical surface elevations for (RW_H = 0.25 m, T = 1.5 s) at Probes P1 (a) and P2 (b) for the 3-Slope Proposition Design. 102
Figure 7.22 Experimental and numerical surface elevations for (RW_H = 0.25 m, T = 2.0 s) at Probes P1 (a) and P2 (b) for the 3-Slope Proposition Design. 103
Figure 7.23 Experimental and numerical surface elevations for (RW_H = 0.25 m, T = 2.5 s) at Probes P1 (a) and P2 (b) for the 3-Slope Proposition Design. 103

Figure 7.24 Experimental and numerical surface elevations for (RW_H = 0.22 m, T = 1.5 s) at Probes P1 (a) and P2 (b) for the 3-Slope Proposition Design. 104
Figure 7.25 Experimental and numerical surface elevations for (RW_H = 0.22 m, T = 2.0 s) at Probes P1 (a) and P2 (b) for the 3-Slope Proposition Design. 105
Figure 7.26 Experimental and numerical surface elevations for (RW_H = 0.22 m, T = 2.3 s) at Probes P1 (a) and P2 (b) for the 3-Slope Proposition Design. 105
Figure 7.27 Experimental and numerical surface elevations for (RW_H = 0.22 m, T = 3.0 s) at Probes P1 (a) and P2 (b) for the 3-Slope Proposition Design. 106
Figure 7.28 Experimental and numerical surface elevations for (RW_H = 0.20 m, T = 1.5 s) at Probes P1 (a) and P2 (b) for the 3-Slope Proposition Design. 107
Figure 7.29 Experimental and numerical surface elevations for (RW_H = 0.20 m, T = 2.0 s) at Probes P1 (a) and P2 (b) for the 3-Slope Proposition Design. 107
Figure 7.30 Experimental and numerical surface elevations for (RW_H = 0.20 m, T = 2.7 s) at Probes P1 (a) and P2 (b) for the 3-Slope Proposition Design. 108
Figure 7.31 Experimental and numerical surface elevations for (RW_H = 0.20 m, T = 3.0 s) at Probes P1 (a) and P2 (b) for the 3-Slope Proposition Design. 109
Figure 7.32 Experimental and numerical surface elevations for (RW_H = 0.17 m, T = 1.5 s) at Probes P1 (a) and P2 (b) for the 3-Slope Proposition Design. 109
Figure 7.33 Experimental and numerical surface elevations for (RW_H = 0.17 m, T = 2.0 s) at Probes P1 (a) and P2 (b) for the 3-Slope Proposition Design.. 110
Figure 7.34 Experimental and numerical surface elevations for (RW_H = 0.17 m, T = 2.5 s) at Probes P1 (a) and P2 (b) for the 3-Slope Proposition Design. 111
Figure 7.35 Experimental and numerical surface elevations for (RW_H = 0.17 m, T = 3.1 s) at Probes P1 (a) and P2 (b) for the 3-Slope Proposition Design. 111
Figure 7.36 Experimental and numerical surface elevations for (RW_H = 0.17 m, T = 3.5 s) at Probes P1 (a) and P2 (b) for the 3-Slope Proposition Design. 112
Figure 7.37 Experimental and numerical surface elevations for (RW_H = 0.13 m, T = 1.5 s) at Probes P1 (a) and P2 (b) for the 3-Slope Proposition Design. 113
Figure 7.38 Experimental and numerical surface elevations for (RW_H = 0.13 m, T = 2.0 s) at Probes P1 (a) and P2 (b) for the 3-Slope Proposition Design. 113

Figure 7.39 Experimental and numerical surface elevations for (RW_H = 0.13 m, T = 2.5 s) at Probes P1 (a) and P2 (b) for the 3-Slope Proposition Design.. 114
Figure 7.40 Experimental and numerical surface elevations for (RW_H = 0.13 m, T = 3.0 s) at Probes P1 (a) and P2 (b) for the 3-Slope Proposition Design. 115
Figure 7.41 Experimental and numerical surface elevations for (RW_H = 0.13 m, T = 3.6 s) at Probes P1 (a) and P2 (b) for the 3-Slope Proposition Design. 115
Figure 7.42 Experimental and numerical surface elevations for (RW_H = 0.25 m, T = 1.5 s) at Probes P1 (a) and P2 (b) for the 2-Slope Proposition Design. 116
Figure 7.43 Experimental and numerical surface elevations for (RW_H = 0.25 m, T = 2.0 s) at Probes P1 (a) and P2 (b) for the 2-Slope Proposition Design. 117
Figure 7.44 Experimental and numerical surface elevations for (RW_H = 0.25 m, T = 2.5 s) at Probes P1 (a) and P2 (b) for the 2-Slope Proposition Design. 118
Figure 7.45 Experimental and numerical surface elevations for (RW_H = 0.22 m, T = 1.5 s) at Probes P1 (a) and P2 (b) for the 2-Slope Proposition Design. 118
Figure 7.46 Experimental and numerical surface elevations for (RW_H = 0.22 m, T = 2.0 s) at Probes P1 (a) and P2 (b) for the 2-Slope Proposition Design. 119
Figure 7.47 Experimental and numerical surface elevations for (RW_H = 0.22 m, T = 2.3 s) at Probes P1 (a) and P2 (b) for the 2-Slope Proposition Design. 120
Figure 7.48 Experimental and numerical surface elevations for (RW_H = 0.22 m, T = 3.0 s) at Probes P1 (a) and P2 (b) for the 2-Slope Proposition Design. 120
Figure 7.49 Experimental and numerical surface elevations for (RW_H = 0.20 m, T = 1.5 s) at Probes P1 (a) and P2 (b) for the 2-Slope Proposition Design. 121
Figure 7.50 Experimental and numerical surface elevations for (RW_H = 0.20 m, T = 2.0 s) at Probes P1 (a) and P2 (b) for the 2-Slope Proposition Design. 122
Figure 7.51 Experimental and numerical surface elevations for (RW_H = 0.20 m, T = 2.7 s) at Probes P1 (a) and P2 (b) for the 2-Slope Proposition Design. 122
Figure 7.52 Experimental and numerical surface elevations for (RW_H = 0.20 m, T = 3.0 s) at Probes P1 (a) and P2 (b) for the 2-Slope Proposition Design. 123
Figure 7.53 Experimental and numerical surface elevations for (RW_H = 0.17 m, T = 1.5 s) at Probes P1 (a) and P2 (b) for the 2-Slope Proposition Design. 124

Figure 7.54 Experimental and numerical surface elevations for (RW_H = 0.17 m, T = 2.0 s) at Probes P1 (a) and P2 (b) for the 2-Slope Proposition Design. 124
Figure 7.55 Experimental and numerical surface elevations for (RW_H = 0.17 m, T = 2.5 s) at Probes P1 (a) and P2 (b) for the 2-Slope Proposition Design. 125
Figure 7.56 Experimental and numerical surface elevations for (RW_H = 0.17 m, T = 3.1 s) at Probes P1 (a) and P2 (b) for the 2-Slope Proposition Design. 126
Figure 7.57 Experimental and numerical surface elevations for (RW_H = 0.17 m, T = 3.5 s) at Probes P1 (a) and P2 (b) for the 2-Slope Proposition Design. 126
Figure 7.58 Experimental and numerical surface elevations for (RW_H = 0.13 m, T = 1.5 s) at Probes P1 (a) and P2 (b) for the 2-Slope Proposition Design. 127
Figure 7.59 Experimental and numerical surface elevations for (RW_H = 0.13 m, T = 2.0 s) at Probes P1 (a) and P2 (b) for the 2-Slope Proposition Design. 128
Figure 7.60 Experimental and numerical surface elevations for (RW_H = 0.13 m, T = 2.5 s) at Probes P1 (a) and P2 (b) for the 2-Slope Proposition Design. 128
Figure 7.61 Experimental and numerical surface elevations for (RW_H = 0.13 m, T = 3.0 s) at Probes P1 (a) and P2 (b) for the 2-Slope Proposition Design. 129
Figure 7.62 Experimental and numerical surface elevations for (RW_H = 0.13 m, T = 3.6 s) at Probes P1 (a) and P2 (b) for the 2-Slope Proposition Design. 130
Figure 7.63 Experimental and numerical surface elevations for (RW_H = 0.25 m, T = 1.5 s) at Probes P1 (a) and P2 (b) for the Parabolic Proposition Design. 131
Figure 7.64 Experimental and numerical surface elevations for (RW_H = 0.25 m, T = 2.0 s) at Probes P1 (a) and P2 (b) for the Parabolic Proposition Design. 131
Figure 7.65 Experimental and numerical surface elevations for (RW_H = 0.25 m, T = 2.5 s) at Probes P1 (a) and P2 (b) for the Parabolic Proposition Design. 132
Figure 7.66 Experimental and numerical surface elevations for (RW_H = 0.22 m, T = 1.5 s) at Probes P1 (a) and P2 (b) for the Parabolic Proposition Design. 133
Figure 7.67 Experimental and numerical surface elevations for (RW_H = 0.22 m, T = 2.0 s) at Probes P1 (a) and P2 (b) for the Parabolic Proposition Design. 133
Figure 7.68 Experimental and numerical surface elevations for (RW_H = 0.22 m, T = 2.5 s) at Probes P1 (a) and P2 (b) for the Parabolic Proposition Design. 134

Figure 7.69 Experimental and numerical surface elevations for (RW_H = 0.22 m, T = 3.0 s) at Probes P1 (a) and P2 (b) for the Parabolic Proposition Design. 135
Figure 7.70 Experimental and numerical surface elevations for (RW_H = 0.20 m, T = 1.5 s) at Probes P1 (a) and P2 (b) for the Parabolic Proposition Design. 135
Figure 7.71 Experimental and numerical surface elevations for (RW_H = 0.20 m, T = 2.0 s) at Probes P1 (a) and P2 (b) for the Parabolic Proposition Design 136
Figure 7.72 Experimental and numerical surface elevations for (RW_H = 0.20 m, T = 2.7 s) at Probes P1 (a) and P2 (b) for the Parabolic Proposition Design 137
Figure 7.73 Experimental and numerical surface elevations for (RW_H = 0.20 m, T = 3.0 s) at Probes P1 (a) and P2 (b) for the Parabolic Proposition Design. 137
Figure 7.74 Experimental and numerical surface elevations for (RW_H = 0.17 m, T = 1.5 s) at Probes P1 (a) and P2 (b) for the Parabolic Proposition Design. 138
Figure 7.75 Experimental and numerical surface elevations for (RW_H = 0.17 m, T = 2.0 s) at Probes P1 (a) and P2 (b) for the Parabolic Proposition Design. 139
Figure 7.76 Experimental and numerical surface elevations for (RW_H = 0.17 m, T = 2.5 s) at Probes P1 (a) and P2 (b) for the Parabolic Proposition Design. 139
Figure 7.77 Experimental and numerical surface elevations for (RW_H = 0.17 m, T = 3.1 s) at Probes P1 (a) and P2 (b) for the Parabolic Proposition Design. 140
Figure 7.78 Experimental and numerical surface elevations for (RW_H = 0.17 m, T = 3.5 s) at Probes P1 (a) and P2 (b) for the Parabolic Proposition Design. 141
Figure 7.79 Experimental and numerical surface elevations for (RW_H = 0.13 m, T = 1.5 s) at Probes P1 (a) and P2 (b) for the Parabolic Proposition Design. 141
Figure 7.80 Experimental and numerical surface elevations for (RW_H = 0.13 m, T = 2.0 s) at Probes P1 (a) and P2 (b) for the Parabolic Proposition Design. 142
Figure 7.81 Experimental and numerical surface elevations for (RW_H = 0.13 m, T = 2.5 s) at Probes P1 (a) and P2 (b) for the Parabolic Proposition Design. 143
Figure 7.82 Experimental and numerical surface elevations for (RW_H = 0.13 m, T = 3.0 s) at Probes P1 (a) and P2 (b) for the Parabolic Proposition Design. 143
Figure 7.83 Experimental and numerical surface elevations for (RW_H = 0.13 m, T = 3.6 s) at Probes P1 (a) and P2 (b) for the Parabolic Proposition Design. 144

Figure 7.84 Reflection coefficient of the 2-slopes proposition versus wave steepness of the regular waves. 146
Figure 7.85 Scatter diagram for experimental and numerical results of the 2-slopes proposition of the regular waves with R2 and SI values. 147
Figure 7.86 Reflection coefficient of the 3-slopes proposition versus wave steepness of the regular waves. 147
Figure 7.87 Scatter diagram for experimental and numerical results of the 3-slopes proposition of the regular waves with R2 and SI values. 148
Figure 7.88 Reflection coefficient of the parabolic proposition versus wave steepness of the regular waves. 148
Figure 7.89 Scatter diagram for experimental and numerical results of the parabolic proposition of the regular waves with R^2 and SI values. 149
Figure 7.90 The experimental reflection coefficient of the selected propositions versus wave steepness of the regular waves. 150
Figure 7.91 Experimental and numerical surface elevations for (IRW_H_s = 0.25 m, T_s = 2.0 s) at Probes P1 (a) and P2 (b) for the 3-Slope Proposition Design. 151
Figure 7.92 Experimental and numerical surface elevations for (IRW_H_s = 0.22 m, T_s = 2.3 s) at Probes P1 (a) and P2 (b) for the 3-Slope Proposition Design. 152
Figure 7.93 Experimental and numerical surface elevations for (IRW_H_s = 0.20 m, T_s = 2.7 s) at Probes P1 (a) and P2 (b) for the 3-Slope Proposition Design. 153
Figure 7.94 Experimental and numerical surface elevations for (IRW_H_s = 0.17 m, T_s = 3.1 s) at Probes P1 (a) and P2 (b) for the 3-Slope Proposition Design. 153
Figure 7.95 Experimental and numerical surface elevations for (IRW_H_s = 0.13 m, T_s = 3.6 s) at Probes P1 (a) and P2 (b) for the 3-Slope Proposition Design. 154
Figure 7.96 Experimental and numerical surface elevations for (IRW_H_s = 0.25 m, T_s = 2.0 s) at Probes P1 (a) and P2 (b) for the 2-Slope Proposition Design. 155
Figure 7.97 Experimental and numerical surface elevations for (IRW_H_s = 0.22 m, T_s = 2.3 s) at Probes P1 (a) and P2 (b) for the 2-Slope Proposition Design. 156
Figure 7.98 Experimental and numerical surface elevations for (IRW_H_s = 0.20 m, T_s = 2.7 s) at Probes P1 (a) and P2 (b) for the 2-Slope Proposition Design. 157

Figure 7.99 Experimental and numerical surface elevations for (IRW_H_s = 0.17 m, T_s = 3.1 s) at Probes P1 (a) and P2 (b) for the 2-Slope Proposition Design. 157
Figure 7.100 Experimental and numerical surface elevations for (IRW_H_s = 0.13 m, T_s = 3.6 s) at Probes P1 (a) and P2 (b) for the 2-Slope Proposition Design. 158
Figure 7.101 Experimental and numerical surface elevations for (IRW_H_s = 0.25 m, T_s = 2.0 s) at Probes P1 (a) and P2 (b) for the Parabolic Proposition Design. ...159
Figure 7.102 Experimental and numerical surface elevations for (IRW_H_s = 0.22 m, T_s = 2.3 s) at Probes P1 (a) and P2 (b) for the Parabolic Proposition Design. ...160
Figure 7.103 Experimental and numerical surface elevations for (IRW_H_s = 0.20 m, T_s = 2.7 s) at Probes P1 (a) and P2 (b) for the Parabolic Proposition Design. ...161
Figure 7.104 Experimental and numerical surface elevations for (IRW_H_s = 0.17 m, T_s = 3.1 s) at Probes P1 (a) and P2 (b) for the Parabolic Proposition Design. ...161
Figure 7.105 Experimental and numerical surface elevations for (IRW_H_s = 0.13 m, T_s = 3.6 s) at Probes P1 (a) and P2 (b) for the Parabolic Proposition Design. ...162
Figure 7.106 Experimental (left) and Numerical (right) power density spectrum of irregular wave with H_s=0.25 m, and T_s= 2.0 s, in case of 2-slopes proposal design. 163
Figure 7.107 Experimental (left) and Numerical (right) power density spectrum of irregular wave with H_s=0.22 m, and T_s= 2.3 s, in case of 2-slopes proposal design. 163
Figure 7.108 Experimental (left) and Numerical (right) power density spectrum of irregular wave with H_s=0.20 m, and T_s= 2.7 s, in case of 2-slopes proposal design. 164
Figure 7.109 Experimental (left) and Numerical (right) power density spectrum of irregular wave with H_s=0.17 m, and T_s= 3.1 s, in case of 2-slopes proposal design. 164
Figure 7.110 Experimental (left) and Numerical (right) power density spectrum of irregular wave with H_s=0.13 m, and T_s= 3.6 s, in case of 2-slopes proposal design. 164

Figure 7.111 Experimental (left) and Numerical (right) power density spectrum of irregular wave with H_s=0.25 m, and T_s= 2.0 s, in case of 3-slopes proposal design 165
Figure 7.112 Experimental (left) and Numerical (right) power density spectrum of irregular wave with H_s=0.22 m, and T_s= 2.3s, in case of 3-slopes proposal design 165
Figure 7.113 Experimental (left) and Numerical (right) power density spectrum of irregular wave with H_s=0.20 m, and T_s= 2.7 s, in case of 3-slopes proposal design. 166
Figure 7.114 Experimental (left) and Numerical (right) power density spectrum of irregular wave with H_s=0.17 m, and T_s= 3.1 s, in case of 3-slopes proposal design. 166
Figure 7.115 Experimental (left) and Numerical (right) power density spectrum of irregular wave with H_s=0.13 m, and T_s= 3.6 s, in case of 3-slopes proposal design. 166
Figure 7.116 Experimental (left) and Numerical (right) power density spectrum of irregular wave with H_s=0.25 m, and T_s= 2.0 s, in case of parabolic proposal design. 167
Figure 7.117 Experimental (left) and Numerical (right) power density spectrum of irregular wave with H_s=0.22 m, and T_s= 2.3 s, in case of parabolic proposal design. 167
Figure 7.118 Experimental (left) and Numerical (right) power density spectrum of irregular wave with H_s=0.20 m, and T_s= 2.7 s, in case of parabolic proposal design. 168
Figure 7.119 Experimental (left) and Numerical (right) power density spectrum of irregular wave with H_s=0.17 m, and T_s= 3.1 s, in case of parabolic proposal design. 168
Figure 7.120 Experimental (left) and Numerical (right) power density spectrum of irregular wave with H_s=0.13 m, and T_s= 3.6 s, in case of parabolic proposal design. 168

LIST OF TABLES

Page

Table 3.1 Validation of the generated wave with the target parameters. 16
Table 3.2 Validation of the adjusted wave with the target parameters. 18
Table 3.3 An example piston displacement for the second-order regular wave. 34
Table 5.1 Probes location and positioning. 62
Table 7.1 Experiments set and simulations results. 82
Table 7.2 Theoretical and numerical data error ratios. 88
Table 7.3 Experimental and numerical data error ratios 88
Table 7.4 Theoretical and experimental data error ratios 89
Table 7.5 Reflection coefficient of the series of numerical simulations. 90
Table 7.6 Reflection coefficient of the experiments on the rocks fill with 1/7 slope. 97
Table 7.7 Reflection coefficient of regular waves of the 3-slopes proposition design. 98
Table 7.8 Reflection coefficient of regular waves of the 2-slopes proposition design. 99
Table 7.9 Reflection coefficient of regular waves of the parabolic proposition design. 100
Table 7. 10 Comparison of the experimental reflection coefficients of regular waves for the selected proposition designs and the rock fill with 1/7 slopes. 101
Table 7.11 Reflection coefficient of regular waves of the selected propositions design. 145
Table 7.12 Reflection coefficient of irregular waves of the 3-slopes proposition design. 150
Table 7.13 Reflection coefficient of irregular waves of the 2-slopes proposition design. 154
Table 7.14 Reflection coefficient of irregular waves of the parabolic proposition design. 158

CHAPTER ONE
INTRODUCTION

Wave flumes allow to investigate fundamental wave phenomena and test theoretical models of wave behavior by generating controlled waves and precisely measuring wave parameters.

1.1 Wave Generation

Hydraulic physical model tests and numerical models constitute the two primary methodologies for studying wave phenomena (formation transformation and breaking) and solving various coastal engineering problems related to coastal infrastructure planning, design, and construction. Today, hydraulic model tests with irregular waves are generally preferred. For this reason, all laboratories are trying to obtain the types of equipment to produce irregular waves for such tests.

Numerical models offer the benefit of being easily applicable to flow fields on a large scale, without the need for costly infrastructure, spaces, or equipment.; and they have a high degree of flexibility in application, adaptation, maintenance, and extension. A numerical model simulated the piston-type wavemaker displacement time series to generate random waves from a target JONSWAP spectrum with FLOW3D. FLOW3D is a software solution designed for the purpose of computational fluid dynamics, allowing for the simulation and modeling of fluid flow. The software is specifically tailored to meet the needs of engineers who are involved in the study of dynamic properties of liquids in physical processes and academic research. The software produces current and accurate simulation results, aiding engineers in their quest for precise data and insights into the behavior of fluids.

The primary objective of this research is to develop a deterministic merger of physical and numerical models for analyzing regular and irregular waves. Due to the research problem, laboratory conditions, and the high initial investment cost, it is challenging to have a wave channel with an irregular wave generator. Achieving this through imports from Europe or the United States is impossible for some developing countries. The system

has been created to generate all forms of regular and irregular waves with domestic capabilities without using expensive types of equipment.

1.2 Wave Absorber

The solid physical model structure constrains all experimental basins and wave flumes in laboratories, causing wave reflection from these boundaries. Unwanted wave reflection distorts the free surface, substantially affecting the incident wave field and disrupting the experiments. Thoroughly executed model analyses aimed to reduce wave reflection by installing wave absorbers at the reflecting boundaries of the flumes. Wave absorbers are divided into two types: passive absorbers, which dump the incident wave through different approaches, and active absorbers that respond to incident wave. Due to the low manufacturing cost and ease of assessment, we'll focus on passive absorber approaches in our research.

Passive wave absorption refers to the process of reducing or eliminating unwanted wave reflections using non-mechanical means. This approach usually involves the careful design and arrangement of materials or structures within the wave tank to dissipate or absorb wave energy, thus minimizing reflections. Several passive wave absorption methods have been developed over the years, each with its unique advantages and limitations. Some of the most common techniques include porous beach systems, perforated wave-absorbing walls, and sloping or stepped beach designs.

This research was carried out in two phases. The first phase was to investigate the various designs for the passive absorption system numerically using FLOW 3D under regular and irregular waves of varying heights and periods, which could be investigated experimentally. The purpose of this step is to assess the capacity to perform to the desired hydraulic characteristics (low value of reflection coefficient), the design's ability to be readily changed, to shorten the passive wave absorber, and the cheap cost of manufacture. The second phase specifies the most efficient and appropriate proposals for carrying out a set of physical modeling tests.

CHAPTER TWO
LITERATURE REVIEW

Previous studies on wave generation and wave absorption in wave channels have explored various methodologies and models to understand the intricate dynamics of these phenomena.

2.1 Wave Generation

In physical modeling, numerous techniques exist for generating waves, with the piston and flap methods being the most prevalent types. Biésel and Suquet (1951) made significant contributions to the theory of wave generation in hydraulic laboratories. They conducted a theoretical investigation based on the linearized Stokes theory and practical analysis of various wave generator types and developed a mathematical model for generating waves in a tank of water, which is still widely used today.

Fontanet (1961) made significant advancements in the theory of regular waves. He developed a mathematical model for generating regular waves of different amplitudes and frequencies in hydraulic laboratories. He presented second order approximation theory for waves generated by a straight-fronted wave generator.

Madsen (1971) formulated an approximate solution for spurious superharmonics generated in shallow water in case of regular waves. He provided valuable insights into wave generation and wave characteristics in shallow water environments, thus minimizing these superharmonics.

Dean and Dalrymple (1984) wrote a book on coastal engineering, which includes a chapter on wave generation techniques. In this chapter, they discuss the design and operation of wave generators, as well as the use of wave generators for studying wave behavior.

Hughes (1993) also wrote a book that includes a chapter on wave generation techniques. In this chapter, Hughes discusses the principles of wave generation and the design of wave generators. He also discusses the use of wave generators for studying the behavior of waves and their effects on coastal structures.

Sand and Mansard (1986), Schäffer (1996) and Schäffer (2003) made significant advancements in the theory of irregular waves. Develops a thorough theory of second order wavemakers for generating multidirectional waves in a semi-infinite basin.

Goda (2000) wrote a book that includes a chapter on wave generation techniques. In this chapter, Goda discusses various wave generation methods used in hydraulic laboratories, such as the piston-type wave generator and the paddle-type wave generator. these studies have contributed significantly to our understanding of wave generation techniques and have paved the way for further research and development in this field.

Eskinja (2008) outlines the development of a wave maker system designed for generating both regular and irregular waves. This system is intended for evaluating the impact of ocean waves on ships and coastal structures. The study includes the generation of irregular waves using various density spectral functions.

Frigaard (2010) authored a technical report that includes a chapter introducing numerical techniques for wave generation and provides a detailed discussion on the application of the Biesl transfer function within the context of piston and flap-type wave generators.

Schmittner (2013) primarily concentrated on providing an extensive overview of the latest advancements in advanced basin wave modeling. This encompassed various aspects, such as realistic wave spreading, deterministic wave generation, focused waves, directional wave analysis, spurious wave effects, and the generation of shallow water waves.

Aktas (2020) focuses on investigating the dynamic performance of various designs for Floating Offshore Wind Turbines (FOWT) when subjected to wind and wave forces. The study establishes a laboratory setup for wave generation, analysis, and testing. The study provides theoretical background information on creating both regular and irregular waves and explains the oscillations needed for the wave generator paddle. It utilizes wavemaker theory to derive second-order solutions, which are then applied to a piston-type wave generator to better mimic natural waves in laboratory conditions.

2.2 Wave Absorber

Research has shown that various structural (perforated screen, transversal bars, porous materials) and geometrical (sloping-faced system, parabolic-faced system) designs that might take up valuable space in the wave flume can be used for passive wave absorbers. Studies have been conducted to evaluate the effectiveness of different wave absorbers in reducing the reflection of waves (lowest ratio of the reflection coefficient Cr). For example, researchers have compared the performance of foam and concrete absorbers in terms of their ability to absorb wave energy and reduce wave height. Some studies have also focused on optimizing the design of wave absorbers, including the shape, size, and arrangement of the absorbers.

Lean (1967) conducted an analysis to ascertain the reflection coefficient for permeable wave absorbers of different shapes using the linear long wave theory. Experimental investigations on absorbers with vertical-wall, uniformly sloped, and parabolic profiles. The findings suggested that utilizing a parabolic profile had the benefit of decreasing the length of the absorber. Lean recommended a length range of roughly 0.5 to 0.75 times the incident wavelength (represented as L), to achieve reflection coefficient value less than 0.05 are theoretically attainable.

Le Méhauté (1972) introduced a progressive wave absorber design that achieves gradual dissipation of incident wave energy. The absorber consists of multiple sections, where each of section dissipates a portion of the wave energy while reflecting or

transmitting the remaining energy as shown in Figure 2.1. Experimental investigations were conducted using a 1 m length wave absorber installed vertically in a towing tank, constructed from 10 mm chicken wire mesh. For specific parameters of a wavelength of 1.080 mm, a wave period T of 1 second, a water depth of 150 mm, and wave height of 40 mm. At a particular cell position, the reflection coefficient was observed to be approximately 0.02.

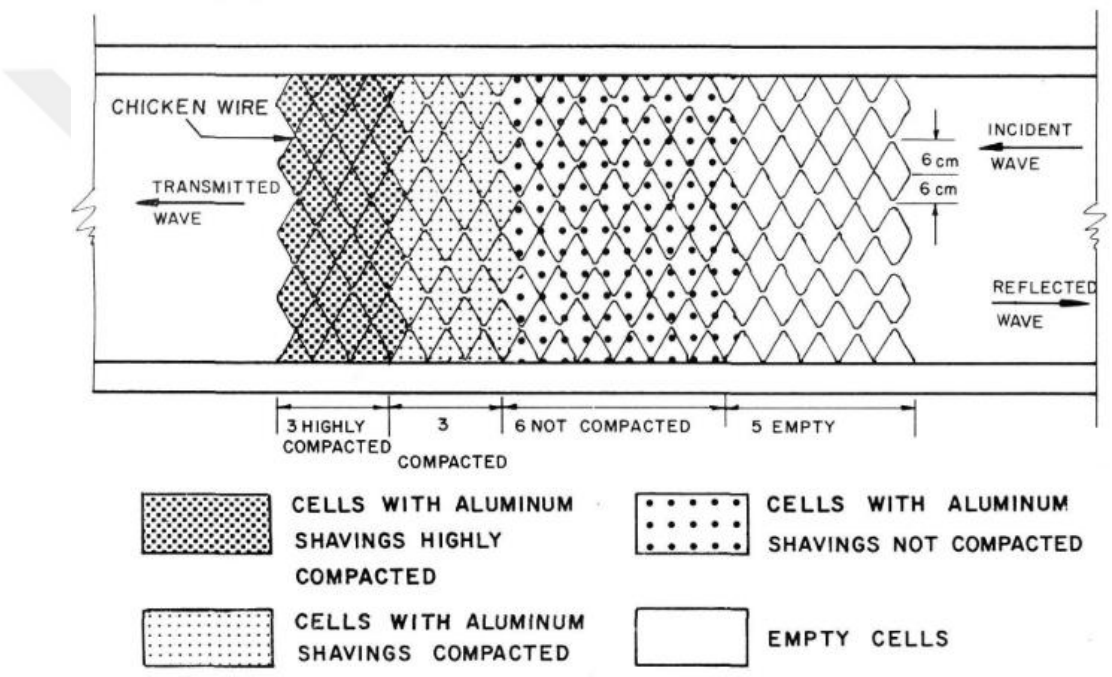

Figure 2.1 The wave absorber designed by Le Méhauté (Le Méhauté, 1972).

Ouellet and Datta (1986) investigated wave absorber systems (Figure 2.2) by doing a complete literature analysis of existing literature and the distribution of a questionnaire to 162 hydraulics and ship model facilities. The study aimed to ascertain the ideal wave absorber and offer suggestions for forthcoming research. Results unveiled that, under a specific slope, the reflection coefficient of impermeable plane-sloped wave absorbers diminished with an increase in wave steepness. Additionally, similar changes in the reflection coefficient with regard to the wave absorber slope were also noted. observed to be comparable between stone crushed rocks and wire meshes for slope angles below 15°.

Based on these outcomes, the most efficient configuration for a wave absorber was suggested to be the parabolic profile.

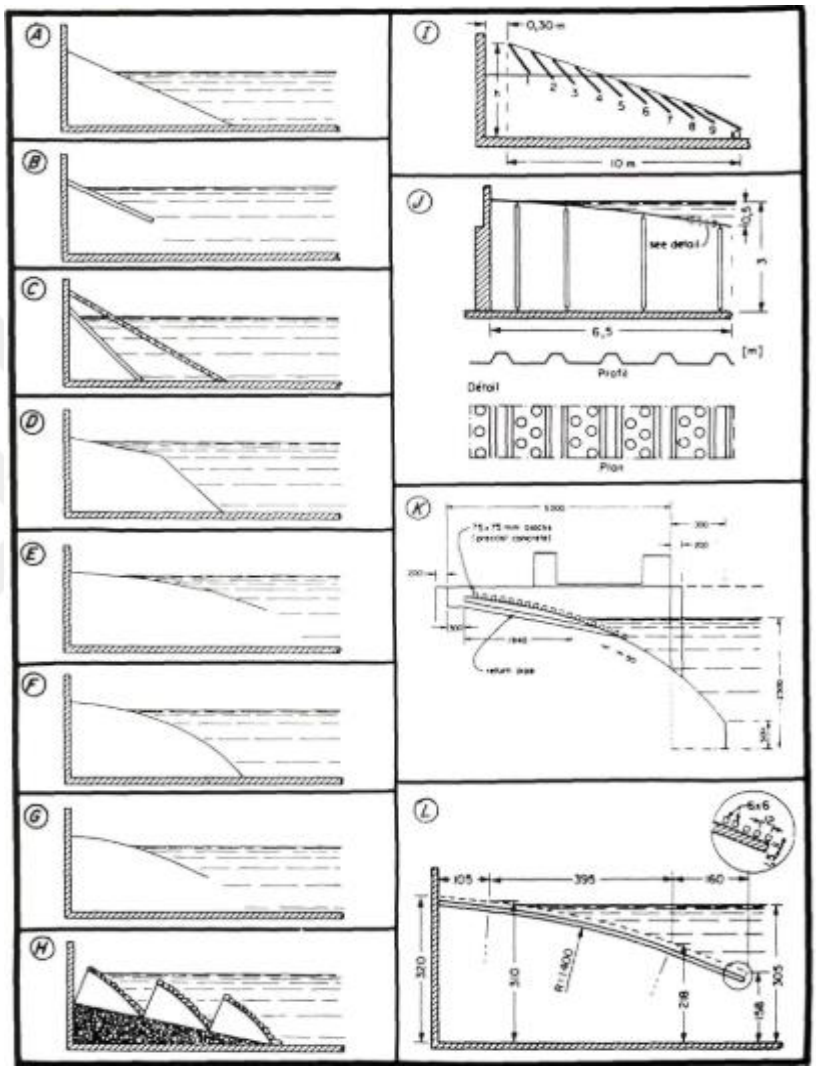

Figure 2.2 The different wave absorbers systems investigated (Ouellet and Datta, 1986) .

Chegini (1993) conducted laboratory experiments using a permeable sloping wave absorber that was coated with a layer of artificial horsehair material (Figure 2.3). Experiments were conducted on the absorber using inclinations of 10%, 15%, and 20%. The findings demonstrated that, under a given slope, the reflection coefficient declined with rising wave steepness. Notably, the reflection coefficient for the 10% slope was lower than that for the 6% slope within the wave steepness range of 0.01 to 0.1. Furthermore,

the study revealed that relative water depths (water depth to wavelength ratio) variations within the range of 0.125 to 0.4 did not exert a notable influence on the reflection coefficient.



Figure 2.3 The permeable sloping absorber (Chegini, 1993).

Chegini (1995) conducted experimental investigations to analyze the reflection and transmission characteristics of vertically perforated plates, exploring diverse porosity levels and wave steepness magnitudes. The experiment included two categories of plates, conventional perforated plates (Figure 2.4) with porosity levels of 23%, 40%, and 62%, along with expanded metal plates (Figure 2.5) exhibiting porosity levels of 26%, 42%, and 58%. The experiments were conducted using a consistent water depth of 80 centimeters, while the wave steepness values varied between 0.003 and 0.01. The results indicated a positive correlation between the reflection coefficient and increasing wave steepness.

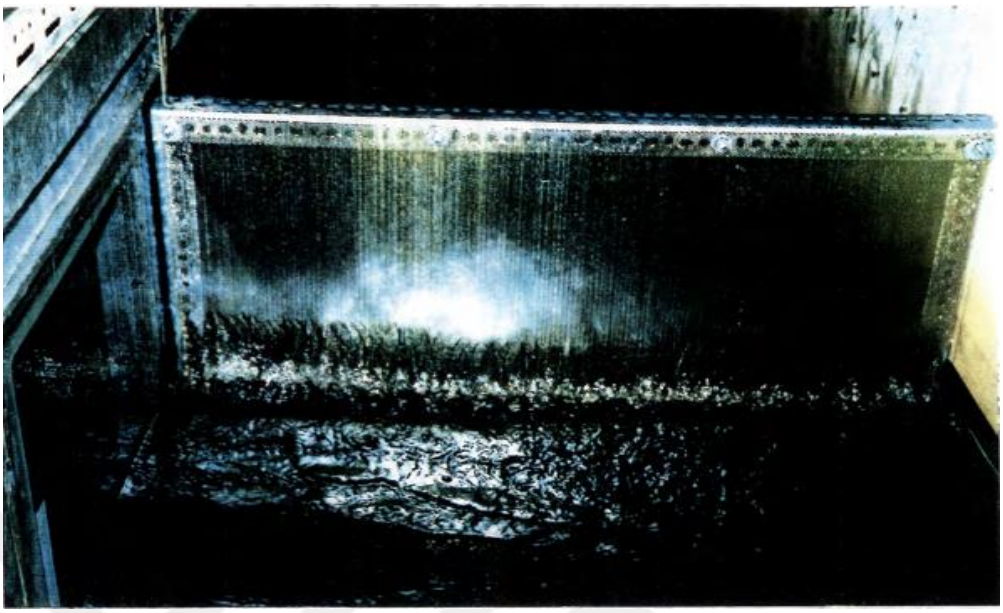

Figure 2.4 Front view of the screen perforations (Chegini, 1995).

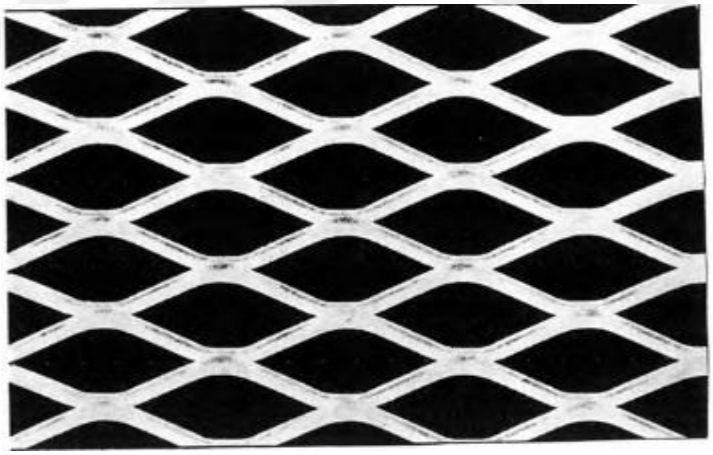

Figure 2.5 A view of the expanded metal sheet (Chegini, 1995).

Wu et al. (1998) Conducted a numerical investigation into the reflection coefficient of a wave absorber profile that included a submerged horizontal porous plate and an end wall. Through their numerical analysis, they found that the reflection coefficient exhibited a decreasing trend as the porosity of the absorber system increased. Additionally, they observed that the reflection coefficient initially decreased and then increased with increasing relative water depth for a specific porosity level.

Twu and Chieu (2000) proposed an offshore breakwater design (Figure 2.6) aimed at achieving low values of both the reflection coefficient (Cr) and the transmission coefficient (Ct). The breakwater consisted of multiple layers of porous materials with varying porosities. To validate their theoretical computations, experimental tests were conducted using wave periods ranging from 0.3 to 1.5 seconds and wave heights reaching up to 150 mm. showed that as the spacing between porous plates increased, the reflection coefficient initially rose but eventually reached a steady state. Moreover, the results indicated a gradual decrease in the wave transmission coefficient with increasing spacing between the porous plates. Additionally, the wave reflection coefficient demonstrated an upward trend as porosity decreased, whereas alterations in porosity and spacing had negligible impact on the reflection and transmission coefficients.

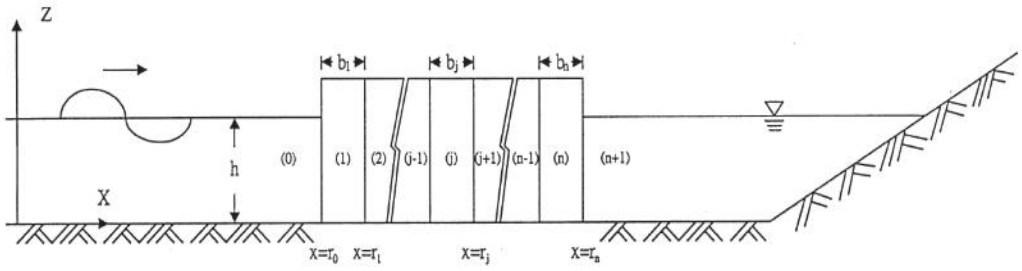

Figure 2.6 Sketch diagram of an offshore breakwater of porous materials (Twu and Chieu, 2000).

Liu et al. (2007) conducted a numerical investigation on the reflection coefficient of a wave absorber setup. The setup comprised an end wall, a perforated vertical wall, and a perforated horizontal plate in between. The addition of the horizontal perforated plate improved both stability and absorption efficiency of the absorber. The research unveiled an initial increase and subsequent decrease in the reflection coefficient as the relative water depth grew. Furthermore, optimal performance of the absorber was achieved when the horizontal porous plate was positioned closer to the surface of water. As a practical recommendation for engineering applications, the researchers proposed that the vertical perforated plate should exhibit a porosity ranging from 20% to 40%.

Rostaminia and Chegini (2008) conducted a comprehensive investigation into the wave reflection and transmission characteristics exhibited by a singular perforated flat plate. This flat plate was methodically positioned at inclinations of 60°, 75°, and 90° relative to the horizontal plane, and its structural composition encompassed porosity levels of 21%, 44%, and 48%. The empirical validation of their study was conducted within a controlled laboratory environment utilizing a wave flume of precise dimensions: 32.5 meters in length, 5.5 meters in width, and 1 meter in depth, with a constant water depth of 0.5 meters. The experimental setup involved the generation of regular waves with periods ranging from 1.25 to 2.5 s and wave heights between 76 mm and 184 mm. The findings demonstrated that an increase in the sloped screen parameter Resulted in a reduction of the reflection coefficient (Cr) and a corresponding augmentation in the transmission coefficient (Ct). Additionally, the study revealed concomitant with heightened incident wave steepness, the reflection coefficient demonstrated an escalation, whereas the transmission coefficient exhibited a decrement.

Tideman (2012) represent an extensive review of passive absorber methods is conducted, followed by the development and deployment of a device designed to operate beneath the water's surface. The modeling tests presented herein illustrate that a parabolic submerged beach can effectively absorb waves, achieving reflection coefficients well below 10%.

Hodaei (2016) conducted a series of experimental trials to investigate the impact of perforated plate curvature on wave reflection coefficient. The investigations centered around a curved model, mathematically defined as $y = -x^2$ (Figure 2.7). The researchers systematically manipulated the curvature of a reference perforated plate by implementing a rotational transformation based on a parabolic equation. A plunger type wave generator was employed to induce regular wave patterns. The outcomes substantiated the notable efficacy of perforated plates with curved configurations in substantial mitigation of the wave reflection coefficient.

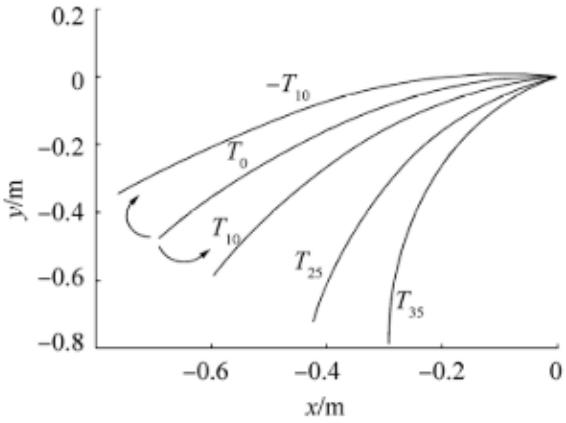

Figure 2.7 Geometry of a few models tested by Hodaei (Hodaei, 2016).

As there are relatively few studies on sloped plate-type wave absorbers, we have established both numerical and experimental investigations on a range of non-perforated sloped plates in the Dokuz Eylül University Hydraulic Laboratory wave flume.

CHAPTER THREE
WAVE GENERATION AND ANALYSIS

The purpose of this chapter is to explore the various methods and techniques used in wave generation and analysis. Specifically, it will delve into the analysis of JONSWAP spectrum, the utilization of the Random Phase Method, and the theoretical aspects of the Wave maker theory.

3.1 Wave Analysis

3.1.1 Wave Spectral Analysis

Spectrum analysis is extensively used in the study of noise-like signals because it gives a frequency split into harmonics, the behavior of which may be analyzed independently. It is usual to describe a wave train using its energy. A mathematical formula is frequently used to characterize a wave train's spectrum. Relevant actual recorded wave data under various settings yielded these mathematical calculations. Spectral densities are expressed as a function of variables (such as wind speed and fetch length) or as data defining the sea state (significant wave height H_s and peak frequency f_p). The Equation (3.1) used in this study employs the JONSWAP spectra $S(f)$ as described by Y. Goda (2000, Chapter 2), which is formulated with reference to parameters encompassing wave height and period.. The JONSWAP is a widely used spectrum in wave estimation applications representing fully-developed sea states and may be expressed as the following:

$$S(f) = \beta_J H_{\frac{1}{3}}^2 T_p^{-4} f^{-5} \; exp\left[-1.25\left(T_p f\right)^{-4}\right] \gamma^{exp\left[-\frac{\left(T_p f-1\right)^2}{2\sigma^2}\right]} \tag{3.1}$$

The JONSWAP parameter β_J ,the spectral shape parameter σ , the significant wave height $H_{1/3}$, the peak period T_p , the frequency f, and the peak enhancement factor γ ,which varied from 1 to 7 with a mean value of γ=3.3, are all involved in the study.

$$\beta_J = \frac{0.0624}{0.230 + 0.0336\gamma - 0.185(1.9 + \gamma)^{-1}}[1.094 - 0.01915ln\gamma] \quad (3.2)$$

$$T_p \cong T_{\frac{1}{3}}/[1 - 0.132(\gamma + 0.2)^{-0.559}] \quad (3.3)$$

$T_{1/3}$ Is the significant period.

$$\sigma=0.07\ for\ f \leq fp \qquad \sigma=0.09\ for\ f>fp \quad (3.4)$$

f_p indicates the peak frequency

3.1.2 Time-domain Analysis

The time-domain analysis in this study utilizes the zero-up crossing technique to characterize the wave. This involves identifying the points in the irregular wave time series where the surface elevation crosses the zero-line or mean water level (MWL) upward, and continuing to track the wave until the next crossing point. The zero line or still water level is established by calculating the average of the entire water surface profile. A single wave is defined as the event between two consecutive zero-up crossing points, as shown in Figure 3.1. The wave height H is determined as the vertical distance between the highest and lowest points, while the wave period T is measured as the time interval between the starting and finishing points of each wave.

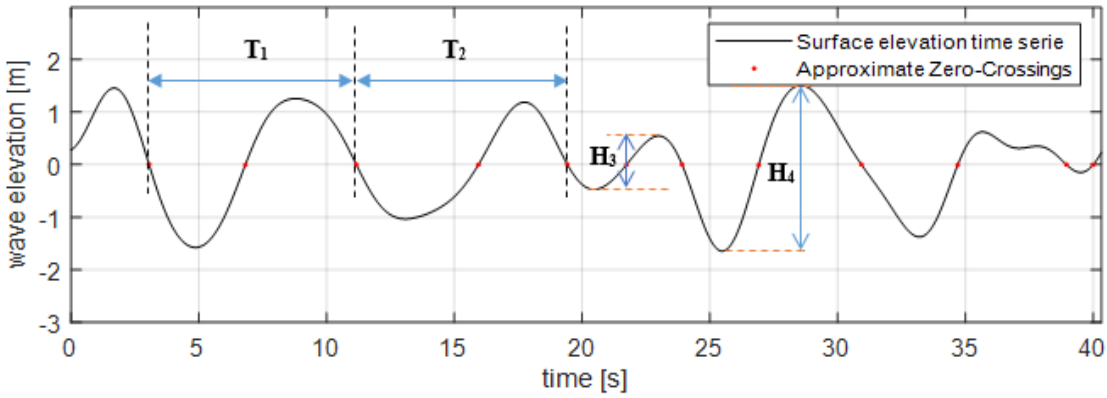

Figure 3.1 Waves defined by zero-up crossing.

3.1.3 Random Wave Generation

Two methods are available for creating random wave surface profiles from a specified target spectrum: the deterministic spectral amplitude method and non-deterministic spectral amplitude methods. This study calculates waveforms from the JONSWAP spectrum using a deterministic wave generation technique called the Random Phase Method.

After the specification of the energy density spectra of the surface wave profile (target spectrum) and choosing the sampling frequency, the wave amplitude and phase angle associated with a frequency f may be obtained from the following:

$$a(f) = \sqrt{2S(f)\Delta f}$$
$$\varepsilon(f) = 2\pi r_N \tag{3.5}$$

As the phase angle ε is a uniformly distributed random number between zero and one, it is deemed to be an arbitrary. The choice affects the value of the wave height. However, as long as it is small, this approach gives an excellent random wave profile. The random wave surface elevation is created by superposing linear waves with varying wave heights, periods, and phases; the superposed wave surface elevation is given as the following:

$$\eta(t) = \sum_{n=1}^{N} a(n)\, cos[2\pi f(n)t + \varepsilon(n)] \tag{3.6}$$

3.1.4 Random Phase Method Improvement

This study presents an example of generating irregular waves, with the parameters set as T_s = 7.8 s and H_s = 3.6 m. The frequency spectrum type used is JONSWAP with a peak enhancement factor of γ = 3.3, and a frequency step of Δf = 0.001 Hz. The time step is set at Δt = 0.01 s**.** A comparative analysis is conducted between the spectrum derived from the time series of irregular waves and the theoretically target spectrum. in Table 3.1. Figure 3.2 shows the time series of the water surface profile and its corresponding JONSWAP spectrum.

Table 3.1 Validation of the generated wave with the target parameters.

Parameters	**Values from zero-up crossing**	**Target values**
The significant wave height $\boldsymbol{H_s}$ (m)	3.3674	3.6000
Significant wave period $\boldsymbol{T_s}$ (s)	7.3317	7.8000
Peak frequency $\boldsymbol{f_p}$ (Hz)	0.1275	0.1198
Max energy $\mathbf{S}(\boldsymbol{f_p})$ (m^2s)	18.3867	22.380

(a) Time series.

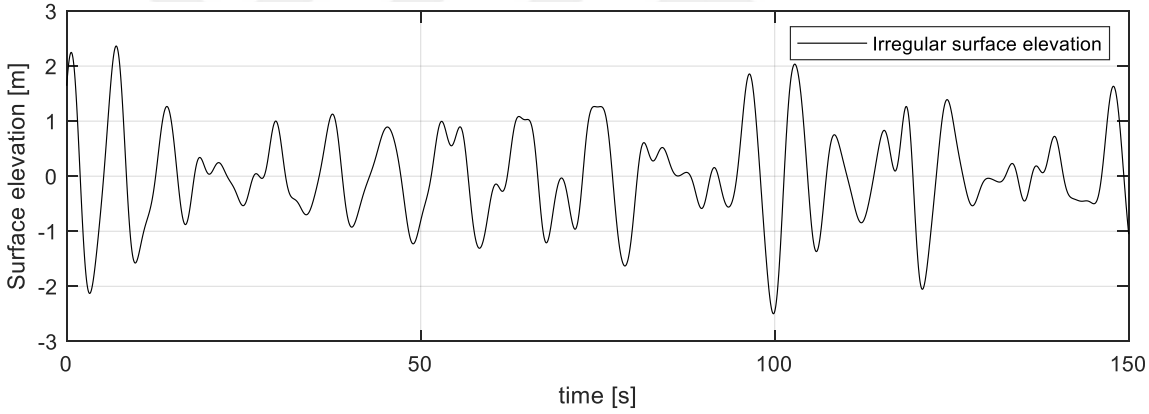

(b) JONSWAP spectrum

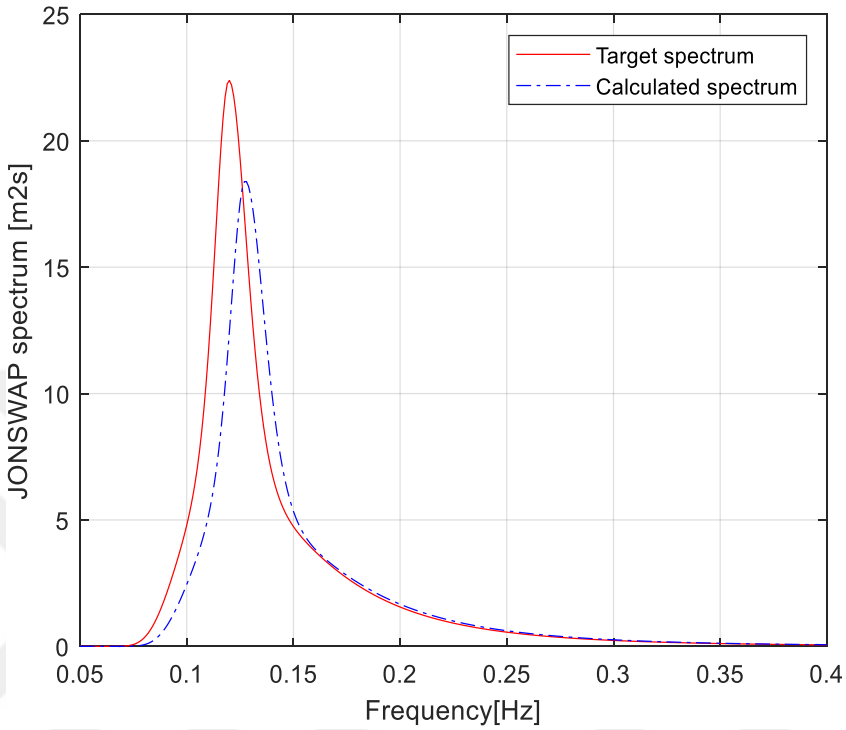

Figure 3.2 An irregular wave's surface elevation time series and its JONSWAP spectrum.

To validate the wave generation technique, we suggest a correction factor for the significant height and another for the significant period, which will be sufficient to obtain the target spectrum.

$$CF_{H_s} = \frac{H_{s_{target}}}{H_{s_{calculated}}}$$
$$CF_{T_s} = \frac{T_{s_{target}}}{T_{s_{calculated}}} \tag{3.7}$$

The wave profile will be adjusted with the following equation:

$$\eta_{adj}(t) = \sum_{n=1}^{N} (a_{cal}(n) \times CF_{H_s}) \cos\left[2\pi f(n)\left(\frac{1}{CF_{T_s}}\right)t + \varepsilon_{cal}(n)\right] \tag{3.8}$$

In Table 3.2 , a comparison is made between the wave properties obtained from the zero up crossing analysis of the adjusted random wave time series and those obtained from the target spectrum, as shown in Figure 3.3.

Table 3.2 Validation of the adjusted wave with the target parameters.

Parameters	**Values from adjusted time-series**	**Target values**
The significant wave height $\boldsymbol{H_s}$ (m)	3.600	3.600
Significant wave period $\boldsymbol{T_s}$ (s)	7.790	7.800
Peak frequency $\boldsymbol{f_p}$ (Hz)	0.119	0.119
Max energy $\mathbf{S}(\boldsymbol{f_p})$ (m^2s)	22.380	22.380

(a) Probe P1 Time series.

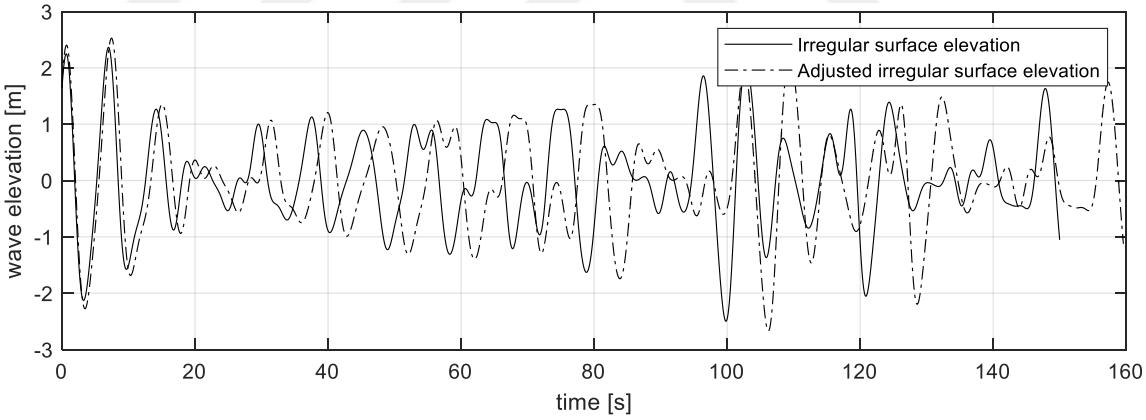

(b) Probe P2 JONSWAP spectrum.

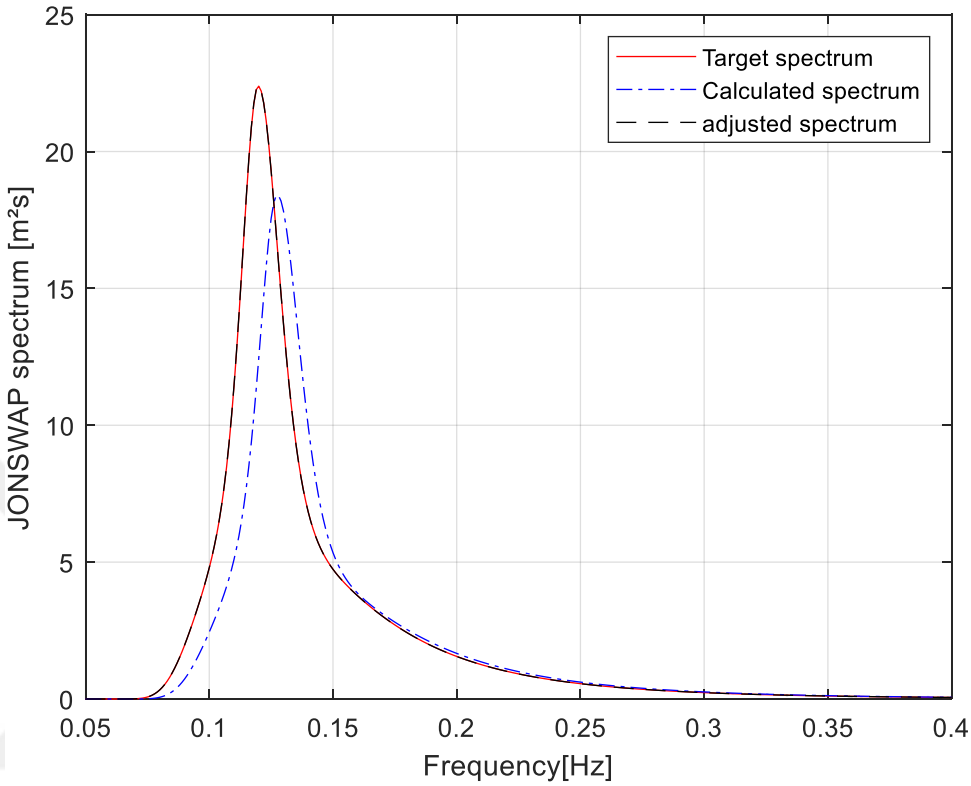

Figure 3.3 An irregular wave's adjusted surface elevation time series and its JONSWAP spectrum.

According to the data in Table 3.2 and as indicated in Figure 3.3 , the target JONSWAP spectrum and the adjusted random wave series are precisely matched, indicating that the random phase method was correctly applied in this study.

3.1.5 Wave Board Displacement Time Series

In accordance with the information presented in section 3.2.1.2.1, Equation (3.65) is employed to determine the target spectrum of the wave paddle motion, denoted as $S_{paddle}(f)$, based on the target wave spectrum, $S(f)$.The wave paddle motion (Figure 3.4) is then achieved using the Random Phase Method, employing identical randomly generated phases as those utilized for the irregular waves. Figure 3.10 shows a plot of the paddle displacement over the number of data points, which equals to the time of the experiment divided by the sampling rate Δt in seconds.

$$S_{paddle}(f) = S(f)/F^2 \tag{3.65}$$

F is the Biesel transfer function for piston-type wavemaker (eq.11).

$$F = \frac{4\ sinh^2}{2k_0h + \sinh(2k_0h)} \tag{3.48}$$

Where h is the water depth, and the wavenumber k_0 is the solution to the dispersion relation:

$$\omega^2 = gk_0 \tanh(k_0h) \tag{3.49}$$

Where g is gravity acceleration, and ω is the angular frequency ($\frac{2\pi}{T}$).

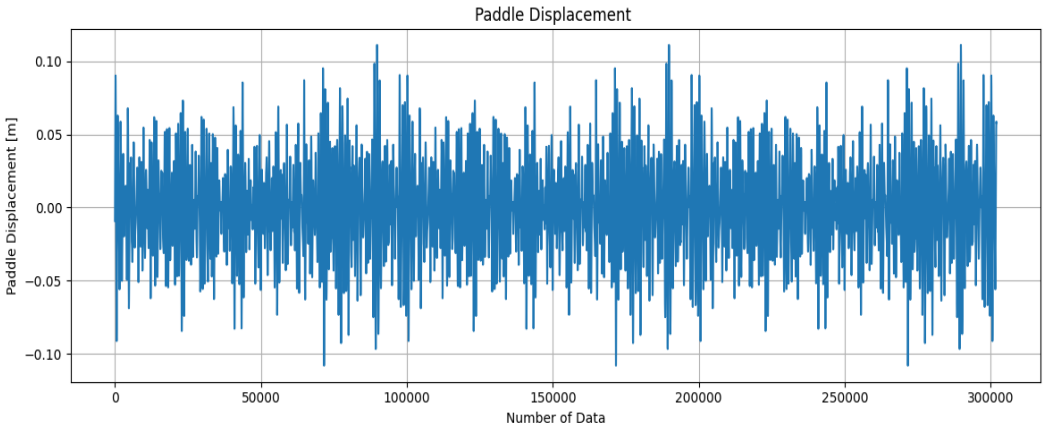

Figure 3.4 An example of the paddle control signal (H_s=0.144 m, T_s=1.56 s, duration=600 s, and Δt=0.002s).

3.1.6 Preparation of Random Wave Generation Signal

Our study typically follows the flow diagram shown in Figure 3.5 to process the input signal and generate irregular waves with the desired characteristics (H_s and T_s).

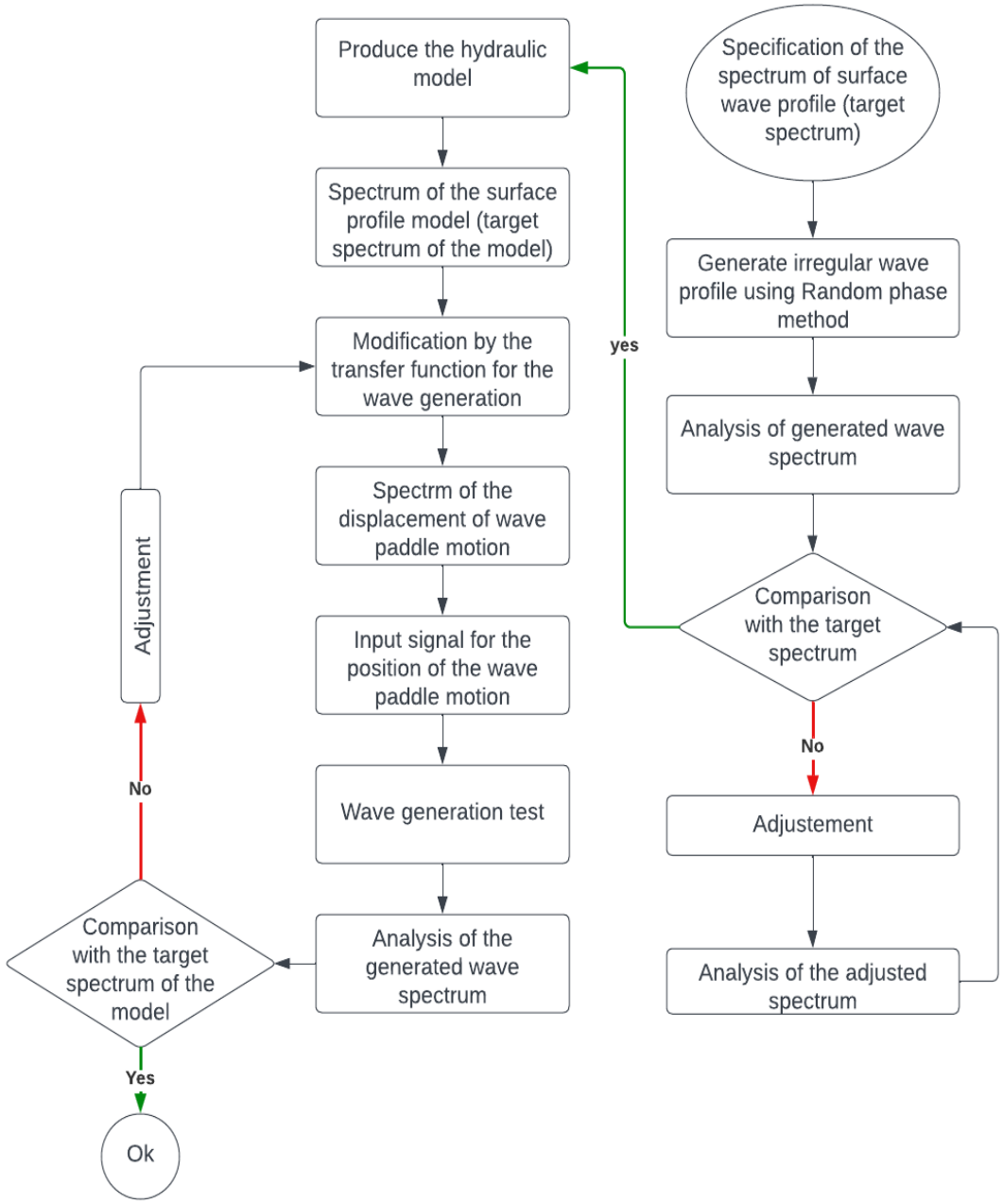

Figure 3.5 Flow diagram of the preparation of the input signal to an irregular wave generator.

3.2 Wave Maker Theory

The wave maker theory refers to the concept of a hypothetical wave maker device that generates regular and irregular waves in a laboratory setting. By accurately replicating the various characteristics of ocean waves, such as wavelength, height, and period. The wave maker theory plays a critical role in advancing our understanding of coastal dynamics and improving the resilience of coastlines.

Havelock's 1929 work laid the groundwork for the theory of wavemakers, which focused on sea surface vertical oscillations caused by planar or cylindrical solid bodies. Biesel later expanded upon the theory in 1951, Offering solutions for various categories of wave generators, encompassing piston and flap mechanisms, the theory has undergone substantial enhancements over time, encompassing both regular and irregular wave scenarios. as seen in Fontanet's 1961 work, and irregular waves, as explored by Sand and Mansard in 1986 and Schäffer in 1996 and 2002.

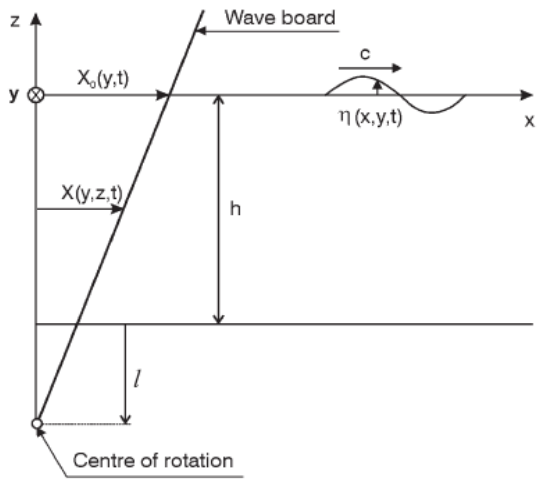

Figure 3.6 Definition sketch (Schäffer 2003).

3.2.1 Governing Equations

The movement of an inviscid, irrotational fluid within a wave flume is governed by the two-dimensional Laplace equation, in combination with the suitable boundary conditions. Specifically, in the Cartesian coordinate system shown in Figure 3.6, the Laplace equation

can be expressed in terms of the velocity potential, which is $\emptyset = \emptyset(x, z, t)$ and $u = \emptyset_x$, $v = \emptyset_z$, as follows:

Laplace Equation:

$$\frac{\partial^2 \emptyset}{\partial x^2} + \frac{\partial^2 \emptyset}{\partial z^2} = 0 \tag{3.9}$$

Bottom Boundary condition Equation : $at\ z = -h$

$$\frac{\partial \emptyset}{\partial z} = 0 \tag{3.10}$$

Kinematic Free Surface Condition : $at\ z = \eta$

$$\frac{\partial \eta}{\partial t} + \frac{\partial \emptyset}{\partial x}\frac{\partial \eta}{\partial x} - \frac{\partial \emptyset}{\partial z} = 0 \tag{3.11}$$

Dynamic Free Surface Boundary Condition : $at\ z = \eta$

$$\frac{\partial \eta}{\partial t} + \frac{1}{2}\left[\left(\frac{\partial \eta}{\partial x}\right)^2 + \left(\frac{\partial \emptyset}{\partial z}\right)^2\right] + g\eta = 0 \tag{3.12}$$

Wave Board Boundary condition: $at\ z = X(z, t)$

$$\frac{\partial \emptyset}{\partial x} = \left(1 + \frac{z}{h + l}\right)\frac{\partial X_0(t)}{\partial t} \tag{3.13}$$

In which: t is time, g is gravitation acceleration, h water depth, η the water surface elevation, X wave board position.

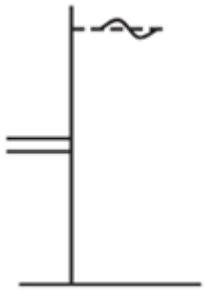

Figure 3.7 Scetch of wave board with translatory motion (piston type) (Schäffer 2003).

The position of wave board position is

$$X(z,t) = f(z)X_0(t) \tag{3.14}$$

Where $f(z)$ denotes the type of wave board motion

$$f(z) = \begin{cases} 1 + \dfrac{z}{h+l} \; for - (h-d) \le z \le 0 \\ 0 \; for - h \le z < -(h-d) \end{cases} \tag{3.15}$$

Denotes that $z = -(h+l)$ describes the center of rotation $(-h < l \le \infty)$. In case of piston type wave maker the center of rotation is at the bottom then $d = 0$ and $l \to \infty$ (Figure 3.7), that make the last case in Equation (3.15) impractical.

The approach involves employing perturbation theory alongside Taylor expansion of boundary conditions at the free surface and wave board. This leads to a derived boundary value problem for the first and second order wave contributions. This leads to perturbation expansions for the surface elevation, velocity potential, and wave board position corrected up to the second order, as shown in Equation (3.14). Therefore, we can obtain a more accurate solution for these parameters by incorporating the second-order corrections obtained through this method.

$$\eta = \varepsilon\eta^{(1)} + \varepsilon^2\eta^{(2)} \tag{3.16}$$

$$\emptyset = \varepsilon\emptyset^{(1)} + \varepsilon^2\emptyset^{(2)} \tag{3.17}$$

$$X_0 = \varepsilon X_0^{(1)} + \varepsilon^2 X_0^{(2)} \tag{3.18}$$

The parameter ε in this context represents the wave steepness and is assumed to be small. Integrating perturbed quantities into Taylor-expanded boundary conditions and organizing terms of first and second order allows us to express the governing equations in the following manner:

$$\emptyset_{xx} + \emptyset_{yy} + \emptyset_{zz} = 0 \ \ in\ fliud \tag{3.19}$$

$$g\emptyset_z + \emptyset_{tt} = R \ \ for\ z = 0 \tag{3.20}$$

$$\emptyset_z = 0 \ \ for\ z = -h \tag{3.21}$$

$$\emptyset_x = Q\ for\ x = 0 \tag{3.22}$$

Equations (3.19) to (3.22) cover the first order problem for $(\emptyset, \eta) = (\emptyset^{(1)}, \eta^{(1)})$,where R, Q, P are given as:

$$R^{(1)} = 0 \tag{3.23}$$

$$Q^{(1)} = f(z)X_{0t}^{(1)} \tag{3.24}$$

$$P^{(1)} = 0 \tag{3.25}$$

And the second order problem for $(\emptyset, \eta) = (\emptyset^{(2)}, \eta^{(2)})$

$$R^{(2)} = -\left\{\left(\emptyset_x^{(1)^2} + \emptyset_z^{(1)^2}\right)_t + \eta^{(1)}\left(\emptyset_{tt}^{(1)} + g\emptyset_z^{(1)}\right)_z\right\} \tag{3.26}$$

$$Q^{(2)} = -X_0^{(1)}\left\{f(z)\emptyset_{xx}^{(1)} - \frac{1}{h+l}\emptyset_z^{(1)}\right\} + f(z)X_{0t}^{(2)} \tag{3.27}$$

$$P^{(2)} = \frac{1}{2}\left(\emptyset_x^{(1)^2} + \emptyset_z^{(1)^2}\right) + \eta^{(1)}\emptyset_{zt}^{(1)} \tag{3.28}$$

Because the second-order Equations (3.19) to (3.22) and (3.26) to (3.28) are linear with respect to $\eta^{(2)}$ and $\emptyset^{(2)}$, the boundary value problem can be divided into a wave problem and problems that consider the wavemaker. To make this easier, the second order problem can be expressed as a combination of three terms, as described in Barthel et al. (1983).

$$\emptyset^{(2)} = \emptyset^{(21)} + \emptyset^{(22)} + \emptyset^{(23)} \tag{3.29}$$

$$\eta^{(2)} = \eta^{(21)} + \eta^{(22)} + \eta^{(23)} \tag{3.30}$$

We have for $(\emptyset, \eta) = (\emptyset^{(21)}, \eta^{(21)})$:

$$R^{(21)} = -\left\{\left(\emptyset_x^{(1)^2} + \emptyset_z^{(1)^2}\right)_t + \eta^{(1)}\left(\emptyset_{tt}^{(1)} + g\emptyset_z^{(1)}\right)_z\right\} \tag{3.31}$$

$$Q^{(21)} = arbitrary \tag{3.32}$$

$$P^{(21)} = \frac{1}{2}\left(\emptyset_x^{(1)^2} + \emptyset_z^{(1)^2}\right) + \eta^{(1)}\emptyset_{zt}^{(1)} \tag{3.33}$$

For $(\emptyset, \eta) = (\emptyset^{(22)}, \eta^{(22)})$:

$$R^{(22)} = 0 \tag{3.34}$$

$$Q^{(22)} = \begin{cases} -X_0^{(1)}\left\{f(z)\emptyset_{xx}^{(1)} - \dfrac{1}{h+l}\emptyset_z^{(1)}\right\} - \emptyset_x^{(21)}, for -(h-d) \le z \le 0 \\ \emptyset_z^{(21)} \qquad\qquad\qquad\qquad\qquad\qquad\qquad\qquad , for -h \le z < -(h-d) \end{cases} \tag{3.35}$$

$$P^{(22)} = 0 \tag{3.36}$$

And for $(\emptyset, \eta) = (\emptyset^{(23)}, \eta^{(23)})$

$$R^{(23)} = 0 \tag{3.37}$$

$$Q^{(23)} = f(z)X_{0t}^{(2)} \tag{3.38}$$

$$P^{(23)} = 0 \tag{3.39}$$

The function $\emptyset^{(21)}$ represents the bound waves that result from the interaction between first order wave components, including mutual evanescent mode interactions from the first order wavemaker problem. On the other hand, $\emptyset^{(22)}$ represents the free waves that occur due to the wavemaker leaving its mean position and $\emptyset^{(21)}$ causing a mismatch in the boundary condition at the wavemaker. Finally, $\emptyset^{(23)}$ represents the free waves that are generated by the second-order wave board motion, which have been adjusted to prevent the generation of free sub- and superharmonics.

In order to eliminate any spurious-free waves, it is necessary to determine the second-order wavemaker solution for $X_0^{(2)}(t)$, which ensures that $\eta_0^{(23)}$satisfies the following equation:

$$\eta_0^{(22)} + \eta_0^{(23)} = 0 \tag{3.40}$$

3.2.1.1 Regular Waves Generation

Madsen (1974) and Gilbert (1976), among others, were able to obtain the first-order solution for the problem described in Equations (3.19) to (3.22)when combined with Equations (3.23) to (3.25). It is important to note that this problem is linear in $\emptyset^{(1)}$. When the separation constant is real $k_1^2 > 0$, $k_2 = 0$, and imaginary $k_3^2 < 0$, the velocity potential can be expressed in the following:

$$\emptyset^{(1)}(x,z,t) = A\cosh[k_1(h+z)]\sin(k_1 x - \omega t) + \cos\omega t \sum_{n=1}^{\infty} C_n e^{-k_{3_n} x}\cos[k_{3_n}(z+h)] \tag{3.41}$$

While:

$$A = \frac{\omega S_0 \int_{-h}^{0} f(z)\cosh[k_1(z+h)]dz}{2k_1\cosh^2[k_1(z+h)]dz} \tag{3.42}$$

$$C_n = \frac{\omega S_0 \int_{-h}^{0} f(z)\cos\left[k_{3_n}(z+h)\right]dz}{2k_{3_n}\cosh^2\left[k_{3_n}(z+h)\right]dz} \tag{3.43}$$

Where S_0 is the wave board stroke at $= 0$.

Assuming that the wave board is subjected to sinusoidal driving motion that corresponds to:

$$X_0^{(1)} = \frac{S_0}{2}\sin\omega t \tag{3.44}$$

To solve the first-order wavemaker problem, the solution needs to be formulated by substituting the velocity potential provided in Equation (3.41) into the dynamic free surface boundary condition given in Equation (3.12). This will result in the determination

of the sea surface elevation in the wave tank. Finally, the boundary condition should be evaluated at z=0.

$$\eta^{(1)}(x,t) = \frac{\omega A}{g}\cosh[k_1 h]\cos(k_1 x - \omega t) + \sin(\omega t)\sum_{n=1}^{\infty}\frac{\omega\, C_n}{g}\, e^{-k_{3n}x}\cos(k_{3_n h}) \tag{3.45}$$

Away from the wave board, all the summation terms become insignificant, and for the first order, the sea surface can be approximated by the progressive wave solution.

$$\eta^{(1)}(x,t) = H\cos(k_1 x - \omega t) \tag{3.46}$$

H is the wave height, evaluating the Equations (3.45) and (3.46) , the base wave maker relationship is :

$$H = \frac{2\omega A}{g}\cosh(k_1 h) \tag{3.47}$$

The substation of Equation (3.15) into Equation (3.47) and after some algebra, the piston type wave maker ($l \to \infty$) yields:

$$F = \frac{H}{S_0} = \frac{4\sinh^2 kh}{\sinh 2kh + 2kh} \tag{3.48}$$

F is the transfer function obtained from Biesl's solution of the wave velocity potential, and k is the wave number calculated by the linear dispersion relation for complex numbers (Schäffer, 2003):

$$\omega^2 = gk\tanh(kh) \tag{3.49}$$

The solution has been extended to include complex wave numbers, as described in the work of Dean and Dalrymple in 1991. In this solution, the component of the wave field that is progressive is represented by the real solution for j = 0, while the series of evanescent modes is represented by the purely imaginary solutions for j = 1 to infinity.

$$\omega^2 = -gk_j \tan(k_j h) \tag{3.50}$$

which is the dispersion relation for the evanescent modes.

Figure 3.8 displays the wave height wave maker stroke ratio graph for piston wavemaker movements in water depths of d=0.55 m. This graph facilitates the quick estimation of wave height based on the stroke of the wavemaker. The solution for a piston-type wave maker at the first order is outlined as follows:

$$X_0^{(1)}(t) = \frac{H}{2F} \sin \omega t \tag{3.51}$$

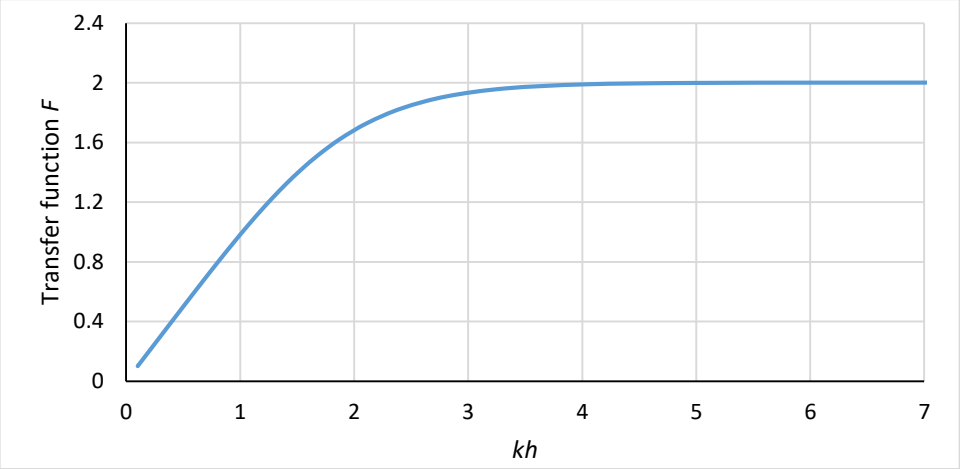

Figure 3.8 Far field Biésel transfer function Equation (3.48) for piston-type wave maker against kh.

3.2.1.2 Transfer Function and Total Evanescent Mode

Figure 3.9 shows the Biesel transfer function F_0 and the sum of the transfer functions for evanescent modes with varying n for a piston-type wavemaker. While F_0 approaches its asymptotic value of 2 at a non-dimensional frequency of $\omega\sqrt{h/g} = 2$, the transfer

function for the evanescent modes continues to increase with increasing frequency. The sum of transfer functions for the evanescent modes also increases as n increases, and it appears that the transfer function at n=20 matches well with that at n=200 when $\omega\sqrt{h/g} < 4$. Additionally, when $\omega\sqrt{h/g}$ reaches a certain high value, the sum of transfer functions for the evanescent modes is greater than F_0. For example, $i\sum_{j=1}^{n} F_j > F_0$ for $\omega\sqrt{h/g} > 3.4$, which indicates that the amplitude of the local disturbance at the wave board exceeds the amplitude of the progressive wave. This illustrates the difficulty of generating high frequency waves using a piston type wavemaker.

$$F_j = \frac{4\sinh^2(k_j h)}{\sinh(2k_j h) + 2k_j h} \tag{3.52}$$

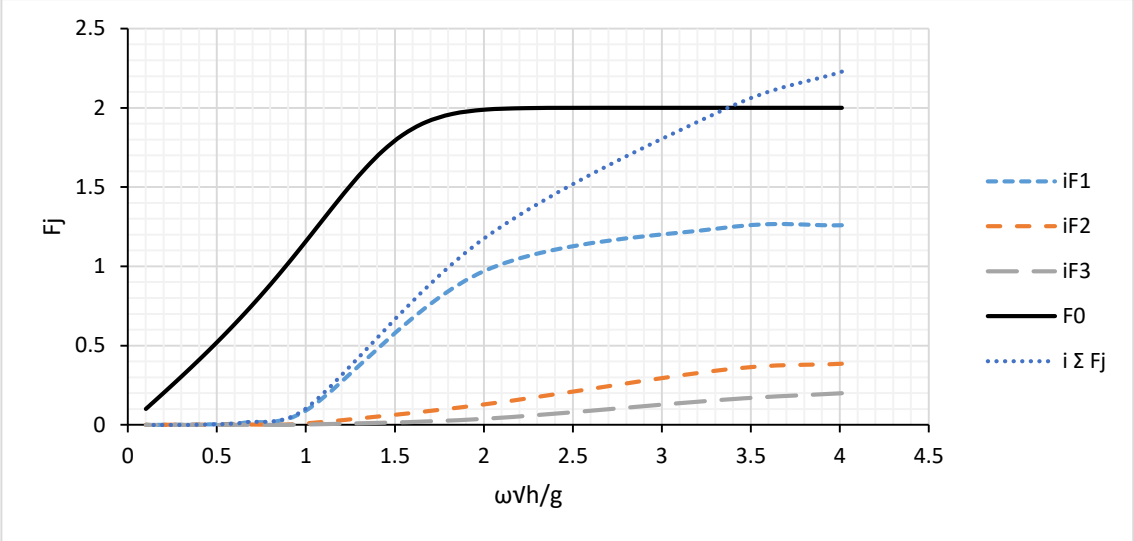

Figure 3.9 The transfer function and the total evanescent-mode transfer function for a piston-type wavemaker, (water depth *h*=1 m).

3.2.1.3 Second Order Solution

The wavemaker problem's second-order derivatives indicate that using the first-order solution to generate waves in laboratory settings can result in undesired harmonics in the wave flume. According to observations by Goda in 1967, these spurious waves have the potential to distort the wave profile and become more conspicuous under conditions of heightened wave steepness *(H/L)* or reduced relative depth *(h/L)* (Hughes ,1993). Madsen

(1970, 1971) developed an approximate second-order theory for generating regular waves using a wavemaker, which requires:

$$\emptyset^{(2)} = \emptyset^{(21)} + \emptyset^{(22)} \tag{3.53}$$

When Equation (3.53) for $\phi^{(21)}$ is inserted within the second order boundary value problems outlined in Equation (3.31) to (3.33), and Equation (3.53) for $\phi^{(22)}$ is inserted into the second order boundary value problems in Equation (3.34) to

(3.36), two crucial terms are produced, solution Away from the Wave board:

$$\emptyset^{(21)}(x,z,t) = \frac{3\omega H^2}{32}\frac{\cosh 2k(h+z)}{\sin^4 kh}\sin 2(kx-\omega t) \tag{3.54}$$

And solution near the wave board:

$$\frac{\partial \emptyset^{(22)}}{\partial x} = \left(1 - \frac{h}{2(h+l)}\right)\frac{dX_{0t}}{dt} + \frac{\omega H^2}{16h}\left(\frac{2}{F} - \frac{3\cosh kh}{\sinh^3 kh}\right)\cos 2\omega t \tag{3.55}$$

Madsen (1971) noted that it is possible to eliminate the free secondary wave generated by a sinusoidally moving wave board by defining the second-order wave board motion $X_0^{(2)}$ such that $\frac{\partial \emptyset^{(22)}}{\partial x} = 0$. By incorporating this motion into the first order term, the required wave board motion can be obtained.

$$X_0(t) = X_0^{(1)} + X_0^{(2)} \tag{3.56}$$

By carrying out the required algebraic manipulations it yields

$$X_0{}^{(2)}(t) = \frac{H^2}{32h\left(1 - \frac{h}{2(h+l)}\right)}\left(\frac{3\cosh kh}{\sinh^3 kh} - \frac{2}{F}\right)\sin 2\omega t \tag{3.57}$$

The expression that describes the motion of the wave board required to eliminate the second harmonic free wave is:

$$X_0(t) = \frac{H}{2F}\sin\omega t + \frac{H^2}{32h\left(1-\frac{h}{2(h+l)}\right)}\left(\frac{3\cosh kh}{\sinh^3 kh} - \frac{2}{F}\right)\sin 2\omega t \tag{3.58}$$

Madsen restricted the application of the above approximate wavemaker theory to waves that satisfied the criterion.

$$\frac{HL^3}{h^3} < \frac{8\,\pi^2}{3} \tag{3.59}$$

Where L is the wave length.

3.2.1.2.1 Example of Second Order Two-Dimensional Wave Maker

In this study, a solution for the second-order regular wave is presented using a piston displacement model. The parameters used for this example include a wave height of 0.2 meters, a wave period of 2 seconds, and a water depth of 0.55 meter. The wave number is calculated by solving Equation (3.89) and found to be 1.48. Using $k = 2\pi/L$ the angular frequency and wavelength are determined to be 3.14 and 4.21 meters, respectively. The essential motion of the wave board needed for the generation of the target regular wave is acquired through the utilization of Equation (3.58). The first and second order components of the combined wave board motion are showcased through Equations (3.51) and (3.57) in Table 3.3, accompanied by Figure 3.10.

Table 3.3 An example piston displacement for the second-order regular wave.

$t(s)$	$\mathrm{X}^{(1)}(m)$	$\mathrm{X}^{(2)}(m)$	$\mathrm{X}(t)(m)$	$\mathrm{H}(m)$	$\mathrm{T}(s)$	$h(m)$	k	ω	$L(m)$	$\mathrm{F}(m)$
0	0.00	0.00	0.00	**0.2**	**2**	**0.55**	**1.48**	**3.14**	**4.21**	**0.81**
0.2	0.07	0.01	0.08							
0.4	0.12	0.00	0.12							
0.6	0.12	0.00	0.11							
0.8	0.07	-0.01	0.07							
1	0.00	0.00	0.00							
1.2	-0.07	0.01	-0.07							
1.4	-0.12	0.00	-0.11							
1.6	-0.12	0.00	-0.12							
1.8	-0.07	-0.01	-0.08							
2	0.00	0.00	0.00							
2.2	0.07	0.01	0.08							
2.4	0.12	0.00	0.12							
2.6	0.12	0.00	0.11							
2.8	0.07	-0.01	0.07							
3	0.00	0.00	0.00							
3.2	-0.07	0.01	-0.07							
3.4	-0.12	0.00	-0.11							
3.6	-0.12	0.00	-0.12							
3.8	0.00	0.00	0.00							
4	0.07	0.01	0.08							

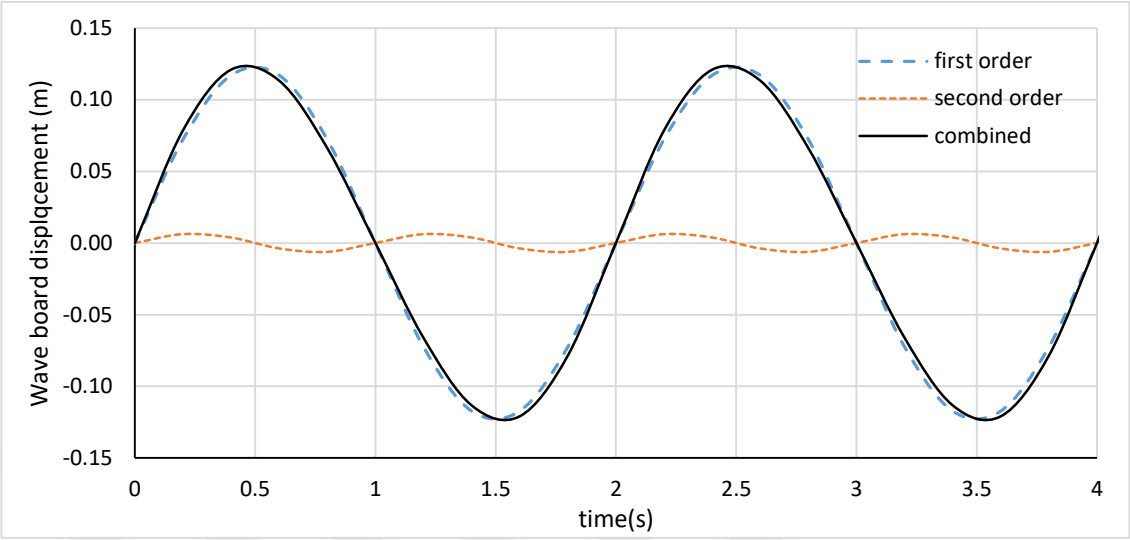

Figure 3.10 The displacement of the second order wave board for a regular wave (H=0.20 m , T=2s).

3.2.1.2 Irregular Wave Generation

3.2.1.2.1 First Order Solution

Assuming an infinitely long continuous wavemaker, the position of the first order paddle at the still water level can be assigned for each of the wave components that make up the first-order spectrum which given by:

$$X_0^{(1)} = \frac{1}{2}\{-i\, X_a e^{i\omega t} + c.c\} \tag{3.60}$$

where X_a represents the constant first-order paddle amplitude at the still water level, and $c.c$ denotes the complex conjugate of the preceding term. The solution to the boundary value problems given by Equations (3.19) through (3.22) for the first-order can be expressed as follows:

$$\emptyset^{(1)} = \frac{1}{2}\left\{\frac{igX_a}{\omega}\sum_{j=0}^{\infty} F_j \frac{\cosh k_j(z+h)}{\cosh k_j} e^{i(\omega t - k_j x)} + c.c\right\} \tag{3.61}$$

$$\eta^{(1)} = \frac{1}{2}\left\{X_a \sum_{j=0}^{\infty} F_j e^{i(\omega t - k_j x)} + c.c\right\} \tag{3.62}$$

The water surface elevation of progressive first-order waves can be represented as follows:

$$\eta_0^{(1)} = \frac{1}{2}\{A e^{i(\omega t - kx)} + c.c\} \tag{3.63}$$

Where *A* is a complex amplitude given by:

$$A = F_0 X_a \tag{3.64}$$

In order to derive the motion of the wave board using the first order theory, Equation (3.65) may be construed as the correlation between the energy spectrum of the intended irregular wave for generation and the required movement of the wave board. Given that the square of the complex wave amplitude corresponds to the magnitudes within spectral density functions, the formal definition of the linear association between the irregular wave and the wave board can be articulated as follows:

$$S_{paddle}(f) = \frac{S_\eta(f)}{F^2} \tag{3.65}$$

Where $S_{Paddle}(f)$ the target spectrum of the paddle,$S_\eta(f)$ the target spectrum and, F the transfer function.

In comparison to the target spectrum, the paddle spectrum exhibits an increase in shape on both the low and high frequency sides (Goda, 2000). Figure 3.11 presents a comparison between the energy spectra of an irregular wave and the corresponding first order wave board motion. This comparison was established by relating the energy spectrum of the irregular wave to the motion of the wave board, as previously described by Equation (3.65).

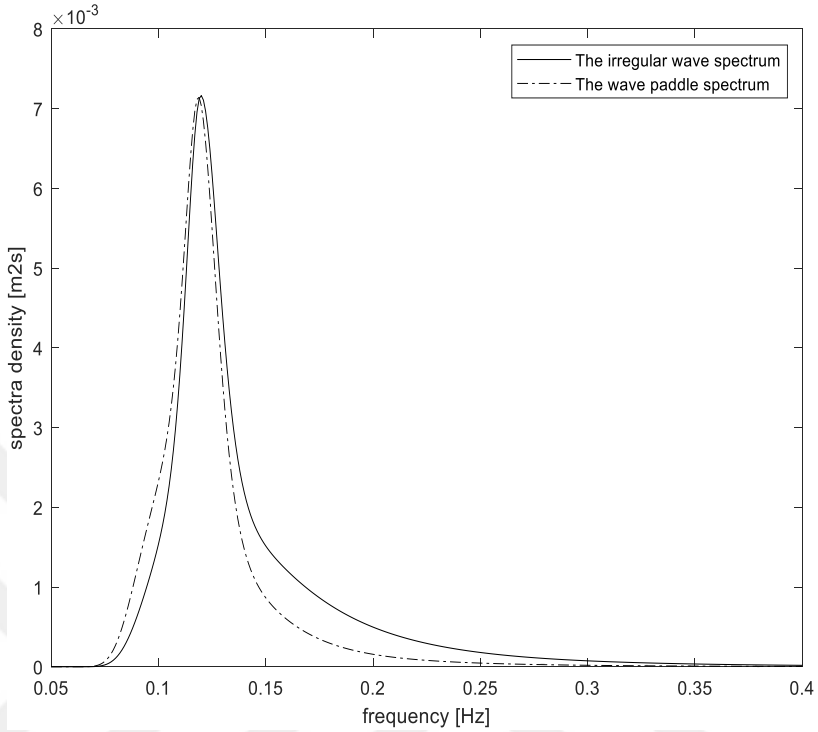

Figure 3.11 The targeted spectrum of the irregular wave and its corresponding spectrum of first order wave paddle motion.

3.2.1.2.2 Second Order Solution Investigation

The second order wave spectrum involves the interaction between two wave components with different angular frequencies, ω_n and ω_m. This interaction gives rise to subharmonics, which are frequencies that are lower than the original frequencies, as well as superharmonics, which are frequencies that are higher than the original frequencies. To analyze this interaction in the frequency domain, a bichromatic approach is required. The goal of generating a second-order bound surface elevation $\eta_0^{(21)\pm}$ is to avoid generating any unwanted free waves. the first-order solution for ω_n and ω_m. are denoted *j* and *l*. in this investigation the notations are proposed by (Schäffer, 2003).

Solution of the $\emptyset^{(22)}$ problem "the bound waves":

$$\emptyset_{jnlm}^{(21)\pm} = \frac{R_{jnlm}^{(21)\pm}}{D_{jnlm}^{\pm}} \frac{\cosh k_{jnlm}^{\pm}(z+h)}{\cosh k_{jnlm}^{\pm} h} \tag{3.66}$$

Where

$$R_{jnlm}^{\pm} = i\delta_{nm} X_n X_m^{-:*} e_{jn} e_{lm}^{-:*} H_{jnlm}^{\pm} e^{i(\theta_{jn} \pm \theta_{lm}^{-:*})} \tag{3.67}$$

$$\delta_{nm} = \begin{cases} \frac{1}{2} & for\ \omega_n = \omega_m \\ 1 & otherwise \end{cases} \tag{3.68}$$

$$H_{jnlm}^{\pm} = (\omega_n \pm \omega_m) \pm \omega_n \omega_m - \frac{g^2 k_{jn} k_{lm}^{-:*}}{\omega_n \omega_m} + \left(\pm \omega_n \omega_m - \frac{g^2 k_{jn} k_{lm}^{-:*}}{\omega_n \omega_m} \right) + \frac{\omega_n^3 \pm \omega_m^3}{2} - \frac{g^2}{2} \left(\frac{k_{jn}^2}{\omega_n} \pm \frac{k_{lm}^2}{\omega_m} \right) \tag{3.69}$$

And the symbol -: $*$ introduced for brevity is defined by

$$Z^{-:*} = \begin{cases} Z & for\ superharmonics \\ Z^* & for\ subharmonics \end{cases} \tag{3.70}$$

$$k_{jnlm}^{\pm} = \sqrt{(k_{xjn} \pm k_{xlm}^{-:*})^2 + (k_{yn} \pm k_{ym})^2} \tag{3.71}$$

$$D_{jnlm}^{\pm} = g k_{jnlm}^{\pm} \tanh k_{jnlm}^{\pm} h - (\omega_n \pm \omega_m)^2 \tag{3.72}$$

$$\eta_{jnlm}^{(21)\pm} = G_{jnlm}^{\pm} X_n X_m^{-:*} e_{jn} e_{lm}^{-:*} e^{i(\theta_{jn} \pm \theta_{lm}^{-:*})} \tag{3.73}$$

Where

$$G_{jnlm}^{\pm} = \frac{\delta_{nm}}{g}\left\{(\omega_n \pm \omega_m)\frac{H_{jnlm}^{\pm}}{D_{jnlm}^{\pm}} L_{jnlm}^{\pm}\right\} \tag{3.74}$$

And

$$L_{jnlm}^{\pm} = \frac{1}{2}\left\{\frac{g^2 k_{jn} k_{lm}^{-:*}}{\omega_n \omega_m} \pm \omega_n \omega_m - (\omega_n^2 \pm \omega_m^2)\right\} \tag{3.75}$$

Solution of the $\emptyset^{(22)}$problem "the unwanted free waves":

$$\emptyset_{nm}^{(22)} = \frac{1}{2}\left\{\frac{igA_n A_m^{-:*}}{h(\omega_n \pm \omega_m)} \sum_{p=0}^{\infty} e_p^{(22)\pm} \frac{\cosh k_p^{\pm}(z+h)}{\cosh k_p^{\pm} h}\, e^{i[(\omega_n \pm \omega_m)t - k_p^{\pm} x]} + c.c\right\} \tag{3.76}$$

$$\eta_{nm}^{(22)} = \frac{1}{2}\left\{\frac{A_n A_m^{-:*}}{h} \sum_{p=0}^{\infty} e_p^{(22)\pm}\, e^{i[(\omega_n \pm \omega_m)t - k_p^{\pm} x]} + c.c\right\} \tag{3.77}$$

Where $k_p^{\pm}$ is the wave number of the free waves and the solution to the linear dispersion equation generalized to complex wave numbers.

$$(\omega_n \pm \omega_m)^2 = g k_p^{\pm} \tanh k_p^{\pm} h \tag{3.78}$$

Solution of the $\emptyset^{(22)}$problem "the compensating free waves" and obtaining the second-order control signal:

$$\emptyset_{nm}^{(23)} = \frac{1}{2}\left\{\frac{ig\mathbf{F}^{\pm}A_nA_m^{-:*}}{h(\omega_n \pm \omega_m)}\sum_{p=0}^{\infty} e_p^{(23)\pm}\frac{\cosh k_p^{\pm}(z+h)}{\cosh k_p^{\pm} h}e^{i[(\omega_n \pm \omega_m)t - k_p^{\pm}x]} + c.c\right\} \tag{3.79}$$

$$\eta_{nm}^{(23)} = \frac{1}{2}\left\{\mathbf{F}^{\pm}\frac{A_nA_m^{-:*}}{h}\sum_{p=0}^{\infty} e_p^{(22)\pm}\, e^{i[(\omega_n \pm \omega_m)t - k_p^{\pm}x]} + c.c\right\} \tag{3.80}$$

$$\begin{aligned}\mathbf{F}^{\pm} = E^{\pm}\Bigg\{ & \pm\frac{g}{2\omega_n}\sum_{j=0}^{\infty}\frac{e_{jn}k_{xjn}^2}{k_{jn}^2 - (K_0^{\pm})^2}[\omega_n^2 - (\omega_n \pm \omega_m)^2] \\ & \pm\frac{g}{2\omega_m}\sum_{l=0}^{\infty}\frac{e_{lm}k_{xlm}^{-:*\,2}}{k_{lm}^{-:*\,2} - (K_0^{\pm})^2}\;\;[\omega_m^2 - (\omega_n \pm \omega_m)^2] \\ & + \sum_{j=0}^{\infty}\sum_{l=0}^{\infty} e_{jn}e_{lm}^{-:*}\frac{k_{jn} \pm k_{xlm}^{-:*}}{k_{jnlm}^{\pm^2} - K_0^{\pm^2}}H_{jnlm}^{\pm}\Bigg\}\end{aligned} \tag{3.81}$$

Where

$$E^{\pm} = \frac{\delta_{nm}K_0^{\pm^2}h}{e_{0n}e_{0m}(\omega_n \pm \omega_m)^3(1 + M_1(K_0^{\pm}))} \tag{3.82}$$

Where $M_1(K_0^{\pm})$ vanish for a piston type wave maker. The second order transfer function, $\mathbf{F}^{\pm}$ is the main result of the theory, which is represented in Figure 3.12 and Figure 3.13 from (Schäffer 2003). The proposed answer for the second-order motion of a piston type wave maker of is:

$$X_0^{(2)} = \frac{1}{2}\left\{-i\mathbf{F}^{\pm}\frac{A_nA_m^{-:*}}{h}e^{i(\omega_n \pm \omega_m)t} + c.c\right\} \tag{3.83}$$

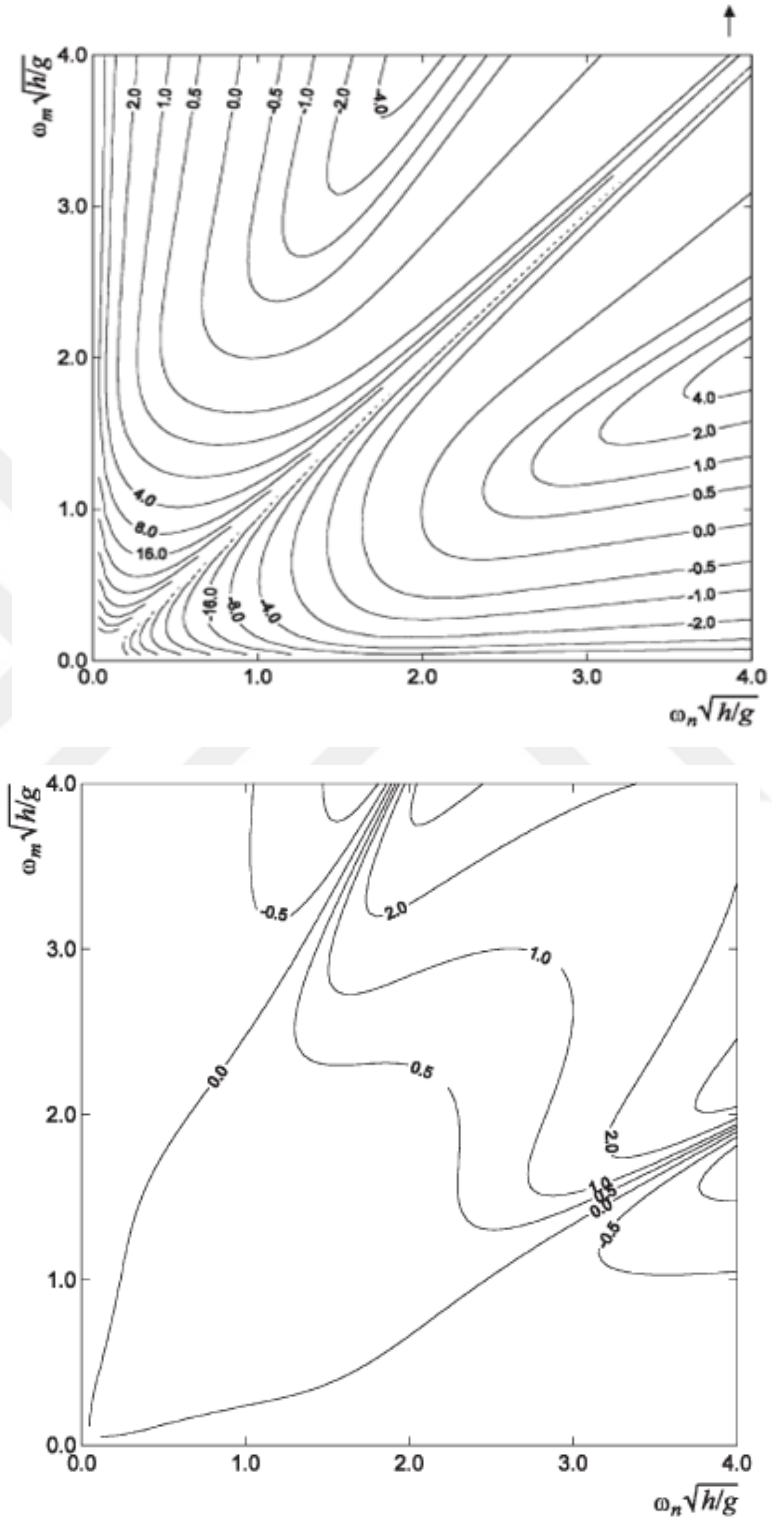

Figure 3.12 Dimensionless first-order frequencies vs real (top) and imaginary (bottom) parts of subharmonic complex transfer functions F^{-}/δ_{nm} for a piston type wavemaker. (Schäffer,2003).

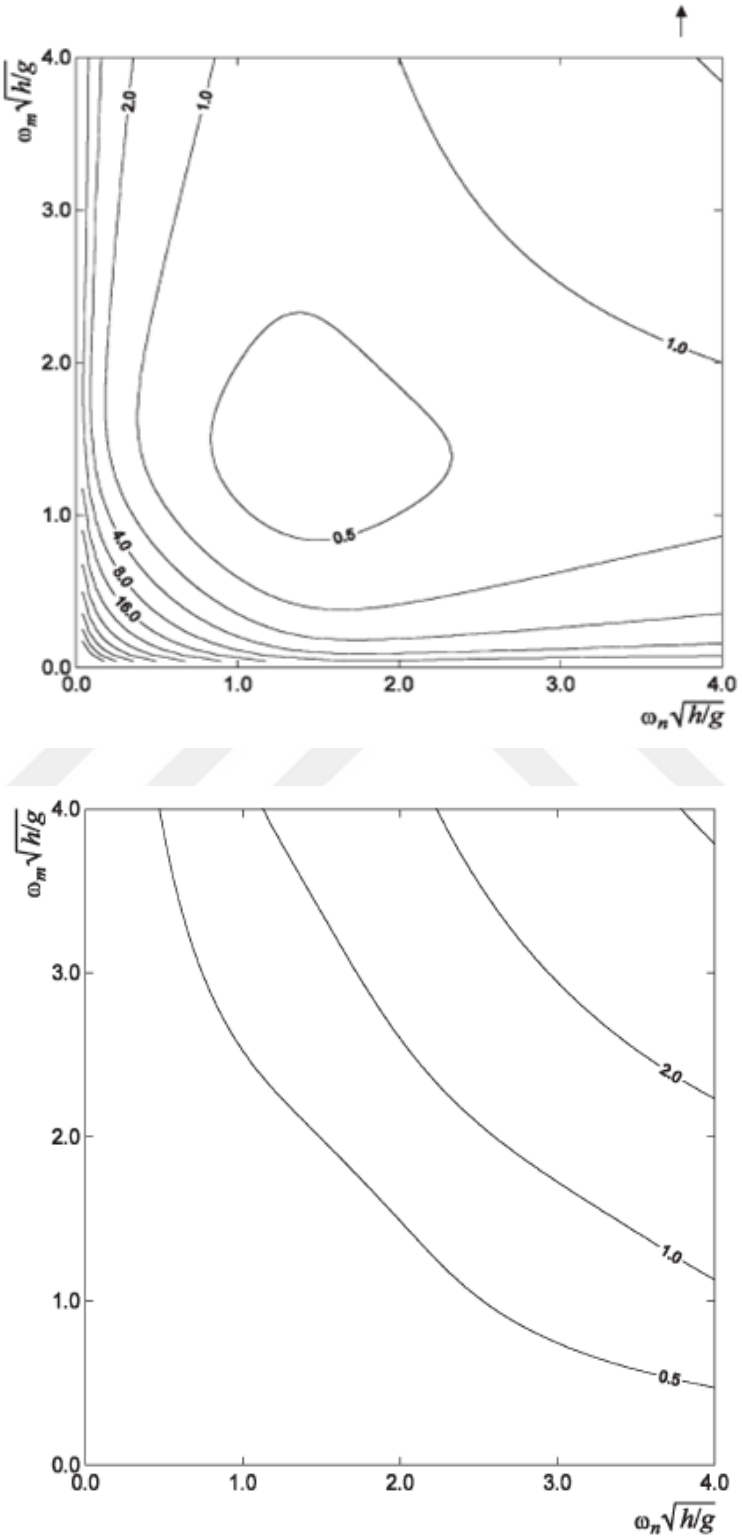

Figure 3.13 Dimensionless first-order frequencies vs real (top) and imaginary (bottom) parts of superharmonic complex transfer functions F^+/δ_{nm} for a piston type wavemaker. (Schäffer,2003).

3.3 Wave Reflection Analysis

Wave reflection in wave flumes is the process of studying how waves interact with the boundaries of a wave tank. Wave flumes are specialized tanks or channels used to generate and study waves in a controlled laboratory setting. By measuring wave height, wave period, and wave direction before and after they interact with the boundaries of the flume, we can quantify the amount of reflection and transmission that occurs and determine how these processes affect wave behavior.

The data collected during experiments is used to calculate the wave reflection coefficient, which is a measure of the fraction of incident wave energy that is reflected back into the flume. This information can be used to evaluate the performance of different types of passive wave absorbers and to determine the most effective design for reducing wave reflection.

The approach formulated by Goda and Suzuki (1976) is commonly used to separate incoming waves from reflected waves in wave flume experiments. This method, also known as the "wave decomposition method", uses the principles of wave superposition to separate the wave field into incident and reflected components. The method is based on the assumption that the wave field in the wave flume can be represented as a superposition of the incident wave field and the reflected wave field. By analyzing the wave characteristics and directions at different locations in the flume, it is possible to separate the incident and reflected wave components and calculate the wave reflection coefficient.

The general form of the incident and reflected waves in a wave flume can be expressed mathematically using wave theory. The incident wave can be represented as:

$$\eta_I = a_I.\cos(kx - \omega t + \epsilon_I)$$
$$\eta_R = a_R.\cos(kx - \omega t + \epsilon_R) \quad (3.84)$$

Where:

η_I and η_R are the surface elevations of incident and reflected waves,

a_I is the amplitude of the incident wave,

a_R is the amplitude of the reflected wave,

k is the wave number of the incident wave of $2\pi/L$ with L in the wavelength,

x is the distance along the wave flume

ω is the angular wave frequency,

t is time, and ϵ_I and $\epsilon_R$are the phase angles of incident and reflected waves.

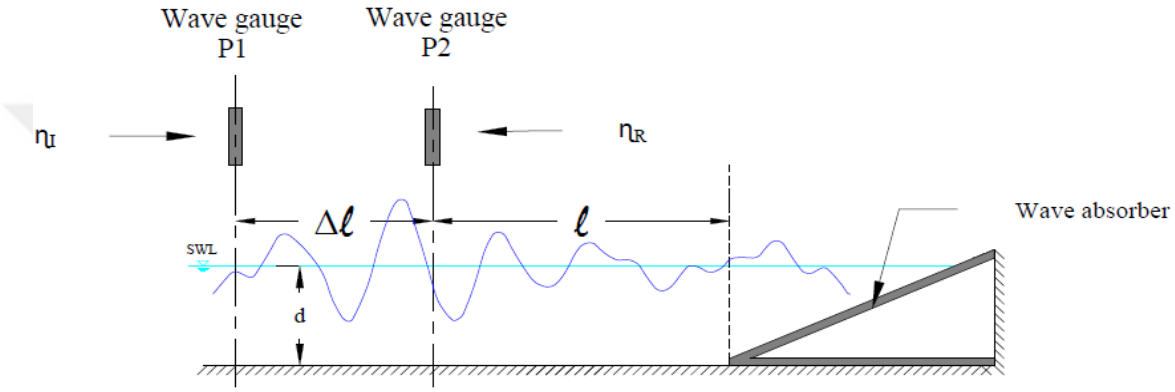

Figure 3.14 Wave measurement setup sketch for the analysis of reflection.

A sketch depicting a basic setup for measuring wave reflection in a wave flume is shown in Figure 3.14 . The surface profile data, represented by $\eta 1$ and $\eta 2$, is obtained from two wave gauge probes positioned at x_1 and $x_2 = x_1 + \Delta l$ respectively. The two probes may be located at distances of 0.2 L and 0.45 L from seawall toe and the distance between them may be performed in range of $0.03 < \Delta L/L < 0.45$.

The data collected at these probes contains a combination of incident and reflected waves, which can be described mathematically as a superposition of waves.

$$\eta_1 = (\eta_I + \eta_R)_{x=x_1} = A_I.\cos(\omega t) + B_1.\sin(\omega t)$$
$$\eta_2 = (\eta_I + \eta_R)_{x=x_2} = A_2.\cos(\omega t) + B_2.\sin(\omega t) \quad (3.85)$$

where;

$$\begin{aligned} \mathrm{A}_1 &= a_I.\cos(\emptyset_I) + a_R.\cos(\emptyset_R) \\ \mathrm{B}_1 &= a_I.\sin(\emptyset_I) + a_R.\sin(\emptyset_R) \\ \mathrm{A}_2 &= a_I.\cos(k\Delta l + \emptyset_I) + a_R.\cos(k\Delta l + \emptyset_R) \\ \mathrm{B}_2 &= a_I.\sin(k\Delta l + \emptyset_I) + a_R.\sin(k\Delta l + \emptyset_R) \end{aligned} \tag{3.86}$$

and,

$$\begin{aligned} \emptyset_I &= kx_1 + \epsilon_I \\ \emptyset_R &= kx_1 + \epsilon_R \end{aligned} \tag{3.87}$$

Solving Equation (3.86) yields the estimate of ;

$$a_I = \frac{1}{2\left|\frac{sin2\pi\Delta l}{L}\right|}\sqrt{(A_2 - A_1 cosk\Delta l - B_1 sink\Delta l)^2 + (B_2 + A_1 sink\Delta l - B_1 cosk\Delta l)^2} \tag{3.88}$$

$$a_R = \frac{1}{2\left|\frac{sin2\pi\Delta l}{L}\right|}\sqrt{(A_2 - A_1 cosk\Delta l + B_1 sink\Delta l)^2 + (B_2 - A_1 sink\Delta l - B_1 cosk\Delta l)^2}$$

The dispersion relationship is used in the calculations.

$$\omega^2 = gk_j \tan(k_j h) \tag{3.89}$$

3.3.1 Regular Wave

In wave flumes, incident and reflected regular waves are typically decomposed using a variety of methods. One approach for analyzing regular waves involves utilizing Fourier analysis to compute coefficients A1, A2, B1, and B2. These coefficients are then employed in Equation (3.88) to determine the amplitudes of both the incident and reflected waves.

In a widely used method for measuring wave reflection in a wave flume, a wave probe is moved along the path of wave propagation in order to quantify the maximum and minimum wave heights, respectively referred to as H_{max} and H_{min} Subsequently, the incident wave height (H_i) and the reflection wave height (H_r) can be derived from these measurements using the established formulas:

$$H_i = \eta_{max} + \eta_{min} = \frac{H_{max} + H_{min}}{2} \tag{3.90}$$

$$H_r = \eta_{max} - \eta_{min} = \frac{H_{max} - H_{min}}{2} \tag{3.91}$$

$$C_R = \frac{H_r}{H_i} = \frac{H_{max} - H_{min}}{H_{max} + H_{min}} \tag{3.92}$$

The reflection coefficient C_R is the ratio of reflected wave height H_r to incident wave height H_i.The choice of method depends on the specific requirements and objectives of the study and the availability of data and resources.

3.3.2 Irregular Wave

The analysis of irregular waves can be conducted by considering them as the composite of an infinite series of regular waves. The coefficients $A1$, $A2$, $B1$, $B2$ can be determined using a fast Fourier transform, which then allows the calculation of the discrete a_I and a_R amplitudes by applying Equation (3.88). Regarding irregular waves, the guideline for determining the placement of wave gauges is provided as follows:

$$\begin{aligned} f_{min}{:}\frac{\Delta l}{L_{max}} &= 0.05 \\ f_{max}{:}\frac{\Delta l}{L_{min}} &= 0.45 \end{aligned} \tag{3.93}$$

Wavelengths at their maximum and minimum (L_{max} and L_{min}) can be calculated based on the minimum and maximum frequencies (f_{min} and f_{max}) respectively. There may be instances where a slightly wider effective range is chosen, for example by selecting $fmin$ in such a way that the ratio of Δl to L_{max} is equal to 0.03 (Goda and Suzuki, 1976). Afterwards, the wave energies for both the incoming and reflected waves are calculated within the frequency range of f_{min} to f_{max}.

$$E_I = \int_{f\ min}^{f\ max} S_I(f)df$$
$$E_R = \int_{f\ min}^{f\ max} S_R(f)df \tag{3.94}$$

The reflection coefficient may be determined by dividing the incident and reflected waves by the ratio.

$$C_R = \sqrt{\frac{E_R}{E_I}} \tag{3.95}$$

CHAPTER FOUR
DESIGN OF WAVE MAKER

This part of the study focuses on the intricate process of designing wave makers for experimental and numerical simulations.

4.1 Wave Flume Setup

The wave channel, measuring 23.4 meters in length, 1.2 meters in depth, and 1 meter in width, is situated within the enclosed area of the Hydraulic Laboratory. This allows experiments to be conducted even during cold and rainy weather conditions. The packed sediment, representing the seabed, is 3 meters long and 30 cm deep. Adjacent to the wave channel is a 1m wide walking platform. Figure 4.1 provide a schematic representation of the wave channel's cross-section and plan view.

To optimize the laboratory space, the wave channel is constructed 3 meters above ground level. It is supported by 10 steel columns to withstand the static loads of the channel's weight and the dynamic loads generated by the wave generator. These steel columns are fixed to the 30 cm deep, 1 m x 1.5 m concrete foundation bolts. To prevent vibration caused by the wave generator's operation, the channel is also fixed to the laboratory columns at specific points.

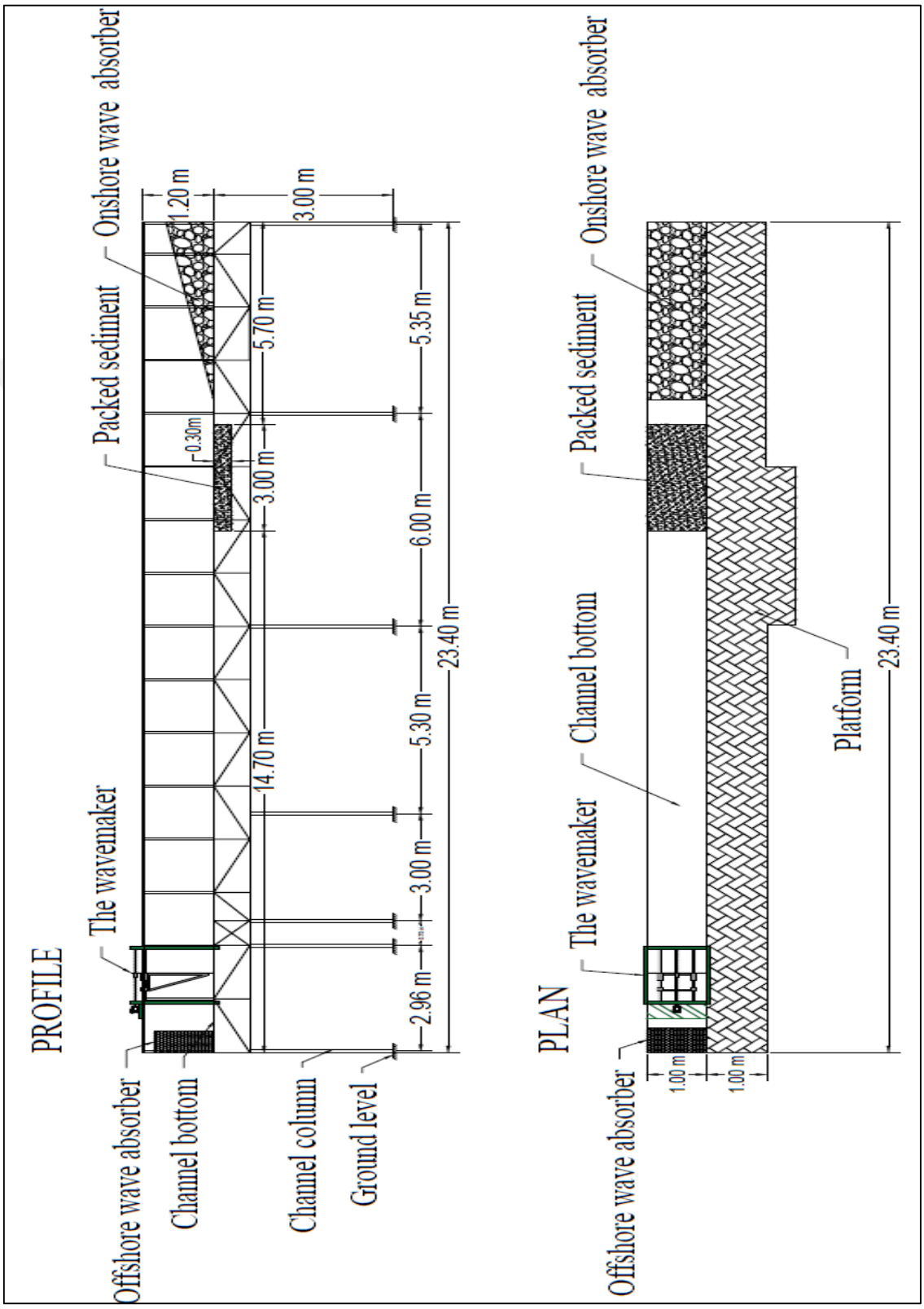

Figure 4.1 Schematic representation of the wave channel's cross-section and plan view.

The construction firm “Atasu muhendislik ltd” carried out the structural analysis of the wave channel, which was then verified by the project team. Figure 4.2 shows the excavated and reinforced foundation. The steel fabrication of the wave channel, including corrosion prevention and painting processes, was completed at the factory before being transported to the laboratory. To place the parts, the laboratory doors were removed, and a spider crane was brought in.



Figure 4.2 Reinforced foundation.

First, the spider crane secured the channel's columns to the ground, ensuring they were level to prevent any slope formation in the wave channel. Continuous checks were performed throughout this process. Figure 4.3 shows the spider crane used to place the wave channel's steel columns and parts.



Figure 4.3 The spider crane and the wave channel's steel columns.

Since the wave channel is 23.4 meters long, it was fabricated in four pieces, placed onto the columns, and welded and bolted together. Continuous checks were made during the assembly of the channel pieces to prevent any slope formation. Figure 4.4 shows a photograph of the installation process of the last piece of the channel.



Figure 4.4 The installation process of the last piece of the channel.

After the channel parts were welded together, 10 mm thick tempered glass was installed on the side facing the laboratory for observation. A 1 m wide platform was constructed adjacent to the channel for the preparation and close monitoring of the experiments. An electrical line was drawn to supply power to the devices and computers used for taking measurements during the experiments. In order to optimize the experimental process and minimize labor requirements, the implementation of two crane systems was undertaken. Specifically, a standing column rotating crane and a rail overhead crane were installed. Figure 4.5 shows the two crane systems.

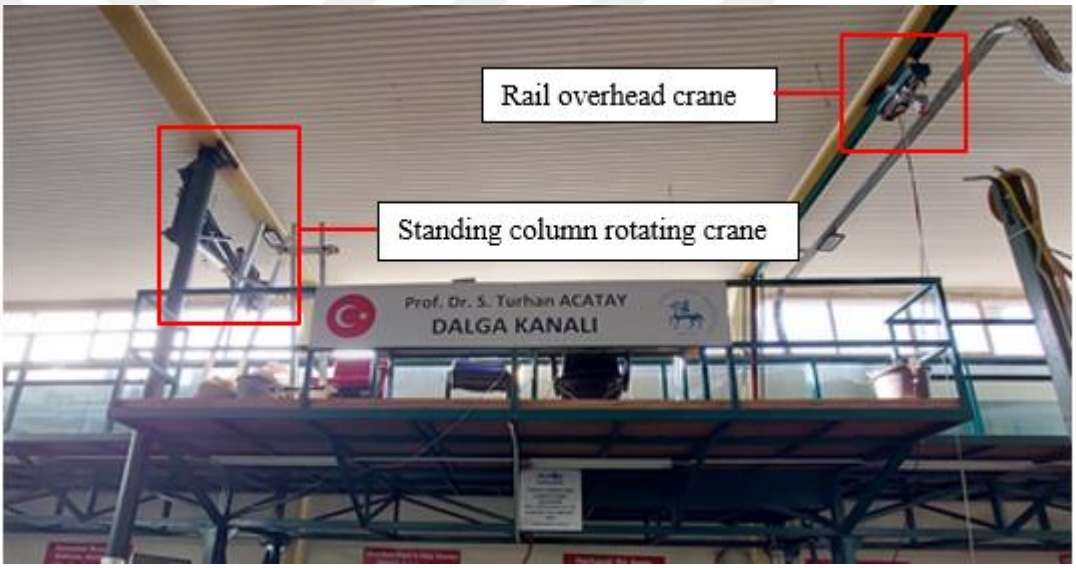

Figure 4.5 The two crane systems.

Upon completion of the structural work for the wave channel, water was pumped into the channel to check for any leaks. The silicone process was meticulously applied to the joint areas in the channel, and their controls were carried out.

The wave channel is named in honor of Prof. Dr. S. Turhan ACATAY, the esteemed founder of the Faculty and Department, a pioneer who initiated engineering education in Izmir in 1968, and the honorary advisor of the laboratory. The overall perspective of the wave flume is depicted in Figure 4.6.



Figure 4.6 Dokuz Eylül University Hydraulic Laboratory wave flume.

A piston-type wave generator moves the water in the flume to generate the proper wave characteristics. The wave generator is positioned near the beginning of the flume (3m from the offshore side). The piston is controlled by a servo motor, which can generate both regular and random waves with a wide range of wave periods and heights.

Two passive wave absorbers are used to reduce wave reflection. The first absorber is a steel cage filled with an absorbent material positioned at the generator's rear, which absorbs waves produced backward on the piston-paddle due to water on both sides, reducing the risk of damage to the motor from splashes and collisions of created and reflected waves in the initial stages of designing the wave channel, the second absorber was chosen to be rocks fill of varying sizes with a slope of 1:7 as shown in Figure 4.7. The experiments were carried out at a constant water depth of d=0.55 m. Our study has considered various suggestions and alternatives aimed at shortening the absorber's length and reducing wave reflection.



Figure 4.7 Varying sizes of rocks fill with a slope of 1:7.

4.2 Wavemaker Setup and Mechanical Construction

The motion control system comprises five main components. Firstly, the operator interface enables the initiation, termination, and adjustment of various functions of the wave maker. Secondly, the PLC (Programmable Logic Controller) dictates the movement of the servo motor by transmitting commands to the amplifier, either in analog signal or data format. The amplifier takes low voltage commands related to torque, speed, or position and amplifies them into a high-powered format compatible with the servo motor. Figure 4.8 shows the motion control system.

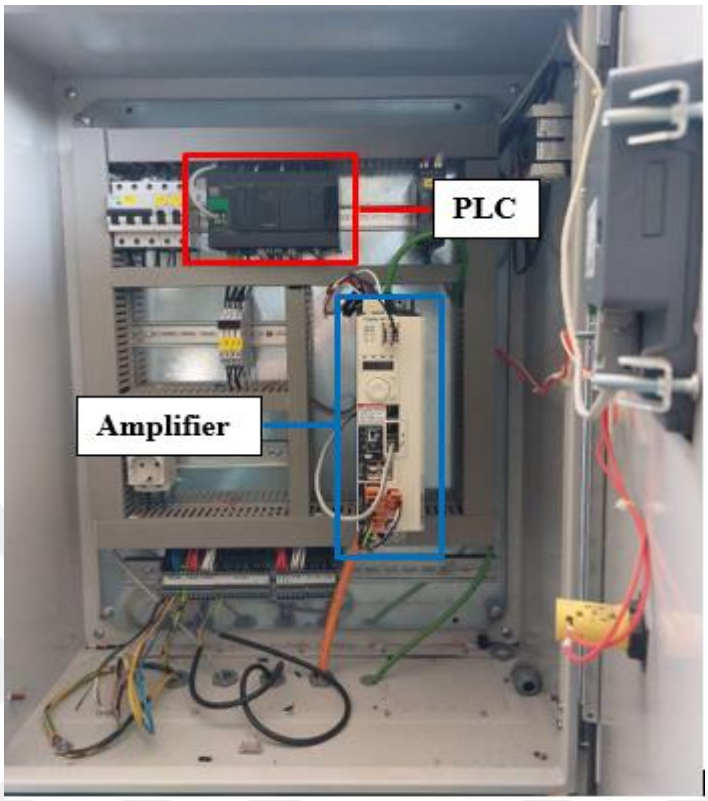

Figure 4.8 The motion control system.

Furthermore, the AC servo motor is attached to a ball-screwed shaft that translates the rotary motion of the servo motor into linear motion (Figure 4.10 and Figure 4.11). This system is supported by a robust stainless-steel frame, which holds the paddle submerged in the water (Figure 4.9).

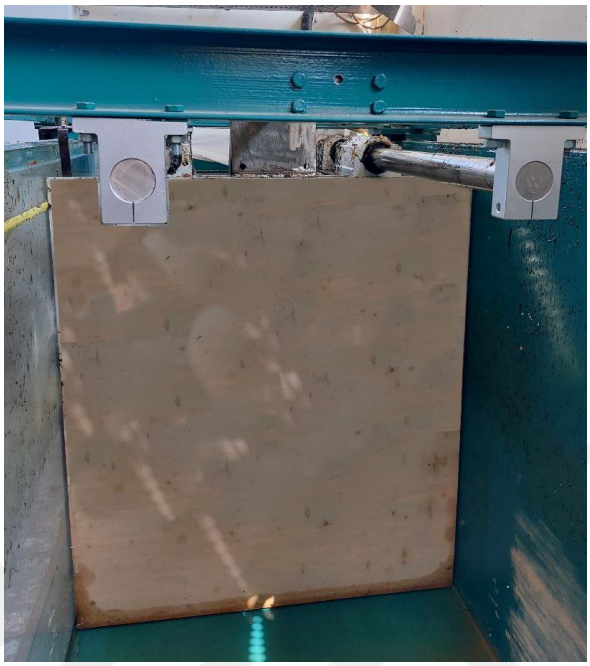

Figure 4.9 The piston-type paddle .

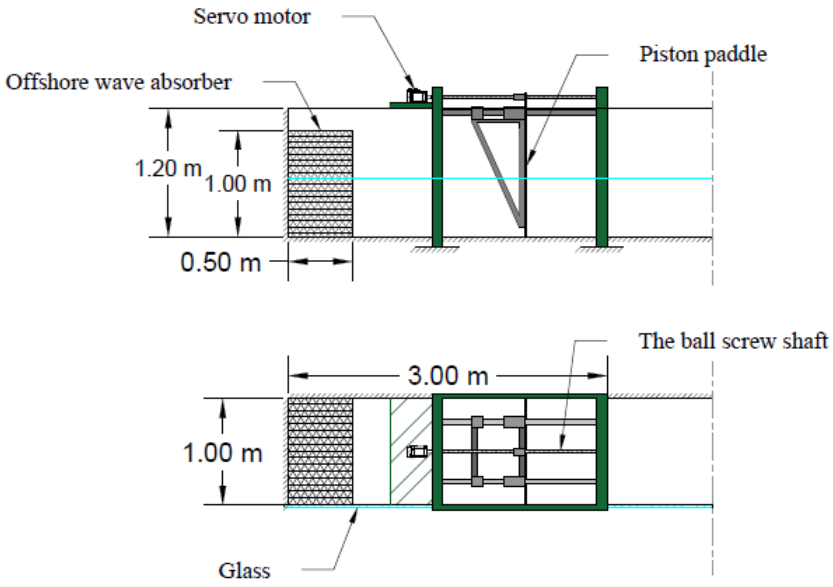

Figure 4.10 Side and top views of the piston-type wavemaker section design (Not to scale).

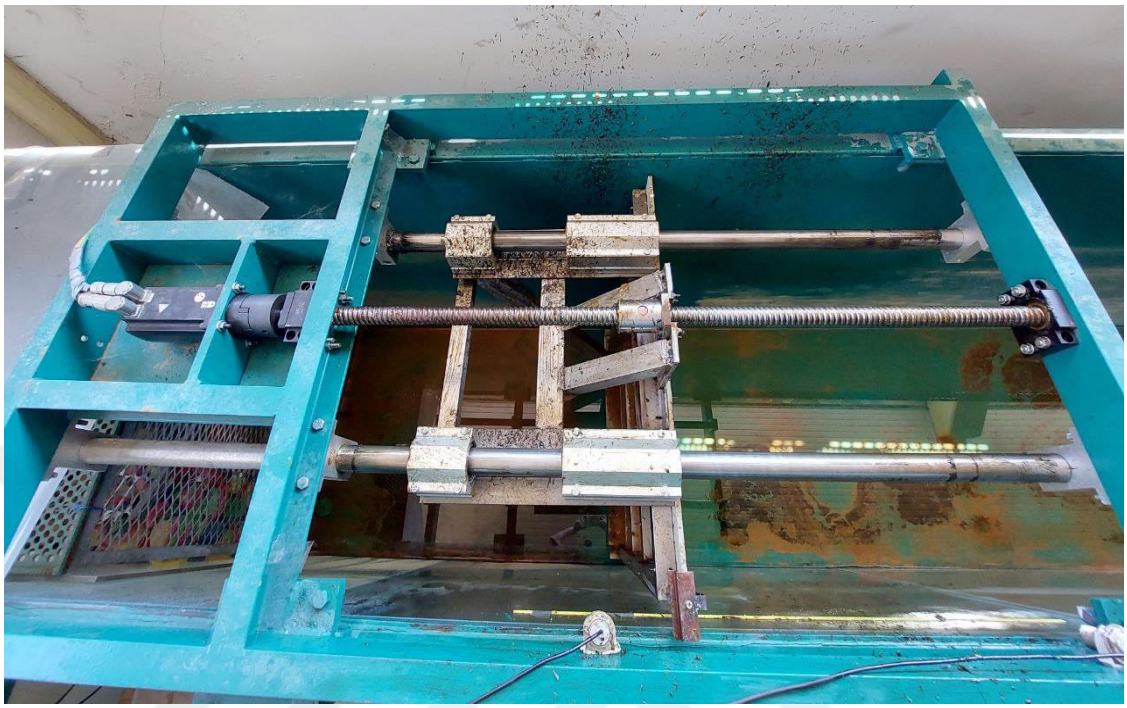

Figure 4.11 Top views of the servo motor and the ball-screwed shaft.

The linear travel distance extends up to sixty centimeters, incorporating two sensors (Figure 4.12) positioned at the ends of the axis to automatically halt the servo upon reaching the boundaries over-travel. Figure 4.13 shows the over view of the piston type wave maker system .

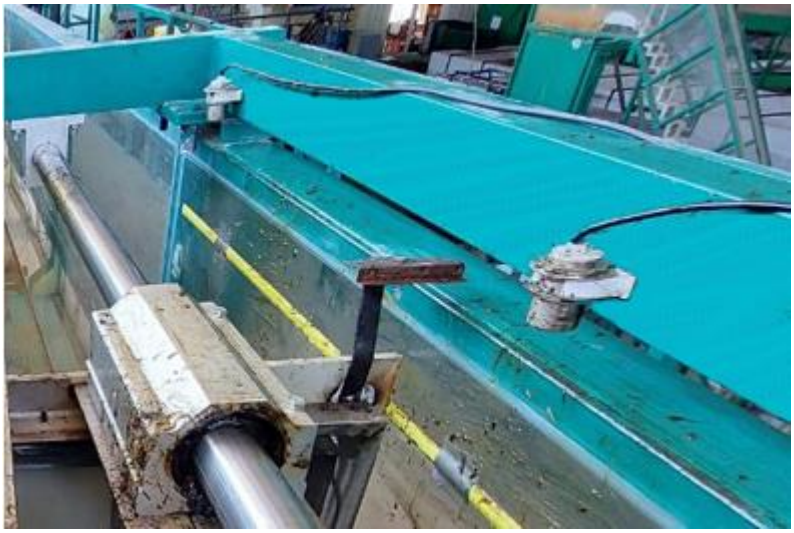

Figure 4.12 Over-travel boundaries sensors.

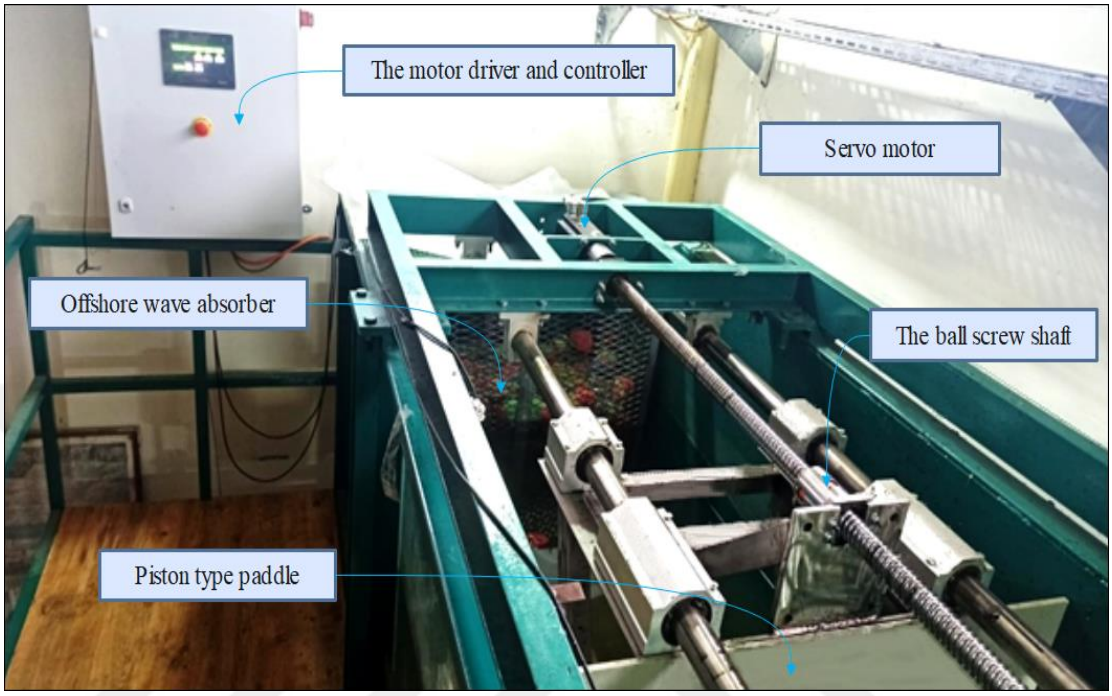

Figure 4.13 The piston-type wave generator system with the control unit.

4.3 Wave Analysis and Measurement

To depict the water surface elevations, two USS (Ultralab Sound Sensor) vertical wave probes were placed at USS P1 and USS P2 to record the composite wave profile. The placement was based on the recommendations of Goda and Suzuki (1976). Additionally, another USS P3 was positioned to measure the incoming wave. The water surface elevations were then plotted as a time series using the data collected by these probes. Three USS20130 sensors at DEU Hydraulic Laboratory were used simultaneously in the experiments within the scope of the study. The USS sensors were attached to the primary device (ULS Ultralab Level System 80-D) with a cable length of 10 m. The wave flume sketch with the measuring equipment shown in Figure 4.14 ,and Images of the USS20130 sensors and the ULS Ultralab are depicted in Figure 4.15.

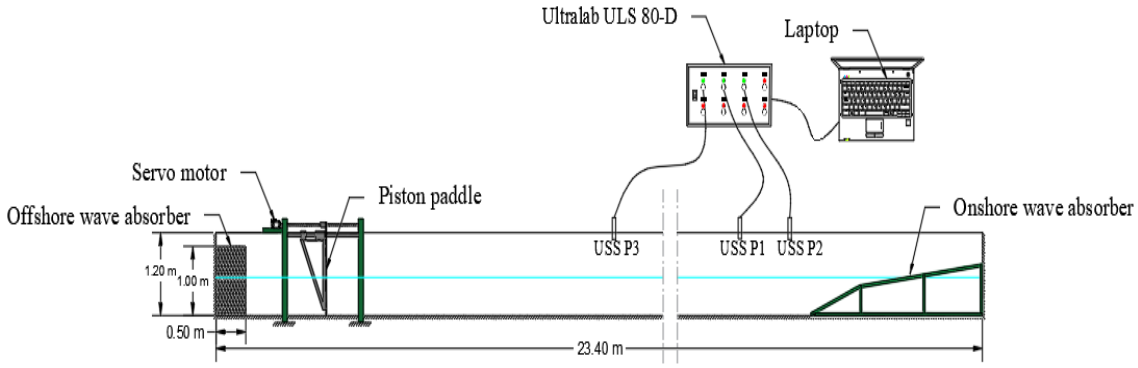

Figure 4.14 The wave flume sketch with the measuring equipment (not to scale).



Figure 4.15 The ULS (Ultralab Level System) device and the USS20130 (Ultralab Sound Sensors).

The ULS utilizes ultrasonic techniques to accurately determine current depths, wave heights, and extract water surface profiles in laboratory settings. With a measurement range spanning from 20 cm to 1.30 m with a precision of 1.0 mm and 0.2 s, the ULS device is capable of taking precise measurements without any interference to the current. The USS 20130 has a distance to water level of 200 mm and a maximum operating depth of 1300 mm. It operates at a frequency of 200 kHz and has a resolution of 0.18 mm. The measurement frequency is 50 Hz and the output voltage ranges from 0 to 10 V. The data obtained using this device is simultaneously transferred to a computer and stored

4.4 The Control Software

The wavemaker is controlled by a user program **(**Figure 4.17) written in the Python language and installed on a Personal Computer (Figure 4.16). The main panel provides

information about the wave type (regular or irregular) and its parameters (wave height and period, experiment duration), some buttons are only activated depending on the wave type. After loading the saved results that were previously calculated depending on the type of experiment, the graphs show the paddle movement, surface elevation signals, and the spectrum. By pressing connect to plc button, the PLC will be activated and be ready to receive the input signal of the paddle displacement from the PC. The servo is activated by pushing the servo On button. In order to protect the paddle from collision at the extremities, the start button that starts the movement of the paddle does not activate until after pressing the home button.

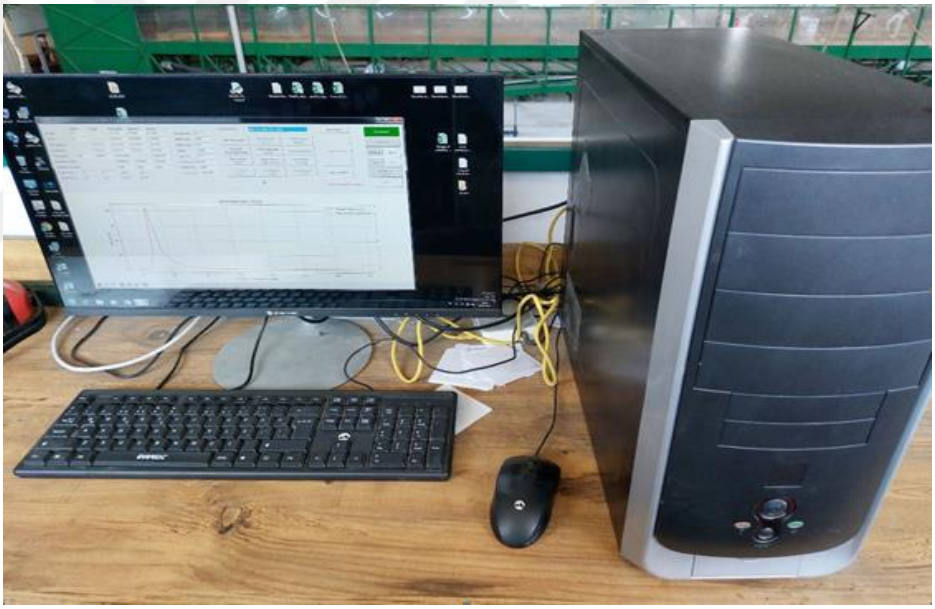

Figure 4.16 The controller Personal Computer.

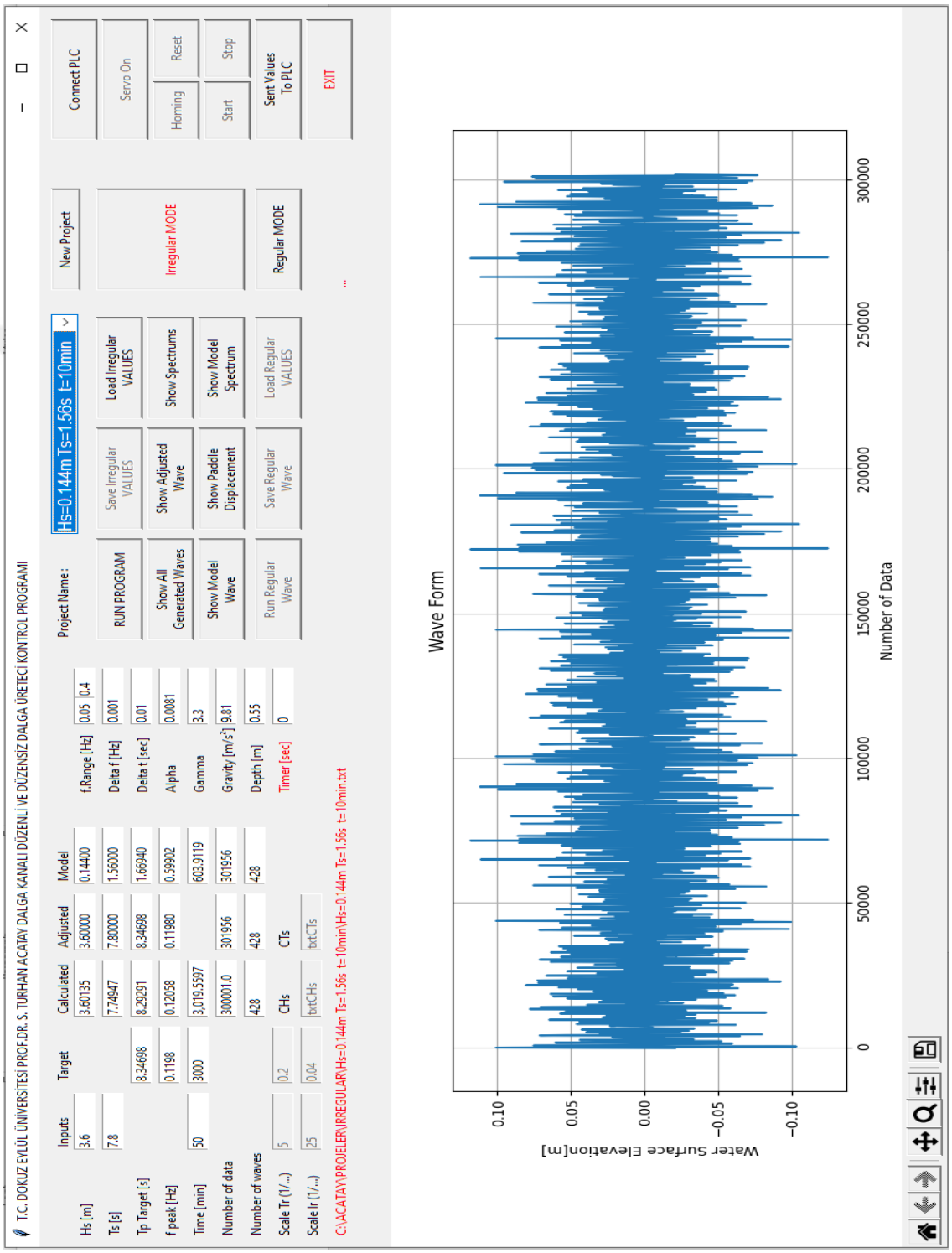

Figure 4.17 The user interface of the control software.

CHAPTER FIVE
DESIGN OF WAVE ABSORAPTER

This part of the study aiming to develop unique alternative shapes for passive wave absorption mechanisms in the wave flume.

5.1 Alternative proposals wave absorbers evaluation

In order to test the effectiveness of these designs, the FLOW 3D software used to simulate the flow dynamics and behavior of these shapes under regular wave conditions. By subjecting these shapes to simulation, we can analyze their performance in reducing wave reflection and determine which shapes are the most effective in minimizing unwanted wave reflection. These simulations will provide valuable insights into the development of passive wave absorption mechanisms that can greatly enhance the laboratory wave environment, enabling more accurate and reliable physical model experiments in the wave flume.

To evaluate the effectiveness of the passive wave absorbers, each proposal underwent five simulations using regular waves. The regular waves (RW) had a range of periods between 2 s to 3.6 s and heights between 0.13 m to 0.25 m in water depth h=0.55 m. Table 5.1 lists the wave heights and periods of the numerical studies conducted with the positioning and distance between the wave gauges within the scope of the study.

Table 5.1 Probes location and positioning.

Wave characteristics				***l* from the reflected structure**			**Distance between probes *Δl***		
Case	**H(m)**	**T(s)**	**L(m)**	***0.2L***	***0.45L***	***l(m)***	***0.05L***	***0.45L***	**Δ*l* *(m)***
RW01	0.25	2.00	4.21	0.84	1.89	1.50	0.21	1.89	0.50
RW02	0.22	2.30	4.96	0.99	2.23	1.50	0.24	2.23	0.50
RW03	0.20	2.70	5.95	1.19	2.67	1.50	0.29	2.67	0.50
RW04	0.17	3.10	6.92	1.38	3.11	1.50	0.34	3.11	0.50
RW05	0.13	3.60	8.12	1.62	3.65	2.00	0.40	3.65	0.50

5.2 Geometrical Characteristics of the Alternatives Passive Wave Absorbers

5.2.1 Proposition 1

The base model is a solid plate measuring 5 cm in thickness, with shape of two slopes as depictedin Figure 5.1, the model was located 19.9 m from the start of the tank .

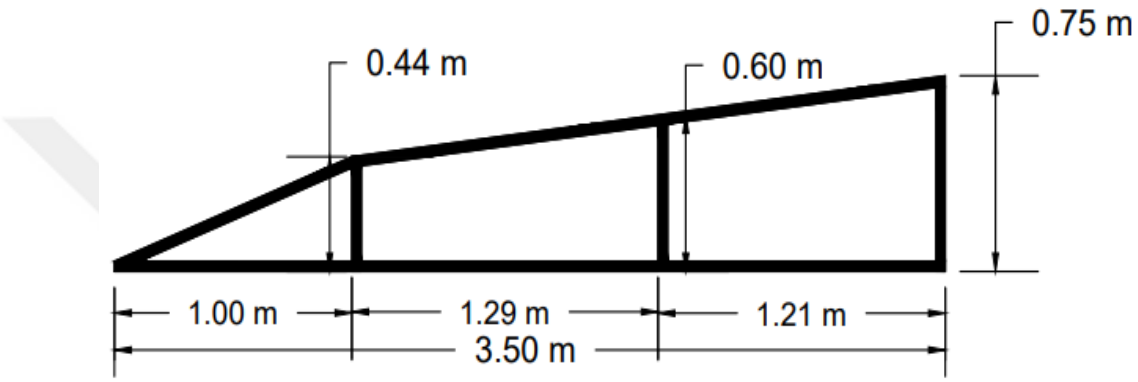

Figure 5.1 Side view of proposition 1.

5.2.2 Proposition 2

The base model is serval layers of vertical mesh screens (14 layers) measuring 10 cm in thickness and having a porosity of 10% of the first layer, 8% second layer ,6% third layer ,4% fourth layer, and 2% for the rest. The model was located 19.9 m from the tank's starting point, with a horizontal length (*x*) equal to 3.5m, and vertical length (*y*) is 1m as depicted in Figure 5.2.

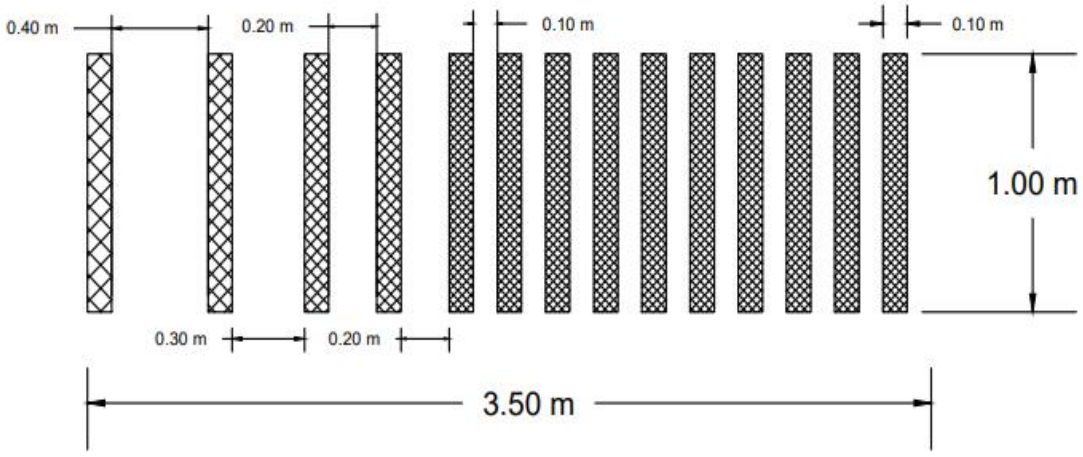

Figure 5.2 Side view of proposition 2.

5.2.3 *Proposition 3*

The base model is a solid plate measuring 5 cm in thickness. The plate had a parabolic profile and the model were located 19.9 m from the tank's starting point, with a horizontal length (x) equal to 3.5 m, and vertical length (y) is 0.75 m as depicted in Figure 5.3.

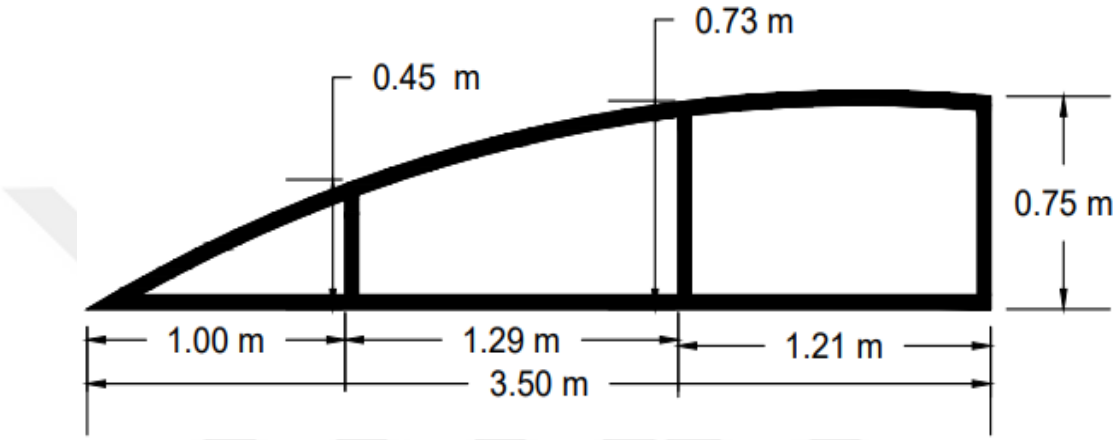

Figure 5.3 Side view of proposition 3.

5.2.4 *Proposition 4*

The model is a solid shape type of two half hexagon at the left and right side of the flume and porous cuboid. The model was located 19.9 m from the tank's starting point, with a horizontal length (x) equal to 3.5 m, and vertical length (y) is 0.75 m as depicted in Figure 5.4.

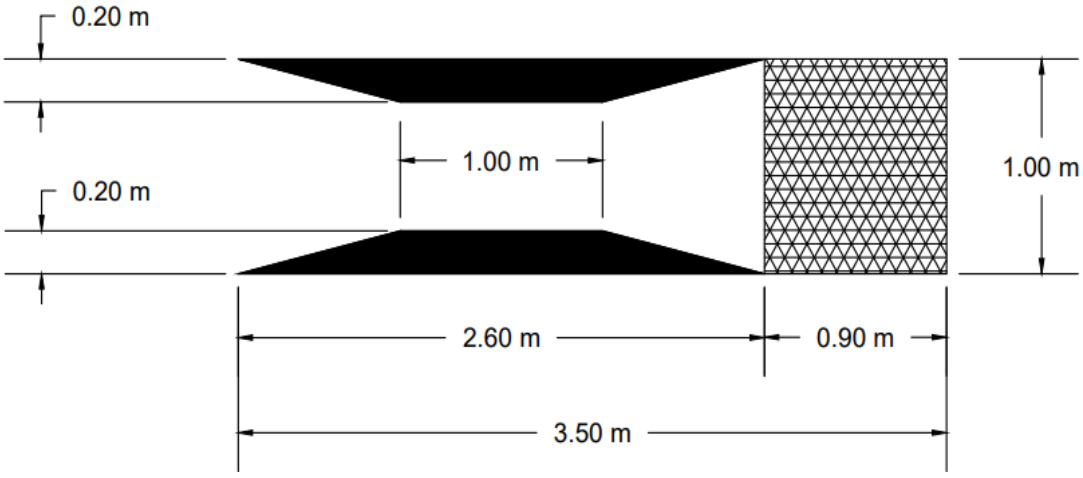

Figure 5.4 Top view of proposition 4.

5.2.5 Proposition 5

The base model is a solid shape with three different slopes. The model was located 19.9 m from the tank's starting point, with a horizontal length (*x*) equal to 3.5 m, and the max vertical length (*y*) is 0.5 m as depicted in Figure 5.5.

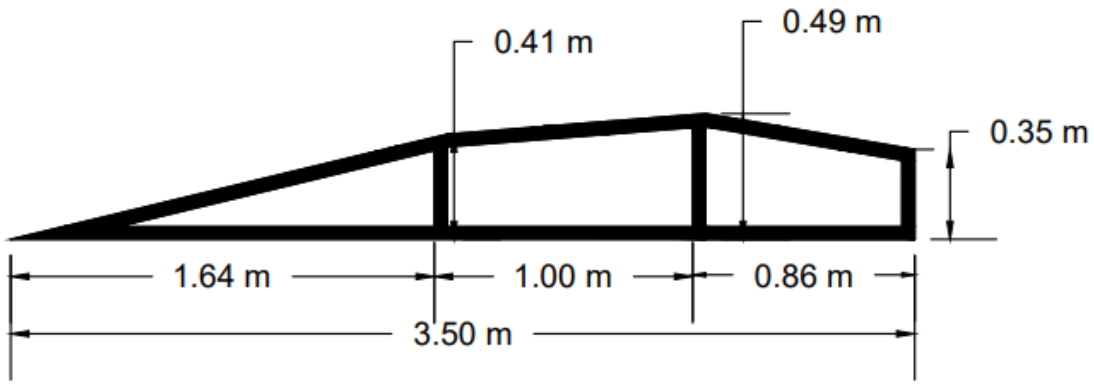

Figure 5.5 Side view of proposition 5.

5.2.6 Proposition 6

The base model is a solid parabolic shape. The plate had a parabolic profile. The model was located 19.9 m from the tank's starting point, with a horizontal length (*x*) equal to 3.5 m, and vertical length (*y*) is 0.55 m as depicted in Figure 5.6.

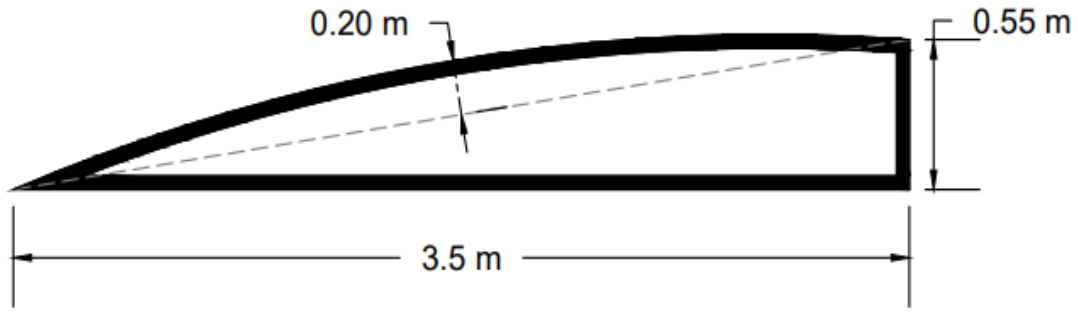

Figure 5.6 Side view of proposition 6.

5.2.7 Proposition 7

The base model is a solid parabolic shape. The plate had a parabolic profile. The model was located 19.9 m the tank's starting point, with a horizontal length (*x*) equal to 3.5 m, and vertical length (*y*) is 0.70 m as depicted in Figure 5.7.

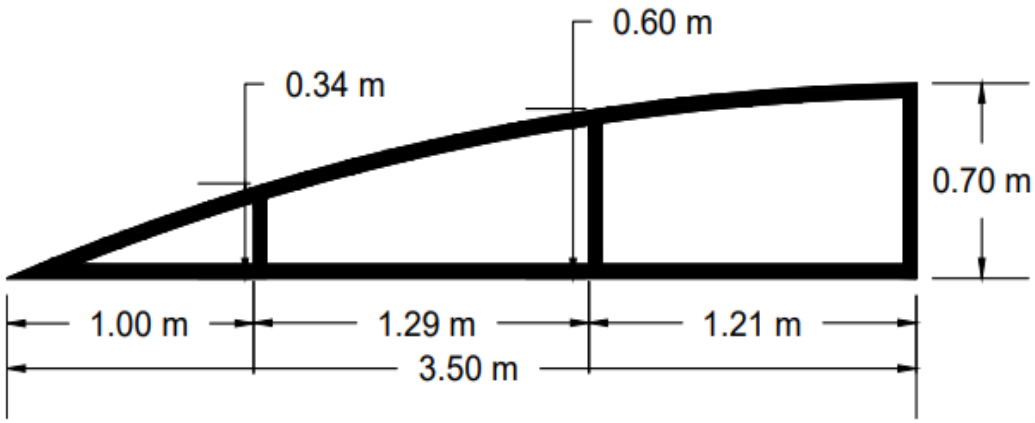

Figure 5.7 Side view of proposition 7.

5.2.8 Proposition 8

The base model is a solid shape with three different slopes. The model was located 19.9 m from the tank's starting point, with a horizontal length (*x*) equal to 3.5 m, and vertical length (*y*) is 0.70 m as depicted in Figure 5.8.

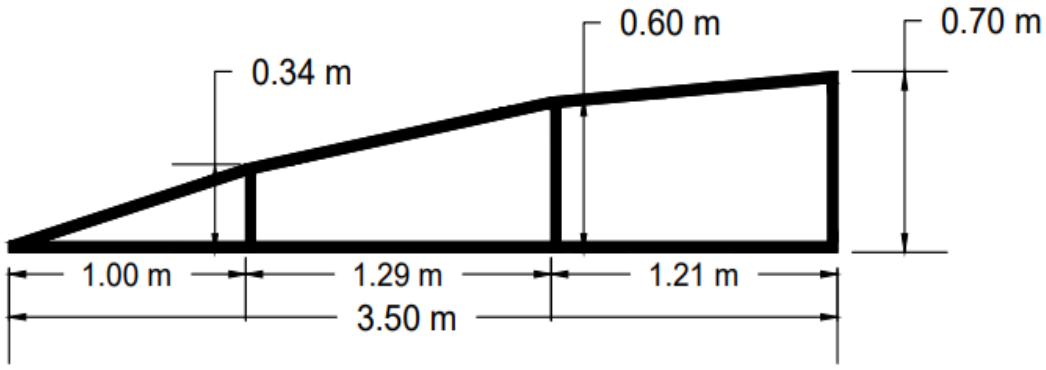

Figure 5.8 Side view of proposition 8.

5.2.9 Proposition 9

The base model is a solid parabolic shape. The plate had a parabolic profile. The model was located 20.9 m from the tank's starting point, with a horizontal length (*x*) equal to 2.5 m, and vertical length (*y*) is 0.70 m as depicted in Figure 5.9.

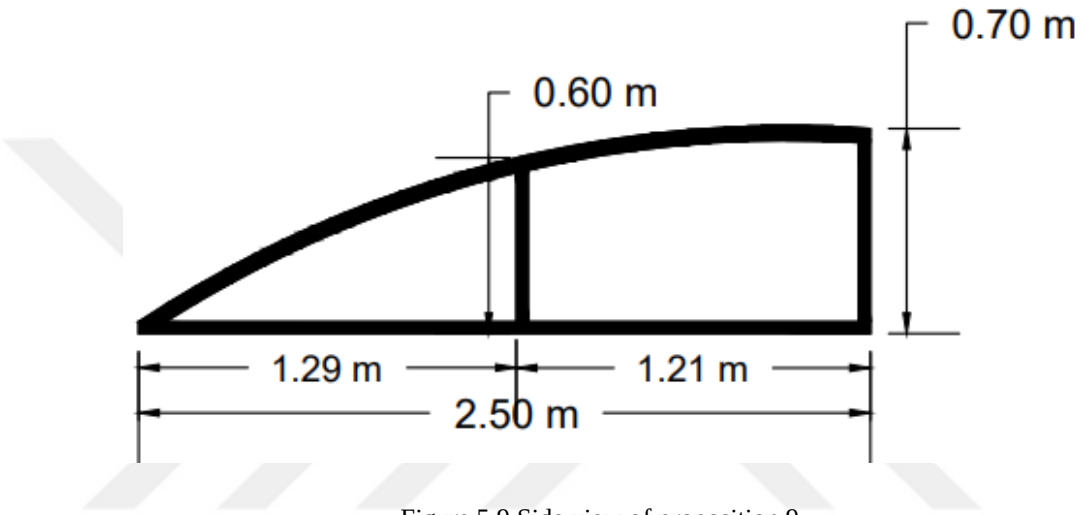

Figure 5.9 Side view of proposition 9.

5.3 The Most Efficient Proposals Fabrication

Based on the analysis of the numerical reflection coefficient (**Section 7.2**) reveals that the 2-slopes proposition and 3-slopes proposition meet the required performance criteria while being cost-effective and easy to implement. Furthermore, the parabolic (curved) proposition is chosen to further reduce the length of the passive wave absorber.

All the propositions were assembled and tested at Dokuz Eylül University Hydraulic Laboratory. Assembling and welding the propositions involves carefully aligning and securing the steel profiles in the desired shapes. The welding process ensures a secure bond between the profiles and the sheet iron, providing structural integrity and stability to the assembled shape. the propositions are securely fixed inside the wave flume by placing supports between both the model and the flume wall.

5.3.1 The 2-slopes proposition

The 2-slopes proposition consists of steel profiles that are 3.5 meters long, 0.75 meters in height, and one meter wide. These profiles are 4 mm thick and are covered with a sheet of iron, which is also 4 mm thick. Figure 5.10 shows the model at welding stage and its final shape .



Figure 5.10 Photograph and the scale model (right bottom) of the 2-slopes proposition.

5.3.2 The 3-slopes proposition

The 3-slopes proposition consists of steel profiles that are 3.5 meters long, 0.70 meters in height, and one meter wide. These profiles are 4 mm thick and are covered with a sheet of iron, which is also 4 mm thick. Figure 5.11 shows the model at welding stage and its final shape .

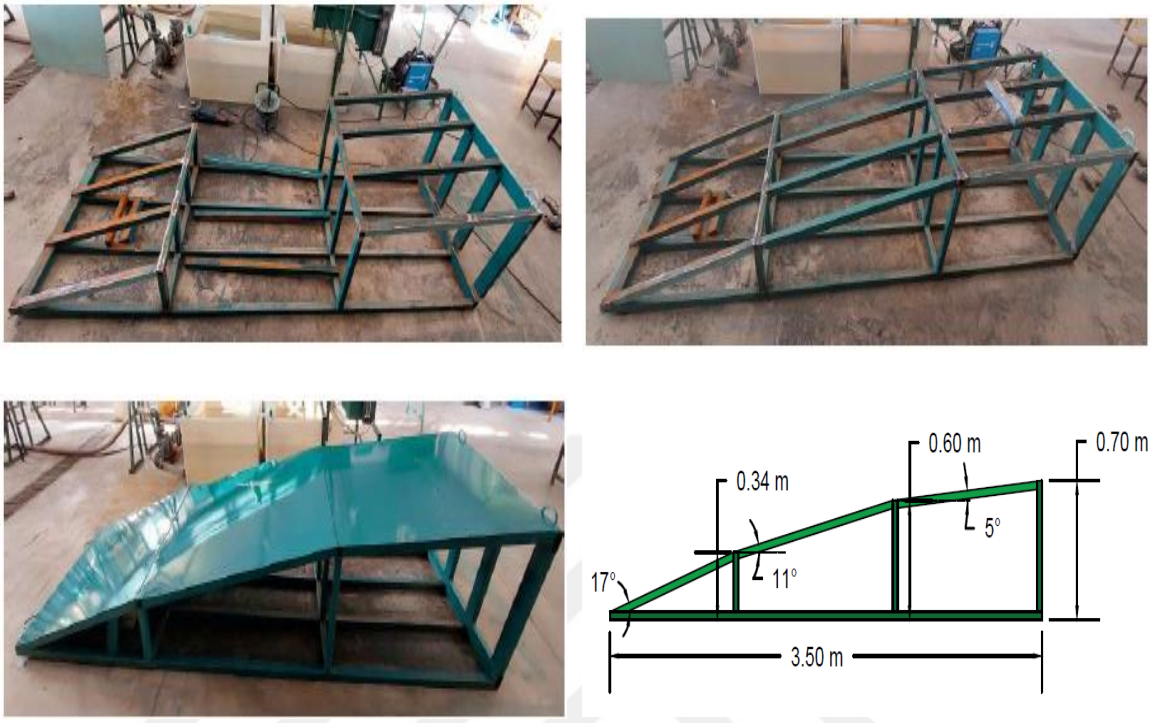

Figure 5.11 Photograph and the scale model (right bottom) of the 3-slopes proposition .

5.3.3 The parabolic (curved) proposition

The parabolic proposition consists of steel profiles that are 2.5 meters long, 0.70 meters in height, and one meter wide. These profiles are 4 mm thick and are covered with a sheet of iron with 2 mm thick. Figure 5.12 shows the model at welding stage and its final shape.



Figure 5.12 Photograph and the scale model (right bottom) of the Parabolic proposition.

A standing column rotating crane is utilized to position and remove each proposition from the wave flume upon completion of the tests. Illustrations of the process are presented in Figure 5.13.


(a)
Prof. Dr. S. Turhan ACATAY
DALGA KANALI


(b)
Prof. Dr. S. Turhan ACATAY
DALGA KANALI



Figure 5.13 Removing stages of the 3-slopes proposition design from the wave flume.

CHAPTER SIX
NUMERICAL SIMULATION

FLOW-3D is a versatile software for computational fluid dynamics (CFD) that utilizes special developed numerical approaches to address the equations of motion governing fluids. This results in time-dependent, three-dimensional solutions for flow problems that involve multiple scales and physical phenomena.

6.1 Equations of Motion

FLOW-3D describes fluid motion through non-linear, transient, second-order differential equations and employs the Volume of Fluid (VOF) method to analyze free-surface dynamics. Although area and volume fractions are constant over time in FLOW-3D, they can fluctuate when using the moving obstacle model.

In a mesh, each fluid parameter is represented by an array of values at discrete points. The regular and structured nature of rectangular grids makes them easy to generate and store, while non-uniform grid spacing allows for greater flexibility when meshing complex flow domains. The earliest numerical algorithms that utilized finite difference and finite volume methods were originally developed on such meshes and they form the foundation of the numerical approach in FLOW-3D.

To model complex geometric regions, FLOW-3D uses FAVOR_{TM}, which is a formulation where the differential equations are expressed in Cartesian coordinates (x, y, z), and area and volume porosity functions are incorporated into all equations. FAVOR_{TM} stands for Fractional Area/Volume Obstacle Representation Method. FLOW-3D employs a set of differential equations, which include three-dimensional continuity and motion equations known as the RANS (Reynolds Averaged Navier Stokes) equations. The mass continuity equation in this formulation is given as:

$$V_f \frac{\partial_p}{\partial_t} + \frac{\partial}{\partial_t}(\rho u A_x) + R\frac{\partial}{\partial_y}(\rho v A_y) + \frac{\partial}{\partial_z}(\rho w A_z) + \xi\frac{(\rho u A_x)}{x} = R_{DIF} + R_{SOR} \qquad (6.1)$$

where:

V_f is the fractional volume open to flow,

- ρ is the fluid density,
- R_{DIF} is a turbulent diffusion term, and
- R_{SOR} is a mass source.

The velocity components (u, v, w) in FLOW-3D are aligned with the coordinate directions (x, y, z) or (r, R_{SOR}, z). Fractional area open to flow in the x, y, and z directions are denoted as A_x, A_y, and A_z, respectively. The coefficient R is dependent on the coordinate system used, and its value is set to 1 and ξ is set to 0 in Cartesian coordinates.

In equation (6.1) , the right-hand side's first term represents turbulent diffusion.

$$R_{DIF} = \frac{\partial}{\partial x}\left(\upsilon_\rho A_x \frac{\partial_\rho}{\partial_x}\right) + R\frac{\partial}{\partial_y}\left(\upsilon_\rho A_y R\frac{\partial_\rho}{\partial_y}\right) + \frac{\partial}{\partial_z}\left(\upsilon_\rho A_z \frac{\partial_\rho}{\partial_z}\right) + \xi\frac{\upsilon_\rho A_x}{x}\frac{\partial_\rho}{\partial_x} \qquad (6.2)$$

The coefficient υ_ρ in FLOW-3D can be calculated using the expression $Sc\mu/\rho$, where μ represents the coefficient of momentum diffusion (viscosity) and Sc is a constant. The reciprocal of Sc is typically known as the turbulent Schmidt number. This form of mass diffusion is applicable only for turbulent mixing phenomena in fluids with non-uniform density.

In case of compressible flow problems, FLOW 3D solves the complete density transport equation as expressed in Equation (6.1). However, in the case of incompressible fluids, density (ρ) remains constant, and Equation (6.1) reduces to the incompressibility condition.

$$\frac{\partial}{\partial_x}(uA_x) + R\frac{\partial}{\partial_y}(vA_y) + \frac{\partial}{\partial_z}(wA_z) + \xi\frac{uA_x}{x} = \frac{R_{SOR}}{\rho} \qquad (6.3)$$

The Navier-Stokes equations, along with some supplementary terms, describe the fluid velocity components (u, v, w) in all three coordinate directions.

$$\frac{\partial u}{\partial t} + \frac{1}{V_F}\left\{uA_x\frac{\delta u}{\delta x} + vA_yR\frac{\partial u}{\partial y} + wA_z\frac{\partial u}{\partial z}\right\} - \xi\frac{A_y v^2}{xV_F} = -\frac{1}{\rho}\frac{\partial_P}{\partial_x} + G_x + f_x - b_x - \frac{R_{SOR}}{\rho V_F}(u - u_w - \delta u_s) \tag{6.4}$$

$$\frac{\partial v}{\partial t} + \frac{1}{V_F}\left\{uA_x\frac{\delta v}{\delta x} + vA_yR\frac{\partial v}{\partial y} + wA_z\frac{\partial v}{\partial z}\right\} + \xi\frac{A_y uv}{xV_F} = -\frac{1}{\rho}\left(R\frac{\partial_P}{\partial_y}\right) + G_y + f_y - b_y - \frac{R_{SOR}}{\rho V_F}(v - v_w - \delta v_s) \tag{6.5}$$

$$\frac{\partial w}{\partial t} + \frac{1}{V_F}\left\{uA_x\frac{\delta w}{\delta x} + vA_yR\frac{\partial w}{\partial y} + wA_z\frac{\partial w}{\partial z}\right\} = -\frac{1}{\rho}\frac{\partial_P}{\partial_x} + G_z + f_z - b_z - \frac{R_{SOR}}{\rho V_F}(w - W_w - \delta w_s) \tag{6.6}$$

Body accelerations are represented by (G_x, G_y, G_z), viscous accelerations by (f_x, f_y, f_z), and flow losses in porous media or across porous baffle plates by (b_x, b_y, b_z). The final terms in the equations describe the injection of mass at a source that is represented by a geometric component.

In the case of a variable dynamic viscosity μ, the viscous accelerations are described as follows:

$$\rho V_F f_x = wsx - \left\{\frac{\partial}{\partial x}(A_x\tau_{xx}) + R\frac{\partial}{\partial y}\left(A_y\tau_{xy}\right) + \frac{\partial}{\partial z}(A_z\tau_{xz}) + \frac{\xi}{x}(A_x\tau_{xx} - A_y\tau_{yy})\right\} \tag{6.7}$$

$$\rho V_F f_y = wsy - \left\{\frac{\partial}{\partial x}\left(A_x \tau_{xy}\right) + R\frac{\partial}{\partial y}\left(A_y \tau_{yy}\right) + \frac{\partial}{\partial z}\left(A_z \tau_{yz}\right) + \frac{\xi}{x}(A_x + A_y)\tau_{xy}\right\} \tag{6.8}$$

$$\rho V_F f_y = wsz - \left\{\frac{\partial}{\partial x}(A_x \tau_{xz}) + R\frac{\partial}{\partial y}\left(A_y \tau_{yz}\right) + \frac{\partial}{\partial z}(A_z \tau_{zz}) + \frac{\xi}{x}(A_x \tau_{xz})\right\} \tag{6.9}$$

The quantities denoted by wsx, wsy, wsz correspond to wall shear stresses, while the stresses enclosed in the parentheses can be expressed as:

$$\tau_{xx} = -2\mu\left\{\frac{\partial u}{\partial x} - \frac{1}{3}\left(\frac{\partial u}{\partial x} + R\frac{\partial v}{\partial y} + \frac{\partial w}{\partial z} + \frac{\xi u}{x}\right)\right\} \tag{6.10}$$

$$\tau_{yy} = -2\mu\left\{R\frac{\partial v}{\partial y} + \xi\frac{u}{x} - \frac{1}{3}\left(\frac{\partial u}{\partial x} + R\frac{\partial v}{\partial y} + \frac{\partial w}{\partial z} + \frac{\xi u}{x}\right)\right\} \tag{6.11}$$

$$\tau_{zz} = -2\mu\left\{\frac{\partial w}{\partial z} - \frac{1}{3}\left(\frac{\partial u}{\partial x} + R\frac{\partial v}{\partial y} + \frac{\partial w}{\partial z} + \frac{\xi u}{x}\right)\right\} \tag{6.12}$$

$$\tau_{xy} = -\mu\left\{\frac{\partial v}{\partial x} + R\frac{\partial u}{\partial y} - \frac{\xi v}{x}\right\} \tag{6.13}$$

$$\tau_{xz} = -\mu\left\{\frac{\partial u}{\partial z} + \frac{\partial w}{\partial x}\right\} \tag{6.14}$$

$$\tau_{yz} = -\mu\left\{\frac{\partial v}{\partial z} + R\frac{\partial w}{\partial y}\right\} \tag{6.15}$$

6.2 Numerical simulation of wavemaker and wave absorbers

The initial configuration of the FLOW 3D simulation is based on the real dimensions of the experiments, so the numerical tank is 23.4 m long, 1 m wide, and 1.2 m tall. The initial water level is 0.55 m. On the offshore side, the wave absorber is defined as a porous component, also 3 m from the offshore side, a solid moving object created to simulate the movement of the piston-type wave generator. Regarding wave absorbers at the end of the flume, solid stainless-steel material is considered for the alternative absorbers, whereas the rocks with a slope of 1:7 are considered as wave absorbing components.

6.3 Geometry Creation and Model Setup

The simulations were performed on a computer equipped with a Core i7 2700-K CPU running at 3.40 GHz and 16 GB of RAM. The geometry of the absorbers was created using SketchUp Pro 2021, which was then converted to a stereolithography (STL) file and loaded into FLOW-3D in the physics of the system, the density is evaluated as a function of other quantities when the Density evaluation tab is selected. The fluid was one fluid (incompressible) Water at 20 C with all its properties uploaded as the fluid in the fluid properties and set to viscous flow. The simulation was set to the RNG model with no-slip wall shear boundary conditions. The movement of objects was activated through the "explicit moving" option. The porous media was set to the Darcian saturated drag option.

6.4 Meshing and Sensitivity Analysis

To ensure precise numerical calculations and prevent stability issues that can yield inaccurate results, it is crucial to perform a thorough mesh quality assessment using Simulation Pre-Check. To achieve optimal mesh quality, a mesh cell size of 0.04 m was selected for irregular wave scenarios, while a size of 0.02 m was chosen for regular waves. It's noteworthy that these choices maintain compliance with the specified aspect ratio limits.

The meshing was performed using non-conforming mesh blocks. The sensitivity analysis was pre-checked according to the results of the FAVOR. Figure 6.1 summarizes

the mesh size and the total number of grids. To get better results, the overall model was simulated.

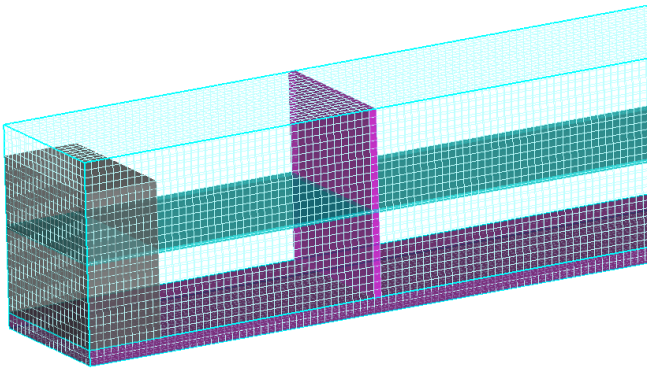

(a) Mesh System for the Moving Object Component.

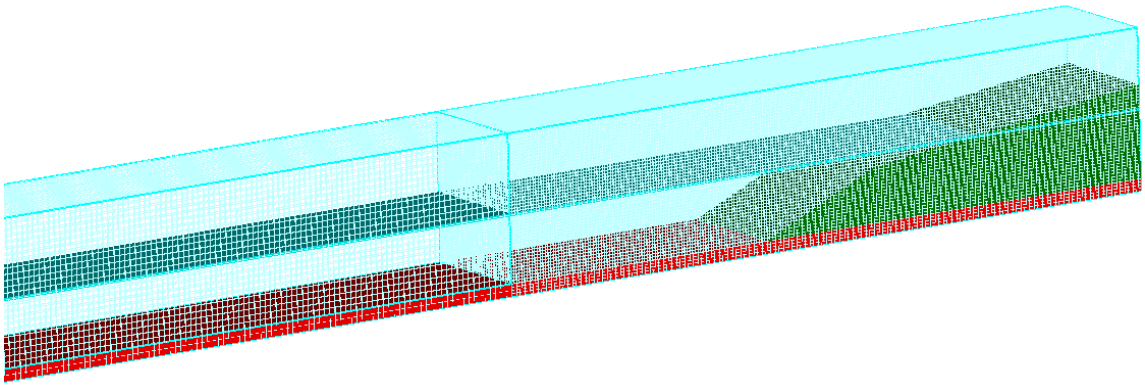

(b) Mesh System for the Wave Absorber Component.

Figure 6.1 The models mesh system.

6.5 Boundary Conditions and Solution Initialization

The wave generated in FLOW-3D used the translational velocity on the x-axis to simulate the movement of a piston-type wavemaker for irregular wave cases in the physical model, the top boundary condition (z max) set to a specified pressure with the fluid fraction equal to 0. While the bottom side (z min), the left side (y min), the right side

(y max), the inlet (x min), and the outlet (x max) were set to "wall", as shown in Figure 6.2 . For regular wave cases the boundary condition z max (z min), (y min), (y max), and (x max) were set to "wall", but the inlet (x min) was set to Stokes and Cnoidal waves (Fourier Series method), as shown in Figure 6.3.

The rocks with a slope of 1:7 is considered as wave absorbing components, whereas the alternatives for passive wave proposals have been selected as a solid stainless-steel material. The simulations have been set to run for one hour for irregular wave cases and ten minutes for regular wave cases, with a data interval of 0.2 seconds. The fluid was initialized with an initial fluid elevation of 0.55 m. Finally, the hydraulic data was selected at the output tab.

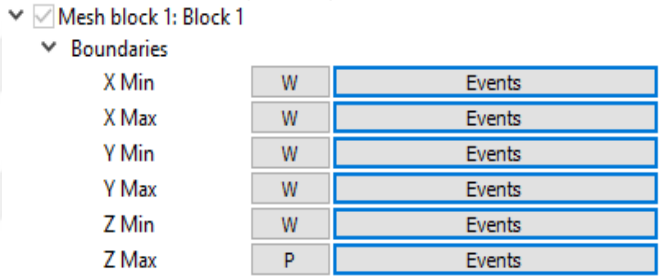

(a) Boundaries condition for irregular wave simulations.

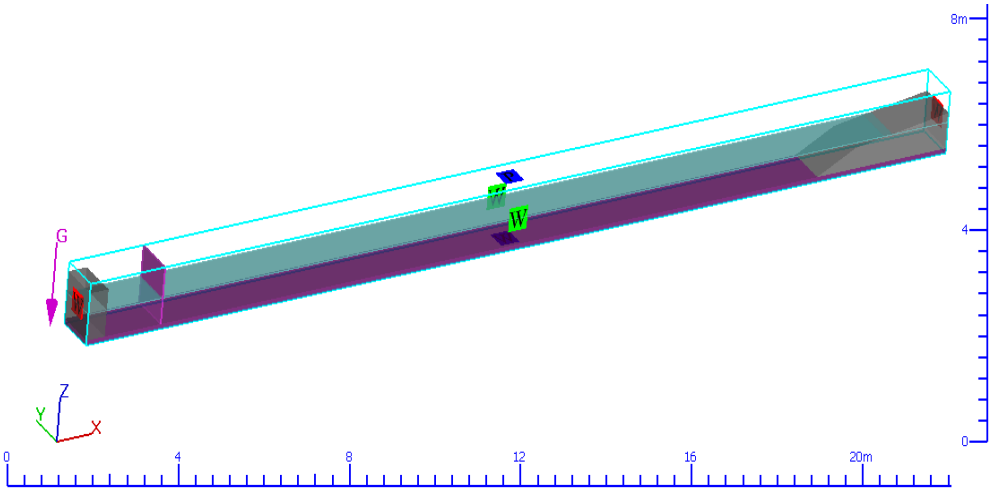

(b) Mesh boundaries for irregular wave simulations (alternatives absorbers).

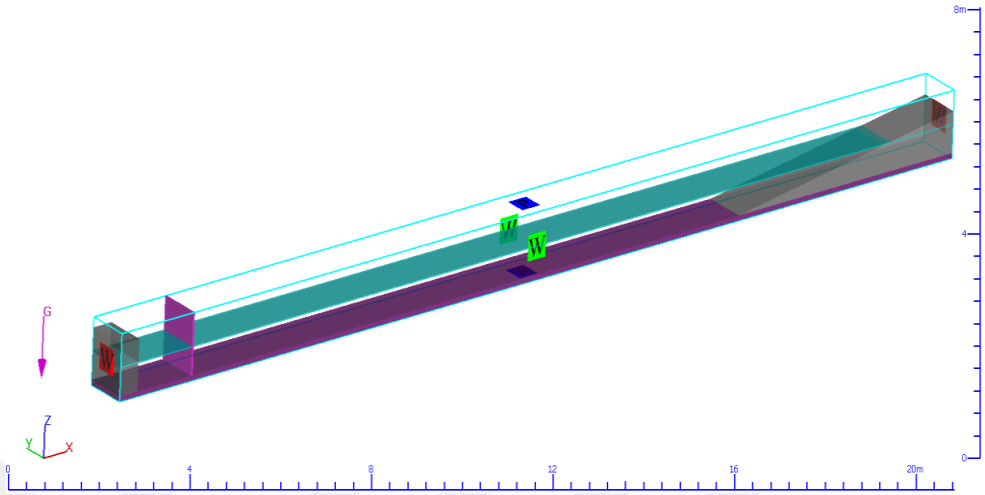

(c) Mesh boundaries for irregular wave simulations in case (slope 1:7).

Figure 6.2 The Boundary conditions system for irregular wave simulations.

Mesh block 1: Block 1

Boundaries

X Min	Wv	Events
X Max	W	Events
Y Min	W	Events
Y Max	W	Events
Z Min	W	Events
Z Max	P	Events

(a) Boundaries condition for regular wave simulations.

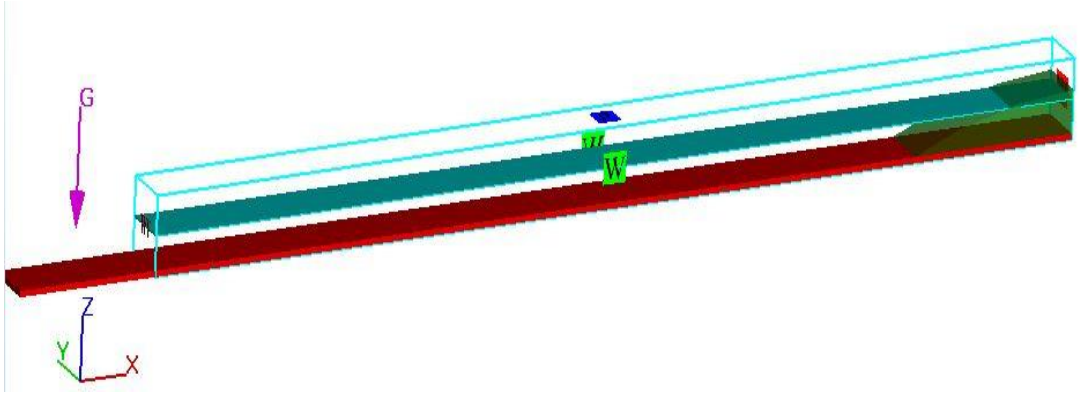

(b) Probe P2 Mesh boundaries for regular wave simulations.

Figure 6.3 The Boundary conditions system for regular wave simulations.

CHAPTER SEVEN
RESULTS AND DISCCUSIONS

The purpose of this study is to establish a suitable laboratory wave environment suitable for conducting physical model experiments in the wave flume.

7.1 Wave Generation

The generation of irregular waves is a particularly significant aspect of this initiative, as it is essential for facilitating such experiments in the wave flume. Within the topic of the study, five experiments and five simulations were performed to test the irregular wave conditions. The irregular waves (IRW) were generated after specifying the target JONSWAP spectrum. The significant wave heights H_s(0.13 to 0.22 m) and of significant periods T_s (1.56 to 3.6 s) were selected. The spectrum is discretized to N=351 samples. The duration of the experiments was set to 1 hour. The water depth at the paddles of the wavemaker is 0.55 m and the wave absorber selected to be rocks fill of varying sizes with a slope of 1:7. The experiment set and the simulation results are summarized in Table 7.1.

The two sensors (probes), P1 and P2, attached to the ULS are used to obtain the surface elevation of the experiments, which are then used to calculate the wave characteristics using the zero-up crossing method. (Hs and Ts denote significant wave height and significant wave period, respectively, which corresponds to the average value obtained from one-third of the total individual wave heights and periods, utilizing the zero-up crossing method, H_{mean} is the mean wave height, H_{RMS} is the root mean square, and H_{max} is the maximum wave height).

Table 7.1 Experiments set and simulations results.

		H_s	T_s	T_p	f_p	H_{mean}	H_{rms}	H_{max}
Target	**IRW 01**	**0.220**	**2.300**	**2.460**	**0.400**	**0.146**	**0.158**	**0.336**
Exp	P1	0.188	2.370	2.540	0.392	0.127	0.139	0.349
FLOW 3D		0.216	2.330	2.490	0.400	0.143	0.157	0.346
Exp	P2	0.185	2.297	2.458	0.406	0.126	0.138	0.390
FLOW 3D		0.189	2.300	2.460	0.400	0.130	0.141	0.305
Target	**IRW 02**	**0.200**	**2.700**	**2.880**	**0.340**	**0.129**	**0.142**	**0.268**
Exp	P1	0.180	2.730	2.920	0.340	0.112	0.130	0.270
FLOW 3D		0.196	2.730	2.920	0.340	0.128	0.141	0.282
Exp	P2	0.190	2.790	2.990	0.330	0.120	0.135	0.317
FLOW 3D		0.189	2.820	3.020	0.330	0.128	0.139	0.260
Target	**IRW 03**	**0.170**	**3.100**	**3.310**	**0.300**	**0.110**	**0.121**	**0.255**
Exp	P1	0.1720	2.920	3.130	0.310	0.101	0.119	0.336
FLOW 3D		0.1829	3.170	3.400	0.290	0.115	0.129	0.267
Exp	P2	0.169	3.050	3.260	0.300	0.103	0.118	0.320
FLOW 3D		0.180	2.980	3.190	0.310	0.111	0.126	0.325
Target	**IRW 04**	**0.130**	**3.600**	**3.850**	**0.259**	**0.084**	**0.093**	**0.178**
Exp	P1	0.133	3.650	3.910	0.255	0.082	0.093	0.187
FLOW 3D		0.140	3.610	3.860	0.259	0.087	0.098	0.200
Exp	P2	0.126	3.420	3.670	0.272	0.077	0.087	0.202
FLOW 3D		0.141	3.430	3.570	0.270	0.082	0.096	0.237
Target	**IRW 05**	**0.144**	**1.560**	**1.669**	**0.599**	**0.093**	**0.100**	**0.237**
Exp	P1	0.136	1.520	1.626	0.614	0.084	0.100	0.330
FLOW 3D		0.139	1.580	1.693	0.590	0.093	0.101	0.237
Exp	P2	0.135	1.520	1.636	0.611	0.088	0.098	0.340
FLOW 3D		0.118	1.620	1.740	0.570	0.078	0.080	0.192

In the context of the study, Figure 7.1 displays two instances depicting the experimental and numerical surface elevations at P2 of IRW_02 and IRW_04, respectively, with reference to P1. Additionally, Figure 7.2 and Figure 7.3 provide an illustration of simulated wave profiles.

(a) IRW_02_P2

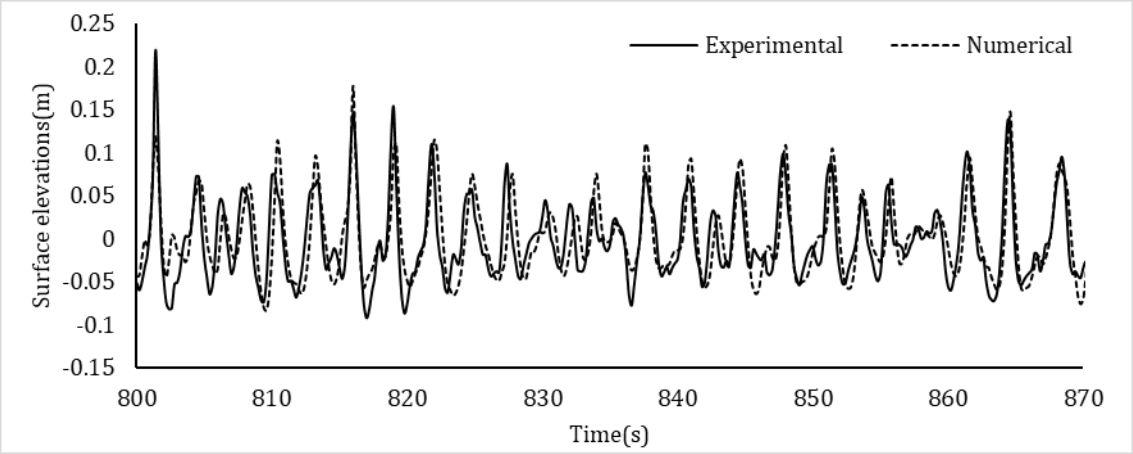

(b) IRW_04_P1

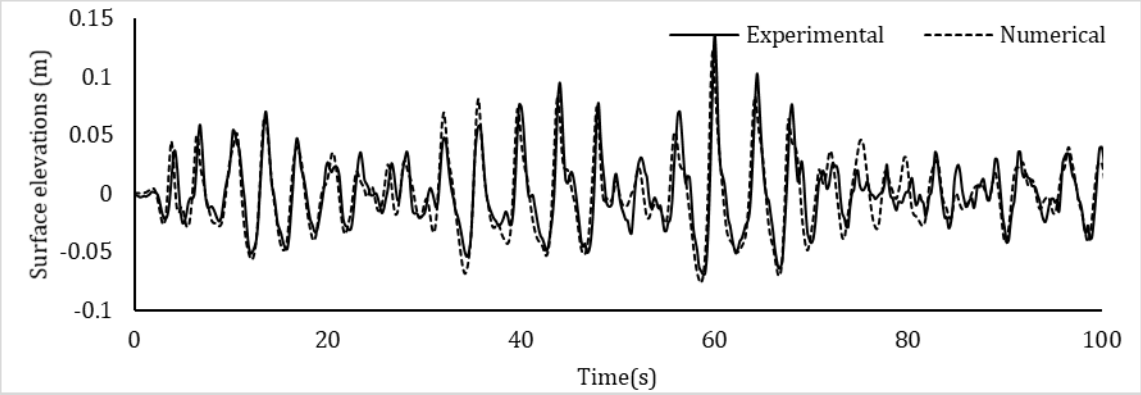

Figure 7.1 Comparison of the experimental and numerical surface elevations.

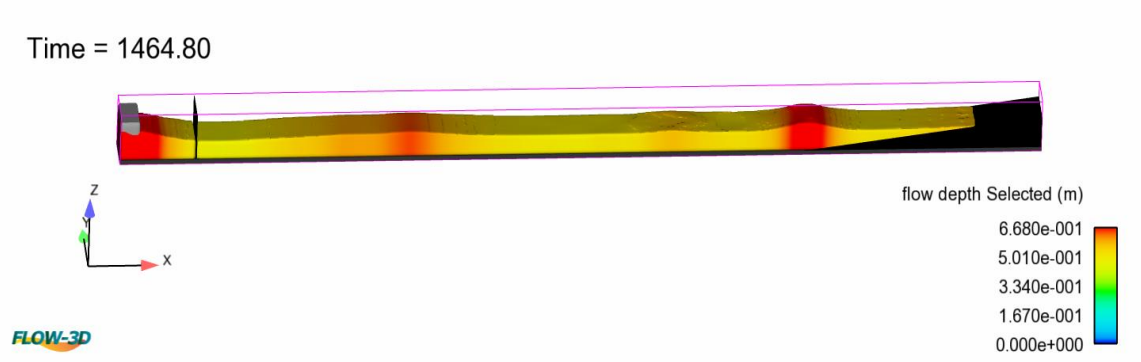

Figure 7.2 Flow depth example of a simulated irregular wave profile.

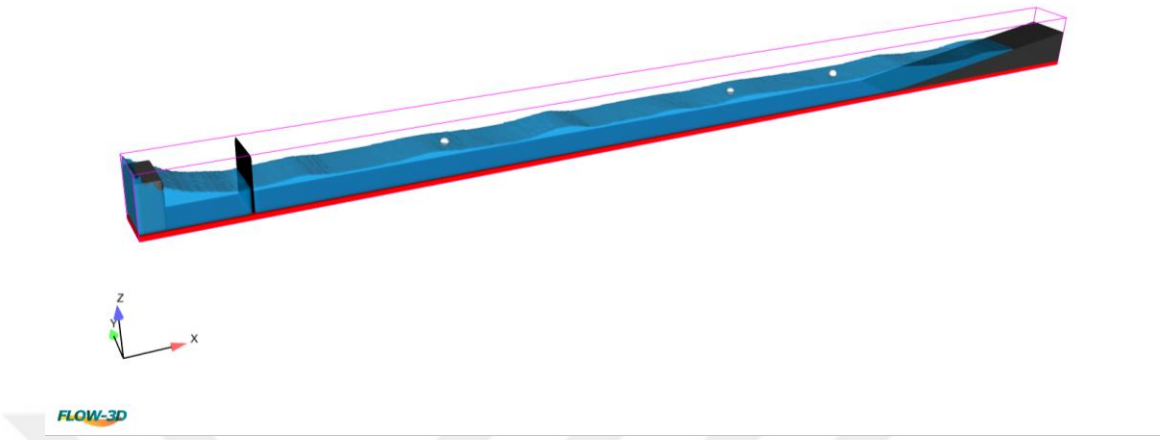

Figure 7.3 An example of a simulated irregular wave profile.

The rapid random movement of the paddle (moving object) can cause some unwanted water dispersion, which can lead to more considerable deviation in some cases. Also, the slope shape of the passive wave absorber can behave differently in the experiment due to the variant shape of the rocks, wherein the model was defined as a wave absorber component. Moving on, Figure 7.4 and Figure 7.5 present scatter diagrams that compare the experimental and numerical results.

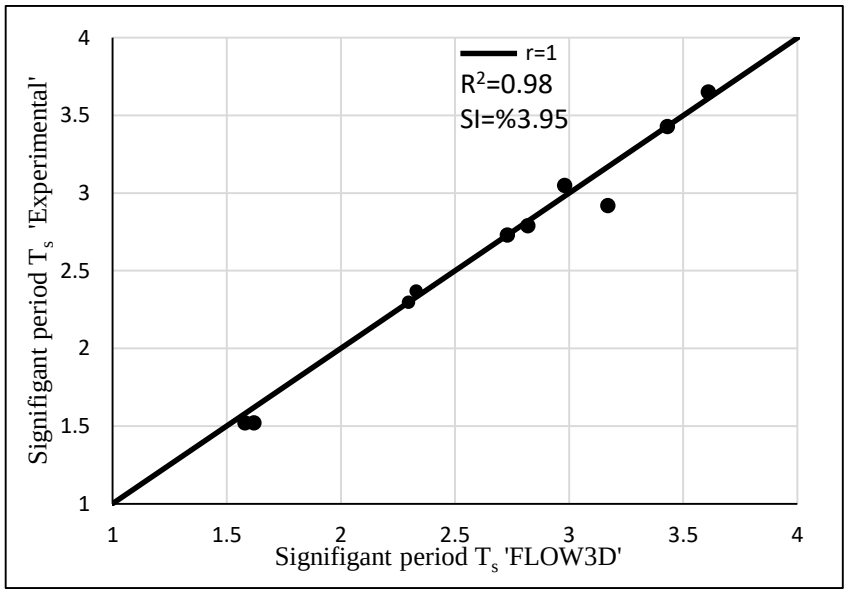

Figure 7.4 Scatter diagram for experimental and numerical T_s.

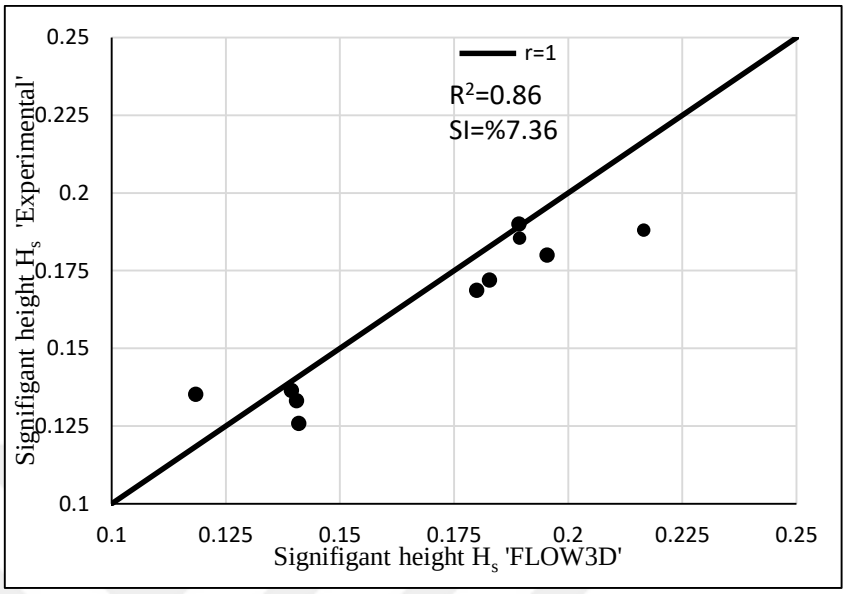

Figure 7.5 Scatter diagram for experimental and numerical H_s.

Figure 7.6 to Figure 7.10 offer a comparison between the JONSWAP spectrum of the experimental wave, as measured by the wave gauges at P1 and P2 (measured H_s and T_s), and the corresponding theoretical spectrum (with target H_s and T_s).

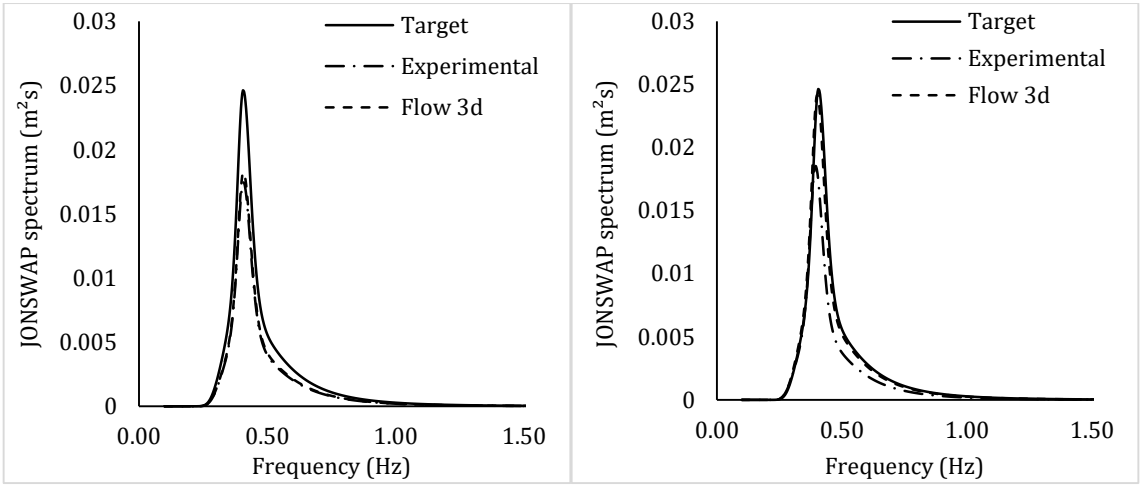

(a) Probe P1 IRW_01_P1 (b) Probe P2 IRW_01_P2

Figure 7.6 Experimental, numerical, and the target JONSWAP spectrum of IRW_01 H_s =0.22 m T_s=2.3 s.

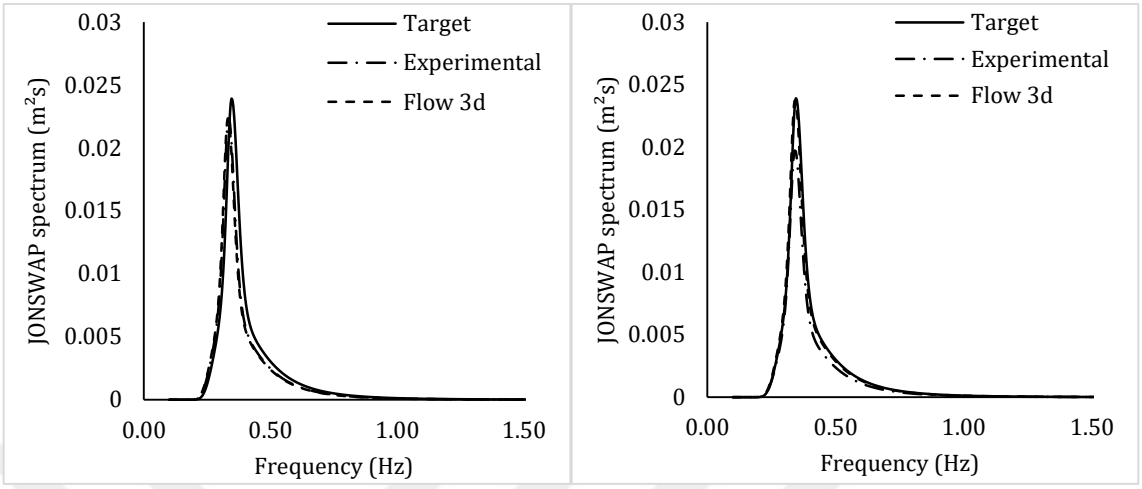

(a) Probe P1 IRW_02_P1 (b) Probe P2 IRW_02_P2

Figure 7.7 Experimental, numerical, and the target JONSWAP spectrum of IRW_02 H_s=0.20 m T_s=2.7 s.

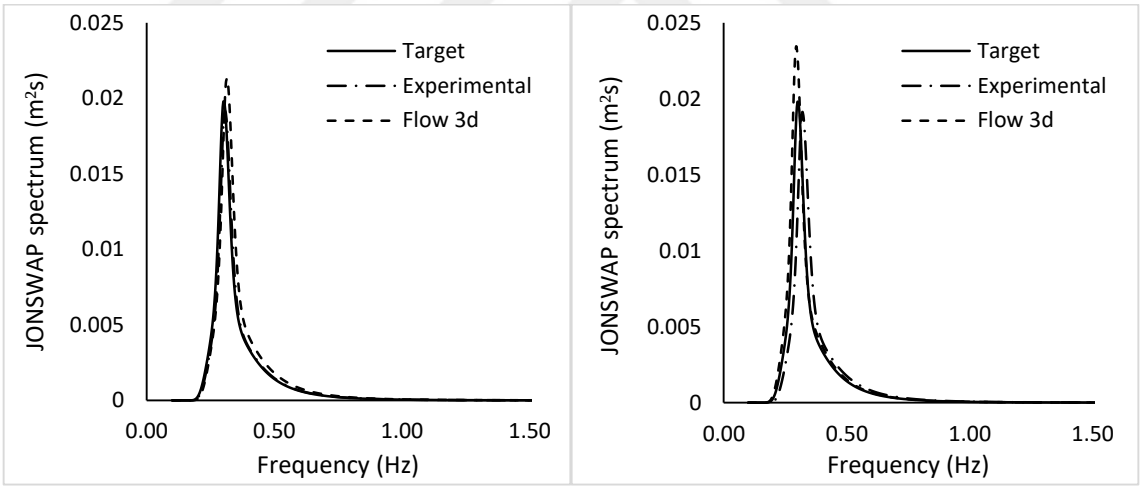

(a) Probe P1. IRW_03_P1 (b) Probe P2. IRW_03_P2

Figure 7.8 Experimental, numerical, and the target JONSWAP spectrum of IRW_03 H_s=0.17 m T_s=3.1 s.

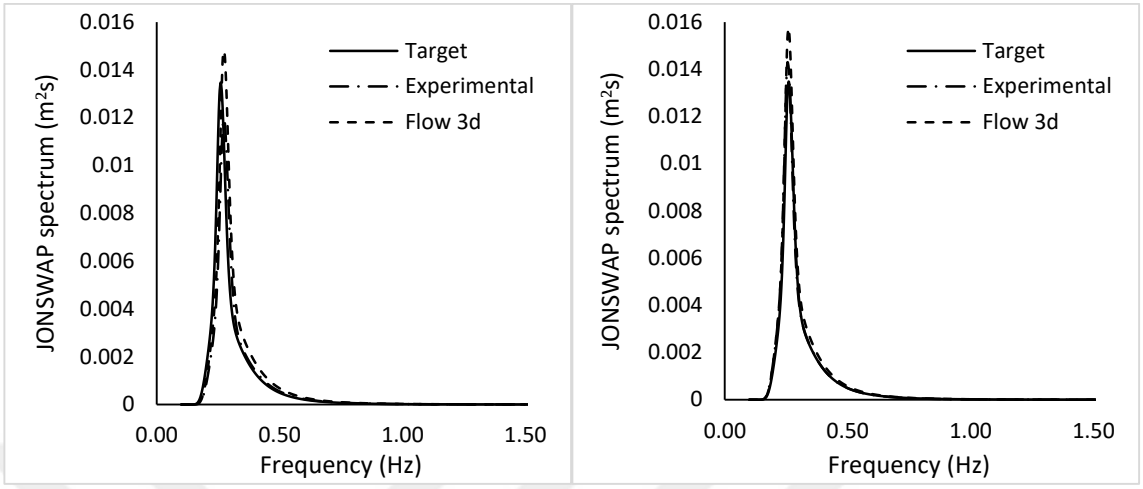

(a) Probe P1. IRW_04_P1 (b) Probe P2. IRW_04_P2

Figure 7.9 Experimental, numerical, and the target JONSWAP spectrum of IRW_04 H_s=0.13 m T_s =3.6 s.

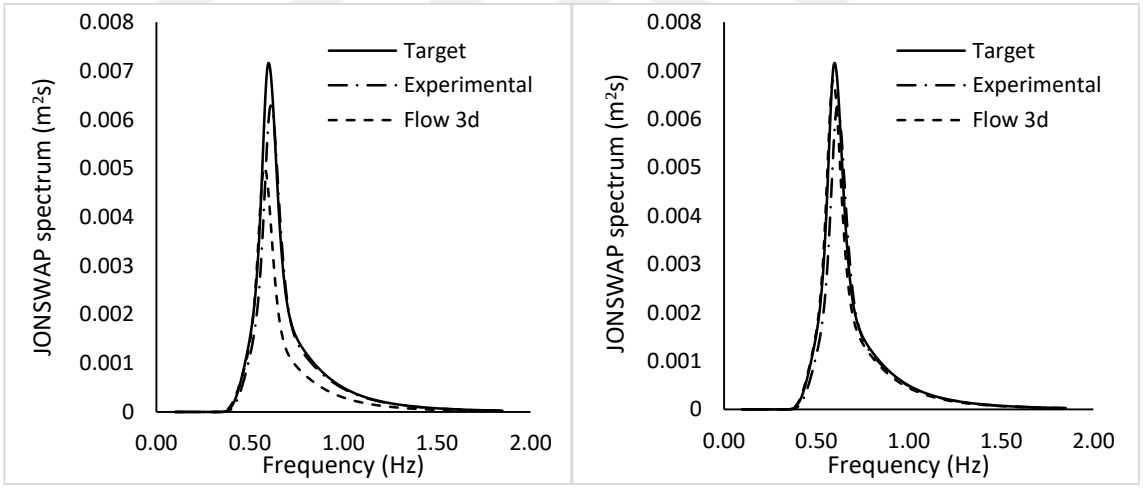

(a) Probe P1. IRW_05_P1 (b) Probe P2. IRW_05_P2

Figure 7.10 Experimental, numerical, and the target JONSWAP spectrum IRW_05 H_s=0.144 m T_s=1.56 s

.

The errors ratios between theoretical and numerical data (Table 7.2) and experimental and numerical data (Table 7.3) are generally less than 10%, except in a few cases (IRW_01_P1, IRW_01_P2, IRW_04_P2, and IRW_05_P2) where the numerical model incorrectly estimates the surface elevations.

In Table 7.4, the major error ratio between the experimental and theoretical data are 14% for the IRW_01_P1 case and 15% for the IRW_01_P2 case. During the physical experiments, the reflection in the flume distorted the wave record in the case of generating big waves (wave height greater than 0.25m), which affects the wave energy. Some experiment tests were repeated for the validation of the results.

Table 7.2 Theoretical and numerical data error ratios.

		Error ratios %	
Case	**Probe**	**H_s**	**T_s**
IRW_01	P1	1.55	1.30
	P2	13.91	0.17
IRW_02	P1	2.30	1.11
	P2	5.40	4.44
IRW_03	P1	7.53	2.26
	P2	5.88	3.87
IRW_04	P1	8.08	0.28
	P2	8.46	4.72
IRW_05	P1	3.19	1.28
	P2	17.78	3.85

Table 7.3 Experimental and numerical data error ratios

		Error ratios %	
Case	**Probe**	**H_s**	**T_s**
IRW_01	P1	15.21	1.69
	P2	2.16	0.04
IRW_02	P1	8.56	0.00
	P2	0.42	1.08
IRW_03	P1	6.28	8.56
	P2	6.70	2.30
IRW_04	P1	5.56	1.10
	P2	12.08	0.03
IRW_05	P1	2.20	3.95
	P2	12.43	6.58

Table 7.4 Theoretical and experimental data error ratios

		Error ratios %	
Case	**Probe**	**H_s**	**T_s**
IRW_01	P1	14.55	3.04
	P2	15.73	0.13
IRW_02	P1	10.00	1.11
	P2	5.00	3.33
IRW_03	P1	1.18	5.81
	P2	0.76	1.61
IRW_04	P1	2.38	1.39
	P2	3.23	4.75
IRW_05	P1	5.28	2.56
	P2	6.11	2.56

The irregular wave surface profile was generated from the given target JONSWAP spectrum using the modified random phase method by the correction factors as in Eq(3.7). After validating the wave generation technique, user software was developed in Python and installed on a personal computer to control the wavemaker. After that the experiments and the numerical model were carried out under identical conditions. The results obtained from the numerical model were compared with the experimental data. Figure 7.1 reveals that the experimental and numerical results (significant wave period Ts) were extremely close to the target data. Figure 7.5 shows that the numerical and experimental error ratios increase when the significant wave height increases.

According to the observations and results of the studies, we can conclude that the wave reflections in the flumes increase the ratio of variances between the target and generated wave characteristics, especially at wave heights greater than 0.25 meters.

In the next phase of the study, we will focus on developing a distinctive alternative shapes of passive wave absorption mechanisms in the wave flume. These mechanisms aim

to shortening the absorber length and minimize wave reflection, thereby improving the overall quality of the laboratory wave environment.

7.2 Wave Absorption

Table 7.5 provides the numerical reflection coefficients of the different alternative propositions. These coefficients were obtained through five simulations conducted using regular waves, referred to as Simulation Regular Wave (SRW). The values of C_r, which represent the reflection coefficient, range from 0 to 1. Lower values of C_r indicate better performance, as suggested by Hughes (1993).

Table 7.5 Reflection coefficient of the series of numerical simulations.

	Case	$\boldsymbol{H\ (m)}$	$\boldsymbol{T\ (s)}$	$\boldsymbol{H_i\ (m)}$	$\boldsymbol{H_r\ (m)}$	$\boldsymbol{C_r}$
Proposition 1	1_SRW01	0.25	2.0	0.1758	0.0137	0.0782
	1_SRW02	0.22	2.3	0.1951	0.0198	0.1014
	1_SRW03	0.20	2.7	0.2152	0.0301	0.1397
	1_SRW04	0.17	3.1	0.1908	0.0280	0.1469
	1_SRW05	0.13	3.6	0.1227	0.0197	0.1608
Proposition 2	2_SRW01	0.25	2.0	0.1725	0.0534	0.3100
	2_SRW02	0.22	2.3	0.1704	0.0350	0.2051
	2_SRW03	0.20	2.7	0.2338	0.0487	0.2083
	2_SRW04	0.17	3.1	0.2168	0.0494	0.2280
	2_SRW05	0.13	3.6	0.1583	0.0363	0.2291
Proposition 3	3_SRW01	0.25	2.0	0.1763	0.0340	0.1942
	3_SRW02	0.22	2.3	0.2037	0.0340	0.1669
	3_SRW03	0.20	2.7	0.1769	0.0400	0.2263
	3_SRW04	0.17	3.1	0.1692	0.0420	0.2485
	3_SRW05	0.13	3.6	0.1302	0.0231	0.1769
Proposition 4	4_SRW01	0.25	2.0	0.2039	0.1497	0.7339
	4_SRW02	0.22	2.3	0.3203	0.1313	0.4099
	4_SRW03	0.20	2.7	0.1554	0.1196	0.7691
	4_SRW04	0.17	3.1	0.1163	0.0880	0.7568
	4_SRW05	0.13	3.6	0.1117	0.0908	0.8119

Table 7.5 Continuous

Proposition 5	5_SRW01	0.25	2.0	0.1700	0.0639	0.3754
	5_SRW02	0.22	2.3	0.1813	0.0707	0.3899
	5_SRW03	0.20	2.7	0.2233	0.0376	0.1684
	5_SRW04	0.17	3.1	0.1911	0.1061	0.5551
	5_SRW05	0.13	3.6	0.1883	0.0942	0.5002
Proposition 6	6_SRW01	0.25	2.0	0.1884	0.0322	0.1709
	6_SRW02	0.22	2.3	0.2067	0.0457	0.2213
	6_SRW03	0.20	2.7	0.2086	0.0483	0.2314
	6_SRW04	0.17	3.1	0.1750	0.0310	0.1772
	6_SRW05	0.13	3.6	0.1349	0.0172	0.1277
Proposition 7	7_SRW01	0.25	2.0	0.1817	0.0287	0.1582
	7_SRW02	0.22	2.3	0.2103	0.0246	0.1172
	7_SRW03	0.20	2.7	0.1813	0.0467	0.2579
	7_SRW04	0.17	3.1	0.1613	0.2390	0.1482
	7_SRW05	0.13	3.6	0.1823	0.0227	0.1245
Proposition 8	8_SRW01	0.25	2.0	0.2175	0.0254	0.1169
	8_SRW02	0.22	2.3	0.2311	0.0248	0.1075
	8_SRW03	0.20	2.7	0.1855	0.0253	0.1367
	8_SRW04	0.17	3.1	0.1639	0.0302	0.1841
	8_SRW05	0.13	3.6	0.1438	0.0149	0.1040
Proposition 9	9_SRW01	0.25	2.0	0.2102	0.0486	0.2313
	9_SRW02	0.22	2.3	0.1825	0.0220	0.1206
	9_SRW03	0.20	2.7	0.2026	0.0261	0.1290
	9_SRW04	0.17	3.1	0.1806	0.0313	0.1734
	9_SRW05	0.13	3.6	0.1874	0.0140	0.0748

Upon analyzing Table 7.5 and Figure 7.11**,** it becomes evident that the reflection coefficient reflects the quality of each proposition. With this in mind, Proposition 1 appears to be the most promising option as it consistently has the lowest values across all measurements. In contrast, Proposition 4 has the highest values, indicating that it may not be the best choice. Propositions 7 and 8 are also notable as it has relatively low values, indicating that it may be good options as well.



Figure 7.11 the reflection coefficient of the numerical simulations of the suggested propositions.

Figure 7.12 to Figure 7.20 illustrate the flow depth obtained from the numerical simulations for each of the proposed propositions under the influence of SRW01 .These figures provide visual representations of the flow depth distribution for each proposition, allowing for a comprehensive analysis of their respective performance.

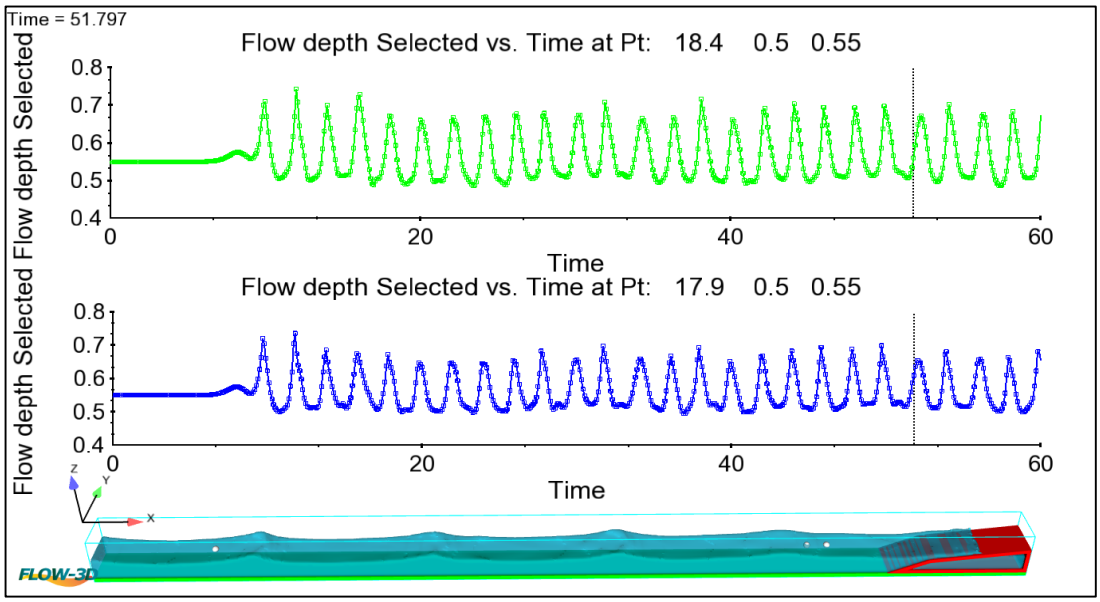

Figure 7.12 The flow depth of the numerical simulations at P1 and P2 of proposition 1 in case of SRW01 H=0.25 m, T=2.0 s.

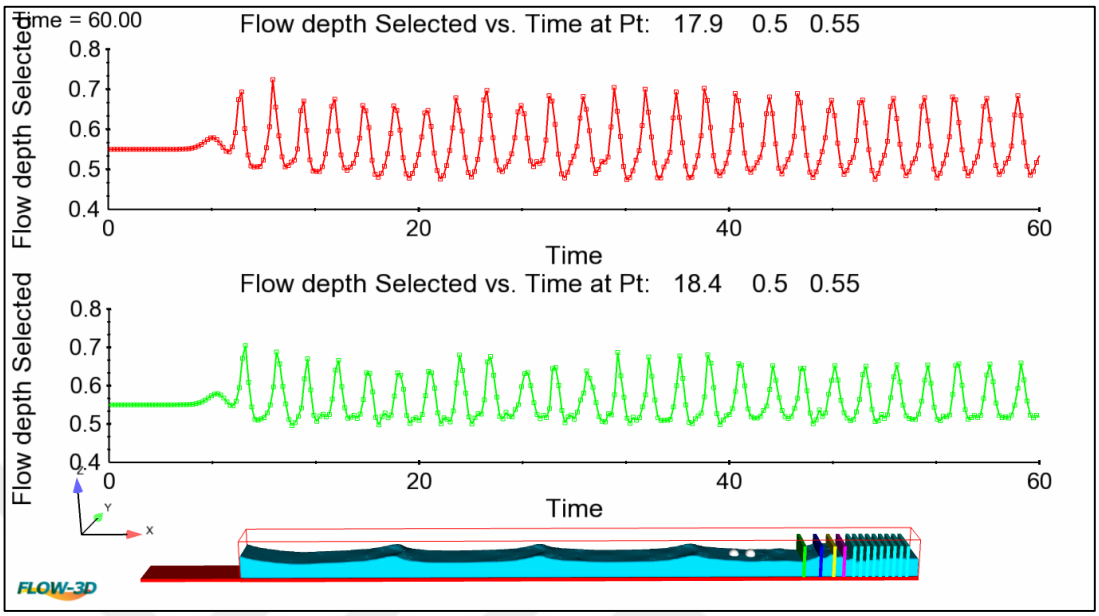

Figure 7.13 The flow depth of the numerical simulations at P1 and P2 of proposition 2 in case of SRW01 H=0.25 m, T=2.0 s.

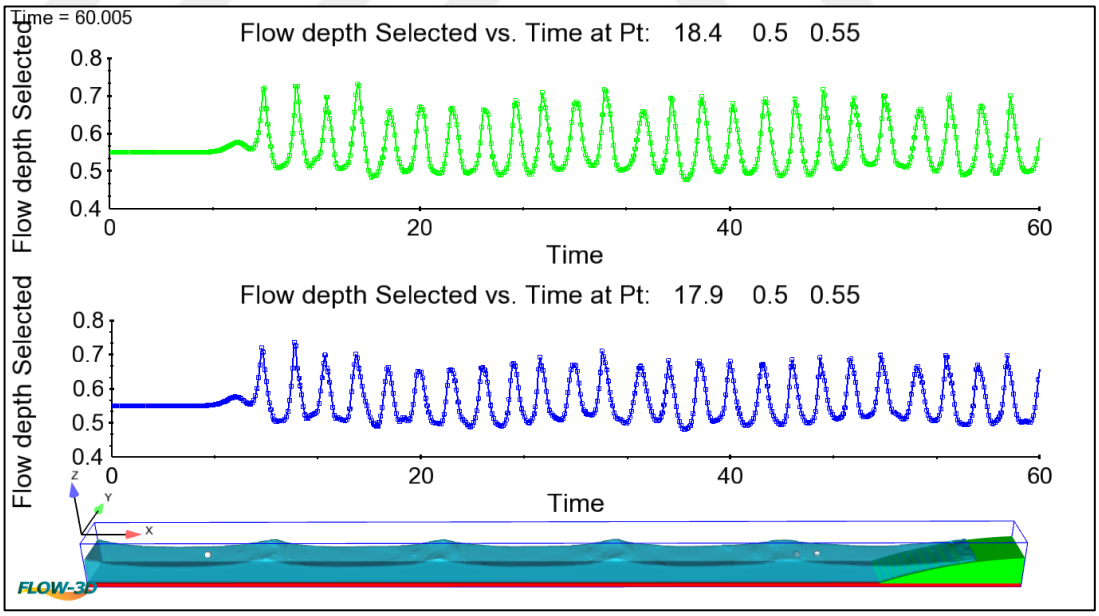

Figure 7.14 The flow depth of the numerical simulations at P1 and P2 of proposition 3 in case of SRW01 H=0.25 m, T=2.0 s.

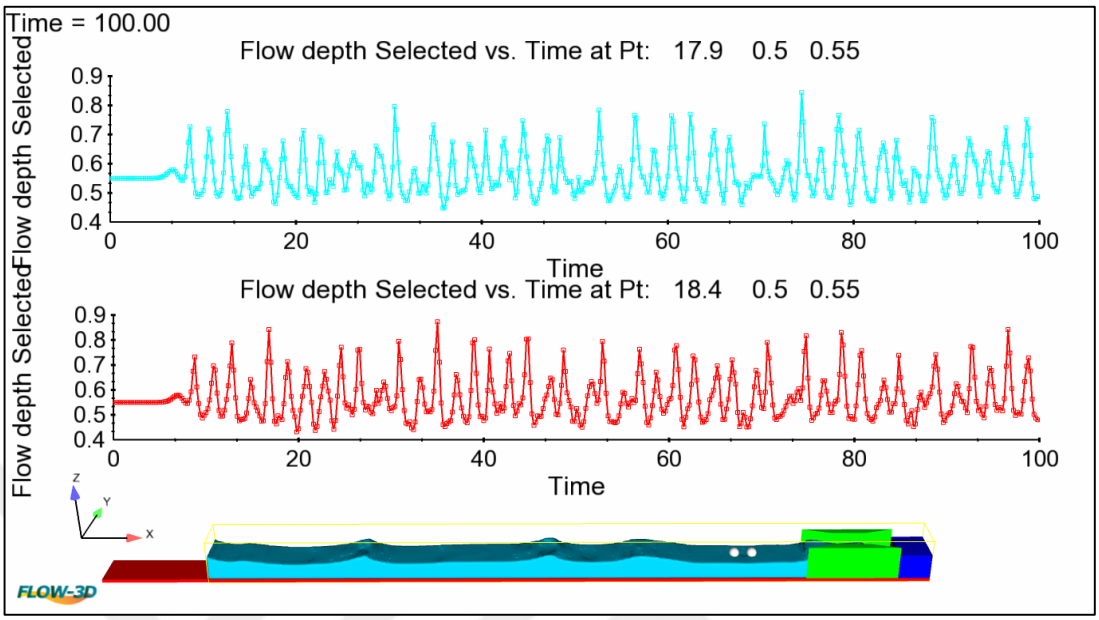

Figure 7.15 The flow depth of the numerical simulations at P1 and P2 of proposition 4 in case of SRW01 H=0.25 m, T=2.0 s.

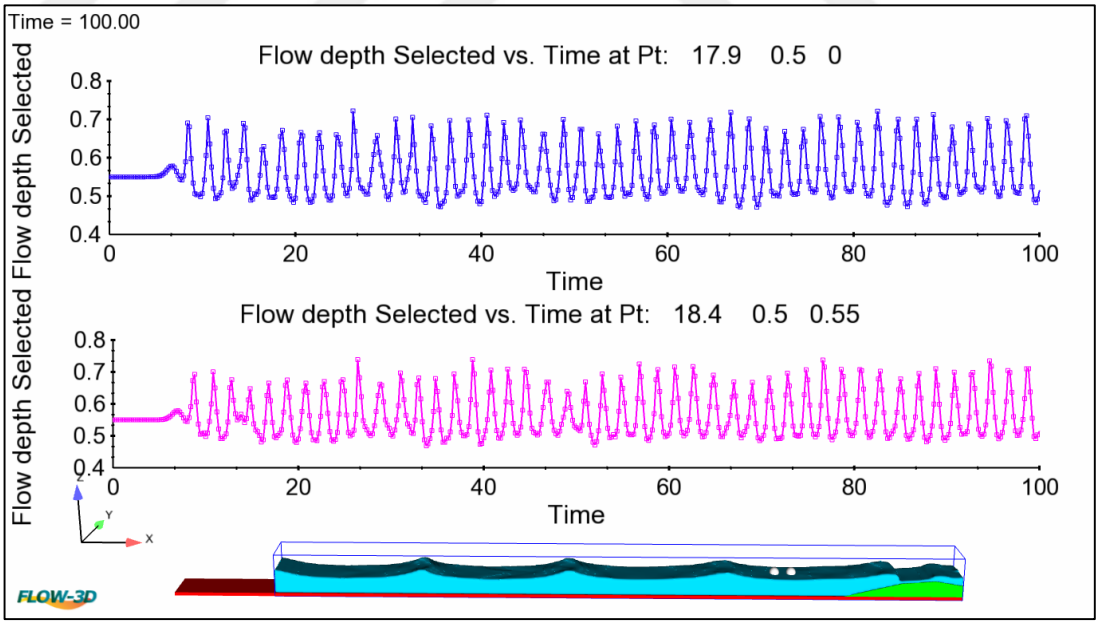

Figure 7.16 The flow depth of the numerical simulations at P1 and P2 of proposition 5 in case of SRW01 H=0.25 m, T=2.0 s.

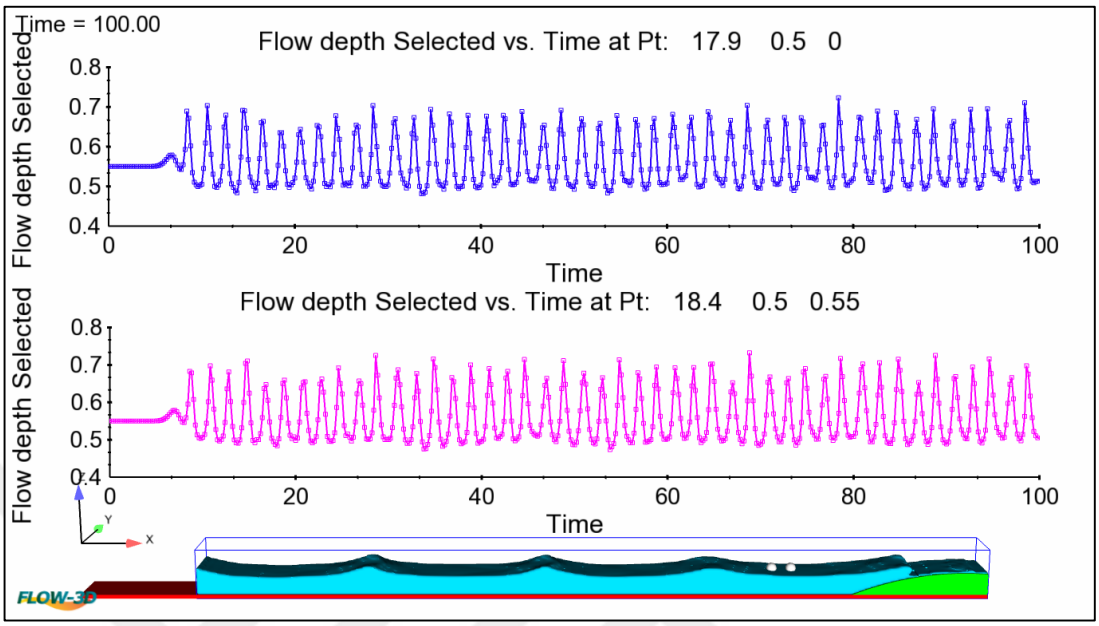

Figure 7.17 The flow depth of the numerical simulations at P1 and P2 of proposition 6 in case of SRW01 H=0.25 m, T=2.0 s.

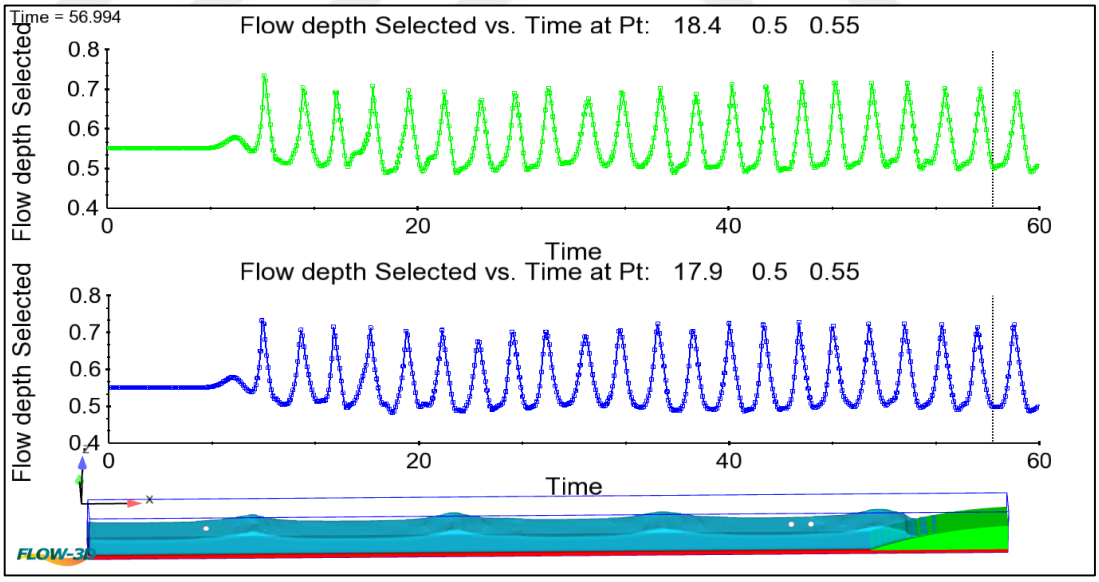

Figure 7.18 The flow depth of the numerical simulations at P1 and P2 of proposition 7 in case of SRW01 H=0.25 m, T=2.0 s.

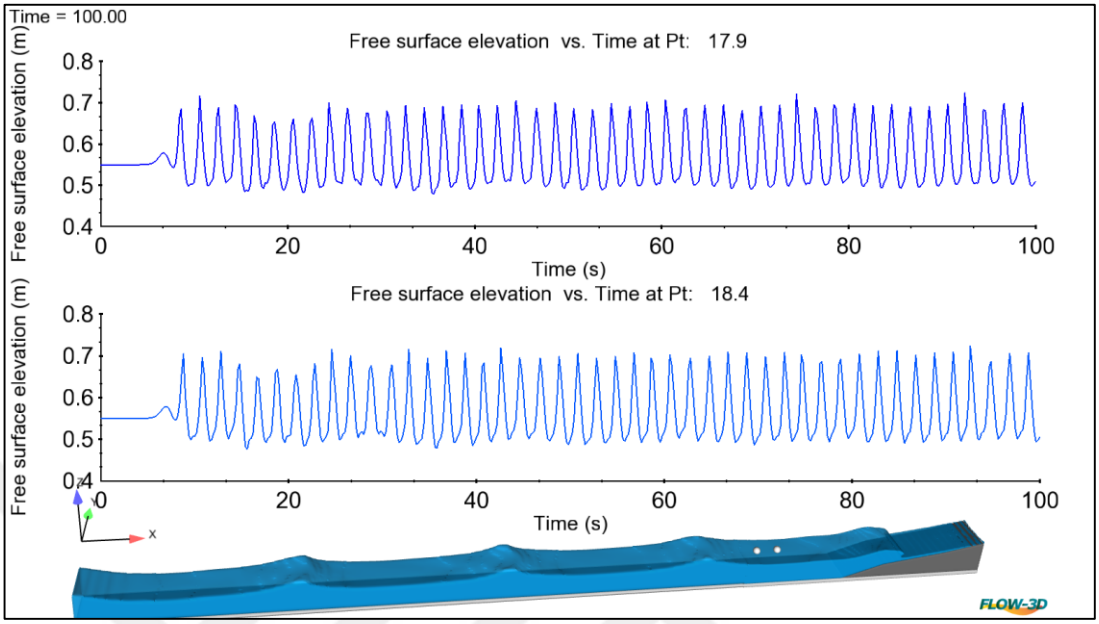

Figure 7.19 The flow depth of the numerical simulations at P1 and P2 of proposition 8 in case of SRW01 H=0.25 m, T=2.0 s.

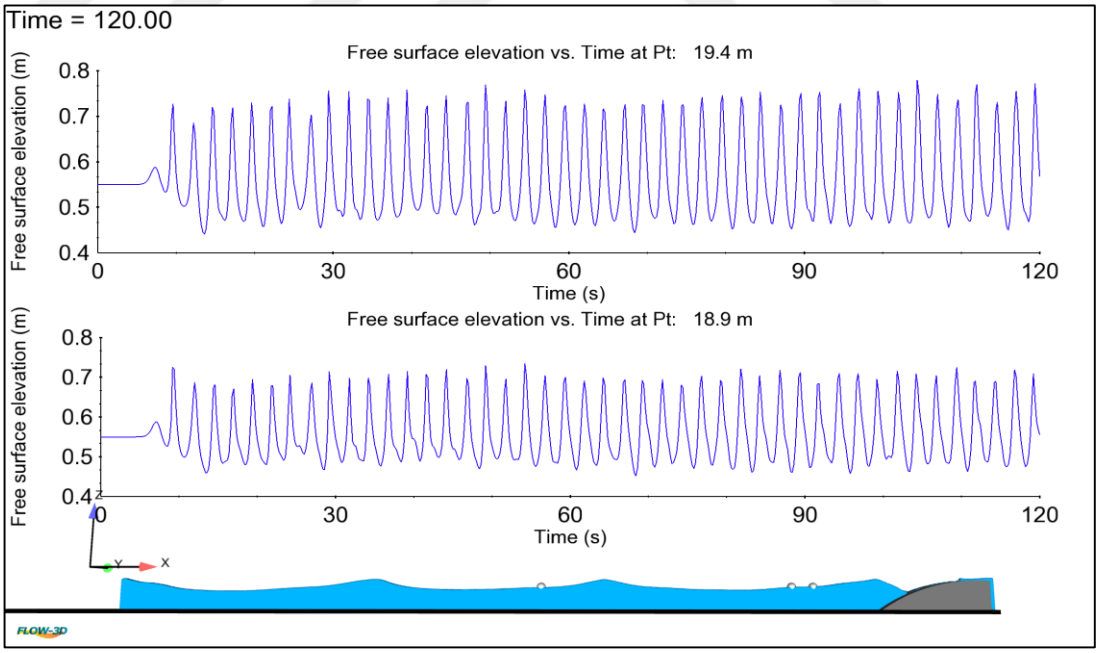

Figure 7.20 The flow depth of the numerical simulations at P1 and P2 of proposition 9 in case of SRW01 H=0.25 m, T=2.0 s.

It's important to keep in mind that the results presented in Figure 7.11 are based solely on the reflection coefficient, and there are other factors to consider when evaluating each proposition. For example, some propositions have higher costs and require more resources and are more difficult to implement. Therefore, it's essential to consider multiple factors before making a final decision.

To determine the most effective proposition for reducing wave reflection, one can compare the reflection coefficient for each proposition at the same wave height and period value. By comparing the results of Table 7.5 with the results of Table 7.6, Proposition 1 and Proposition 8 appear to be the best options.

Table 7.6 Reflection coefficient of the experiments on the rocks fill with 1/7 slope.

	Case	$\boldsymbol{H\ (m)}$	$\boldsymbol{T\ (s)}$	$\boldsymbol{H_i\ (m)}$	$\boldsymbol{H_r\ (m)}$	$\boldsymbol{C_r}$
Rocks fill with 1/7 slope	**ERW01**	**0.25**	**2.0**	0.2282	0.0282	0.1235
	ERW02	**0.22**	**2.3**	0.1991	0.0250	0.1257
	ERW03	**0.20**	**2.7**	0.2038	0.0288	0.1413
	ERW04	**0.17**	**3.1**	0.1898	0.0239	0.1261
	ERW05	**0.13**	**3.6**	0.1433	0.0220	0.1535

7.2.1 The Most Efficient Proposals Substantiation

Based on the numerical reflection coefficient analysis in Table 7.6 and taking into account the low costs of retaliation and simplicity of implementation, propositions 1 and 8 indicate that both of these propositions are capable of meeting the required performance criteria, and proposition 9 is chosen to shorten the passive wave absorber even more.

In this phase twenty-seven simulations and experiments (five irregular wave and twenty-two regular waves) were performed for each proposal to test the selected passive wave absorbers. The irregular waves (IRW) were generated after specifying the target JONSWAP spectrum, the significant wave heights H_s (0.13 to 0.25 m), of significant periods T_s (2 to 3.6 s) are selected. The spectrum is discretized to N=351 samples. Also, Regular waves (RW) periods and heights range were between 1.5 s to 3.6 s and 0.13 m to 0.25 s respectively. The duration of the experiments and simulations in case of irregular

waves was set to 1 hour and ten minutes in case of regular waves. The water depth at the paddles of the wavemaker is 0.55 m. The experiments set and the simulations results of each proposition are summarized in Table 7.7, Table 7.8, and Table 7.9.

The two sensors (probes), P1 and P2, are set in front of the propositions attached to the ULS are used to obtain the surface elevation of the experiments, which are then used to separate the incident (H_i) and reflected (H_r) wave heights and to calculate the wave characteristics using the zero-up crossing method.

7.2.1.1 Regular Waves

In this study, the reflection coefficient of regular waves was measured across a range of periods and heights. The periods ranged from 1.5 s to 3.6 s, while the heights varied between 0.13 m and 0.25 m. The obtained data for the experimental and numerical reflection coefficients are presented in Table 7.7 to Table 7.9 and summarized in Table 7.11. These tables provide a detailed overview of the variation in reflection coefficients for the different wave conditions studied, allowing for a comprehensive analysis of the experimental and numerical results.

Table 7.7 Reflection coefficient of regular waves of the 3-slopes proposition design.

		Experiment					**Numerical**				
H(m)	**T(s)**	**H_{max}**	**H_{min}**	**H_i**	**H_r**	**C_r**	**H_{max}**	**H_{min}**	**H_i**	**H_r**	**C_r**
0.25	**1.50**	0.2617	0.2029	0.2323	0.0294	**0.1264**	0.1956	0.1296	0.1626	0.0330	**0.2028**
	2.00	0.2489	0.2160	0.2324	0.0164	**0.0707**	0.2430	0.1921	0.2175	0.0254	**0.1169**
	2.50	0.2974	0.2507	0.2741	0.0233	**0.0851**	0.3141	0.2171	0.2656	0.0485	**0.1827**
0.22	**1.50**	0.2166	0.1732	0.1949	0.0217	**0.1114**	0.1853	0.1411	0.1632	0.0221	**0.1353**
	2.00	0.2174	0.1882	0.2028	0.0146	**0.0719**	0.2007	0.1604	0.1806	0.0201	**0.1114**
	2.30	0.2168	0.1887	0.2028	0.0141	**0.0694**	0.2559	0.2062	0.2311	0.0248	**0.1075**
	2.50	0.2574	0.2137	0.2356	0.0218	**0.0926**	-	-	-	-	-
	3.00	0.2104	0.1702	0.1903	0.0201	**0.1054**	0.2118	0.1647	0.1882	0.0236	**0.1252**
0.20	**1.50**	0.1985	0.1618	0.1801	0.0183	**0.1018**	0.1836	0.1226	0.1531	0.0305	**0.1995**
	2.00	0.2010	0.1734	0.1872	0.0138	**0.0737**	0.1874	0.1503	0.1688	0.0185	**0.1096**
	2.70	0.2286	0.2025	0.2156	0.0131	**0.0606**	0.2108	0.1601	0.1855	0.0253	**0.1367**
	3.00	0.1973	0.1559	0.1766	0.0207	**0.1171**	0.1975	0.1536	0.1755	0.0220	**0.1252**

Table 7.7 Continuous

0.17	**1.50**	0.1703	0.1388	0.1545	0.0158	**0.1021**	0.1742	0.1116	0.1429	0.0313	**0.2188**
	2.00	0.1643	0.1470	0.1557	0.0086	**0.0554**	0.1917	0.1371	0.1644	0.0273	**0.1662**
	2.50	0.1853	0.1591	0.1722	0.0131	**0.0758**	0.2273	0.1149	0.1711	0.0562	**0.3285**
	3.10	0.1917	0.1709	0.1813	0.0104	**0.0575**	0.1941	0.1337	0.1639	0.0302	**0.1841**
	3.50	0.1813	0.1537	0.1675	0.0138	**0.0825**	0.1973	0.1413	0.1693	0.0280	**0.1653**
0.13	**1.50**	0.1306	0.1020	0.1163	0.0143	**0.1230**	0.1425	0.0995	0.1210	0.0215	**0.1779**
	2.00	0.1232	0.1118	0.1175	0.0057	**0.0485**	0.1218	0.1023	0.1121	0.0098	**0.0871**
	2.50	0.1340	0.1186	0.1263	0.0077	**0.0610**	0.1837	0.0893	0.1365	0.0472	**0.3458**
	3.00	0.1219	0.0987	0.1103	0.0116	**0.1054**	0.1438	0.1163	0.1301	0.0137	**0.1054**
	3.60	0.1253	0.1114	0.1183	0.0070	**0.0589**	0.1588	0.1288	0.1438	0.0149	**0.1040**

Table 7.8 Reflection coefficient of regular waves of the 2-slopes proposition design.

		Experiment					**Numerical**				
H(m)	**T(s)**	**H_{max}**	**H_{min}**	**H_i**	**H_r**	**C_r**	**H_{max}**	**H_{min}**	**H_i**	**H_r**	**C_r**
0.25	**1.50**	0.2458	0.1695	0.2076	0.0381	**0.1837**	0.1885	0.1100	0.1492	0.0393	**0.2632**
	2.00	0.2375	0.2179	0.2277	0.0098	**0.0431**	0.1895	0.1620	0.1758	0.0137	**0.0782**
	2.50	0.2650	0.2073	0.2361	0.0289	**0.1222**	0.2661	0.1954	0.2307	0.0353	**0.1532**
0.22	**1.50**	0.2072	0.1645	0.1859	0.0213	**0.1148**	0.1665	0.1031	0.1348	0.0317	**0.2351**
	2.00	0.2141	0.1850	0.1996	0.0145	**0.0728**	0.1833	0.1493	0.1663	0.0170	**0.1025**
	2.30	0.2461	0.2069	0.2265	0.0196	**0.0867**	0.2148	0.1753	0.1951	0.0198	**0.1014**
	2.50	0.2305	0.1815	0.2060	0.0245	**0.1191**	-	-	-	-	-
	3.00	0.2301	0.1993	0.2147	0.0154	**0.0716**	0.2201	0.1660	0.1930	0.0270	**0.1401**
0.20	**1.50**	0.1764	0.1436	0.1600	0.0164	**0.1024**	0.1941	0.1024	0.1482	0.0458	**0.3092**
	2.00	0.1928	0.1693	0.1810	0.0117	**0.0647**	0.2059	0.1518	0.1788	0.0270	**0.1512**
	2.70	0.2366	0.1935	0.2150	0.0216	**0.1003**	0.2452	0.1851	0.2152	0.0301	**0.1397**
	3.00	0.1998	0.1738	0.1868	0.0130	**0.0694**	0.2178	0.1701	0.1940	0.0238	**0.1229**
0.17	**1.50**	0.1530	0.1246	0.1388	0.0142	**0.1021**	0.1556	0.1014	0.1285	0.0271	**0.2112**
	2.00	0.1565	0.1451	0.1508	0.0057	**0.0379**	0.1580	0.1313	0.1446	0.0134	**0.0923**
	2.50	0.1751	0.1315	0.1533	0.0218	**0.1421**	0.1751	0.1383	0.1567	0.0184	**0.1175**
	3.10	0.1773	0.1699	0.1736	0.0037	**0.0213**	0.2188	0.1628	0.1908	0.0280	**0.1469**
	3.50	0.2112	0.2038	0.2075	0.0037	**0.0178**	0.1830	0.1272	0.1551	0.0279	**0.1797**
0.13	**1.50**	0.1124	0.1059	0.1091	0.0033	**0.0298**	0.1236	0.0871	0.1053	0.0182	**0.1732**
	2.00	0.1215	0.1108	0.1161	0.0053	**0.0458**	0.1293	0.1077	0.1185	0.0108	**0.0908**
	2.50	0.1349	0.1119	0.1234	0.0115	**0.0930**	0.1373	0.1125	0.1249	0.0124	**0.0991**
	3.00	0.1210	0.0997	0.1103	0.0106	**0.0963**	0.1469	0.1053	0.1261	0.0208	**0.1648**
	3.50	0.1380	0.1244	0.1312	0.0068	**0.0519**	-	-	-	-	-
	3.60	0.1718	0.1692	0.1705	0.0013	**0.0076**	0.1425	0.1030	0.1227	0.0197	**0.1608**

Table 7.9 Reflection coefficient of regular waves of the parabolic proposition design.

		Experiment					Numerical				
H(m)	**T(s)**	**H_{max}**	**H_{min}**	**H_i**	**H_r**	**C_r**	**H_{max}**	**H_{min}**	**H_i**	**H_r**	**C_r**
0.25	**1.50**	0.2961	0.1925	0.2443	0.0518	**0.2121**	0.2014	0.1734	0.1874	0.0140	**0.0748**
	2.00	0.2455	0.1780	0.2117	0.0337	**0.1593**	0.2588	0.1616	0.2102	0.0486	**0.2313**
	2.50	0.3641	0.2124	0.2883	0.0758	**0.2630**	0.2594	0.1828	0.2211	0.0383	**0.1732**
0.22	**1.50**	0.2484	0.1729	0.2107	0.0378	**0.1792**	0.2119	0.1587	0.1853	0.0266	**0.1435**
	2.00	0.1982	0.1483	0.1733	0.0250	**0.1440**	0.2276	0.1352	0.1814	0.0462	**0.2546**
	2.30	0.2440	0.1813	0.2126	0.0313	**0.1474**	0.2045	0.1605	0.1825	0.0220	**0.1206**
	2.50	0.2937	0.2475	0.2706	0.0231	**0.0855**	-	-	-	-	-
	3.00	0.2802	0.2266	0.2534	0.0268	**0.1058**	0.2832	0.1988	0.2410	0.0422	**0.1752**
0.20	**1.50**	0.2221	0.1568	0.1895	0.0327	**0.1725**	0.1939	0.1480	0.1709	0.0230	**0.1343**
	2.00	0.1937	0.1331	0.1634	0.0303	**0.1853**	0.2087	0.1201	0.1644	0.0443	**0.2693**
	2.70	0.2260	0.1875	0.2068	0.0193	**0.0932**	0.2288	0.1765	0.2026	0.0261	**0.1290**
	3.00	0.2511	0.2092	0.2301	0.0209	**0.0910**	0.2658	0.2006	0.2332	0.0326	**0.1398**
0.17	**1.50**	0.1939	0.1410	0.1674	0.0264	**0.1579**	0.1761	0.1266	0.1513	0.0247	**0.1635**
	2.00	0.1427	0.1038	0.1233	0.0195	**0.1578**	0.1923	0.1075	0.1499	0.0424	**0.2829**
	2.50	0.2016	0.1770	0.1893	0.0123	**0.0650**	0.1964	0.1789	0.1876	0.0087	**0.0466**
	3.10	0.1860	0.1630	0.1745	0.0115	**0.0660**	0.2118	0.1493	0.1806	0.0313	**0.1734**
	3.50	0.2716	0.2248	0.2482	0.0234	**0.0942**	0.1674	0.1134	0.1404	0.0270	**0.1923**
0.13	**1.50**	0.1420	0.1057	0.1238	0.0182	**0.1468**	0.1443	0.1114	0.1278	0.0164	**0.1286**
	2.00	0.1420	0.1038	0.1229	0.0191	**0.1551**	0.1440	0.0845	0.1143	0.0297	**0.2603**
	2.50	0.1555	0.1044	0.1299	0.0255	**0.1963**	0.1417	0.1063	0.1240	0.0177	**0.1428**
	3.00	0.1975	0.1393	0.1684	0.0291	**0.1728**	0.1799	0.1387	0.1593	0.0206	**0.1293**
	3.50	0.1808	0.1317	0.1563	0.0245	**0.1570**	0.1869	0.1559	0.1714	0.0155	**0.0904**
	3.60	0.2961	0.1925	0.2443	0.0518	**0.2121**	0.2014	0.1734	0.1874	0.0140	**0.0748**

Upon comparing the results presented in the Table 7.10, the experiments shows that the rock fill consistently exhibits moderate reflection coefficients across five wave heights and periods. This suggests that Rock Fill provides reasonable wave absorption under different conditions. The 3-slopes generally performs well, with relatively lower reflection coefficients compared to Rock Fill. This indicates that 3-slopes has the potential for better wave absorption. The 2-slopes shows varying performance, with lower reflection coefficients at some simulated wave values and higher coefficients at others. It may be

suitable for specific wave conditions. The parabolic proposition has the highest reflection coefficients across all simulated wave values, indicating less effective wave absorption.

Table 7.10 Comparison of the experimental reflection coefficients of regular waves for the selected proposition designs and the rock fill with 1/7 slopes.

		Reflection coefficient C_r			
$\boldsymbol{H}$ $\boldsymbol{(m)}$	$\boldsymbol{T}$ $\boldsymbol{(s)}$	**3-slopes**	**2-slopes**	**Parabolic**	**Rocks fill with 1/7 slope**
0.25	**2.0**	0.0707	0.0431	0.1593	0.1235
0.22	**2.3**	0.0694	0.0867	0.1474	0.1257
0.20	**2.7**	0.0606	0.1003	0.0932	0.1413
0.17	**3.1**	0.0575	0.0213	0.0660	0.1261
0.13	**3.6**	0.0589	0.0076	0.2121	0.1535

Figure 7.21 to Figure 7.41 illustrate the comparison between the experimental and numerical surface elevations at probe P1 and P2 for the 3-slopes proposition design under non-breaking regular wave . These figures provide a visual representation of the observed surface elevations, facilitating a comprehensive evaluation of the agreement or disparity between the experimental measurements and the numerical simulations.

(a) Probe P1

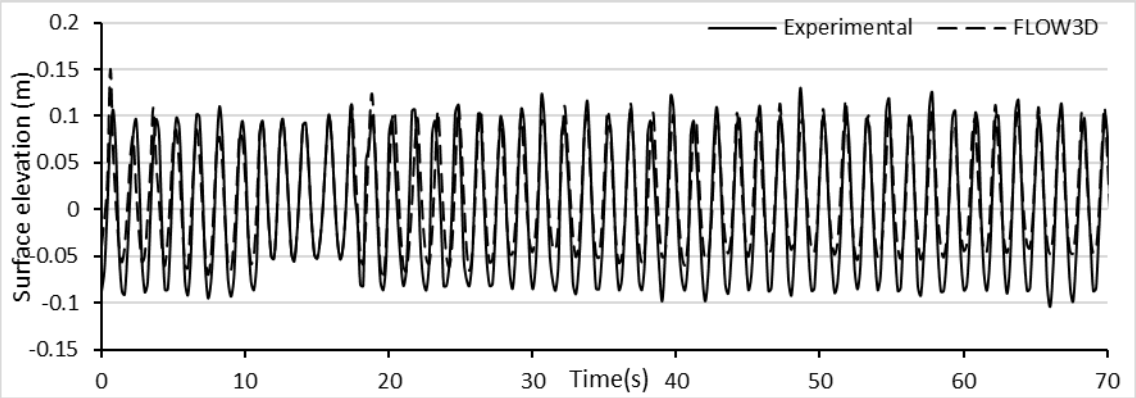

(b) Probe P2

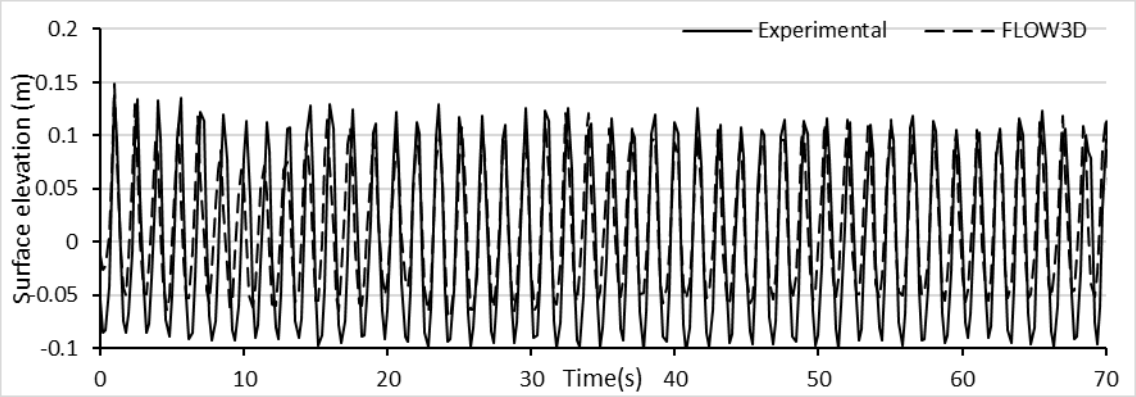

Figure 7.21 Experimental and numerical surface elevations for (RW_H = 0.25 m, T = 1.5 s) at Probes P1 (a) and P2 (b) for the 3-Slope Proposition Design.

(a) Probe P1

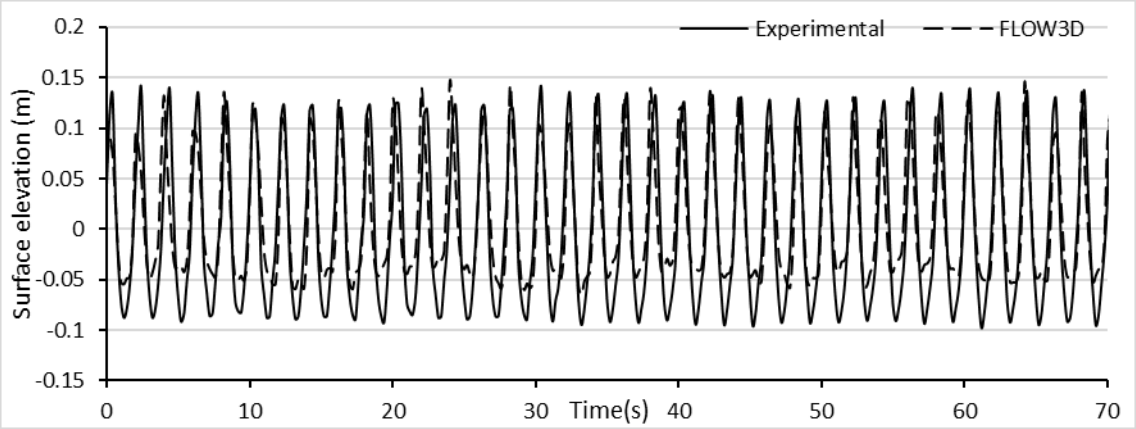

(b) Probe P2

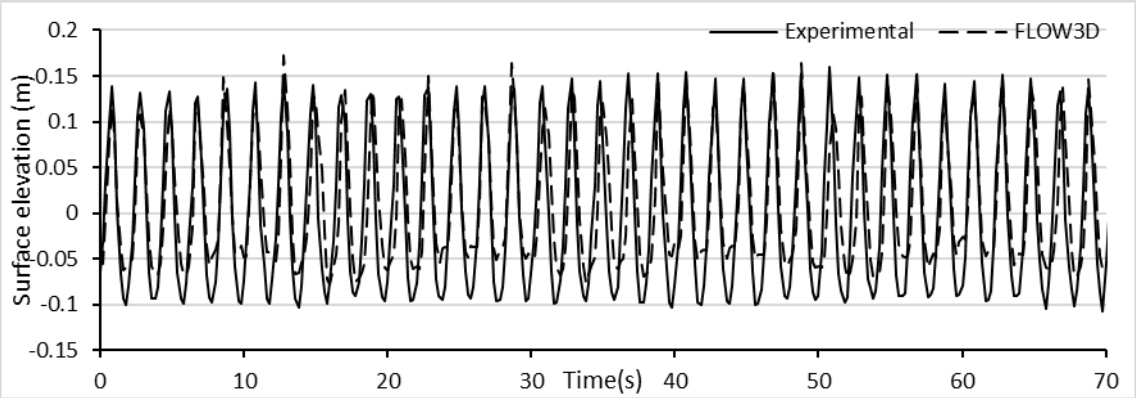

Figure 7.22 Experimental and numerical surface elevations for (RW_H = 0.25 m, T = 2.0 s) at Probes P1 (a) and P2 (b) for the 3-Slope Proposition Design.

(a) Probe P1

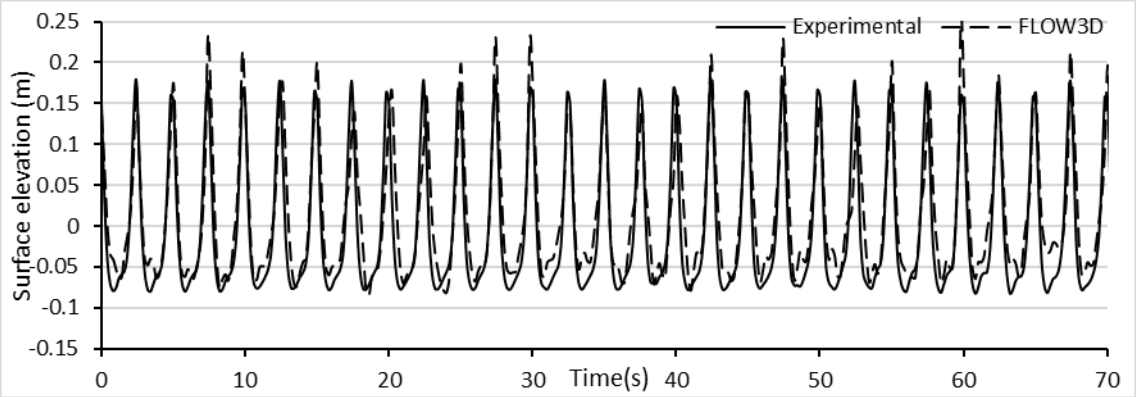

(b) Probe P2

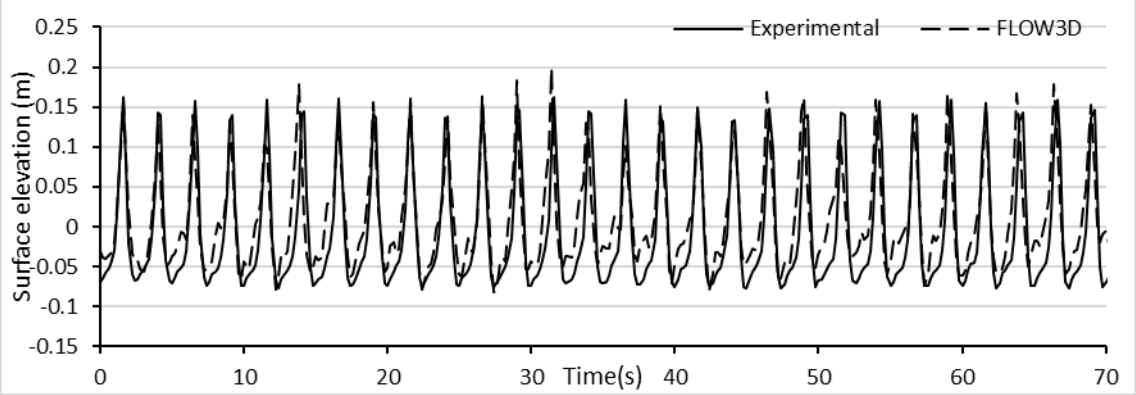

Figure 7.23 Experimental and numerical surface elevations for (RW_H = 0.25 m, T = 2.5 s) at Probes P1 (a) and P2 (b) for the 3-Slope Proposition Design.

(a) Probe P1

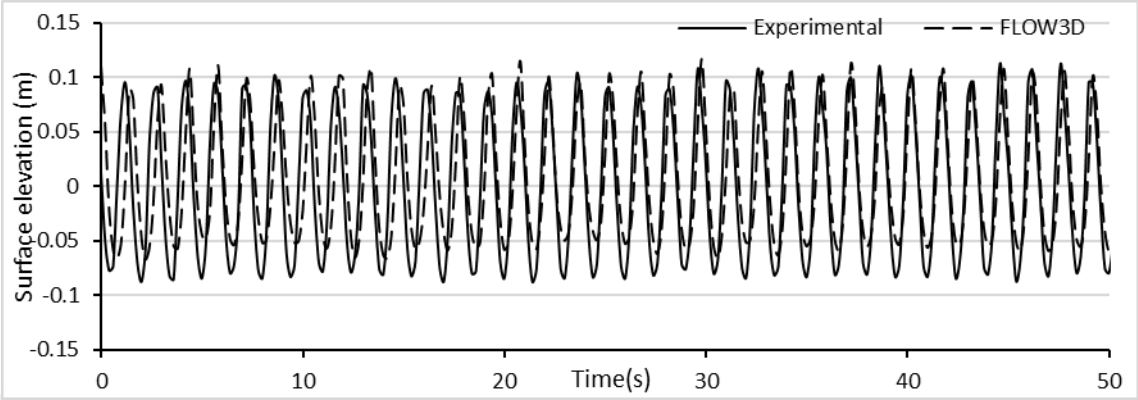

(b) Probe P2

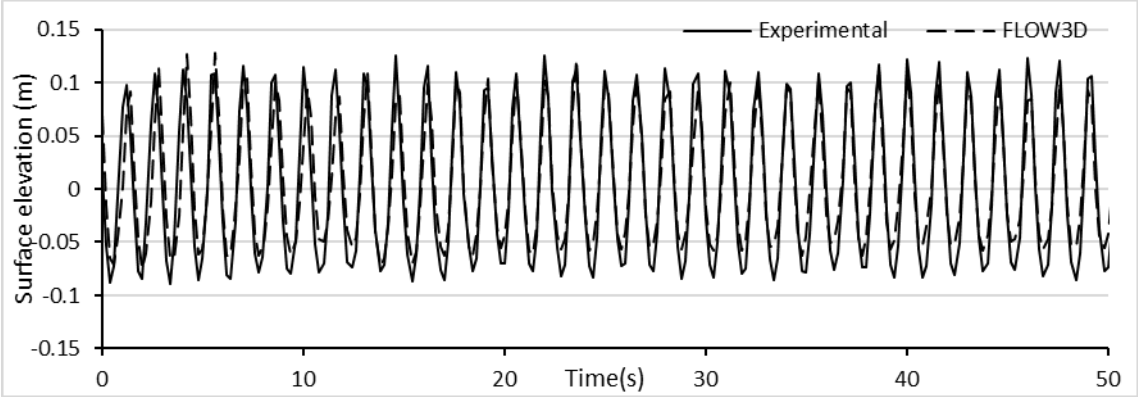

Figure 7.24 Experimental and numerical surface elevations for (RW_H = 0.22 m, T = 1.5 s) at Probes P1 (a) and P2 (b) for the 3-Slope Proposition Design.

(a) Probe P1

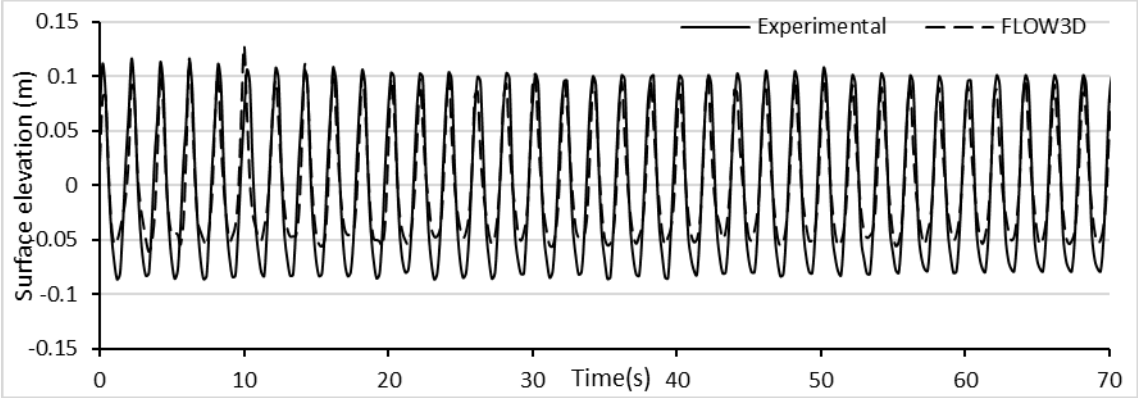

(b) Probe P2

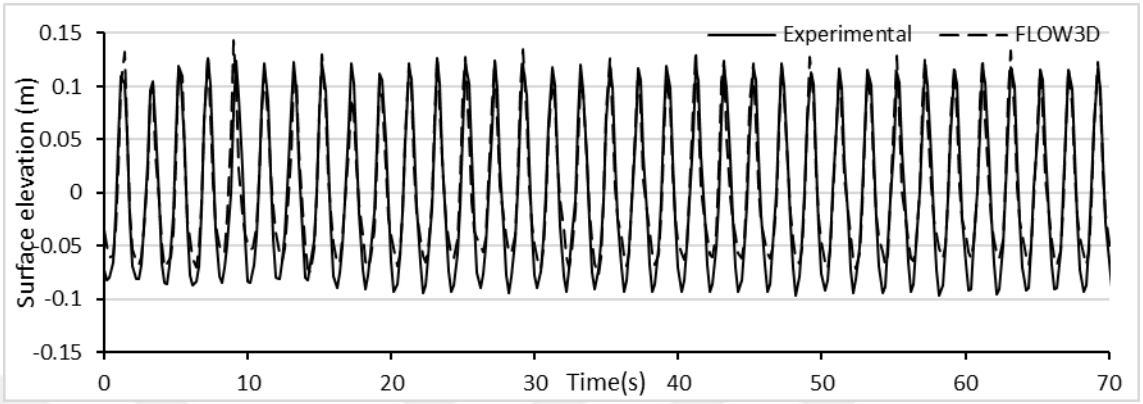

Figure 7.25 Experimental and numerical surface elevations for (RW_H = 0.22 m, T = 2.0 s) at Probes P1 (a) and P2 (b) for the 3-Slope Proposition Design.

(a) Probe P1

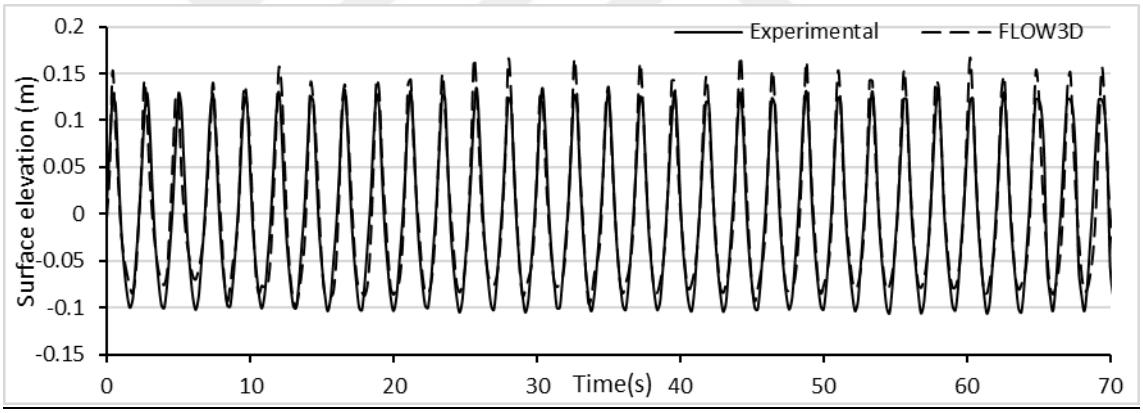

(b) Probe P2

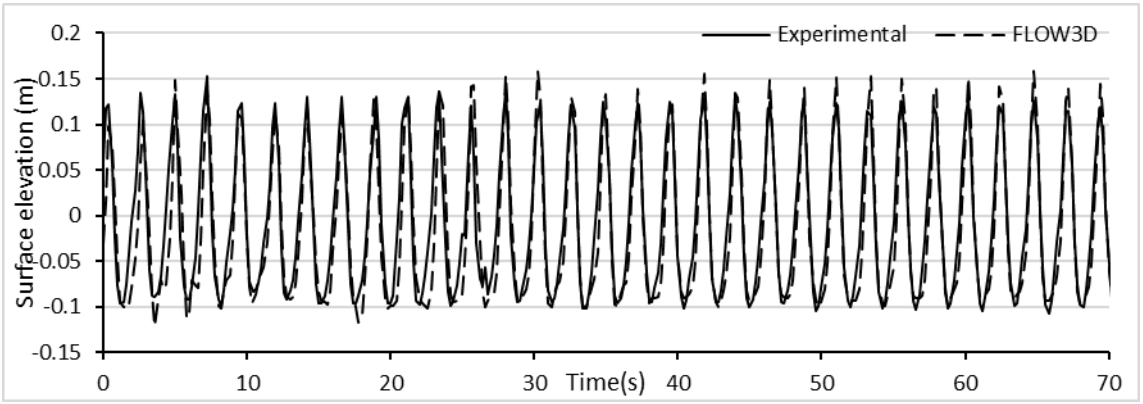

Figure 7.26 Experimental and numerical surface elevations for (RW_H = 0.22 m, T = 2.3 s) at Probes P1 (a) and P2 (b) for the 3-Slope Proposition Design.

(a) Probe P1

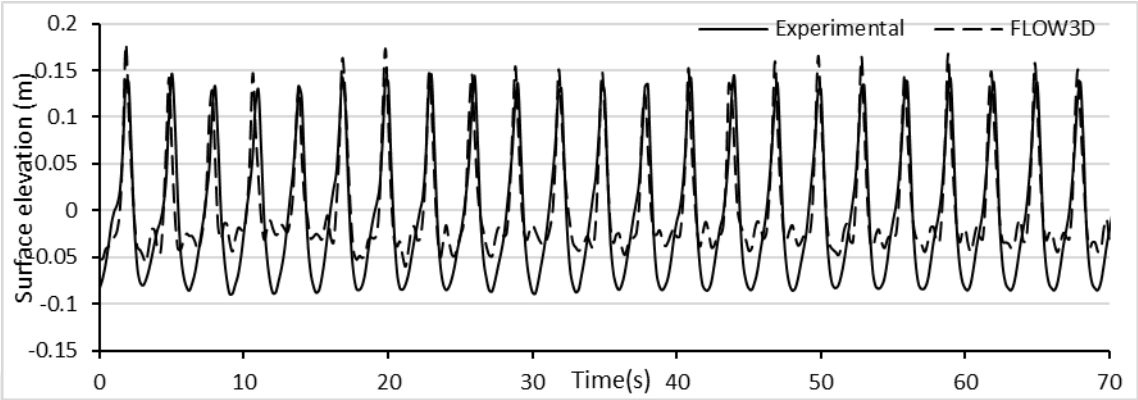

(b) Probe P2

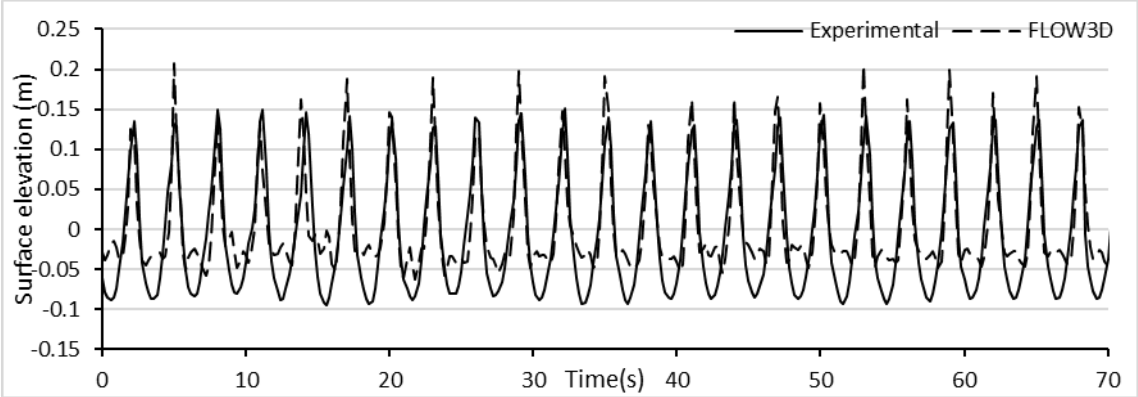

Figure 7.27 Experimental and numerical surface elevations for (RW_H = 0.22 m, T = 3.0 s) at Probes P1 (a) and P2 (b) for the 3-Slope Proposition Design.

(a) Probe P1

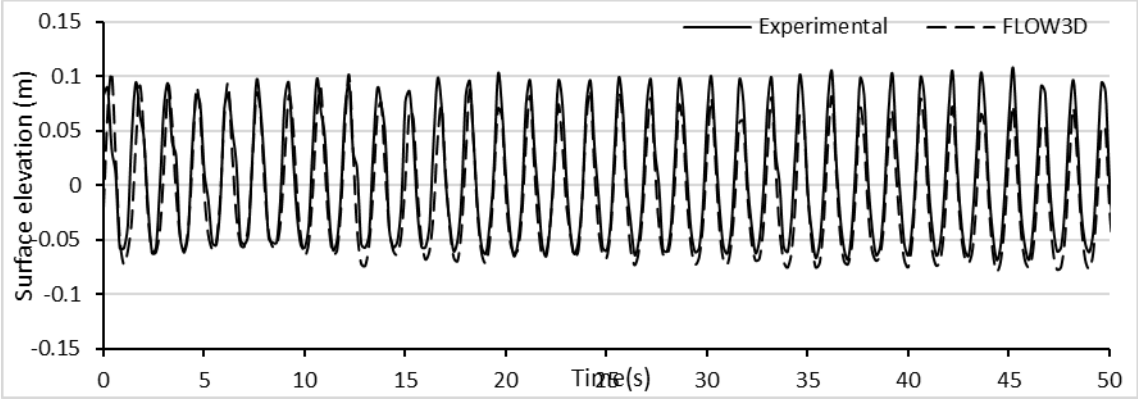

(b) Probe P2

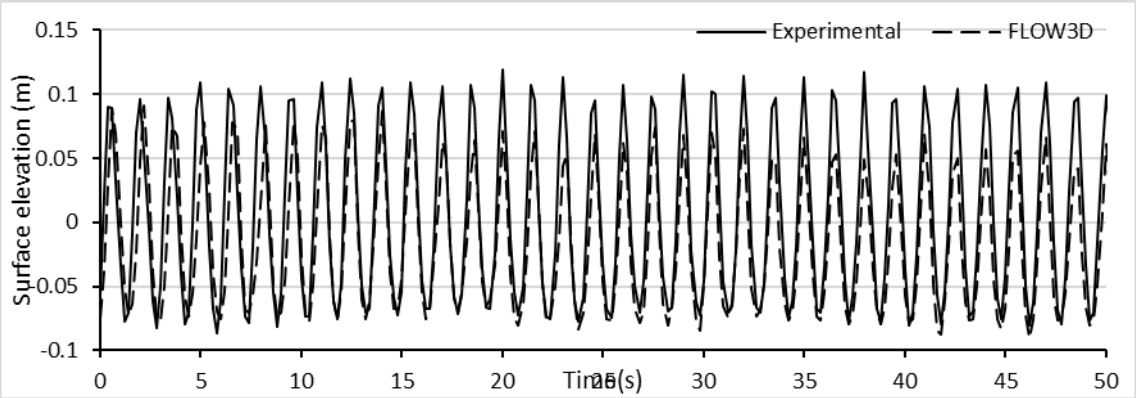

Figure 7.28 Experimental and numerical surface elevations for (RW_H = 0.20 m, T = 1.5 s) at Probes P1 (a) and P2 (b) for the 3-Slope Proposition Design.

(a) Probe P1

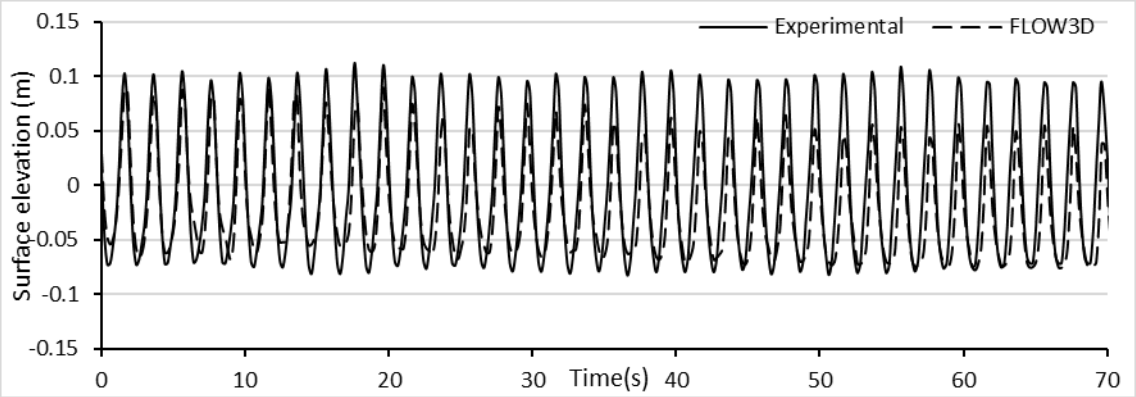

(b) Probe P2

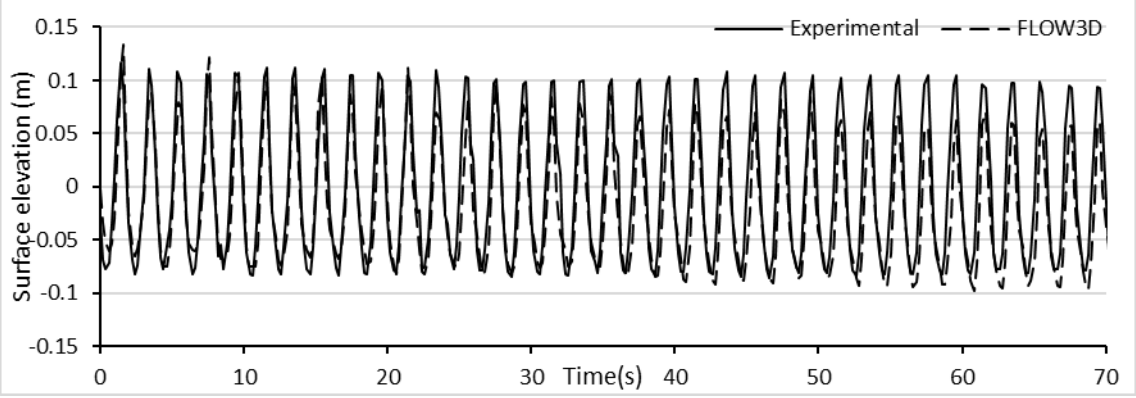

Figure 7.29 Experimental and numerical surface elevations for (RW_H = 0.20 m, T = 2.0 s) at Probes P1 (a) and P2 (b) for the 3-Slope Proposition Design.

(a) Probe P1

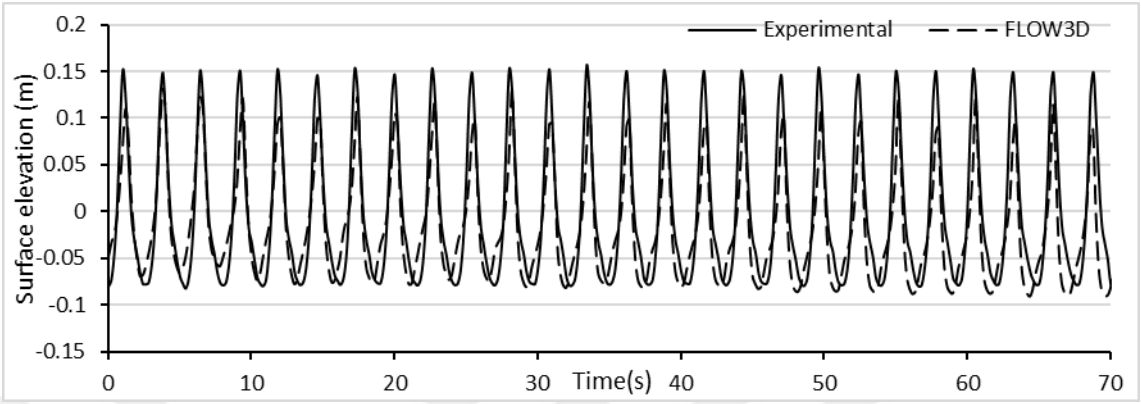

(b) Probe P2

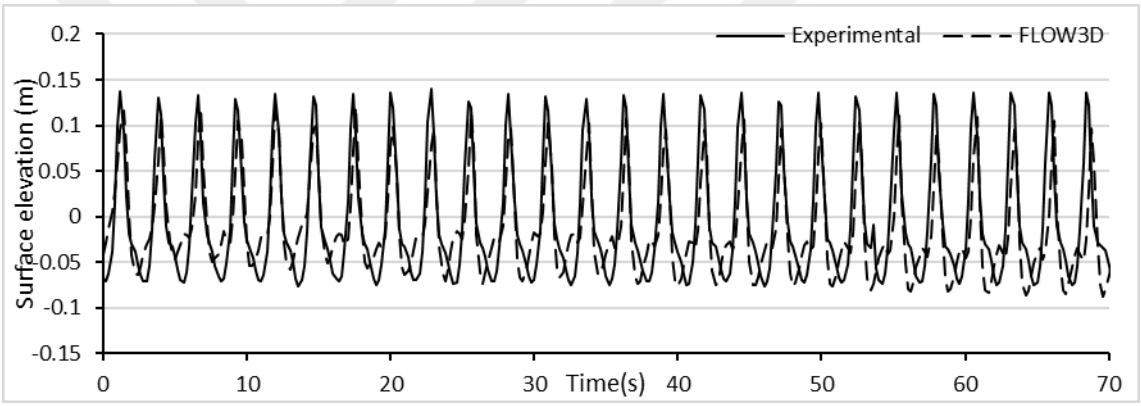

Figure 7.30 Experimental and numerical surface elevations for (RW_H = 0.20 m, T = 2.7 s) at Probes P1 (a) and P2 (b) for the 3-Slope Proposition Design.

(a) Probe P1

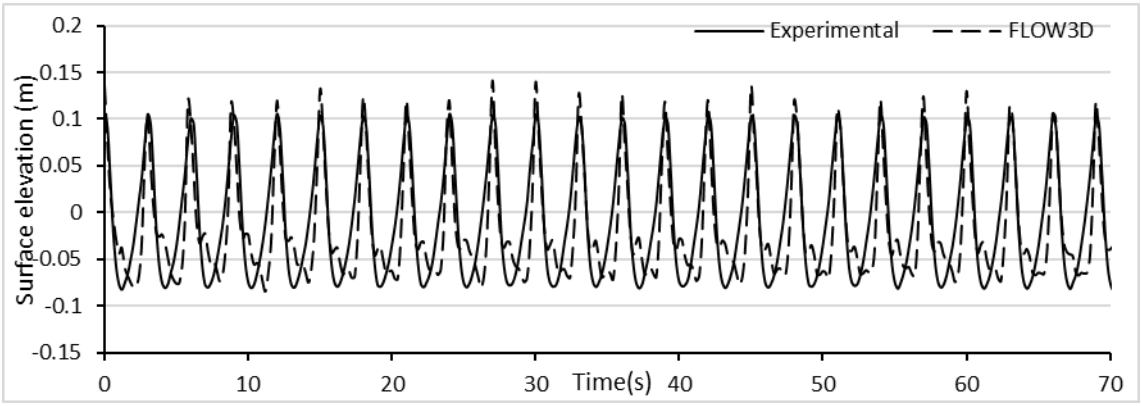

(b) Probe P2

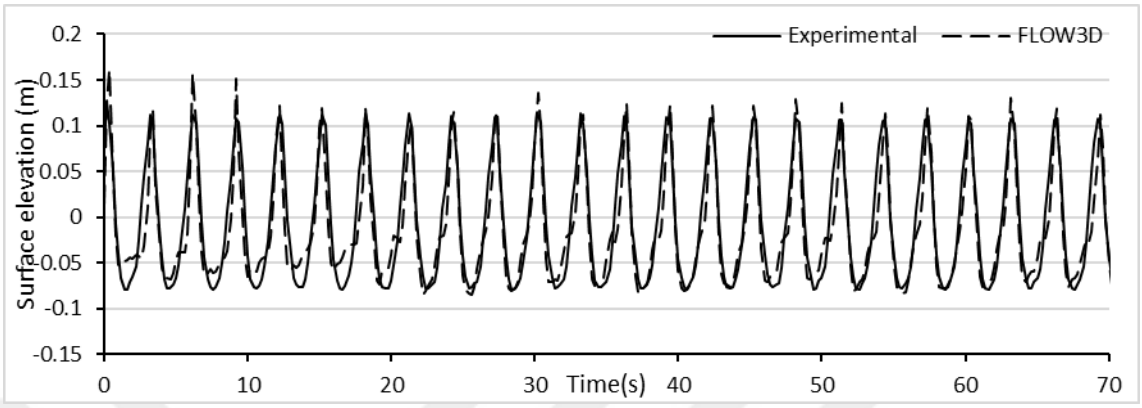

Figure 7.31 Experimental and numerical surface elevations for (RW_H = 0.20 m, T = 3.0 s) at Probes P1 (a) and P2 (b) for the 3-Slope Proposition Design.

(a) Probe P1

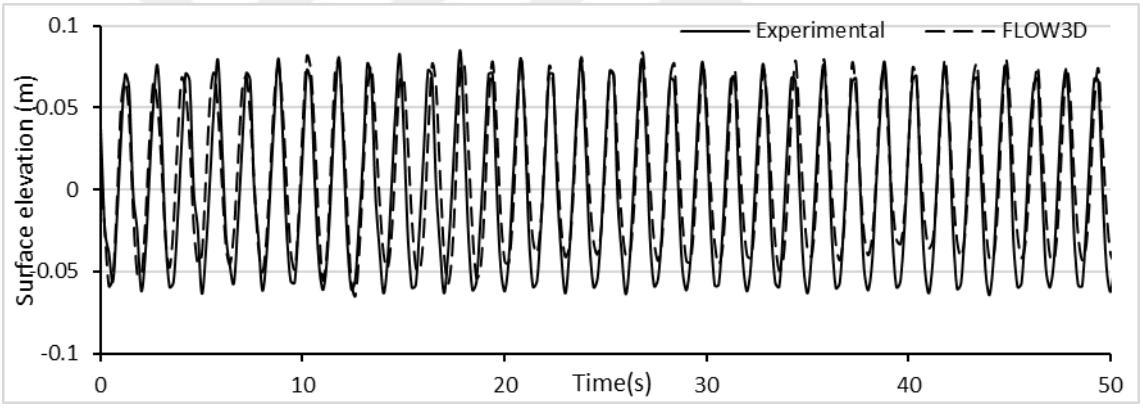

(b) Probe P2

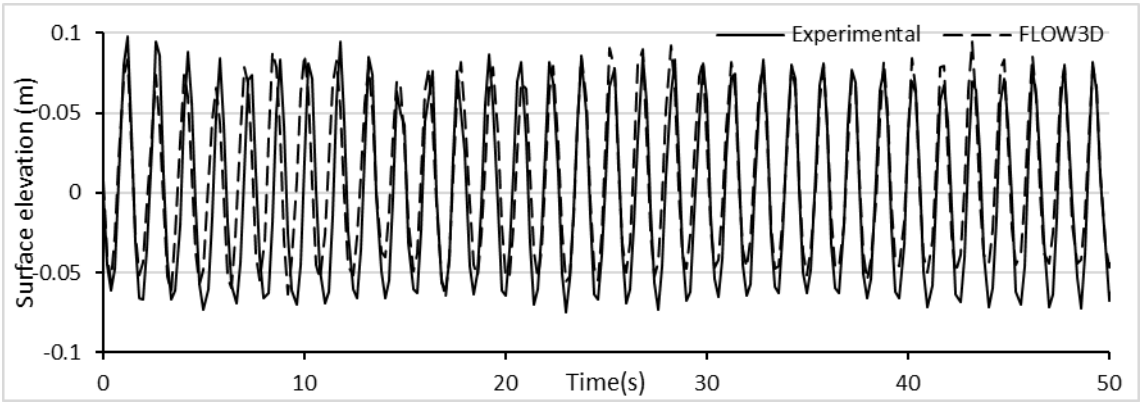

Figure 7.32 Experimental and numerical surface elevations for (RW_H = 0.17 m, T = 1.5 s) at Probes P1 (a) and P2 (b) for the 3-Slope Proposition Design.

(a) Probe P1

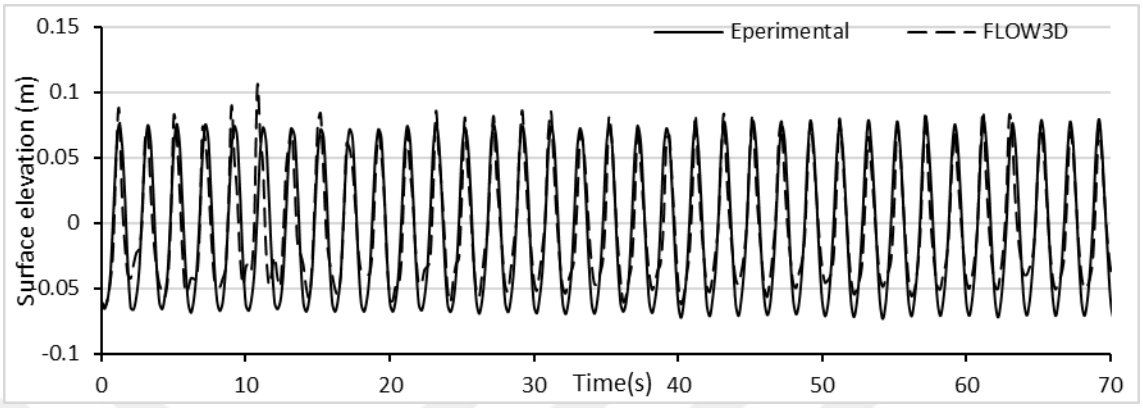

(b) Probe P2

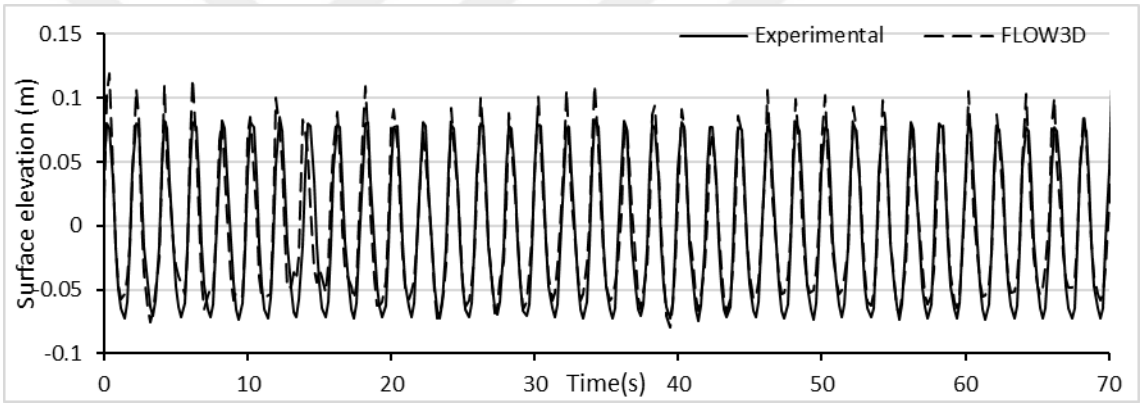

Figure 7.33 Experimental and numerical surface elevations for (RW_H = 0.17 m, T = 2.0 s) at Probes P1 (a) and P2 (b) for the 3-Slope Proposition Design..

(a) Probe P1

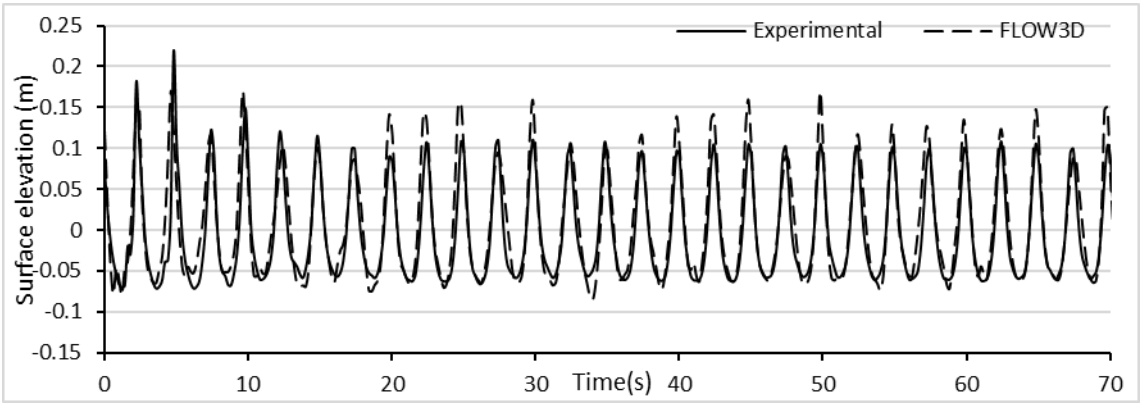

(b) Probe P2

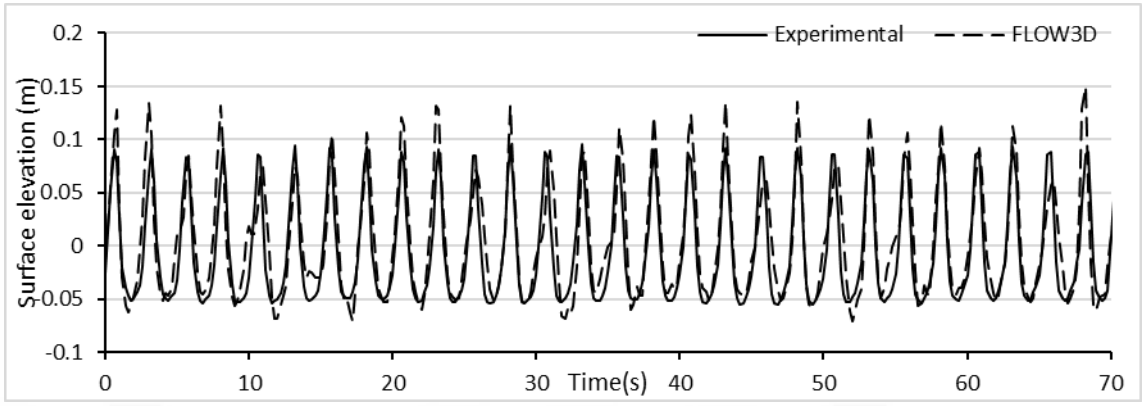

Figure 7.34 Experimental and numerical surface elevations for (RW_H = 0.17 m, T = 2.5 s) at Probes P1 (a) and P2 (b) for the 3-Slope Proposition Design.

(a) Probe P1

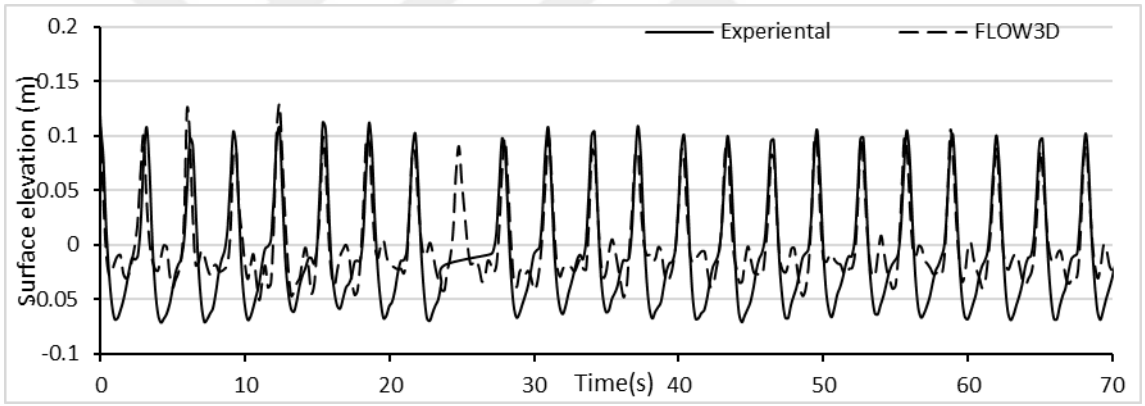

(b) Probe P2

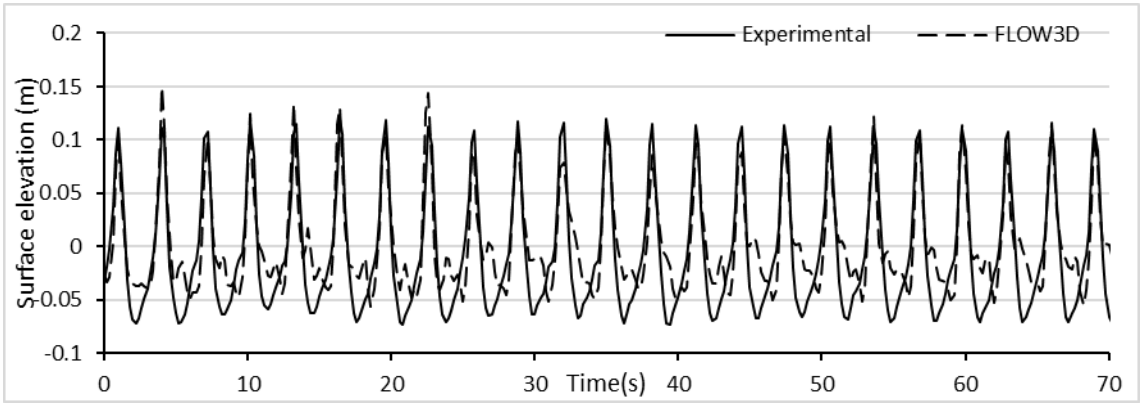

Figure 7.35 Experimental and numerical surface elevations for (RW_H = 0.17 m, T = 3.1 s) at Probes P1 (a) and P2 (b) for the 3-Slope Proposition Design.

(a) Probe P1

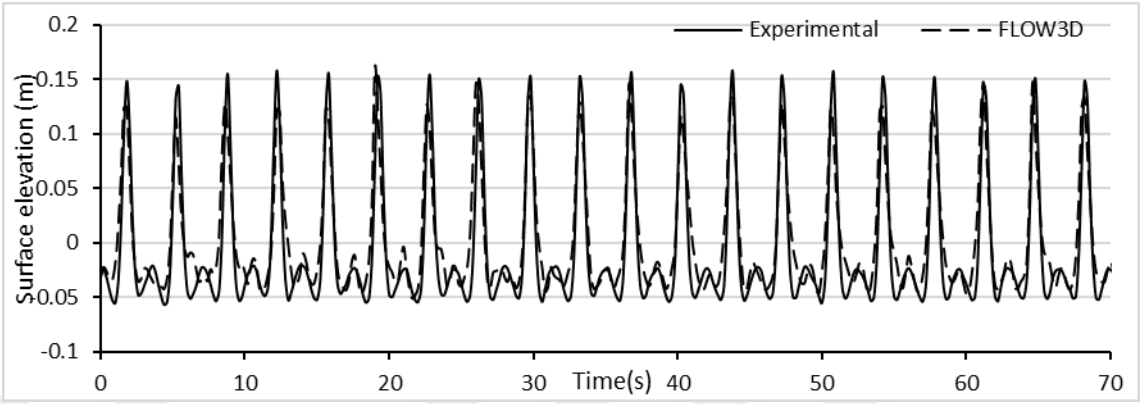

(b) Probe P2

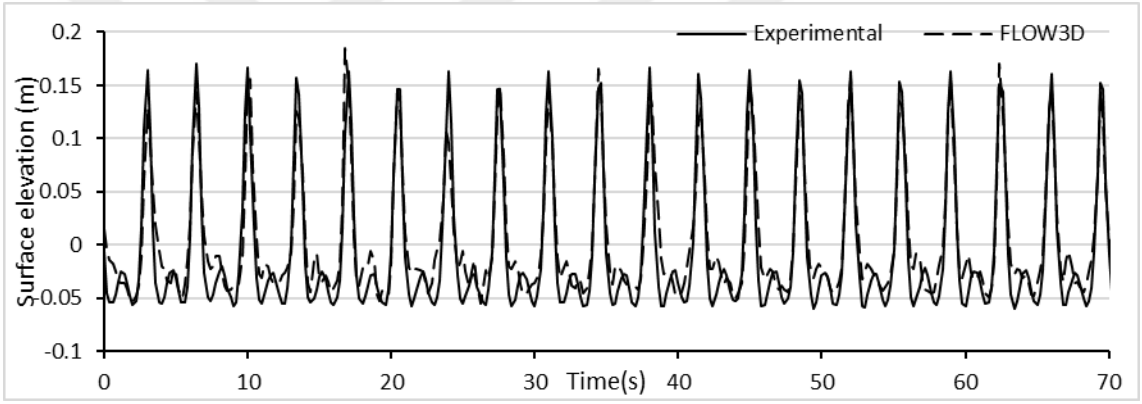

Figure 7.36 Experimental and numerical surface elevations for (RW_H = 0.17 m, T = 3.5 s) at Probes P1 (a) and P2 (b) for the 3-Slope Proposition Design.

(a) Probe P1

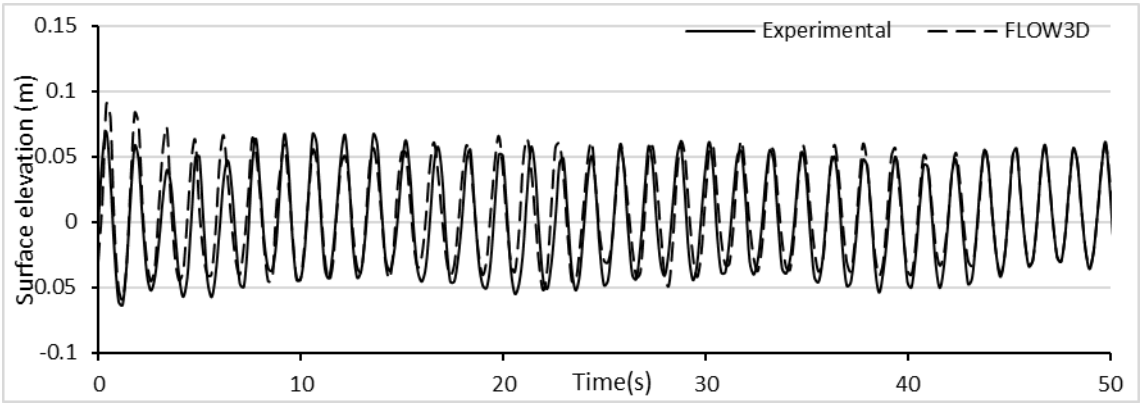

(b) Probe P2

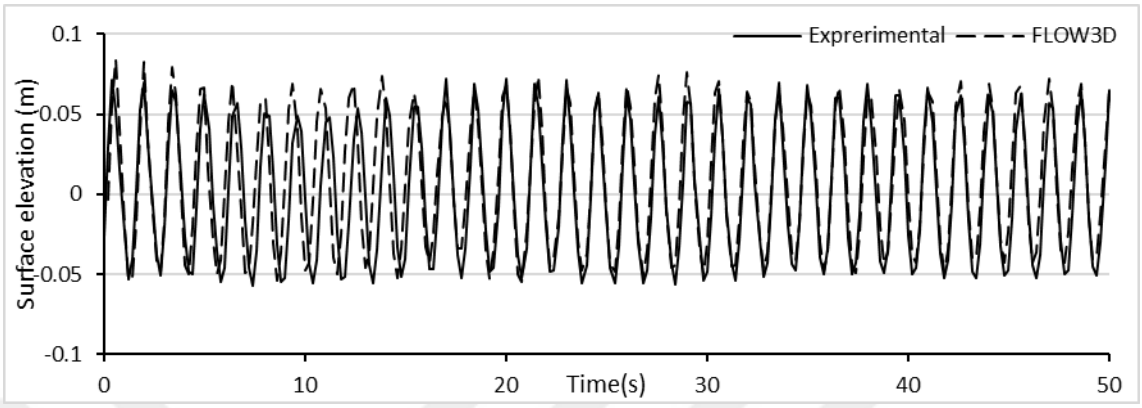

Figure 7.37 Experimental and numerical surface elevations for (RW_H = 0.13 m, T = 1.5 s) at Probes P1 (a) and P2 (b) for the 3-Slope Proposition Design.

(a) Probe P1

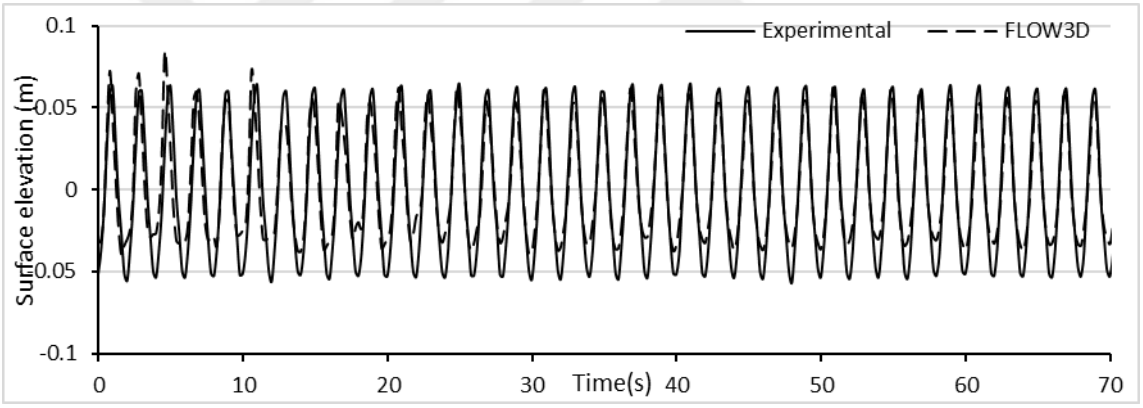

(b) Probe P2

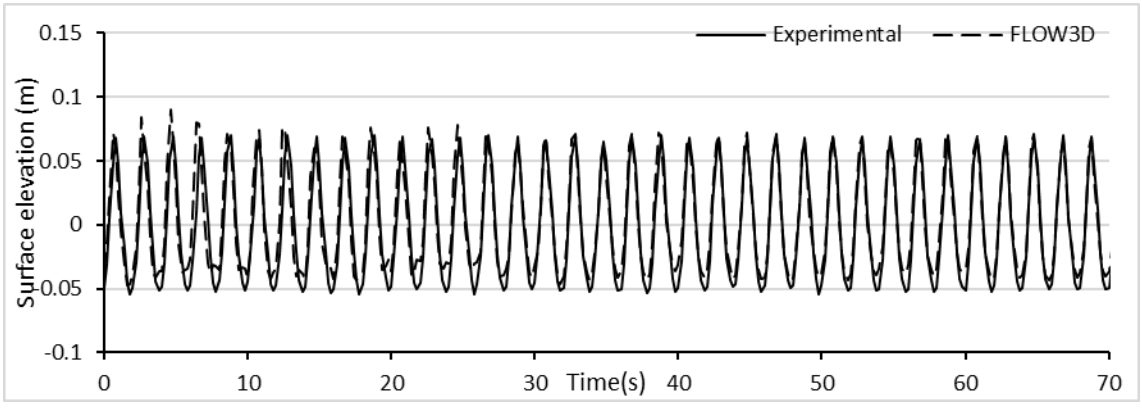

Figure 7.38 Experimental and numerical surface elevations for (RW_H = 0.13 m, T = 2.0 s) at Probes P1 (a) and P2 (b) for the 3-Slope Proposition Design.

(a) Probe P1

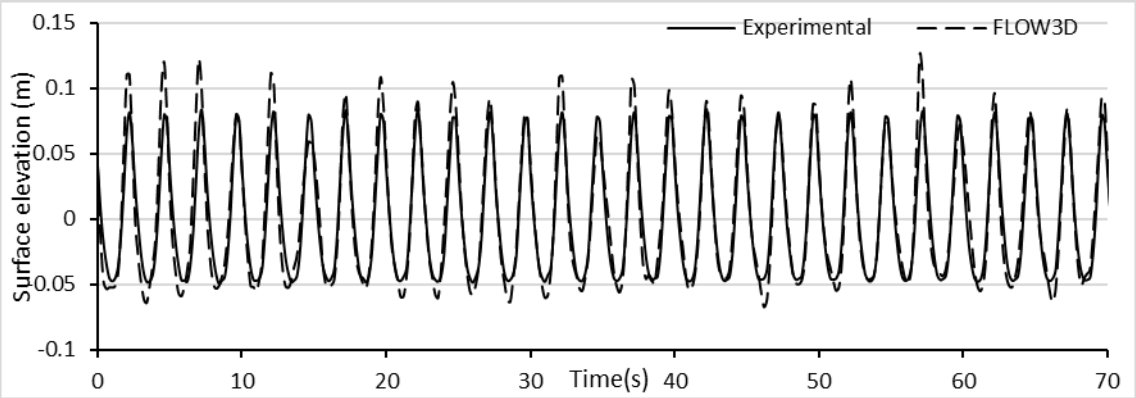

(b) Probe P2

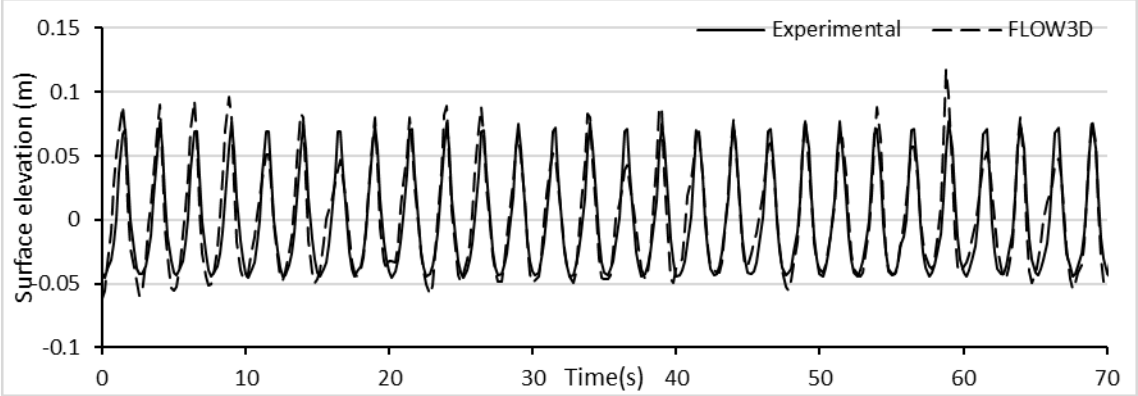

Figure 7.39 Experimental and numerical surface elevations for (RW_H = 0.13 m, T = 2.5 s) at Probes P1 (a) and P2 (b) for the 3-Slope Proposition Design..

(a) Probe P1

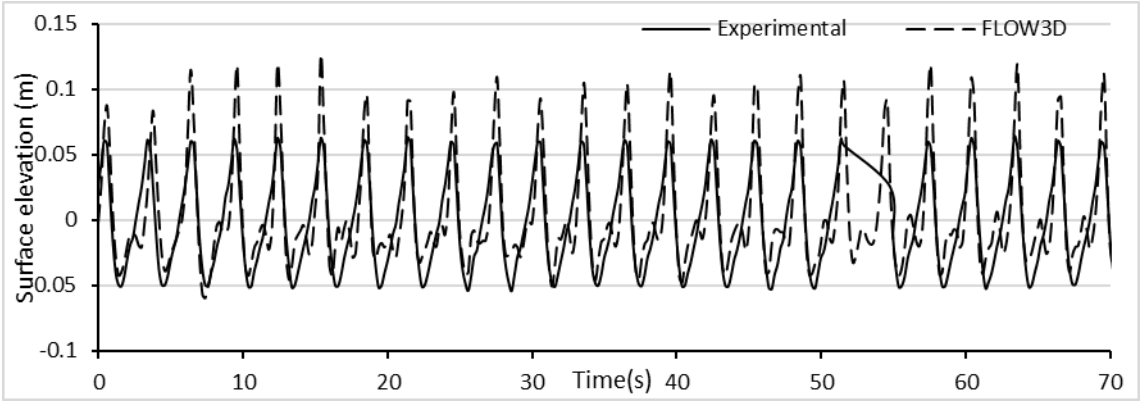

(b) Probe P2

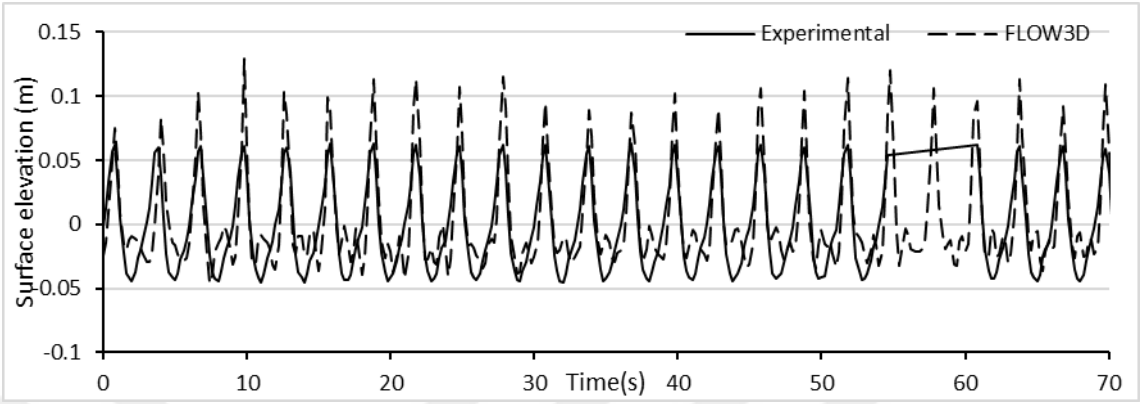

Figure 7.40 Experimental and numerical surface elevations for (RW_H = 0.13 m, T = 3.0 s) at Probes P1 (a) and P2 (b) for the 3-Slope Proposition Design.

(a) Probe P1

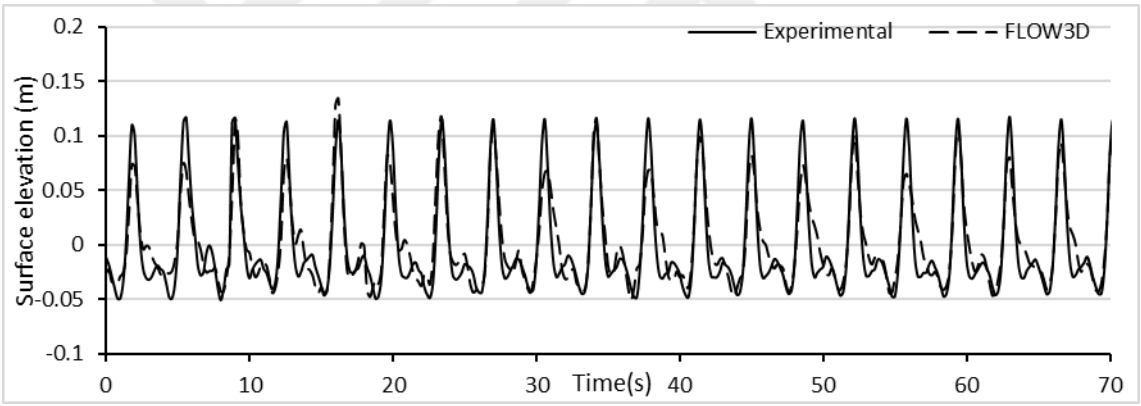

(b) Probe P2

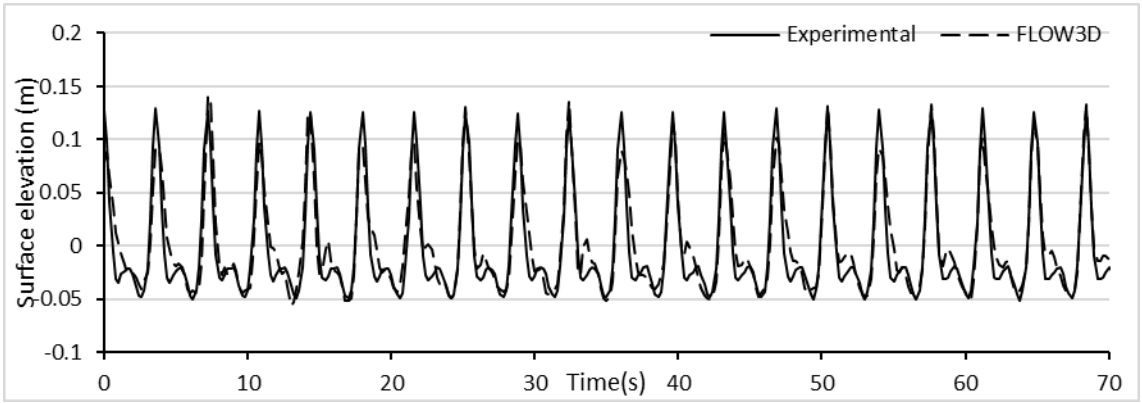

Figure 7.41 Experimental and numerical surface elevations for (RW_H = 0.13 m, T = 3.6 s) at Probes P1 (a) and P2 (b) for the 3-Slope Proposition Design.

Figure 7.42 to Figure 7.62 depict the experimental and numerical surface elevations at probe P1 and P2 of the 2-slopes proposition design under non-breaking regular wave.

(a) Probe P1

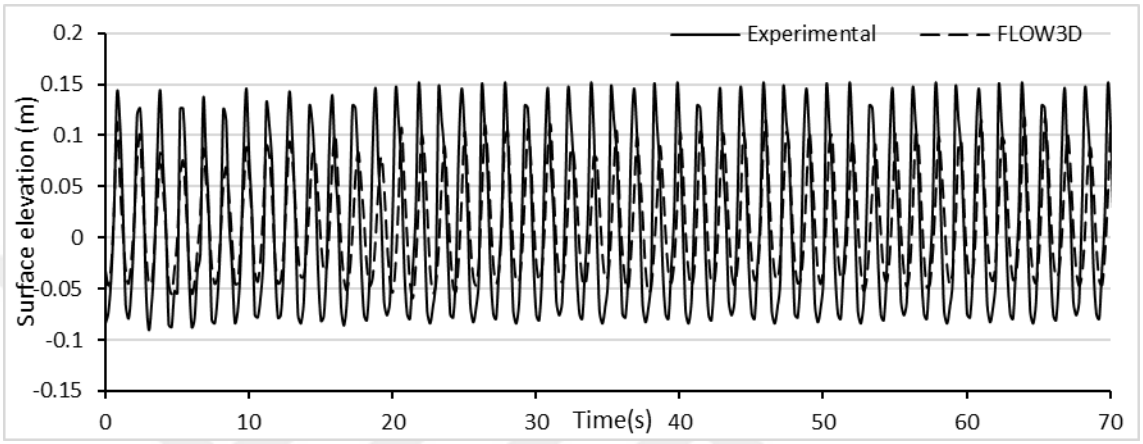

(b) Probe P2

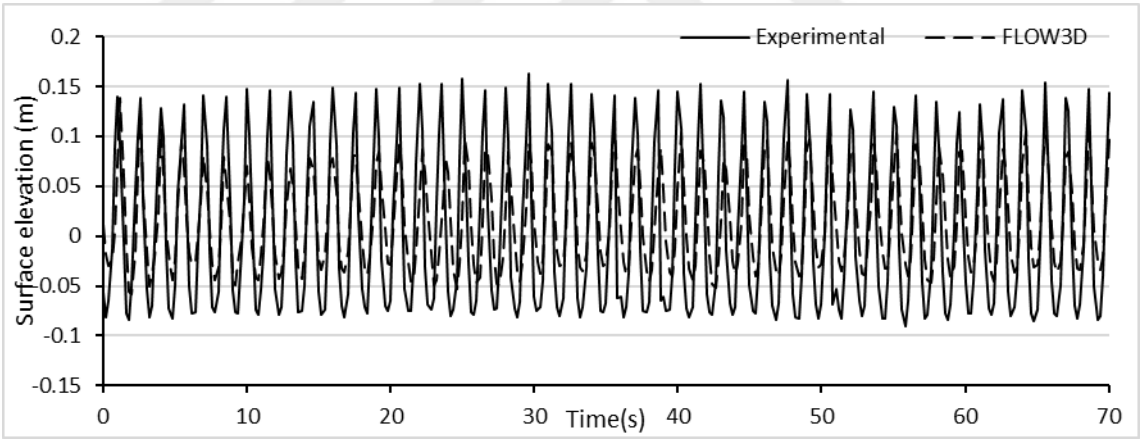

Figure 7.42 Experimental and numerical surface elevations for (RW_H = 0.25 m, T = 1.5 s) at Probes P1 (a) and P2 (b) for the 2-Slope Proposition Design.

(a) Probe P1

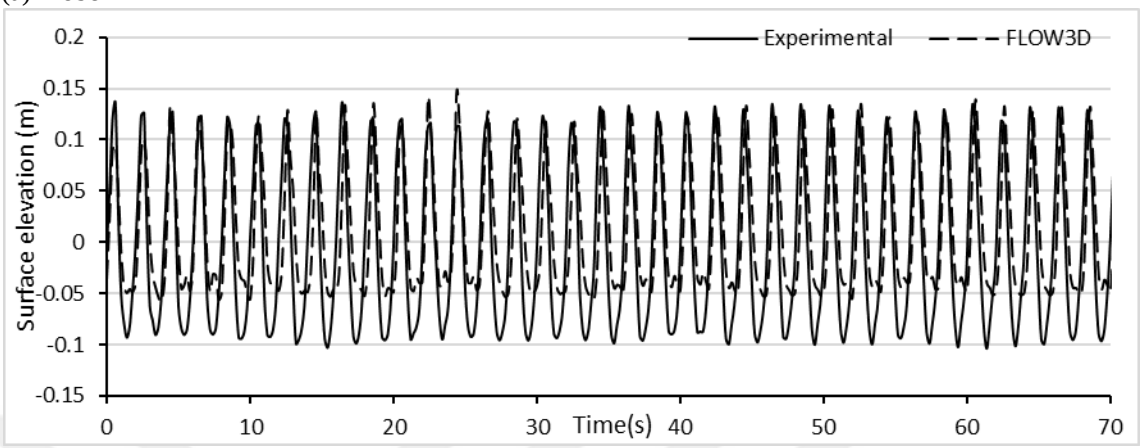

(b) Probe P2

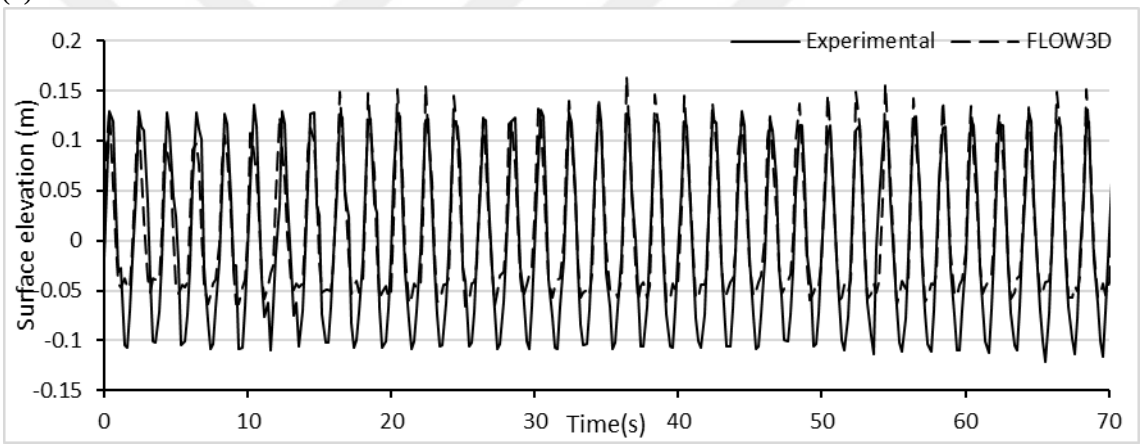

Figure 7.43 Experimental and numerical surface elevations for (RW_H = 0.25 m, T = 2.0 s) at Probes P1 (a) and P2 (b) for the 2-Slope Proposition Design.

(a) Probe P1

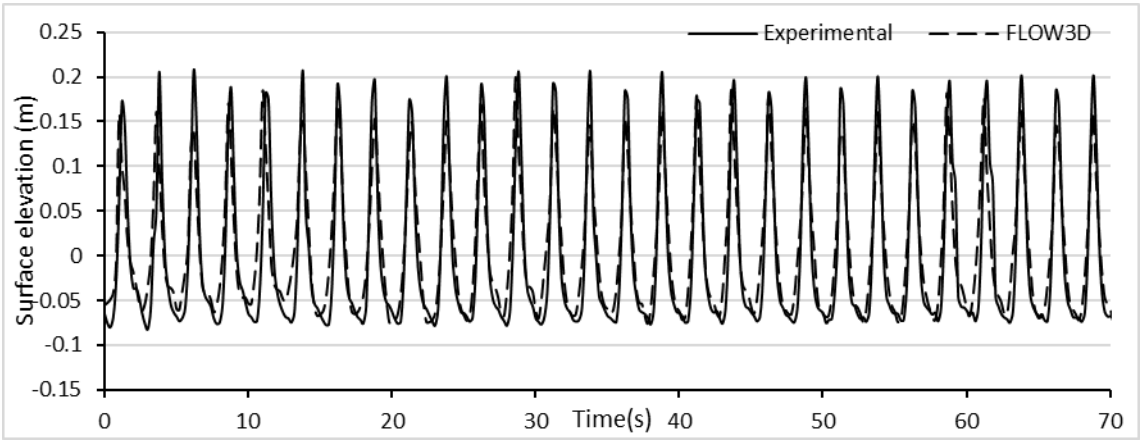

(b) Probe P2

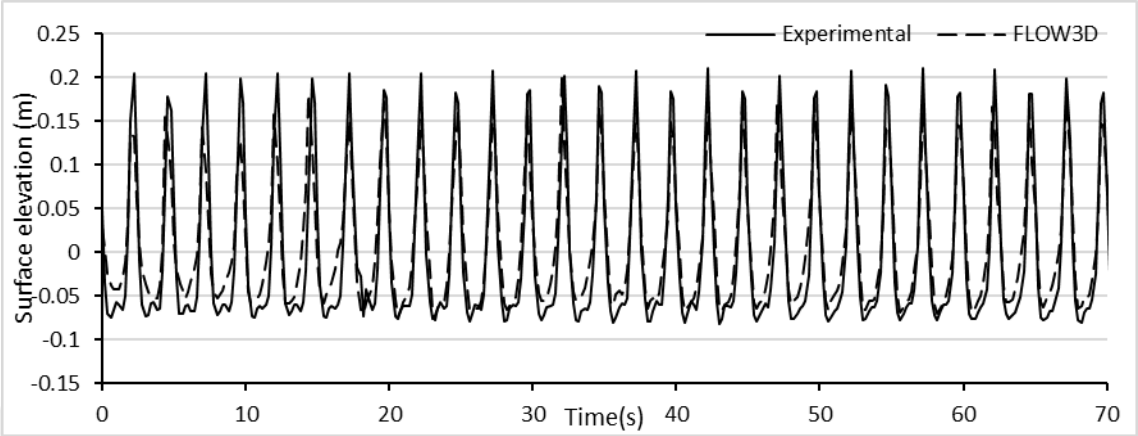

Figure 7.44 Experimental and numerical surface elevations for (RW_H = 0.25 m, T = 2.5 s) at Probes P1 (a) and P2 (b) for the 2-Slope Proposition Design.

(a) Probe P1

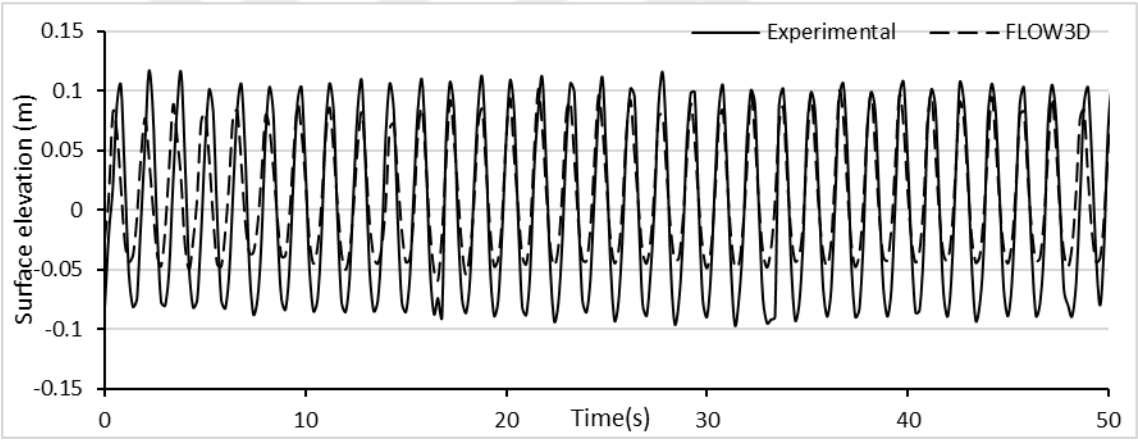

(b) Probe P2

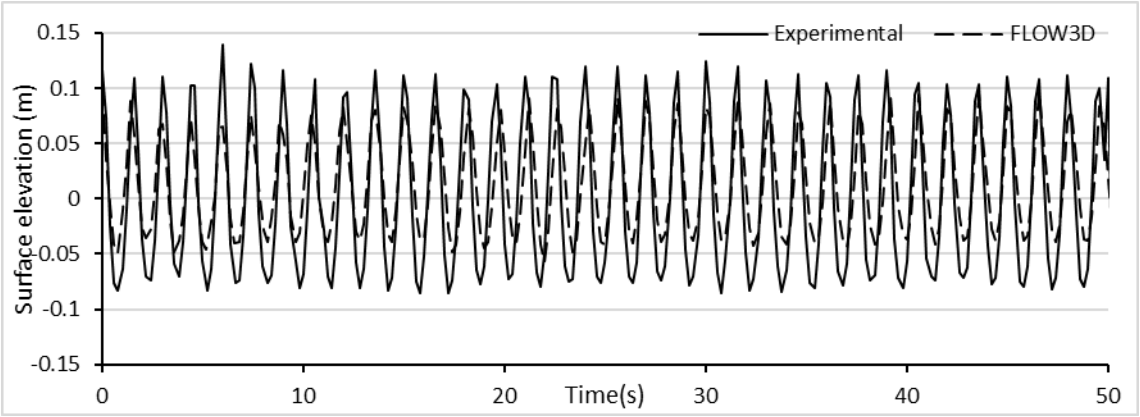

Figure 7.45 Experimental and numerical surface elevations for (RW_H = 0.22 m, T = 1.5 s) at Probes P1 (a) and P2 (b) for the 2-Slope Proposition Design.

(a) Probe P1

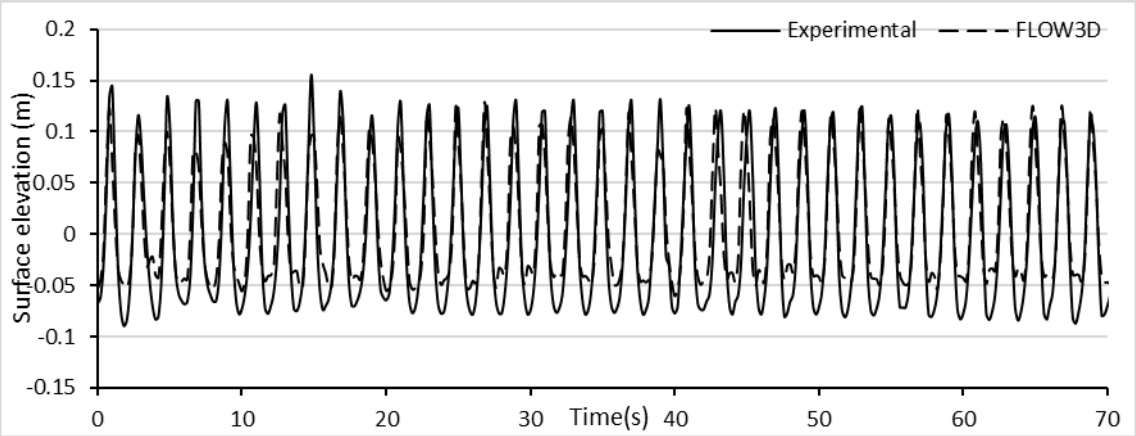

(b) Probe P2

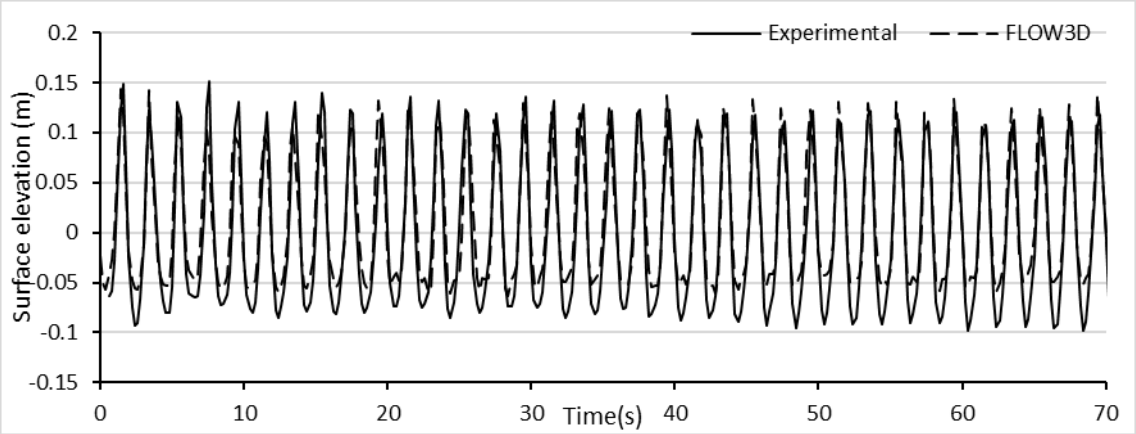

Figure 7.46 Experimental and numerical surface elevations for (RW_H = 0.22 m, T = 2.0 s) at Probes P1 (a) and P2 (b) for the 2-Slope Proposition Design.

(a) Probe P1

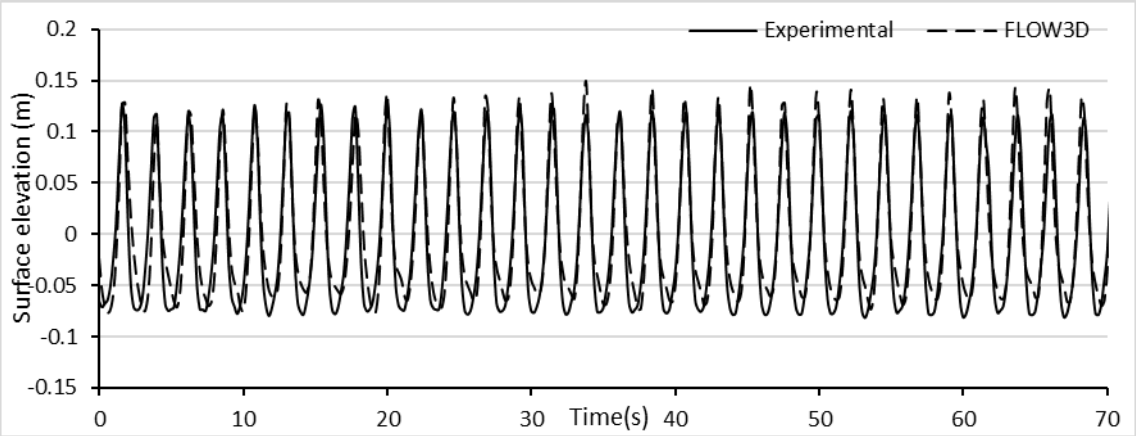

(b) Probe P2

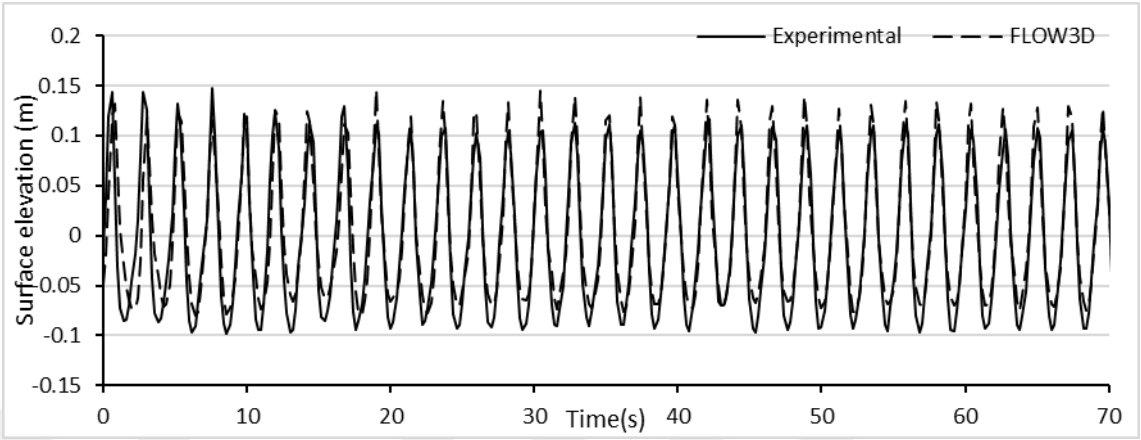

Figure 7.47 Experimental and numerical surface elevations for (RW_H = 0.22 m, T = 2.3 s) at Probes P1 (a) and P2 (b) for the 2-Slope Proposition Design.

(a) Probe P1

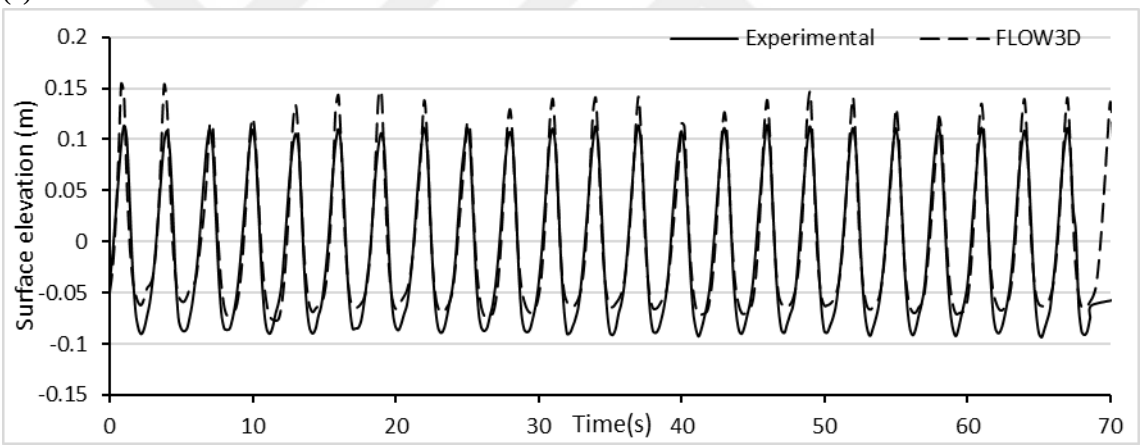

(b) Probe P2

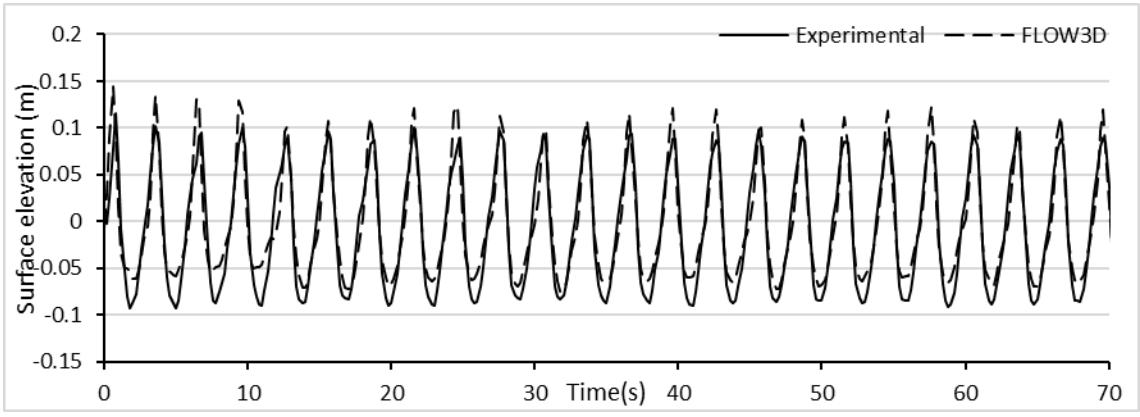

Figure 7.48 Experimental and numerical surface elevations for (RW_H = 0.22 m, T = 3.0 s) at Probes P1 (a) and P2 (b) for the 2-Slope Proposition Design.

(a) Probe P1

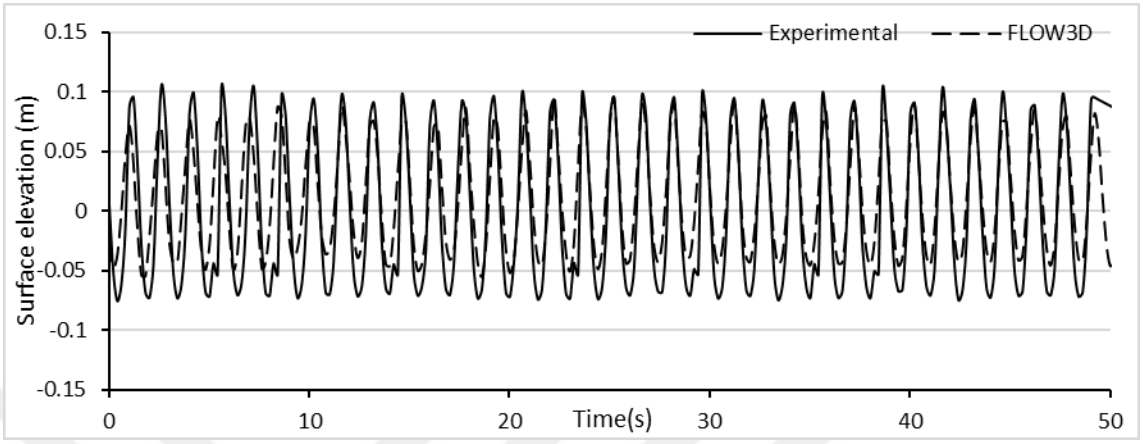

(b) Probe P2

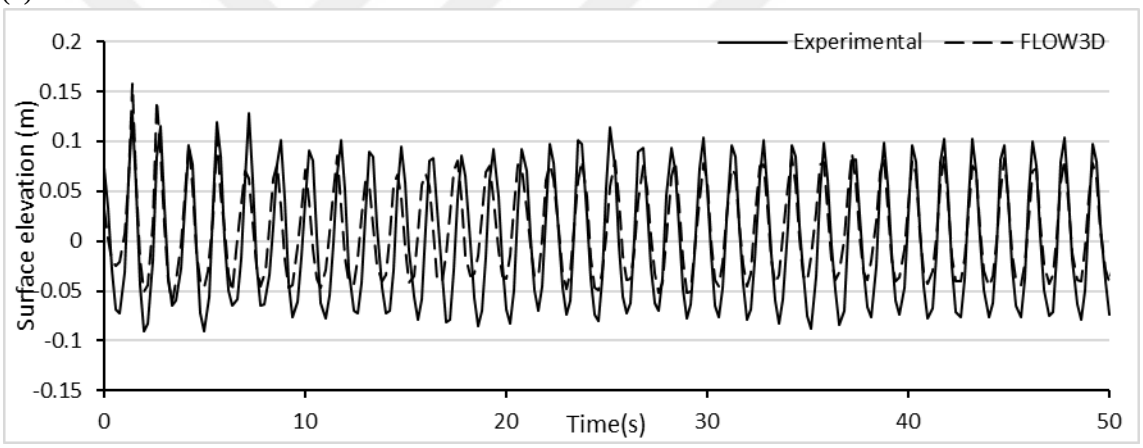

Figure 7.49 Experimental and numerical surface elevations for (RW_H = 0.20 m, T = 1.5 s) at Probes P1 (a) and P2 (b) for the 2-Slope Proposition Design.

(a) Probe P1

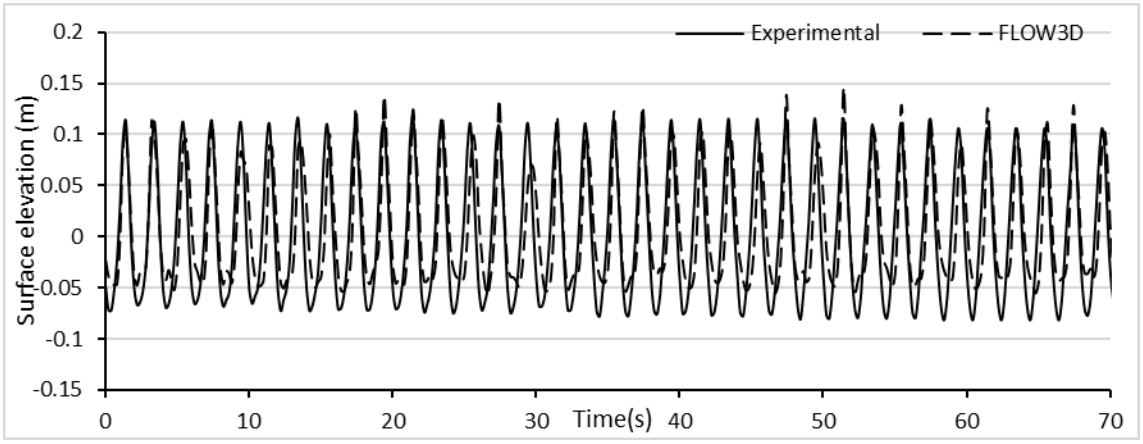

(b) Probe P2

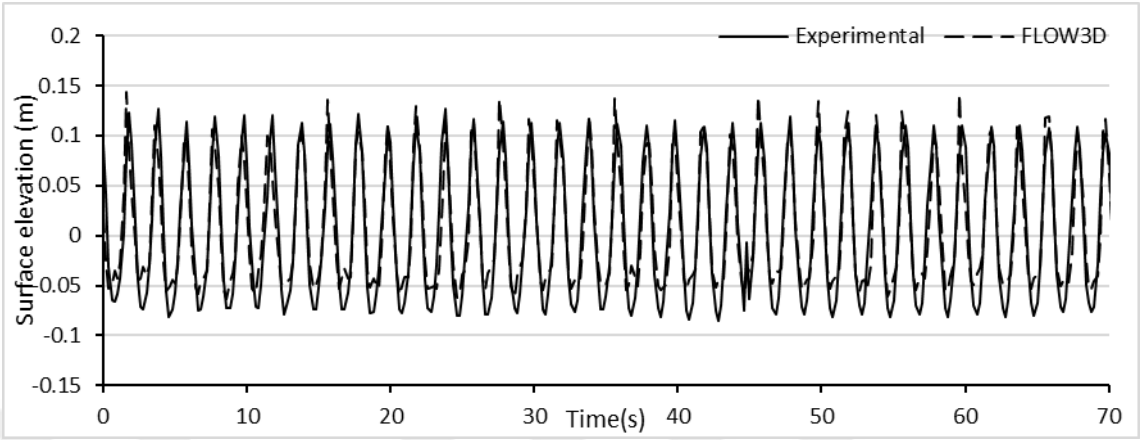

Figure 7.50 Experimental and numerical surface elevations for (RW_H = 0.20 m, T = 2.0 s) at Probes P1 (a) and P2 (b) for the 2-Slope Proposition Design.

(a) Probe P1

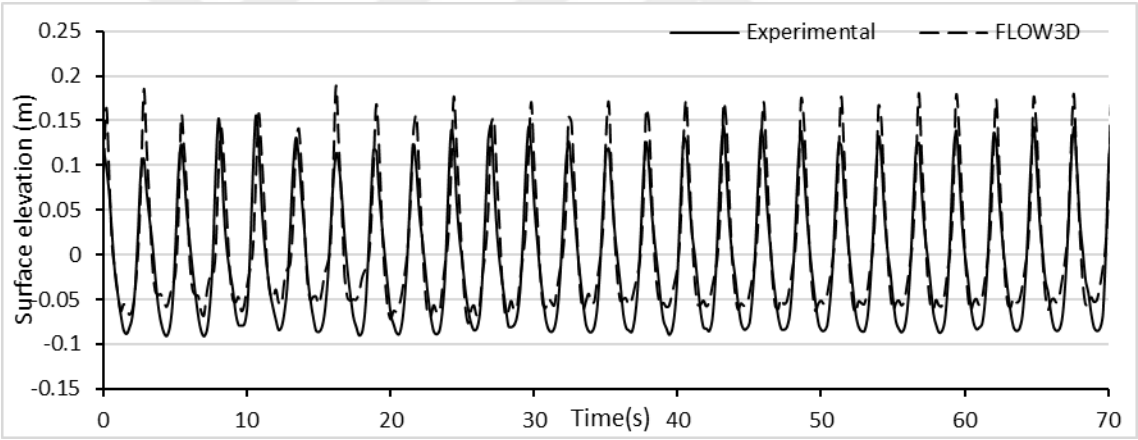

(b) Probe P2

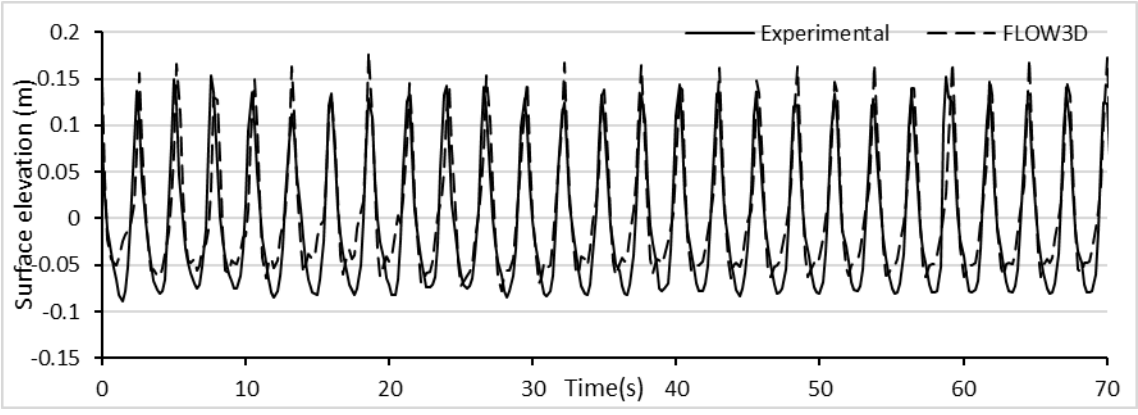

Figure 7.51 Experimental and numerical surface elevations for (RW_H = 0.20 m, T = 2.7 s) at Probes P1 (a) and P2 (b) for the 2-Slope Proposition Design.

(a) Probe P1

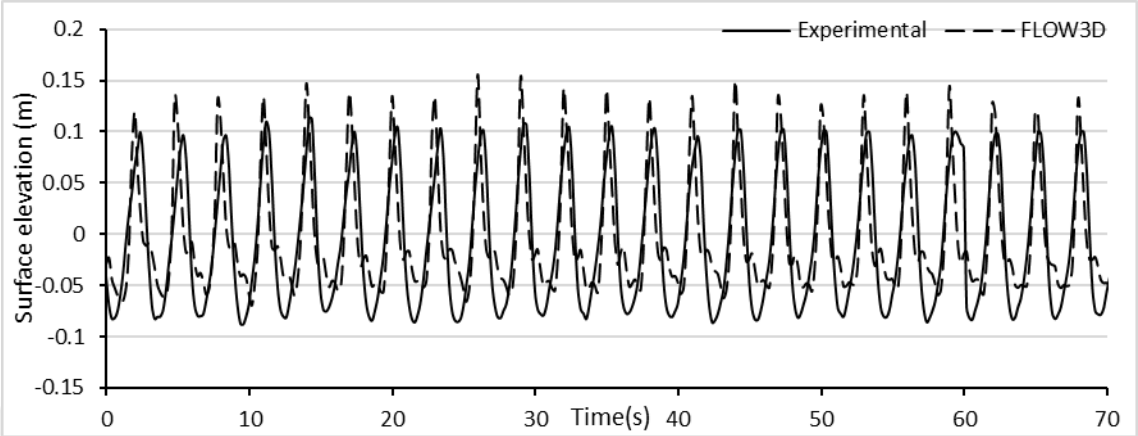

(b) Probe P2

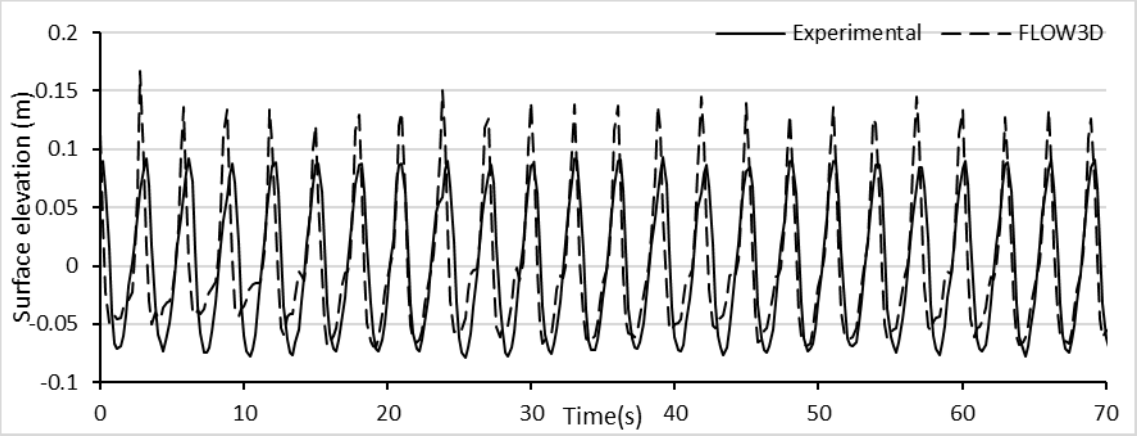

Figure 7.52 Experimental and numerical surface elevations for (RW_H = 0.20 m, T = 3.0 s) at Probes P1 (a) and P2 (b) for the 2-Slope Proposition Design.

(a) Probe P1

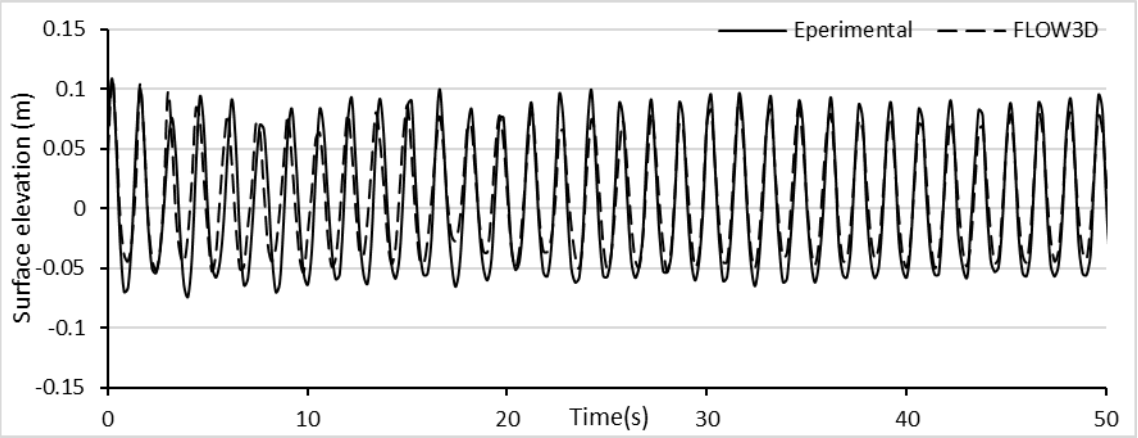

(b) Probe P2

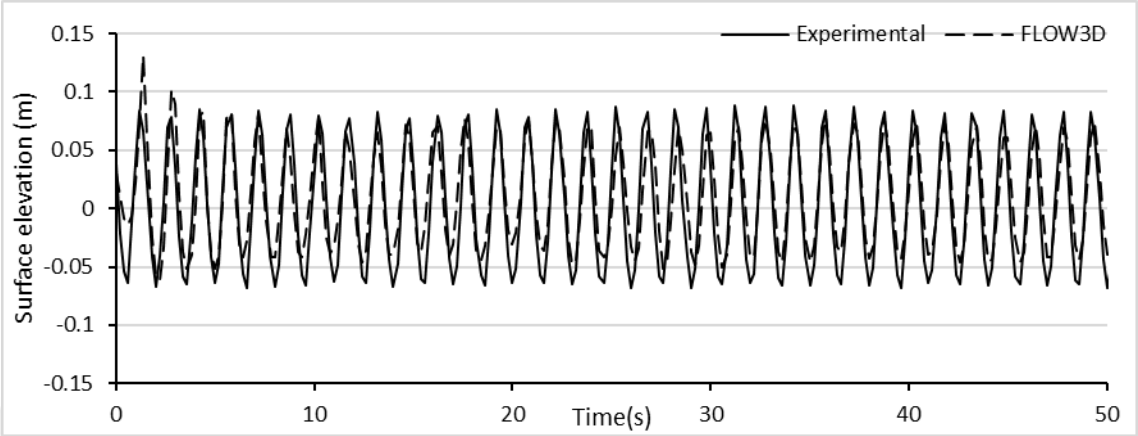

Figure 7.53 Experimental and numerical surface elevations for (RW_H = 0.17 m, T = 1.5 s) at Probes P1 (a) and P2 (b) for the 2-Slope Proposition Design.

(a) Probe P1

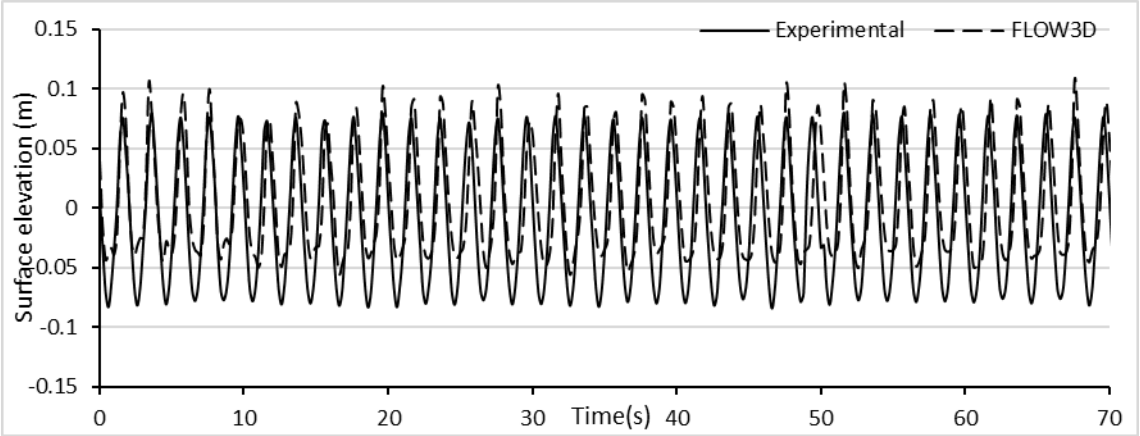

(b) Probe P2

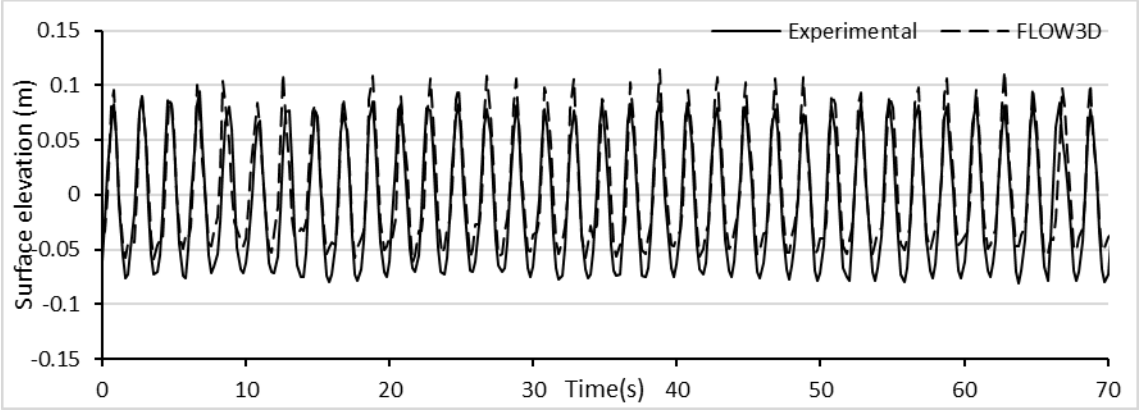

Figure 7.54 Experimental and numerical surface elevations for (RW_H = 0.17 m, T = 2.0 s) at Probes P1 (a) and P2 (b) for the 2-Slope Proposition Design.

(a) Probe P1

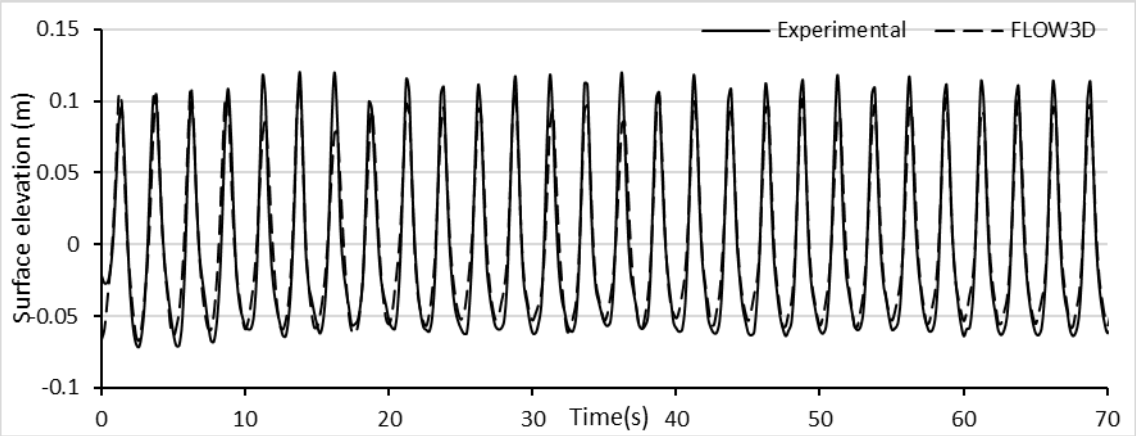

(b) Probe P2

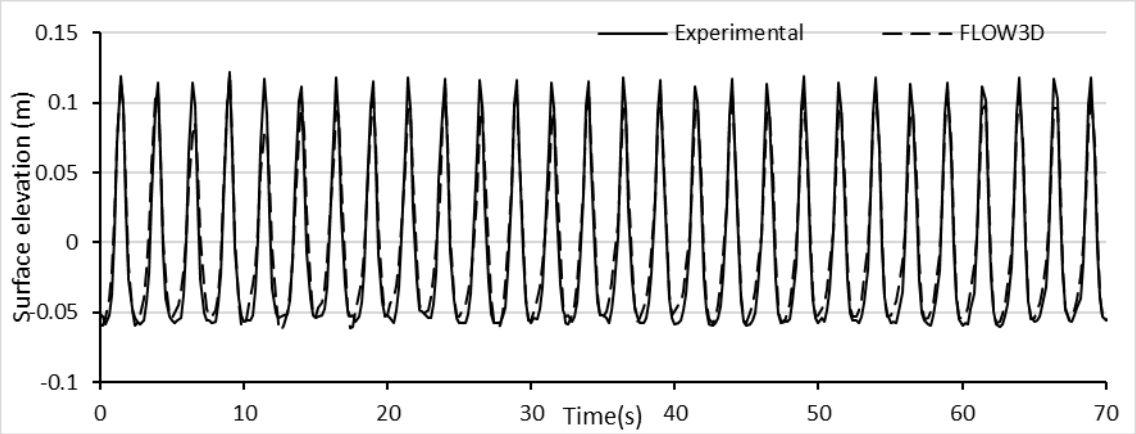

Figure 7.55 Experimental and numerical surface elevations for (RW_H = 0.17 m, T = 2.5 s) at Probes P1 (a) and P2 (b) for the 2-Slope Proposition Design.

(a) Probe P1

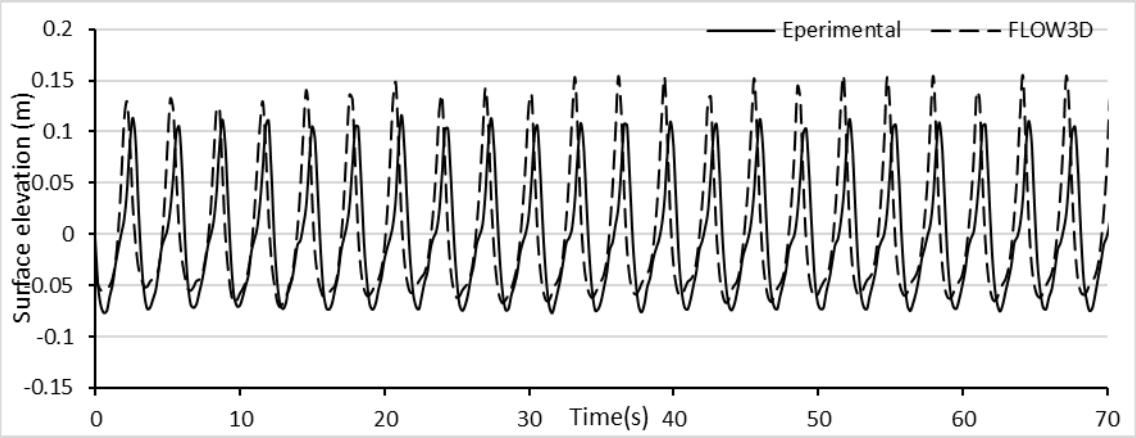

(b) Probe P2

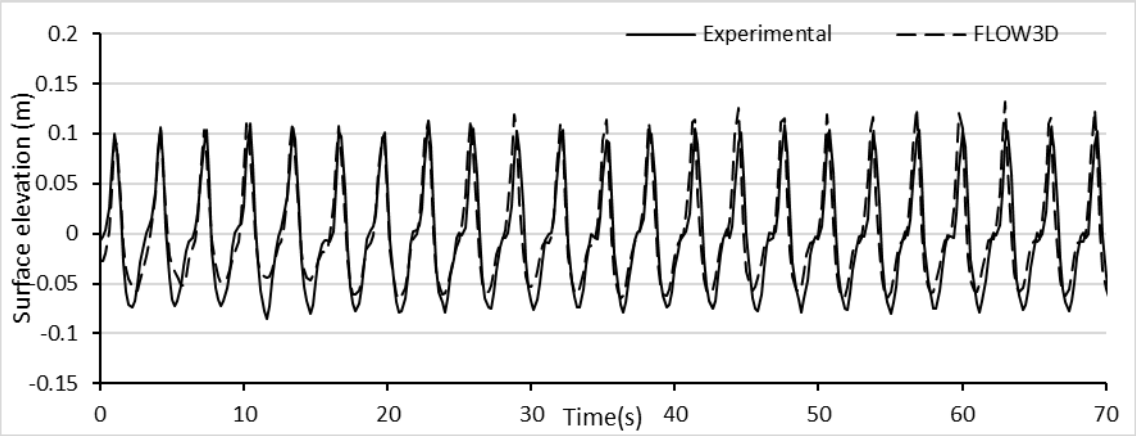

Figure 7.56 Experimental and numerical surface elevations for (RW_H = 0.17 m, T = 3.1 s) at Probes P1 (a) and P2 (b) for the 2-Slope Proposition Design.

(a) Probe P1

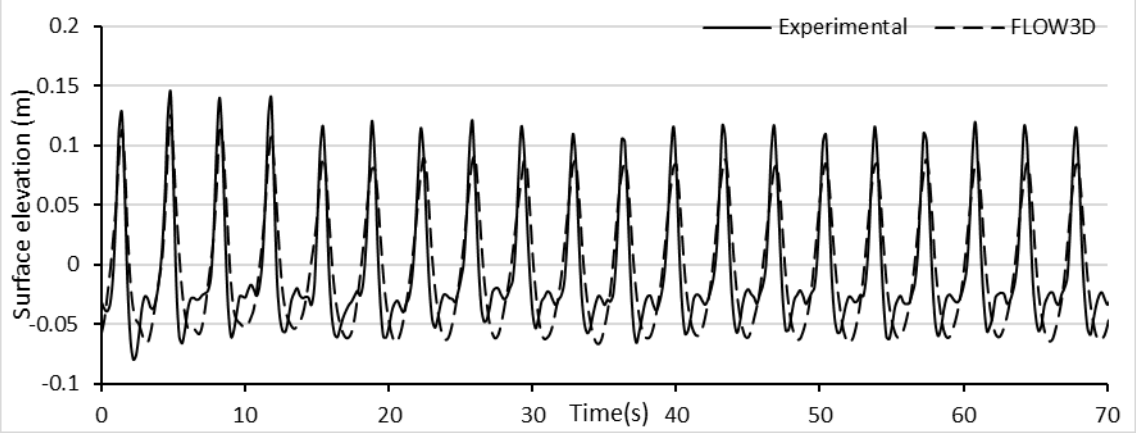

(b) Probe P2

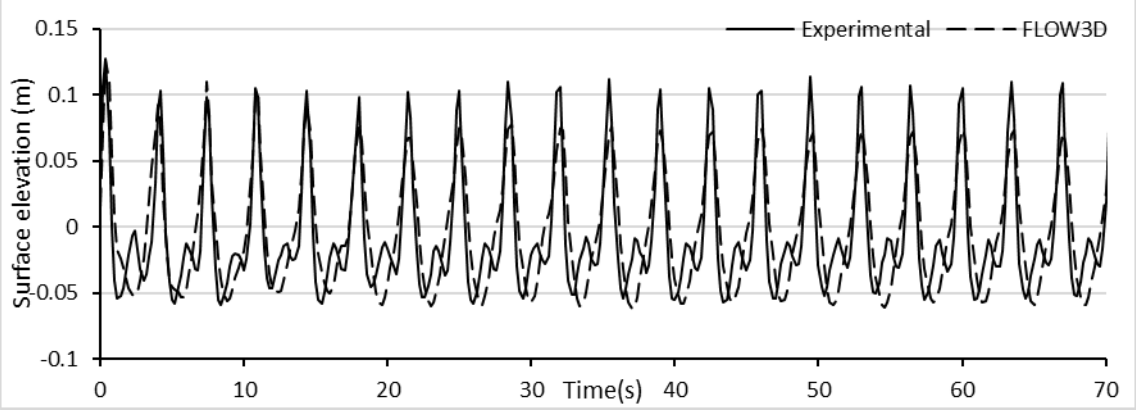

Figure 7.57 Experimental and numerical surface elevations for (RW_H = 0.17 m, T = 3.5 s) at Probes P1 (a) and P2 (b) for the 2-Slope Proposition Design.

(a) Probe P1

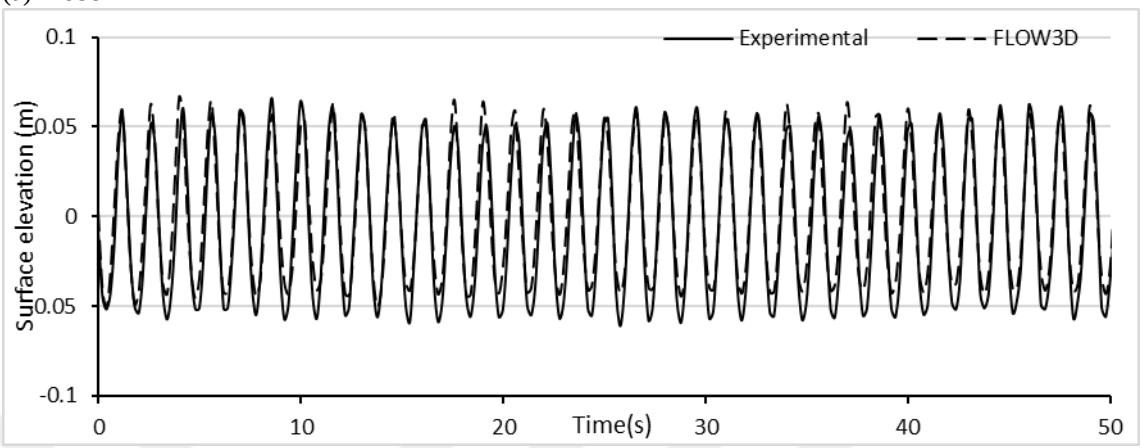

(b) Probe P2

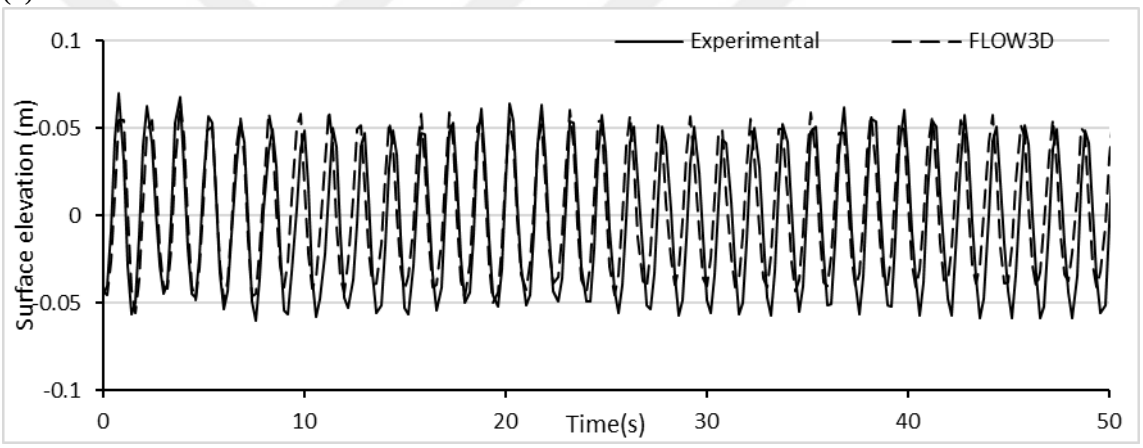

Figure 7.58 Experimental and numerical surface elevations for (RW_H = 0.13 m, T = 1.5 s) at Probes P1 (a) and P2 (b) for the 2-Slope Proposition Design.

(a) Probe P1

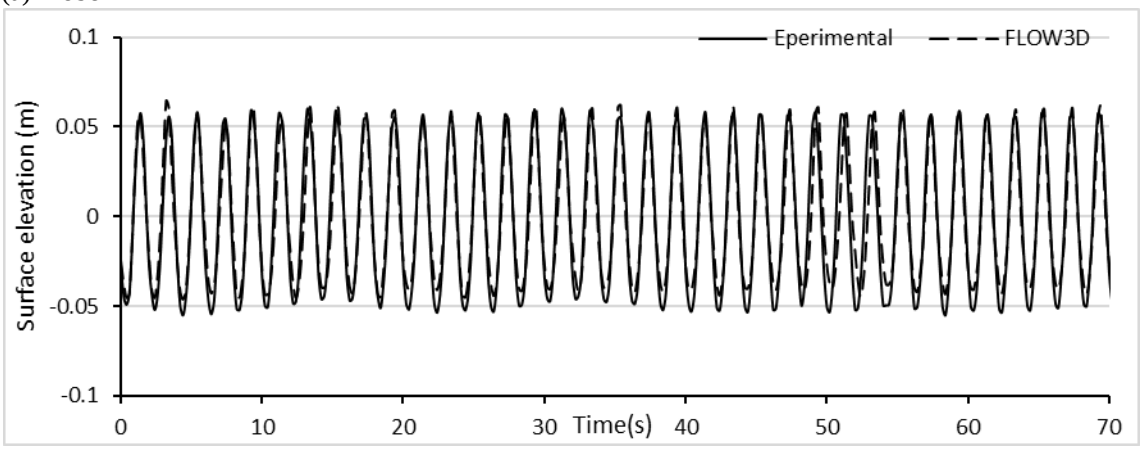

(b) Probe P2

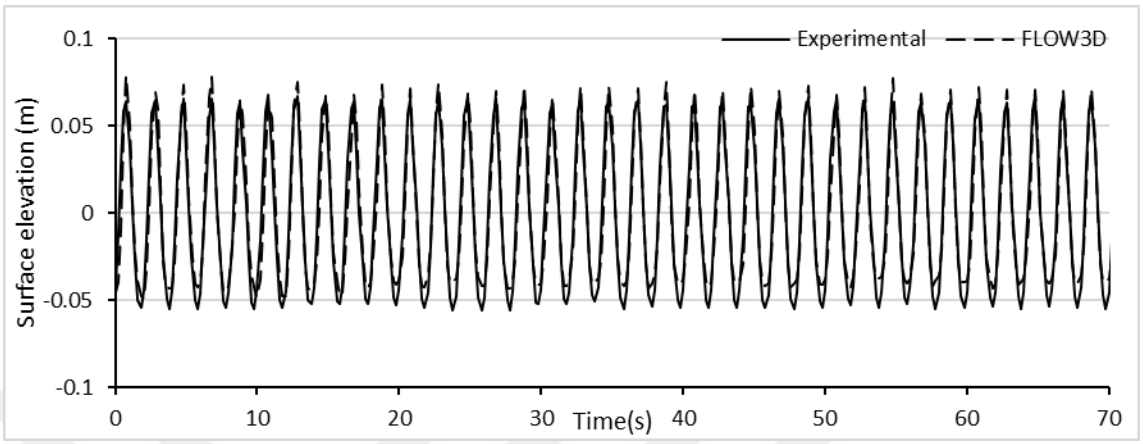

Figure 7.59 Experimental and numerical surface elevations for (RW_H = 0.13 m, T = 2.0 s) at Probes P1 (a) and P2 (b) for the 2-Slope Proposition Design.

(a) Probe P1

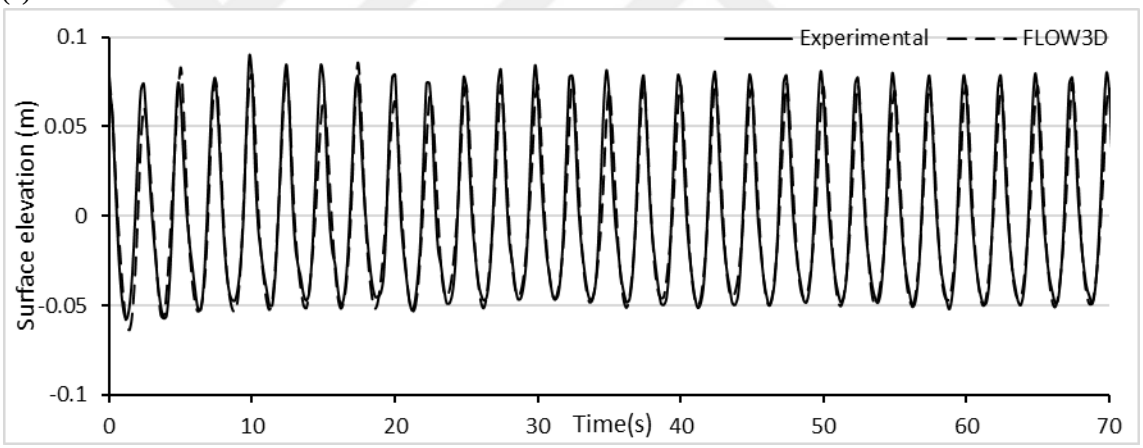

(b) Probe P2

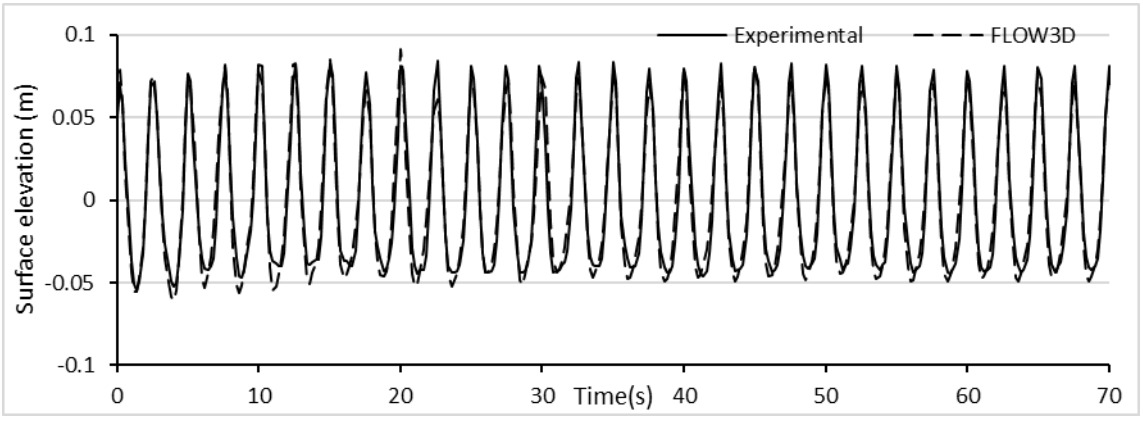

Figure 7.60 Experimental and numerical surface elevations for (RW_H = 0.13 m, T = 2.5 s) at Probes P1 (a) and P2 (b) for the 2-Slope Proposition Design.

(a) Probe P1

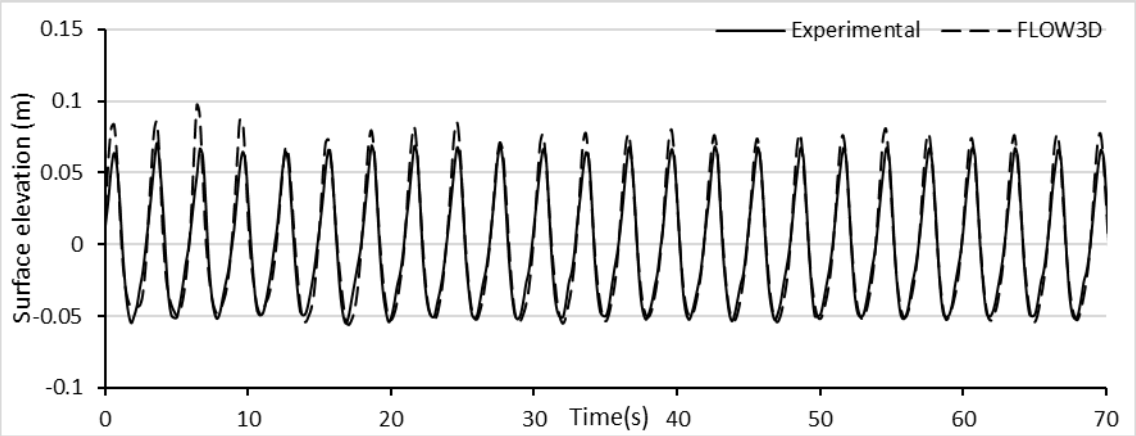

(b) Probe P2

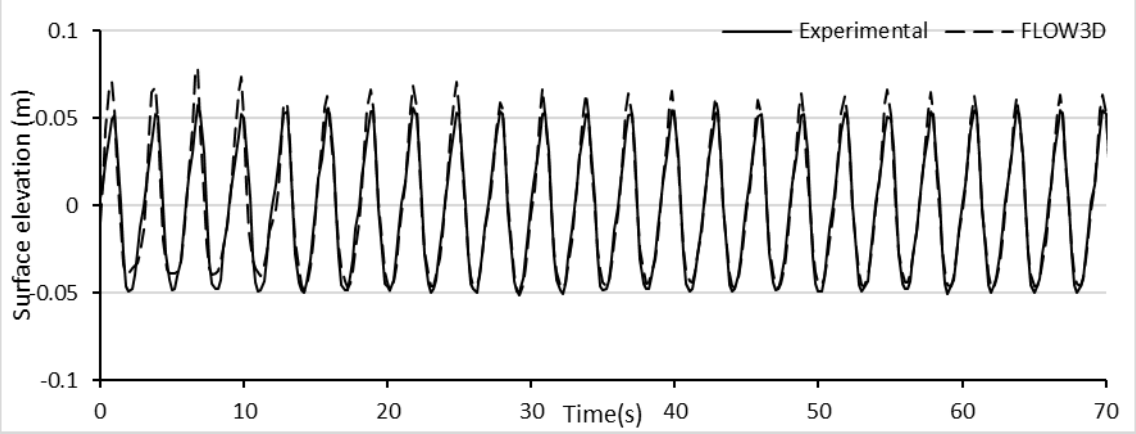

Figure 7.61 Experimental and numerical surface elevations for (RW_H = 0.13 m, T = 3.0 s) at Probes P1 (a) and P2 (b) for the 2-Slope Proposition Design.

(a) Probe P1

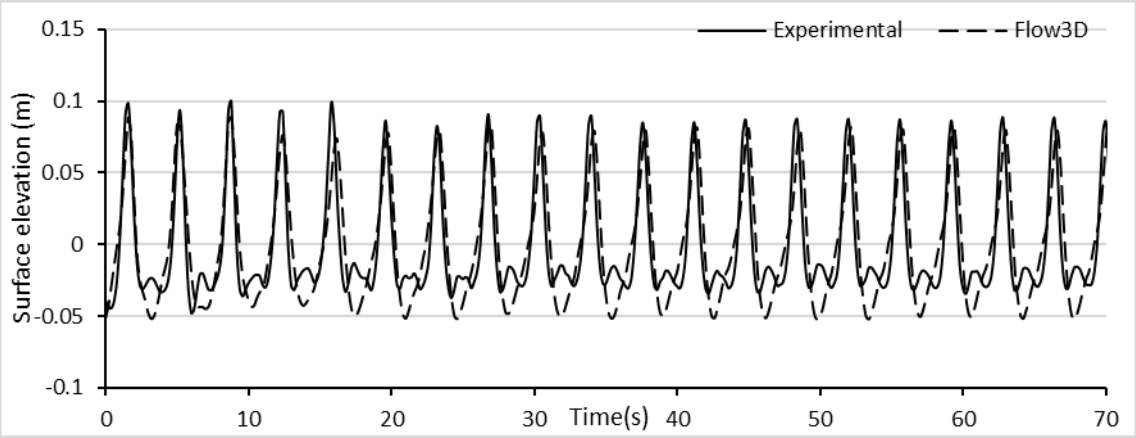

(b) Probe P2

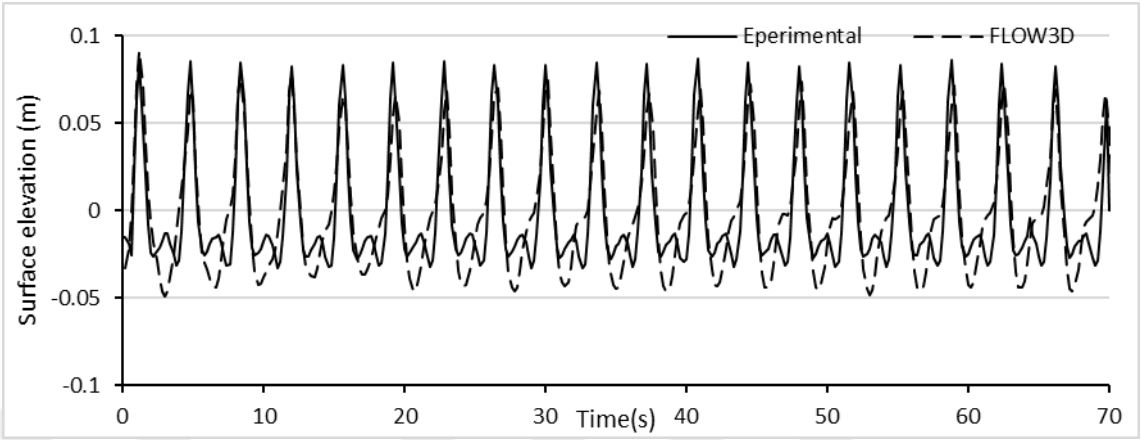

Figure 7.62 Experimental and numerical surface elevations for (RW_H = 0.13 m, T = 3.6 s) at Probes P1 (a) and P2 (b) for the 2-Slope Proposition Design.

Figure 7.63 to Figure 7.83 depict the experimental and numerical surface elevations at probe P1 and P2 of the parabolic proposition design under non-breaking regular wave conditions.

(a) Probe P1

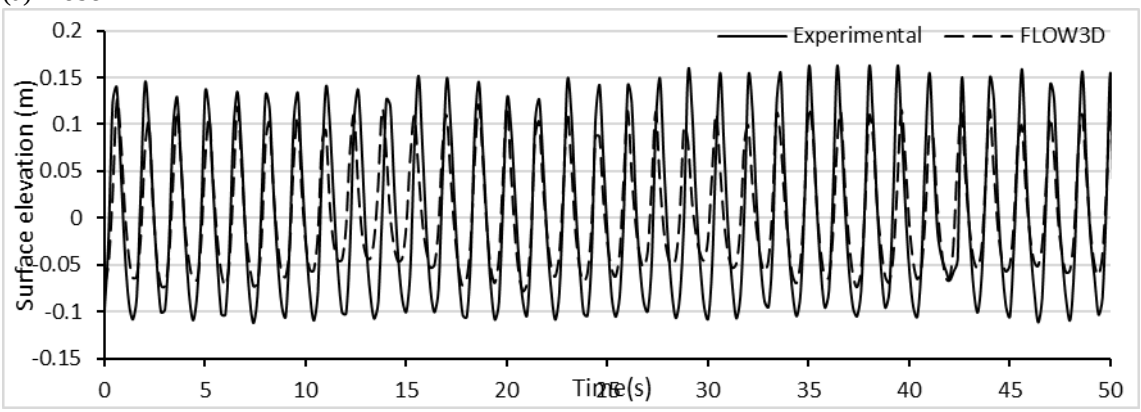

(b) Probe P2

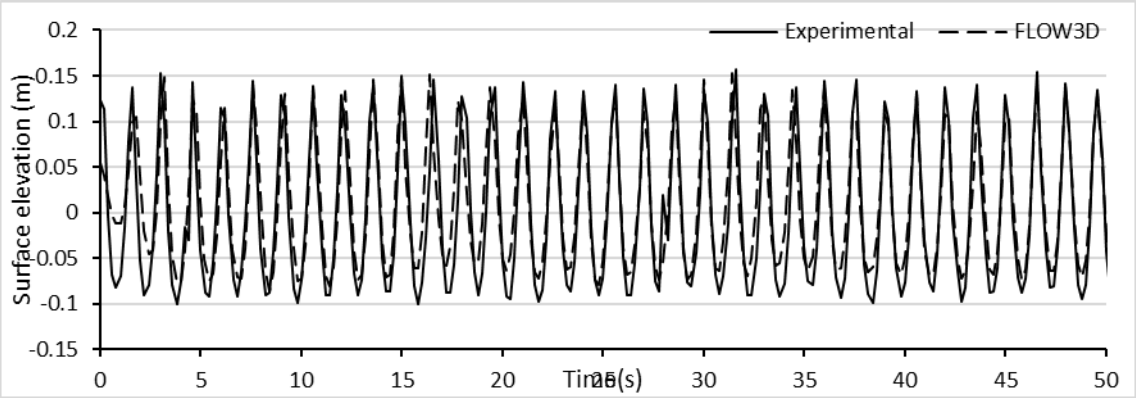

Figure 7.63 Experimental and numerical surface elevations for (RW_H = 0.25 m, T = 1.5 s) at Probes P1 (a) and P2 (b) for the Parabolic Proposition Design.

(a) Probe P1

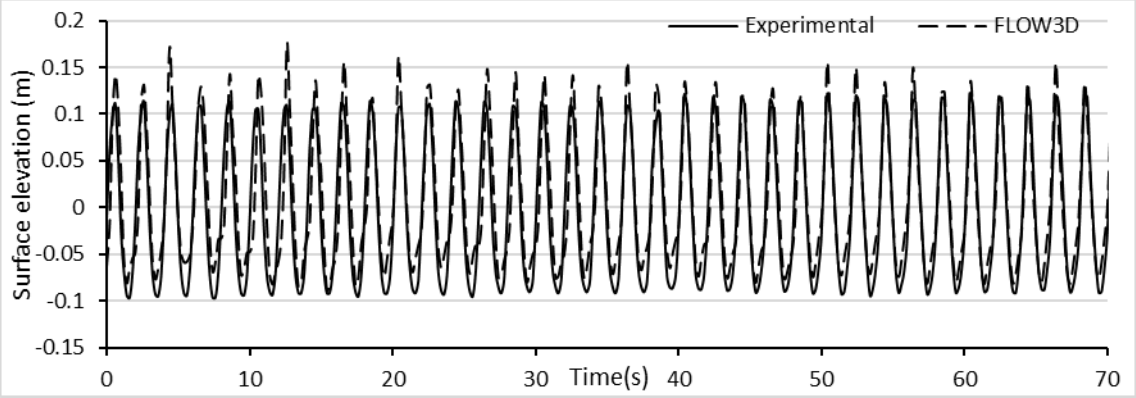

(b) Probe P2

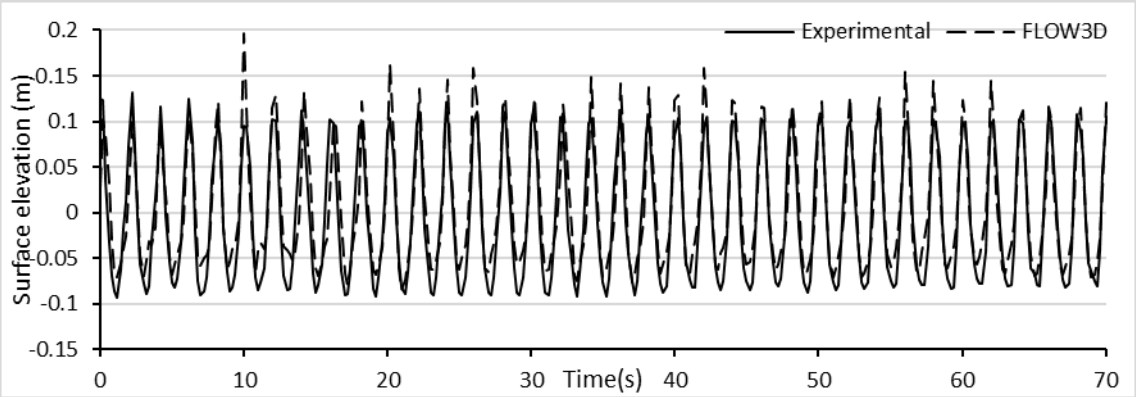

Figure 7.64 Experimental and numerical surface elevations for (RW_H = 0.25 m, T = 2.0 s) at Probes P1 (a) and P2 (b) for the Parabolic Proposition Design.

(a) Probe P1

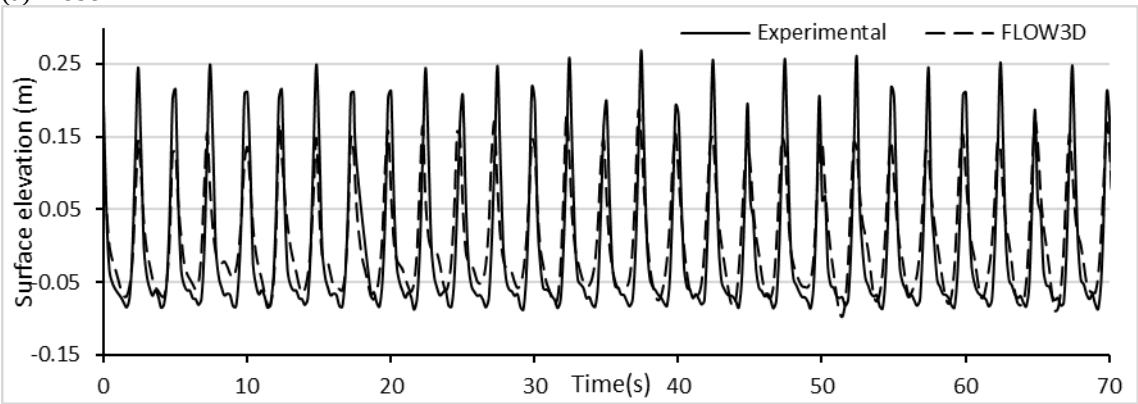

(b) Probe P2

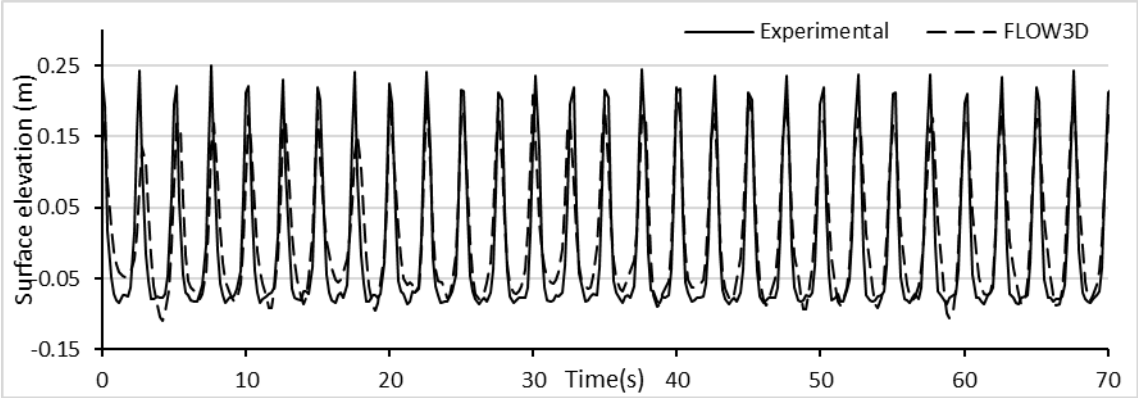

Figure 7.65 Experimental and numerical surface elevations for (RW_H = 0.25 m, T = 2.5 s) at Probes P1 (a) and P2 (b) for the Parabolic Proposition Design.

(a) Probe P1

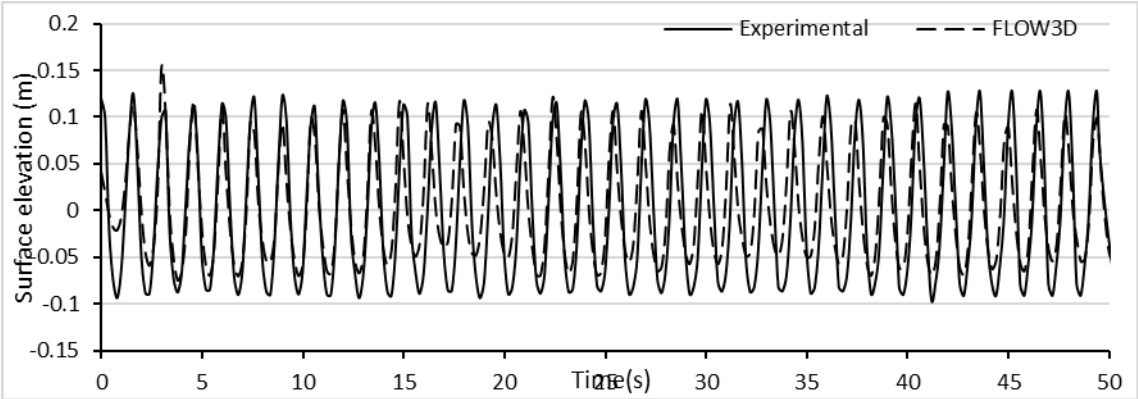

(b) Probe P2

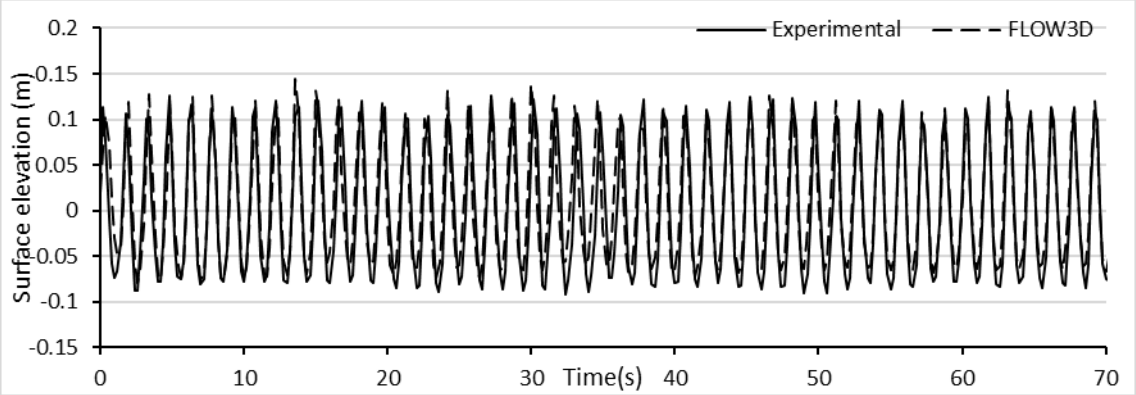

Figure 7.66 Experimental and numerical surface elevations for (RW_H = 0.22 m, T = 1.5 s) at Probes P1 (a) and P2 (b) for the Parabolic Proposition Design.

(a) Probe P1

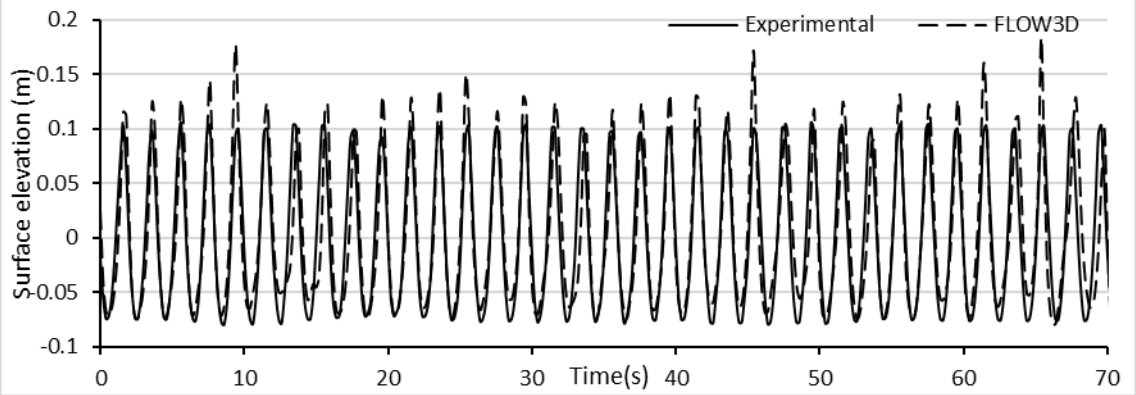

(b) Probe P2

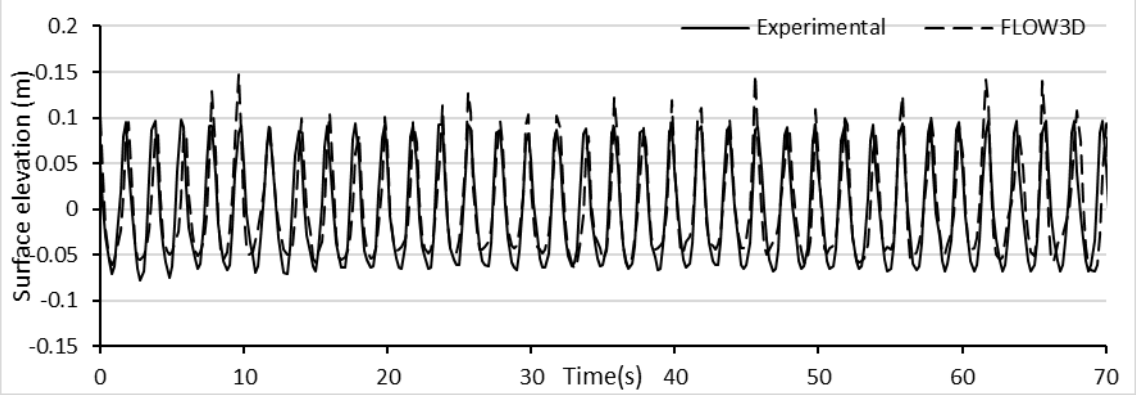

Figure 7.67 Experimental and numerical surface elevations for (RW_H = 0.22 m, T = 2.0 s) at Probes P1 (a) and P2 (b) for the Parabolic Proposition Design.

(a) Probe P1

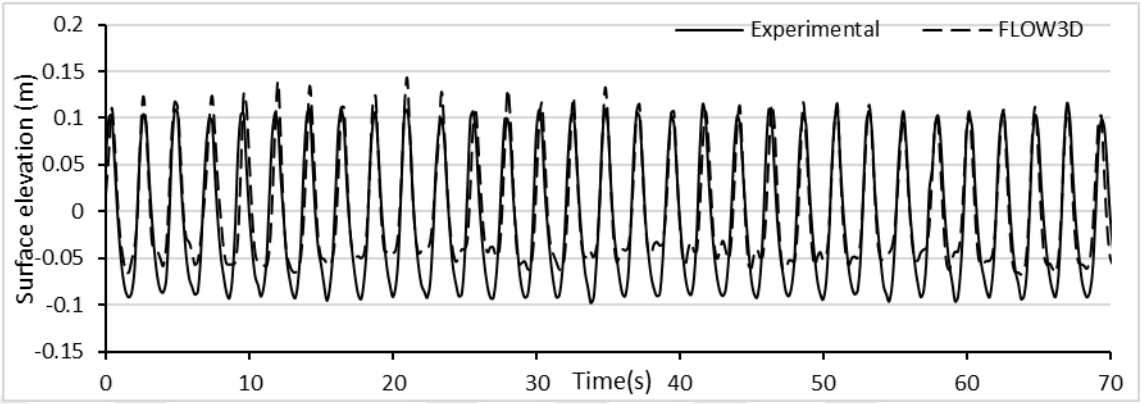

(b) Probe P2

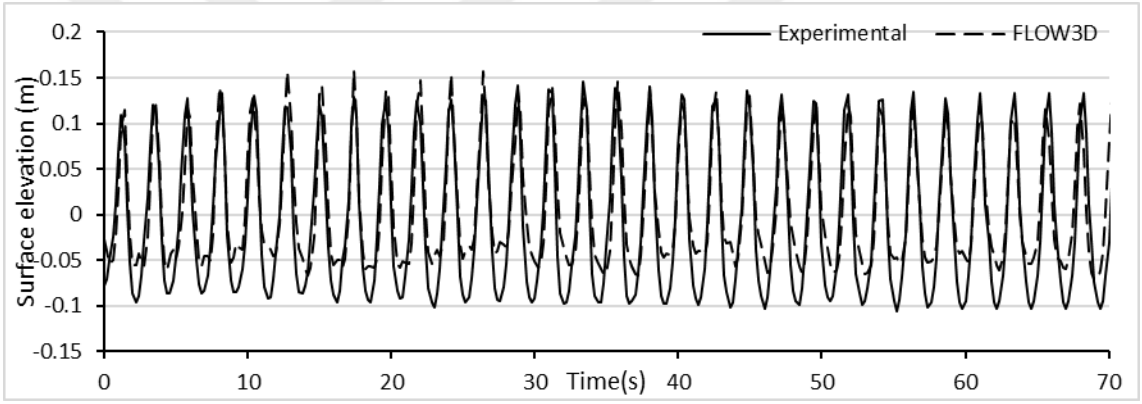

Figure 7.68 Experimental and numerical surface elevations for (RW_H = 0.22 m, T = 2.5 s) at Probes P1 (a) and P2 (b) for the Parabolic Proposition Design.

(a) Probe P1

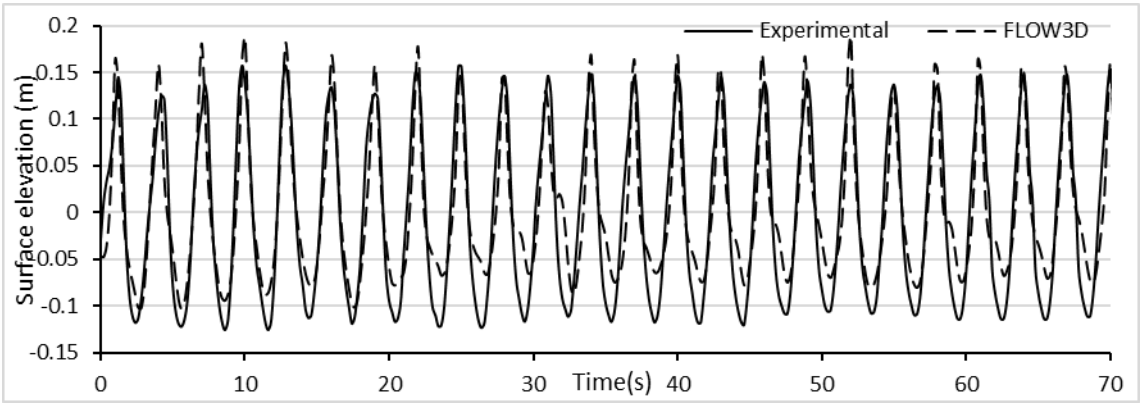

(b) Probe P2

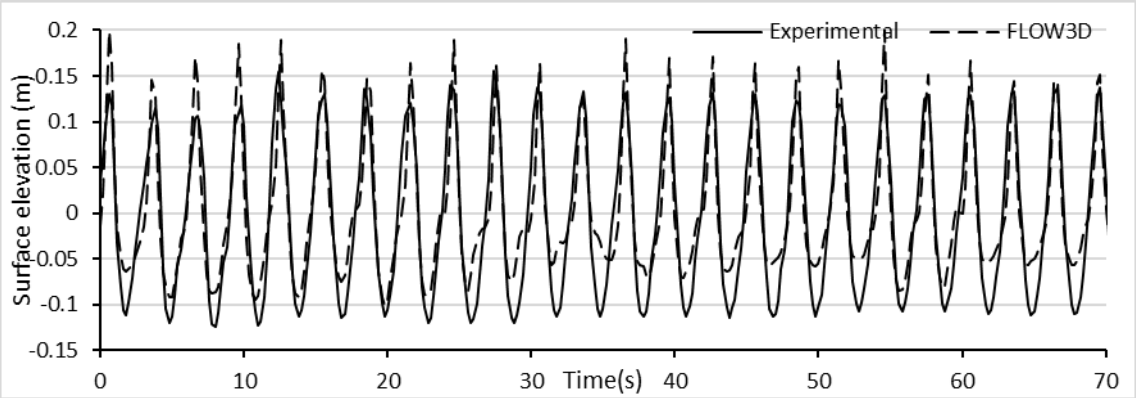

Figure 7.69 Experimental and numerical surface elevations for (RW_H = 0.22 m, T = 3.0 s) at Probes P1 (a) and P2 (b) for the Parabolic Proposition Design.

(a) Probe P1

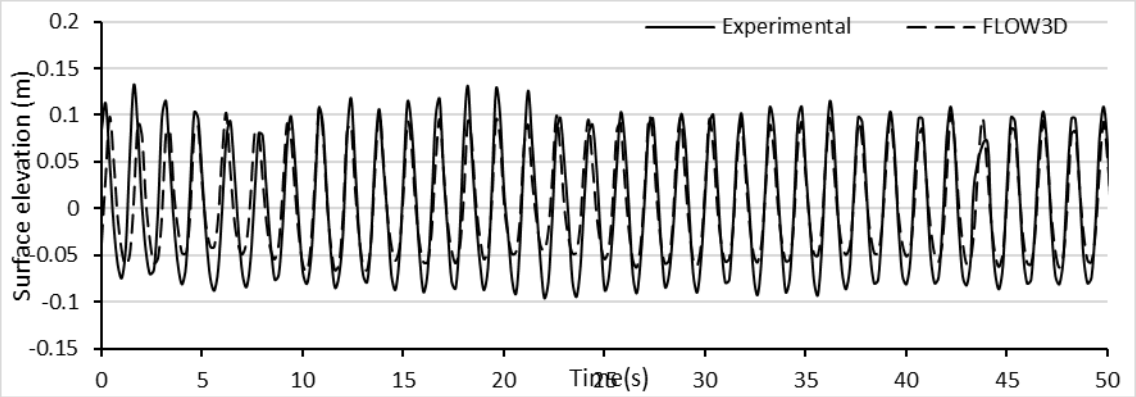

(b) Probe P2

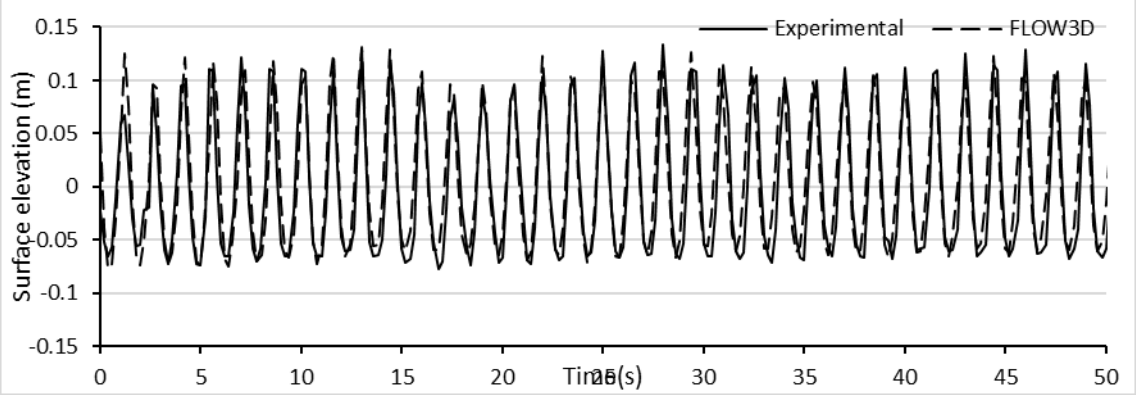

Figure 7.70 Experimental and numerical surface elevations for (RW_H = 0.20 m, T = 1.5 s) at Probes P1 (a) and P2 (b) for the Parabolic Proposition Design.

(a) Probe P1

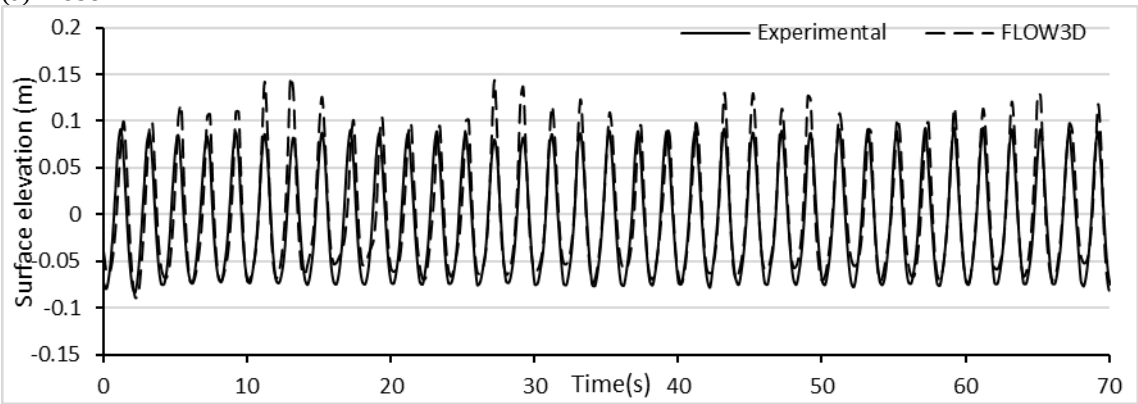

(b) Probe P2

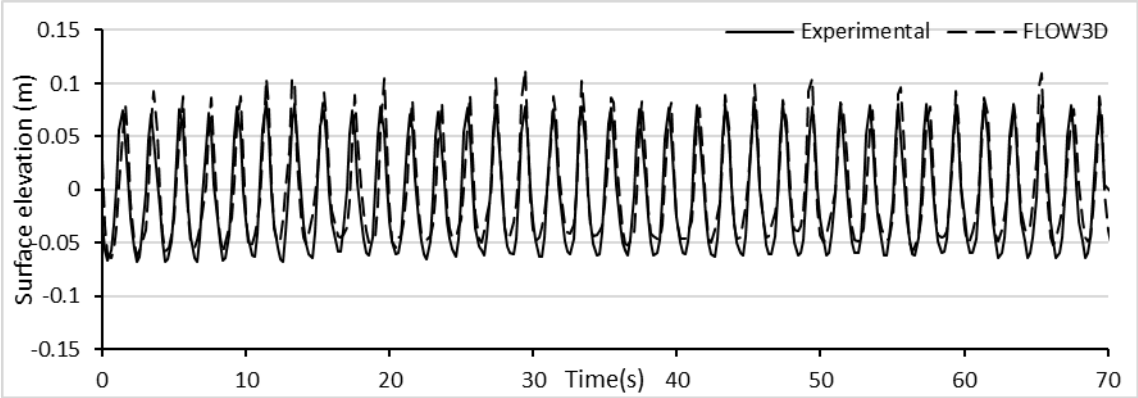

Figure 7.71 Experimental and numerical surface elevations for (RW_H = 0.20 m, T = 2.0 s) at Probes P1 (a) and P2 (b) for the Parabolic Proposition Design

(a) Probe P1

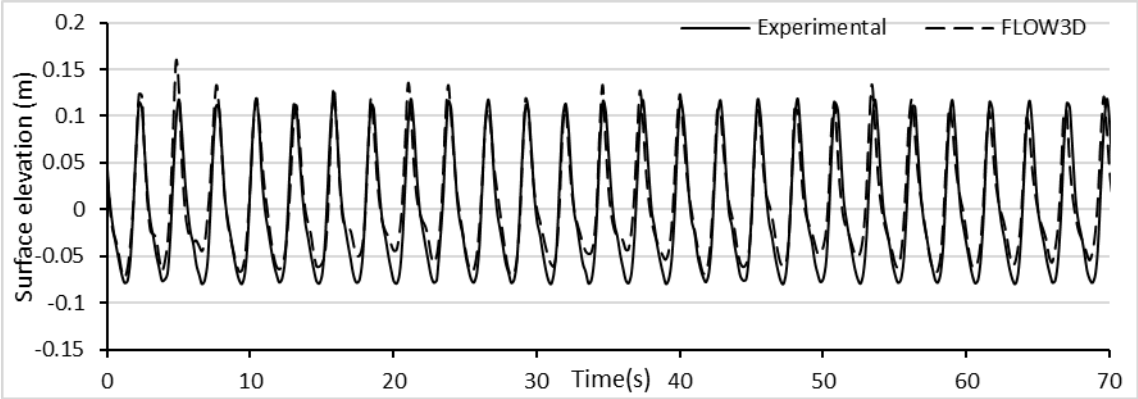

(b) Probe P2

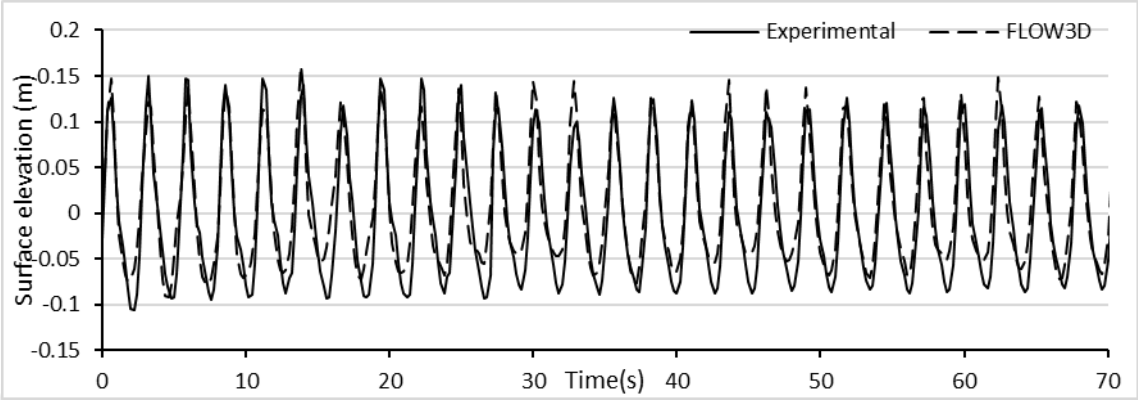

Figure 7.72 Experimental and numerical surface elevations for (RW_H = 0.20 m, T = 2.7 s) at Probes P1 (a) and P2 (b) for the Parabolic Proposition Design

(a) Probe P1

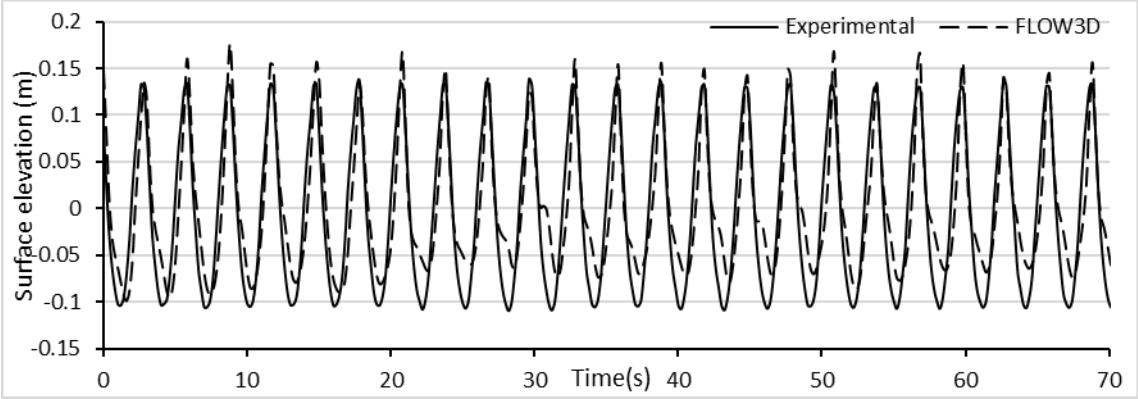

(b) Probe P2

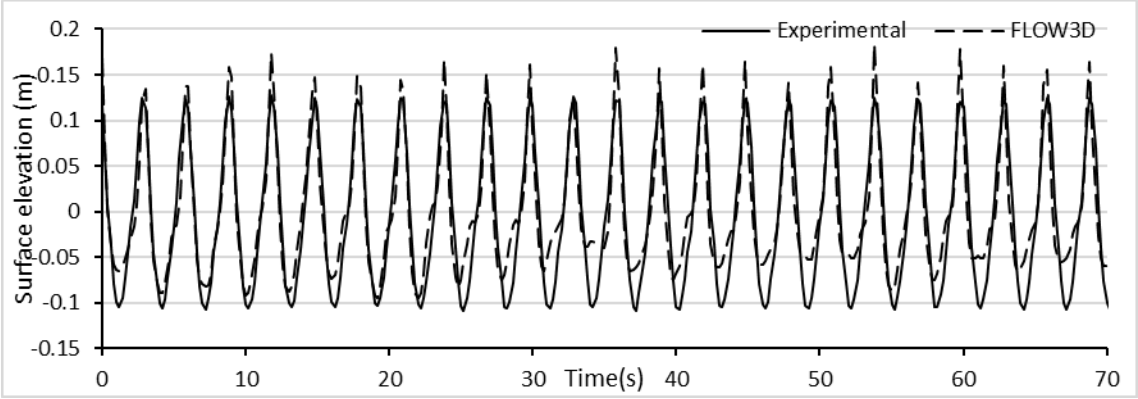

Figure 7.73 Experimental and numerical surface elevations for (RW_H = 0.20 m, T = 3.0 s) at Probes P1 (a) and P2 (b) for the Parabolic Proposition Design.

(a) Probe P1

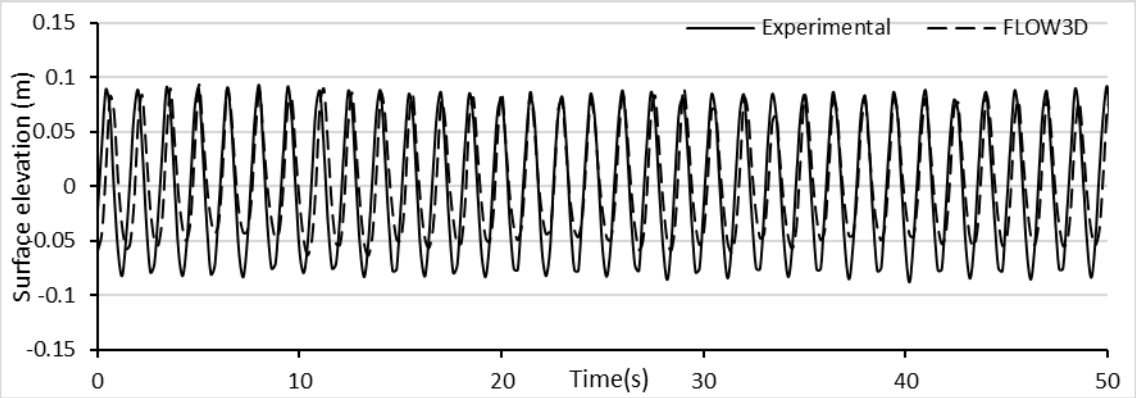

(b) Probe P2

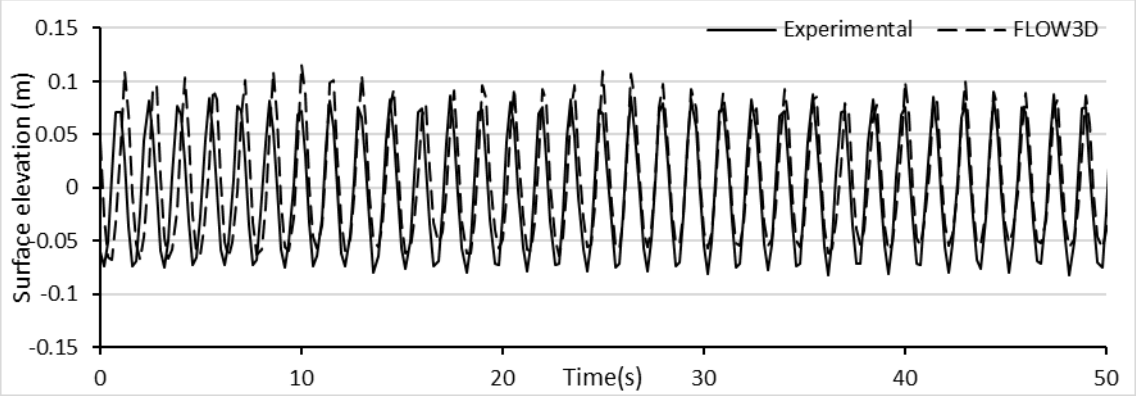

Figure 7.74 Experimental and numerical surface elevations for (RW_H = 0.17 m, T = 1.5 s) at Probes P1 (a) and P2 (b) for the Parabolic Proposition Design.

(a) Probe P1

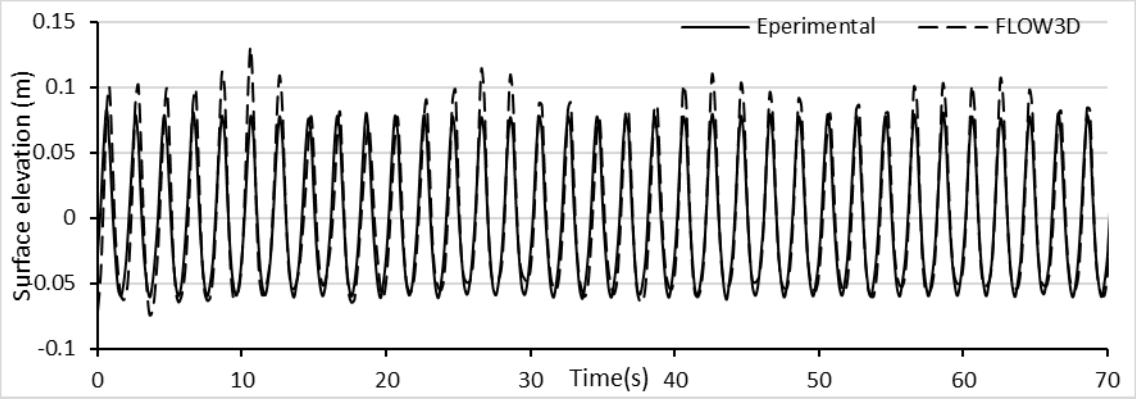

(b) Probe P2

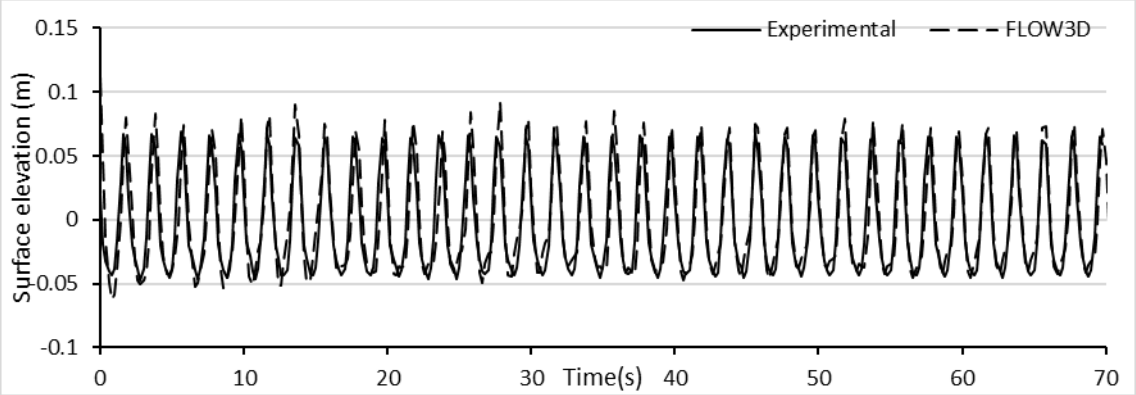

Figure 7.75 Experimental and numerical surface elevations for (RW_H = 0.17 m, T = 2.0 s) at Probes P1 (a) and P2 (b) for the Parabolic Proposition Design.

(a) Probe P1

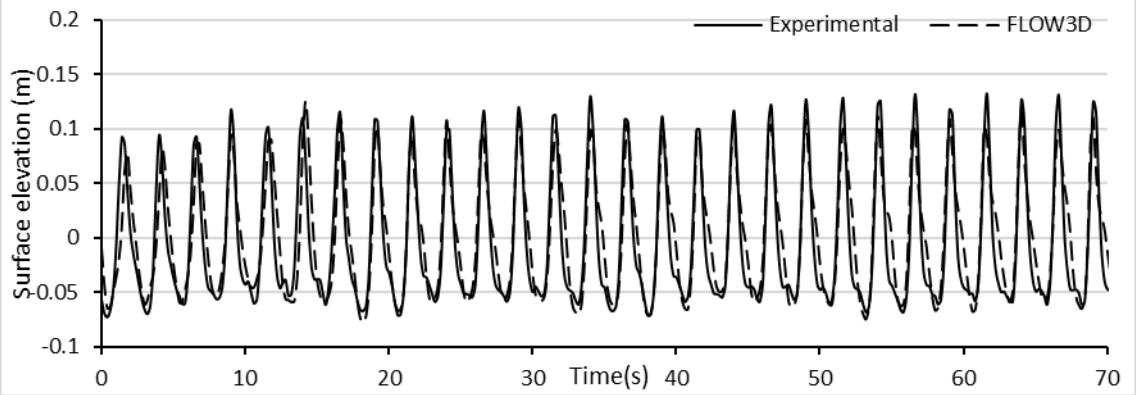

(b) Probe P2

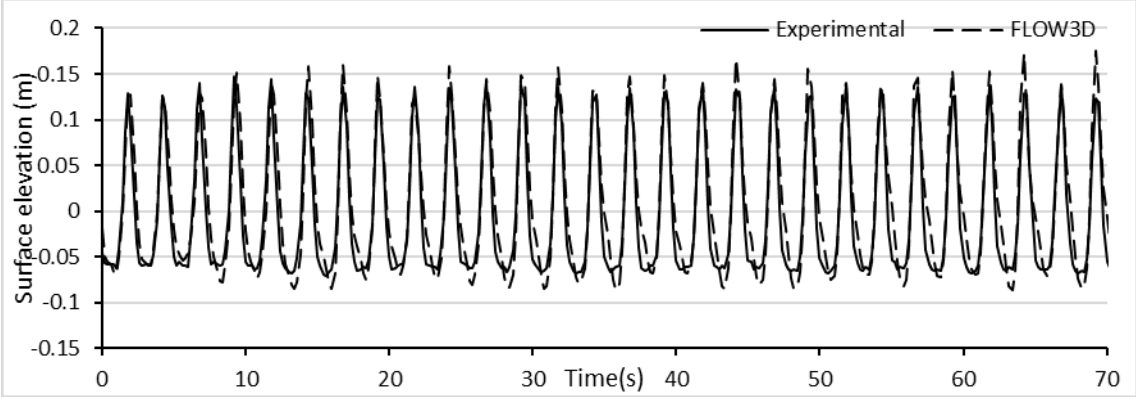

Figure 7.76 Experimental and numerical surface elevations for (RW_H = 0.17 m, T = 2.5 s) at Probes P1 (a) and P2 (b) for the Parabolic Proposition Design.

(a) Probe P1

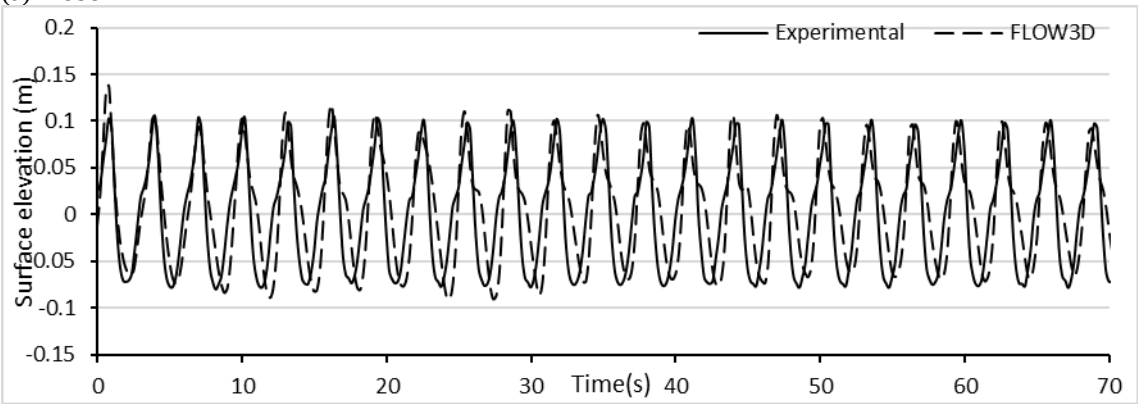

(b) Probe P2

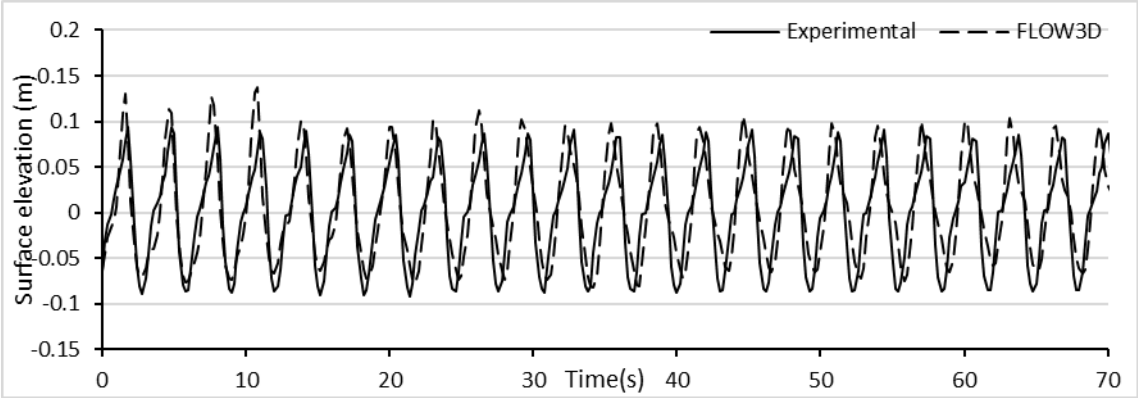

Figure 7.77 Experimental and numerical surface elevations for (RW_H = 0.17 m, T = 3.1 s) at Probes P1 (a) and P2 (b) for the Parabolic Proposition Design.

(a) Probe P1

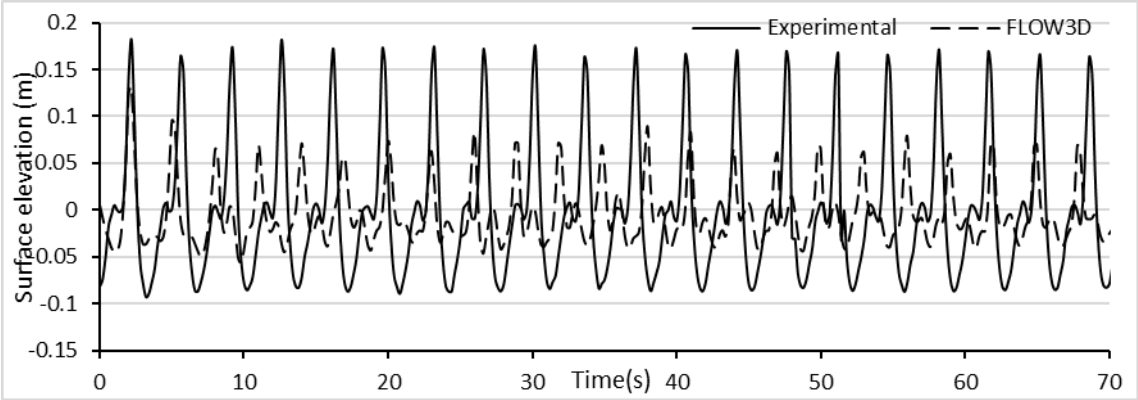

(b) Probe P2

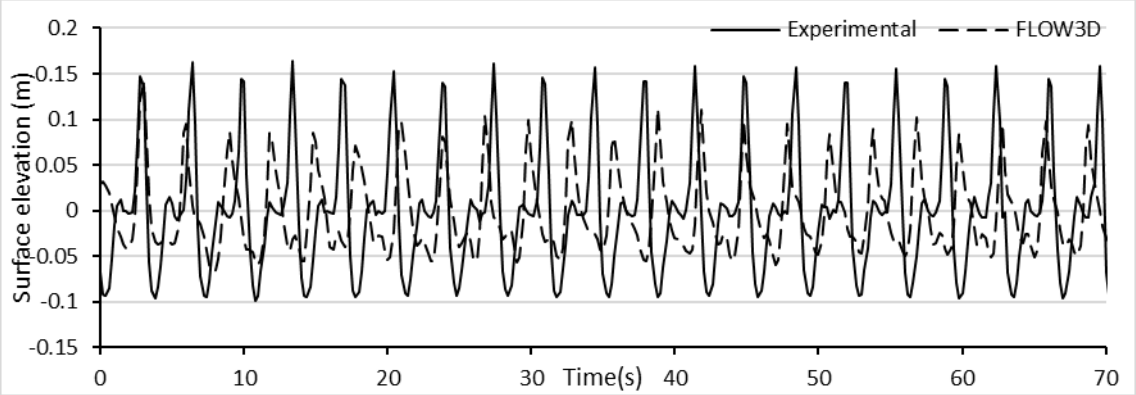

Figure 7.78 Experimental and numerical surface elevations for (RW_H = 0.17 m, T = 3.5 s) at Probes P1 (a) and P2 (b) for the Parabolic Proposition Design.

(a) Probe P1

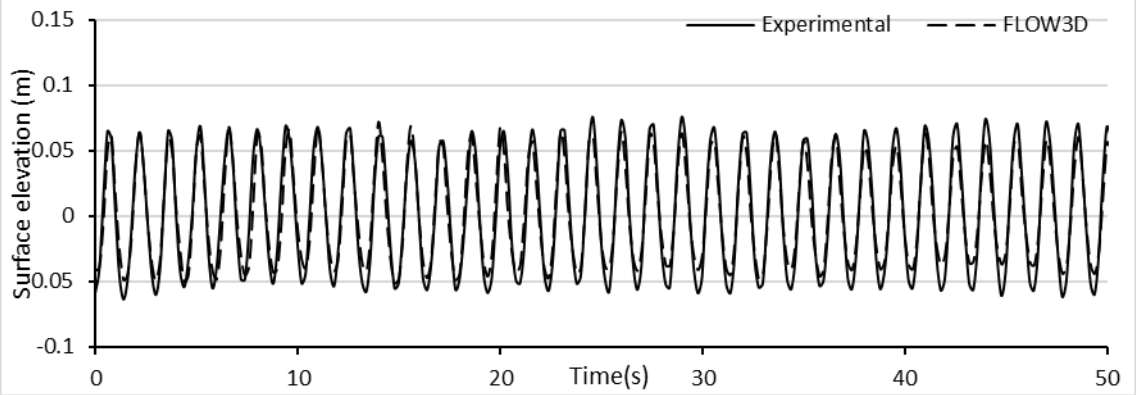

(b) Probe P2

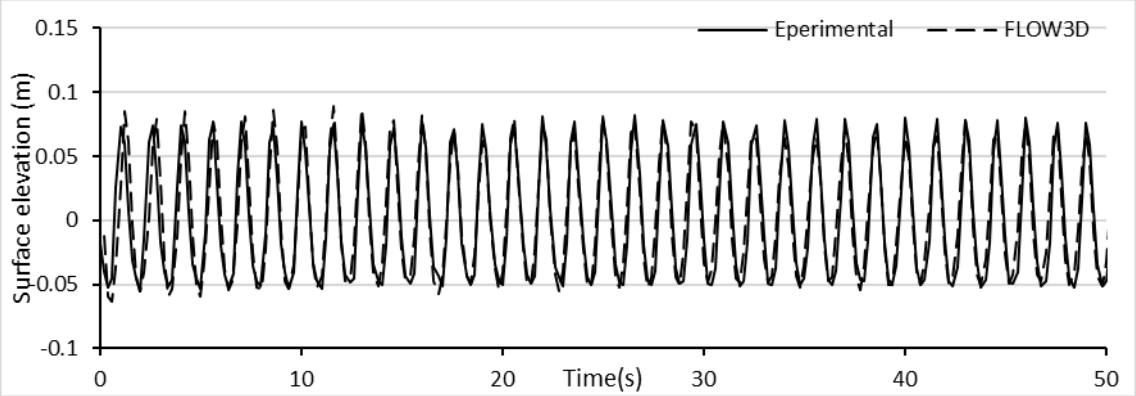

Figure 7.79 Experimental and numerical surface elevations for (RW_H = 0.13 m, T = 1.5 s) at Probes P1 (a) and P2 (b) for the Parabolic Proposition Design.

(a) Probe P1

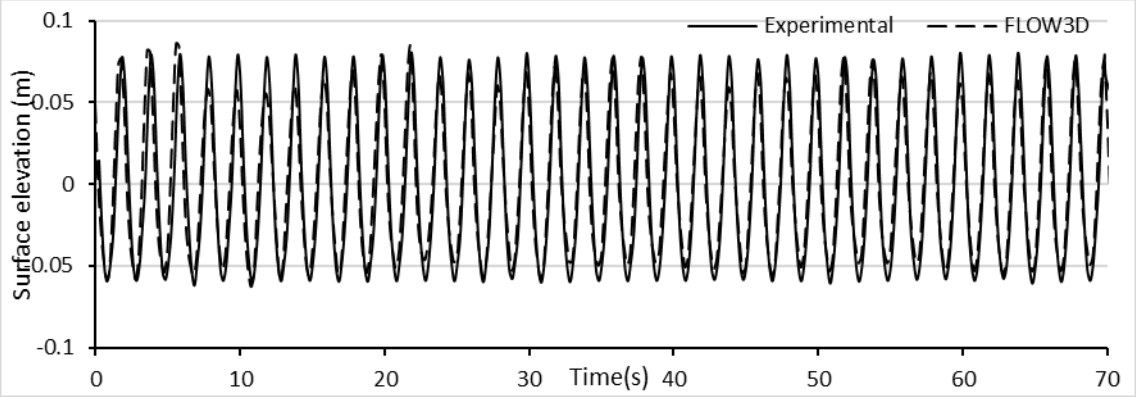

(b) Probe P2

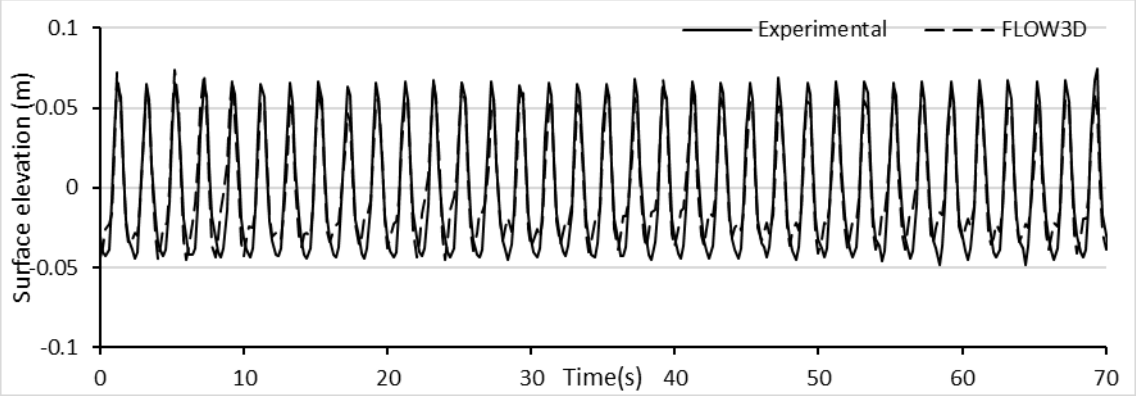

Figure 7.80 Experimental and numerical surface elevations for (RW_H = 0.13 m, T = 2.0 s) at Probes P1 (a) and P2 (b) for the Parabolic Proposition Design.

(a) Probe P1

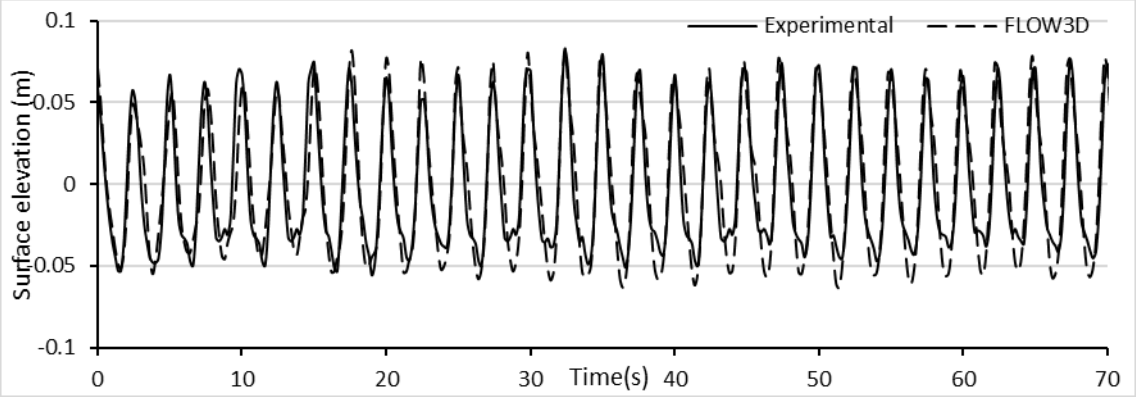

(b) Probe P2

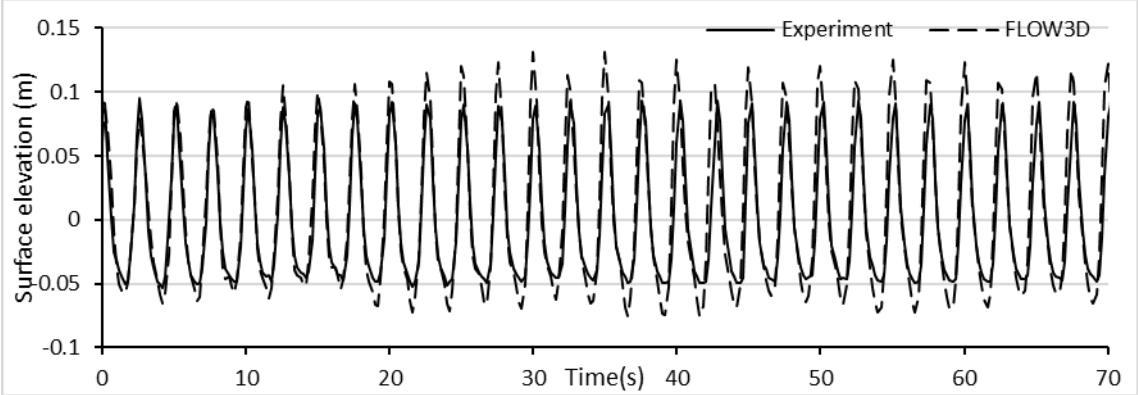

Figure 7.81 Experimental and numerical surface elevations for (RW_H = 0.13 m, T = 2.5 s) at Probes P1 (a) and P2 (b) for the Parabolic Proposition Design.

(a) Probe P1

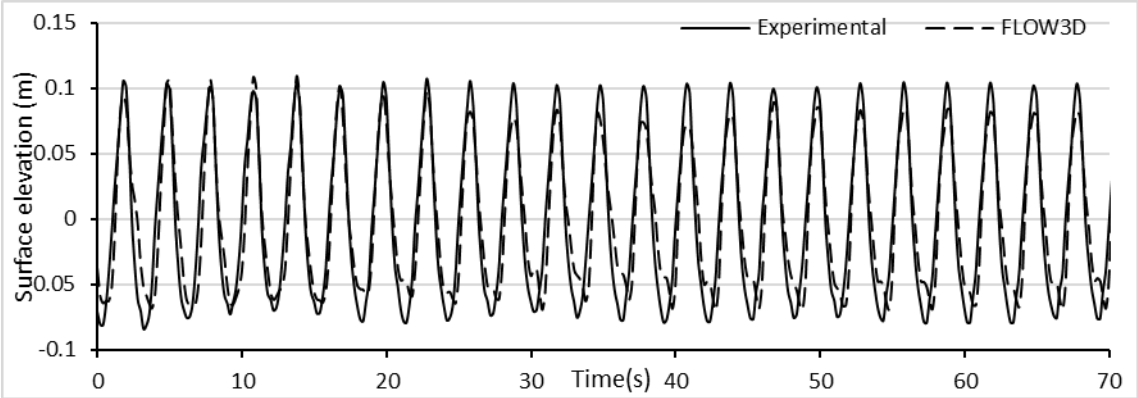

(b) Probe P2

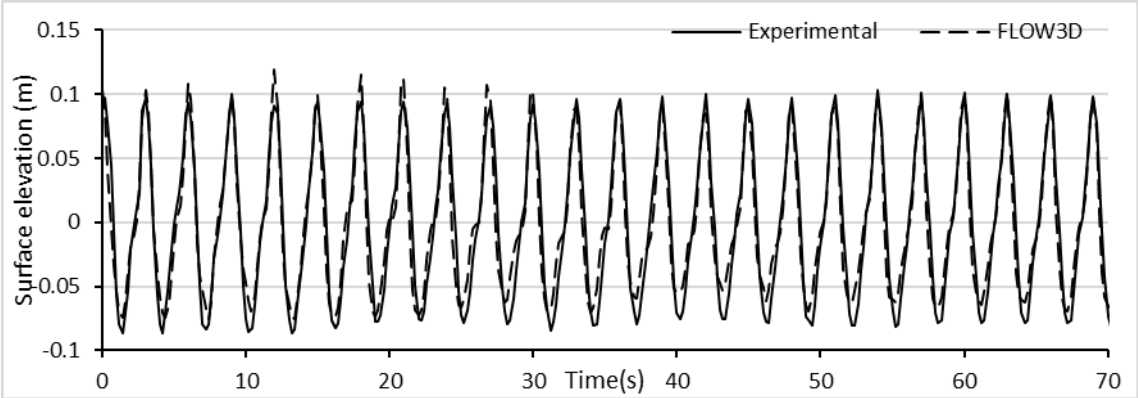

Figure 7.82 Experimental and numerical surface elevations for (RW_H = 0.13 m, T = 3.0 s) at Probes P1 (a) and P2 (b) for the Parabolic Proposition Design.

(a) Probe P1

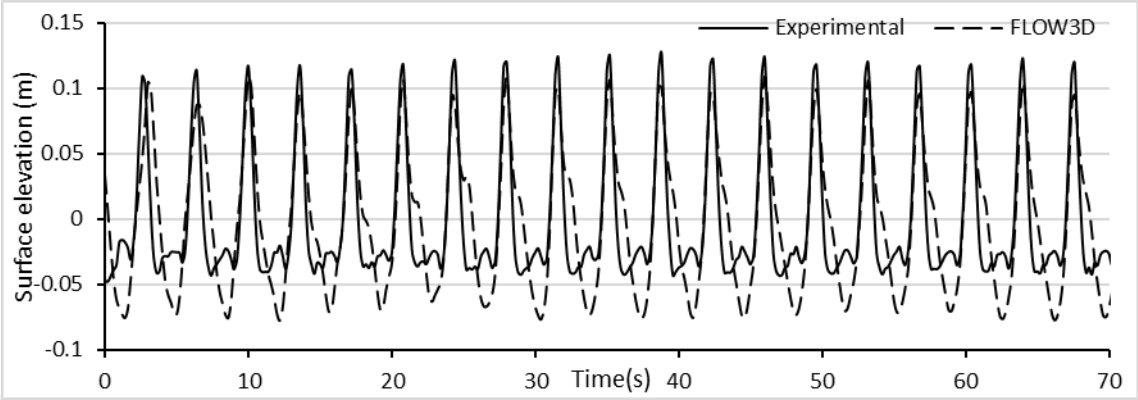

(b) Probe P2

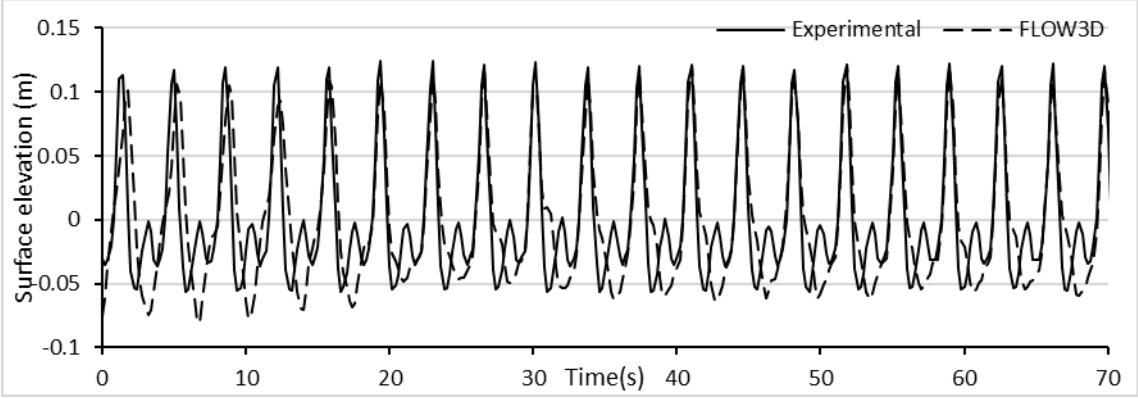

Figure 7.83 Experimental and numerical surface elevations for (RW_H = 0.13 m, T = 3.6 s) at Probes P1 (a) and P2 (b) for the Parabolic Proposition Design.

Table 7.11 summarize the experimental and numerical reflection coefficients of regular waves as a function of wave steepness of the selected propositions.

Table 7.11 Reflection coefficient of regular waves of the selected propositions design.

			Experimental			**Numerical**		
H(m)	**T(s)**	***H/L***	**2slopes**	**3slopes**	**parabolic**	**2slopes**	**3slopes**	**parabolic**
0.25	**1.5**	0.0858	0.1837	0.1264	0.2121	0.2632	0.2028	0.0748
0.25	**2.0**	0.0593	0.0431	0.0707	0.1593	0.0782	0.1169	0.2313
0.25	**2.5**	0.0458	0.1222	0.0851	0.2630	0.1532	0.1827	0.1732
0.22	**1.5**	0.0755	0.1148	0.1114	0.1792	0.2351	0.1353	0.1435
0.22	**2.0**	0.0522	0.0728	0.0719	0.1440	0.1025	0.1114	0.2546
0.22	**2.3**	0.0443	0.0867	0.0694	0.1474	0.1014	0.1075	0.1206
0.22	**2.5**	0.0403	0.1191	0.0927	0.0855	-	-	-
0.22	**3.0**	0.0329	0.0716	0.1054	0.1058	0.1401	0.1252	0.1752
0.20	**1.5**	0.0686	0.1024	0.1018	0.1725	0.3092	0.1995	0.1343
0.20	**2.0**	0.0474	0.0647	0.0737	0.1853	0.1512	0.1096	0.2693
0.20	**2.7**	0.0336	0.1003	0.0606	0.0932	0.1397	0.1367	0.1290
0.20	**3.0**	0.0299	0.0694	0.1171	0.0910	0.1229	0.1252	0.1398
0.17	**1.5**	0.0583	0.1021	0.1021	0.1579	0.2112	0.2188	0.1635
0.17	**2.0**	0.0403	0.0379	0.0554	0.1578	0.0923	0.1662	0.2829
0.17	**2.5**	0.0311	0.1421	0.0758	0.0650	0.1175	0.3285	0.0466
0.17	**3.1**	0.0246	0.0213	0.0575	0.0660	0.1469	0.1841	0.1734
0.17	**3.5**	0.0216	0.0178	0.0825	0.0942	0.1797	0.1653	0.1923
0.13	**1.5**	0.0446	0.0298	0.1230	0.1468	0.1732	0.1779	0.1286
0.13	**2.0**	0.0308	0.0458	0.0485	0.1551	0.0908	0.0871	0.2603
0.13	**2.5**	0.0238	0.0930	0.0610	0.1963	0.0991	0.3458	0.1428
0.13	**3.0**	0.0195	0.0963	0.1054	0.1728	0.1648	0.1054	0.1293
0.13	**3.6**	0.0160	0.0076	0.0589	0.1570	0.1608	0.1041	0.0904

Figure 7.84**,** Figure 7.86**,** and Figure 7.88 show the variations of the experimental and numerical reflection coefficients for regular waves versus wave steepness. The experimental results confirmed that both 2 slope and 3 slope passive absorption systems

are capable of absorbing waves with coefficients of reflection ranging from 4% to 15%, therefore, the numerical reflection coefficient results are between 9% and 25%. On the other hand, the experiments show that the parabolic passive wave proposition is absorbing waves in the range of 8% - 25% and the numerical gives it a range of 7% - 28%.

Scatter plots were generated to compare the experimental and numerical results for regular waves using three propositions: parabolic, 2-slopes, and 3-slopes. Figure 7.85 , Figure 7.87, and Figure 7.89 represents the scatter plots for each proposition include R2 and SI values to evaluate the accuracy of the fit between the experimental and numerical data.

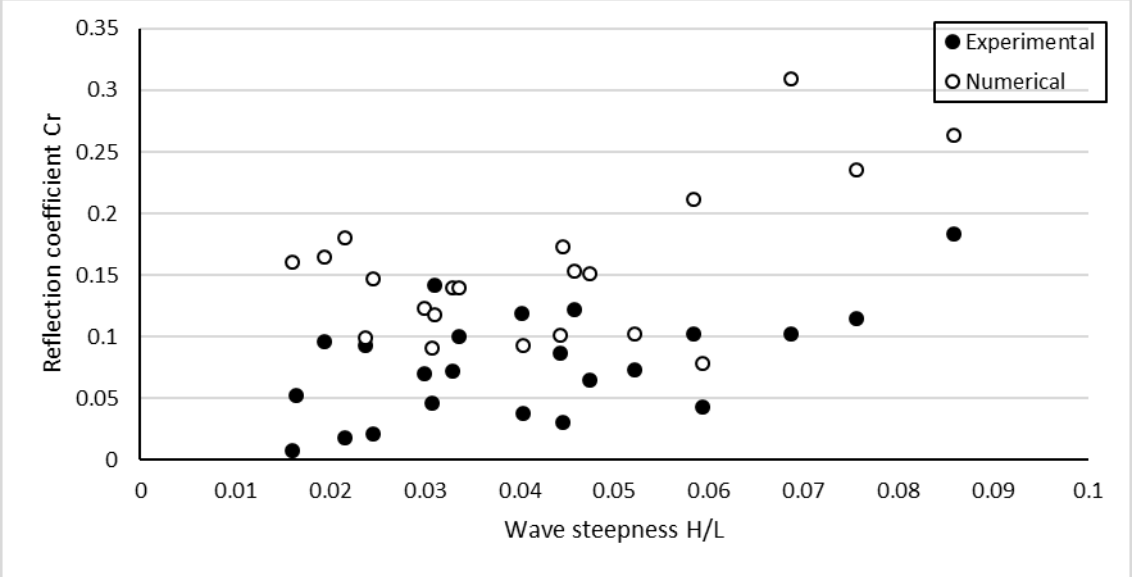

Figure 7.84 Reflection coefficient of the 2-slopes proposition versus wave steepness of the regular waves.

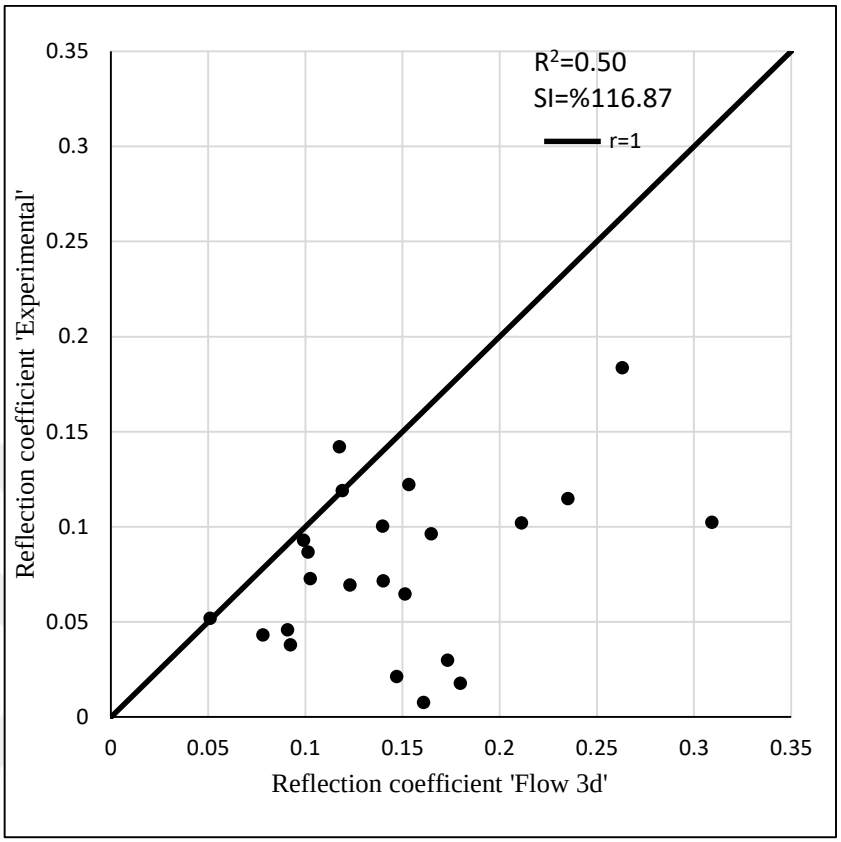

Figure 7.85 Scatter diagram for experimental and numerical results of the 2-slopes proposition of the regular waves with R2 and SI values.

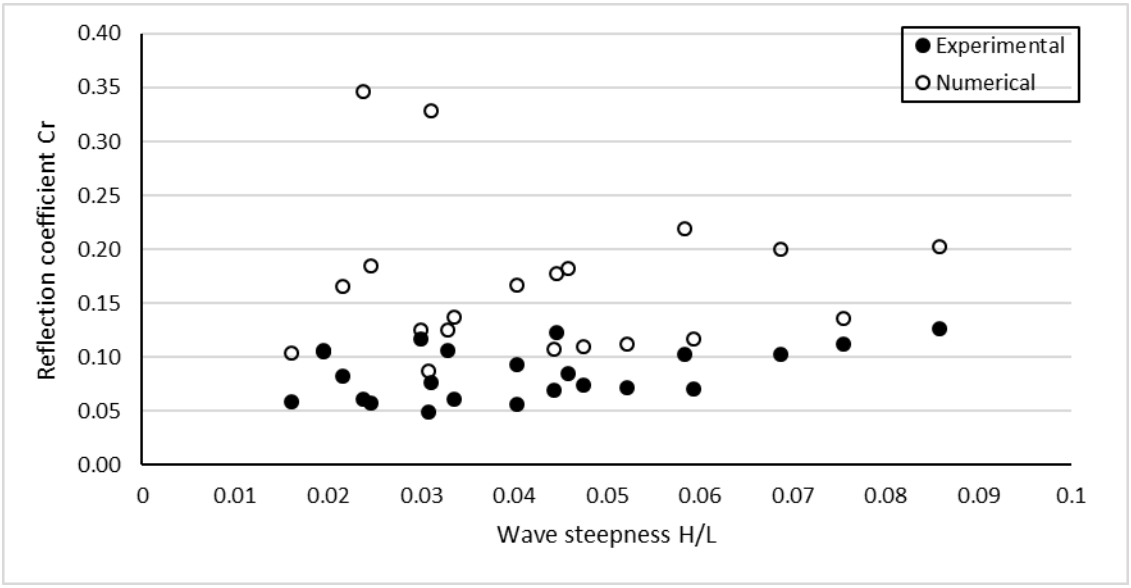

Figure 7.86 Reflection coefficient of the 3-slopes proposition versus wave steepness of the regular waves.

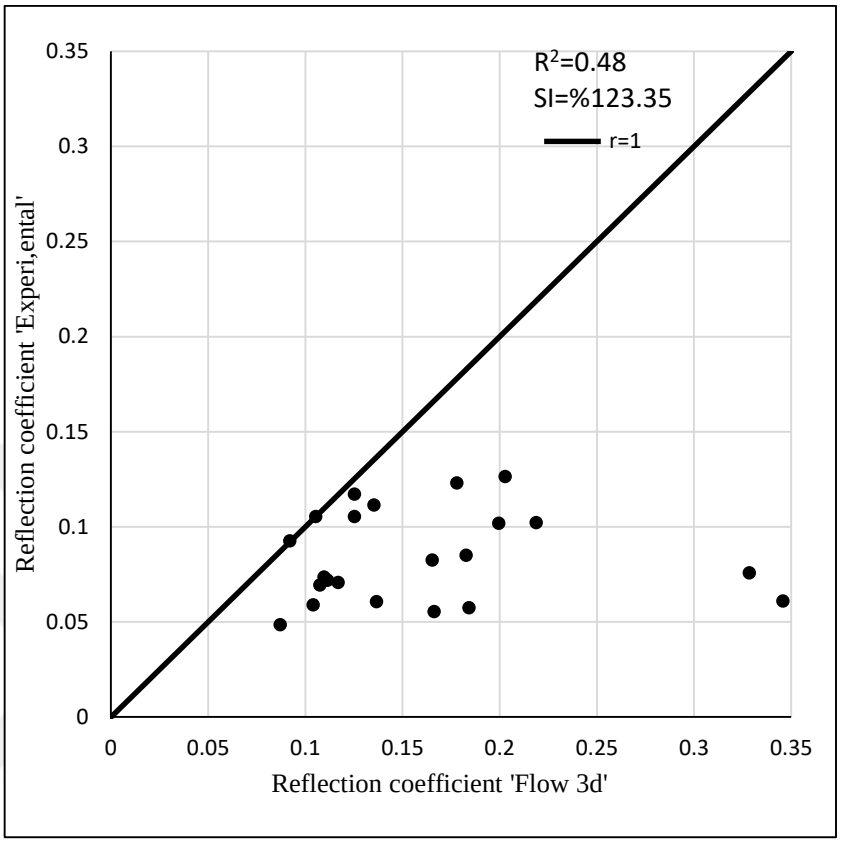

Figure 7.87 Scatter diagram for experimental and numerical results of the 3-slopes proposition of the regular waves with R2 and SI values.

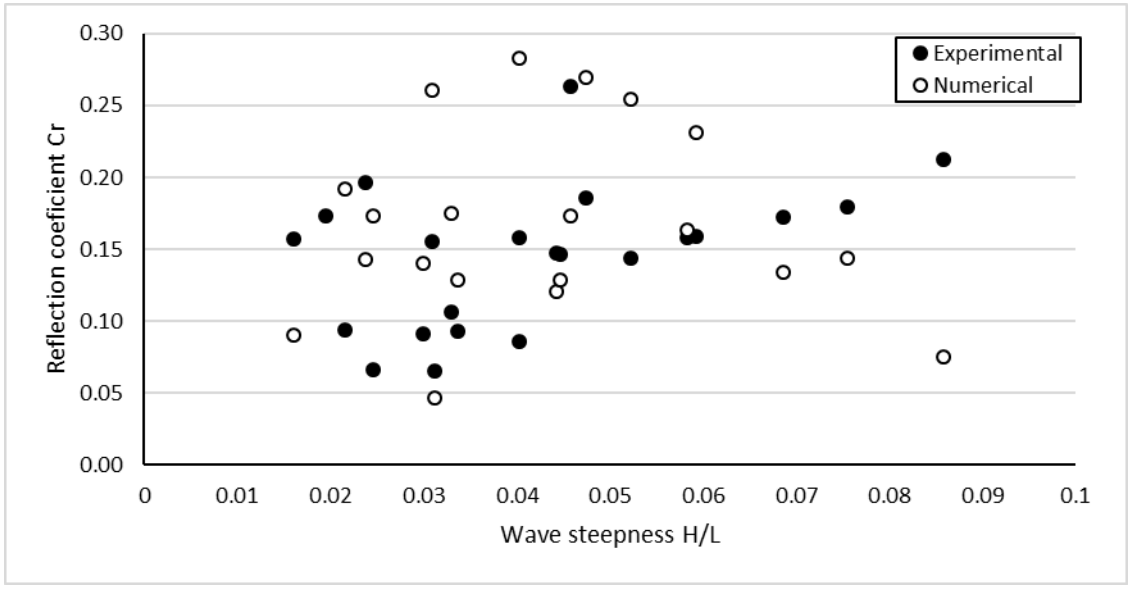

Figure 7.88 Reflection coefficient of the parabolic proposition versus wave steepness of the regular waves.

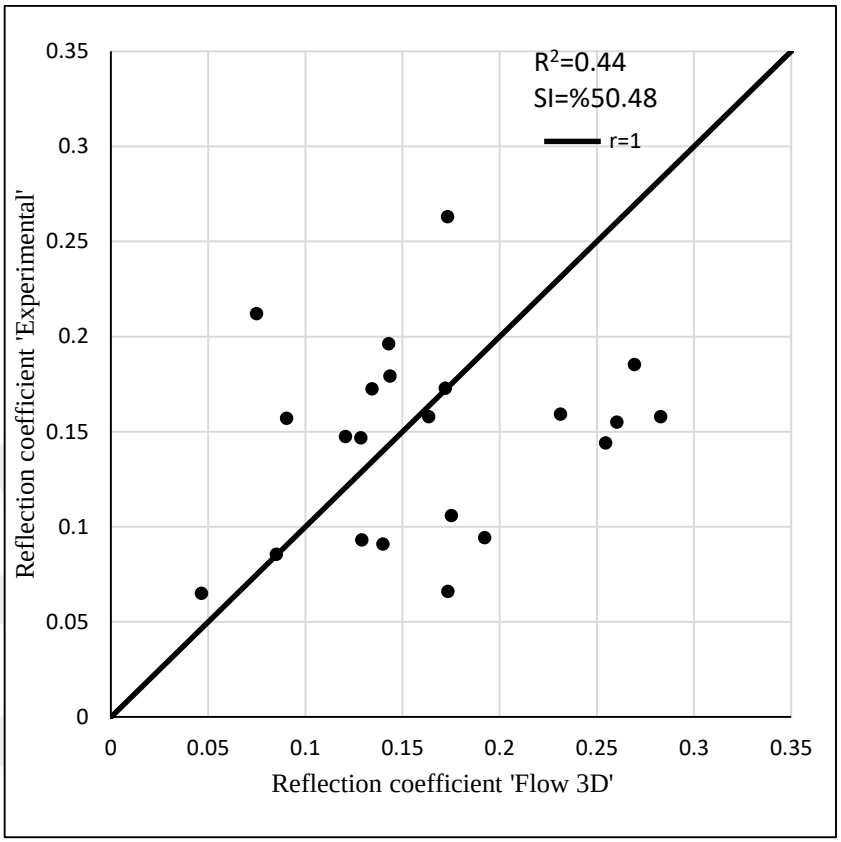

Figure 7.89 Scatter diagram for experimental and numerical results of the parabolic proposition of the regular waves with R^2 and SI values.

Figure 7.90 compare the variation of the experimental reflection coefficients for the three selected propositions. In general, 2-Slopes tend to have lower reflection coefficients compared to 3-Slopes across a range of wave steepness values. This suggests that, for the given conditions, 2-Slopes perform better in reducing wave reflection. The Parabolic proposition consistently has the highest reflection coefficients among the three propositions. This suggests that the Parabolic proposition may have a shorter effective length for reducing wave reflection when dealing with incident waves of long wavelength.

APPENDIX A depict the wave absorber propositions being tested in the case of the regular waves.

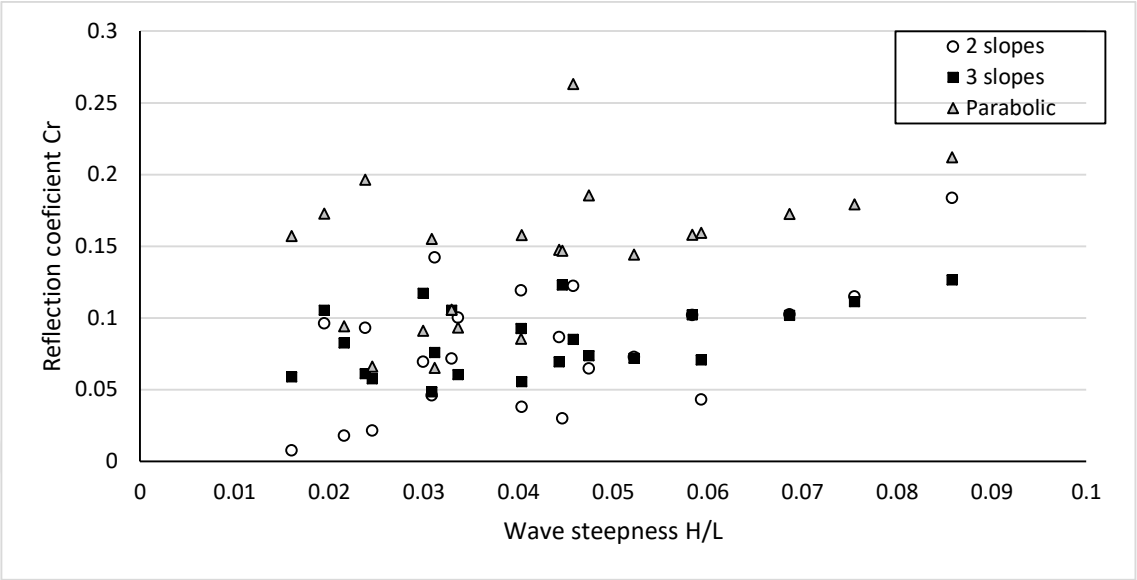

Figure 7.90 The experimental reflection coefficient of the selected propositions versus wave steepness of the regular waves.

7.2.1.2 Irregular waves

Table 7.12, Table 7.13**,** and Table 7.14 shows the variation of the experimental and numerical reflection coefficients for irregular waves. The experimental findings verified that the three passive absorption systems proposed can absorb waves with Cr < 10% coefficients of reflection.

Table 7.12 Reflection coefficient of irregular waves of the 3-slopes proposition design.

		Experimental			**Numerical**		
H_s**(m)**	T_s**(s)**	E_I	E_R	C_r	E_I	E_R	C_r
0.25	**2**	0.1603	0.1673	0.0216	0.2231	0.2267	0.0080
0.22	**2.3**	0.2562	0.2448	0.0225	0.2167	0.2098	0.0160
0.20	**2.7**	0.2122	0.2015	0.0255	0.1849	0.1728	0.0332
0.17	**3.1**	0.1508	0.1644	0.0441	0.2000	0.1874	0.0320
0.13	**3.6**	0.1069	0.1196	0.0577	0.1332	0.1406	0.0274

Figure 7.91 to Figure 7.95 depict the experimental and numerical surface elevations at probe P1 and P2 of the 3-slopes proposition design under non-breaking irregular wave conditions.

(a) Probe P1

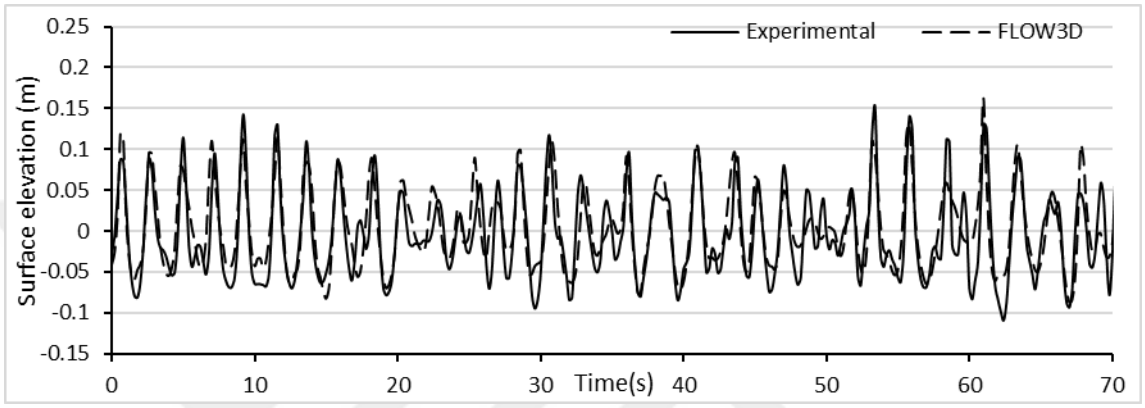

(b) Probe P2

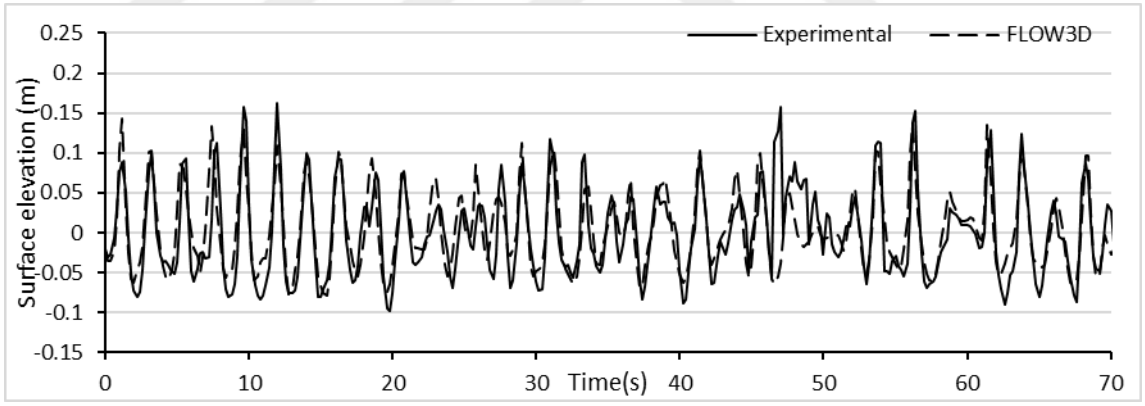

Figure 7.91 Experimental and numerical surface elevations for (IRW_H_s = 0.25 m, T_s = 2.0 s) at Probes P1 (a) and P2 (b) for the 3-Slope Proposition Design.

(a) Probe P1

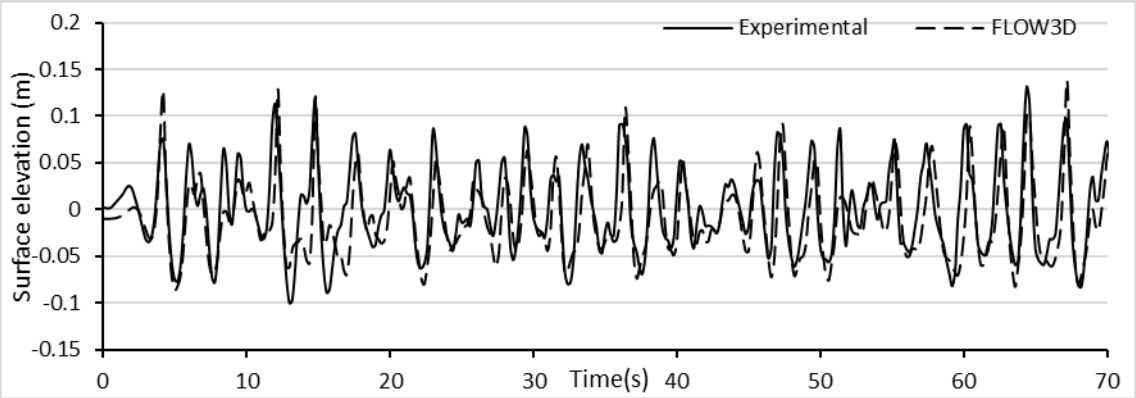

(b) Probe P2

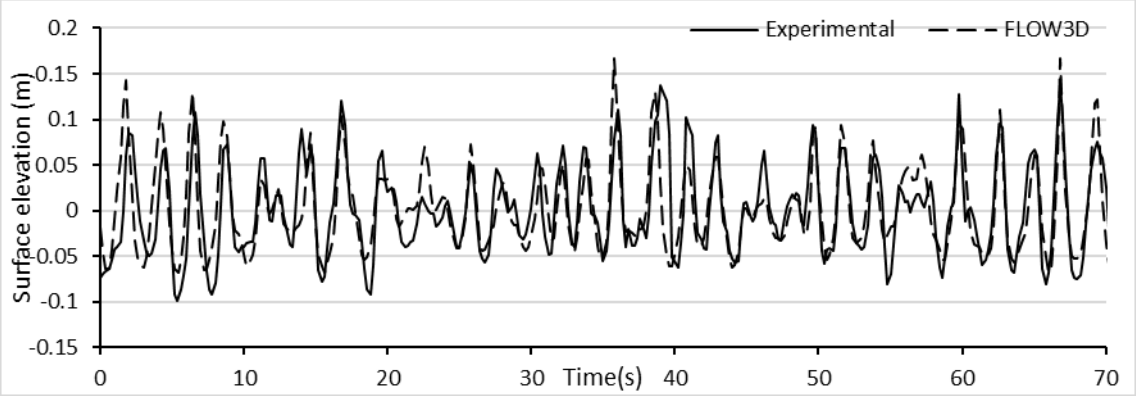

Figure 7.92 Experimental and numerical surface elevations for (IRW_H_s = 0.22 m, T_s = 2.3 s) at Probes P1 (a) and P2 (b) for the 3-Slope Proposition Design.

(a) Probe P1

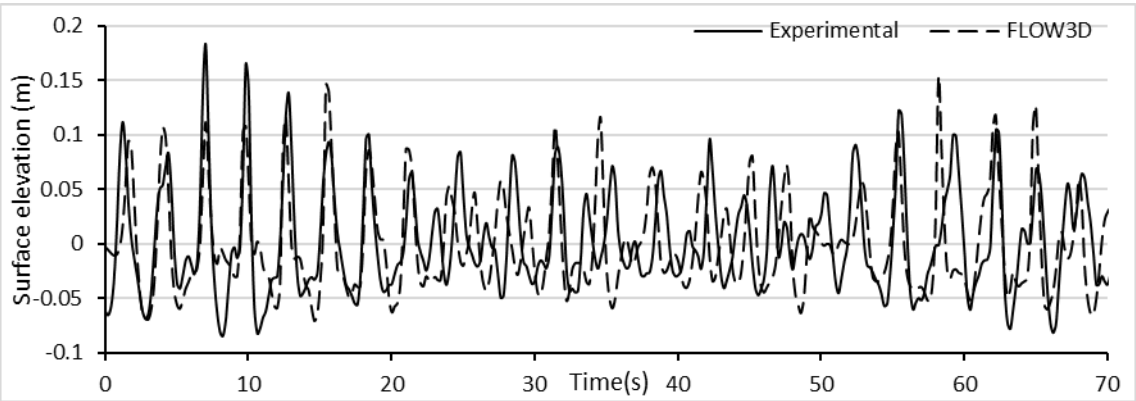

(b) Probe P2

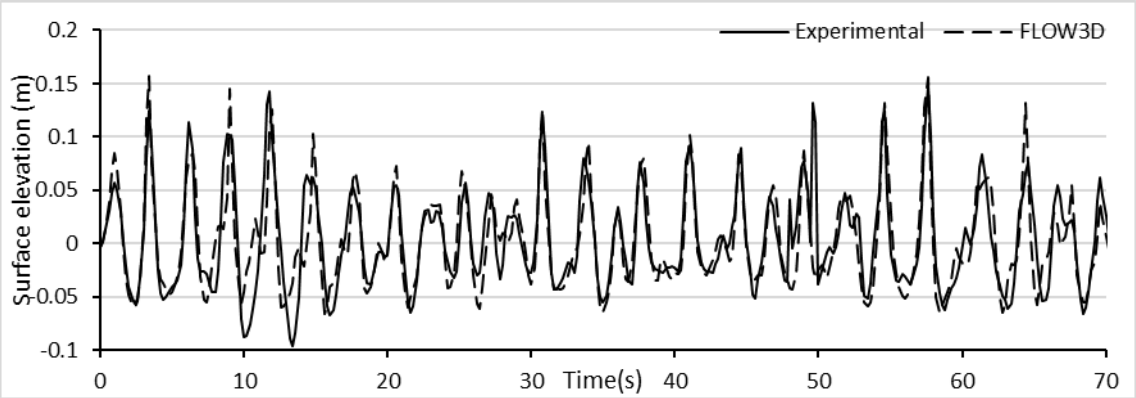

Figure 7.93 Experimental and numerical surface elevations for (IRW_H_s = 0.20 m, T_s = 2.7 s) at Probes P1 (a) and P2 (b) for the 3-Slope Proposition Design.

(a) Probe P1

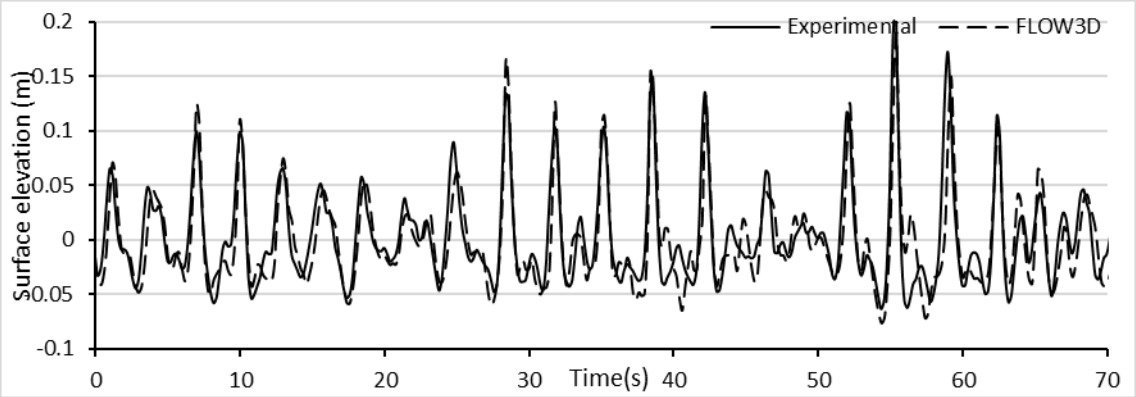

(b) Probe P2

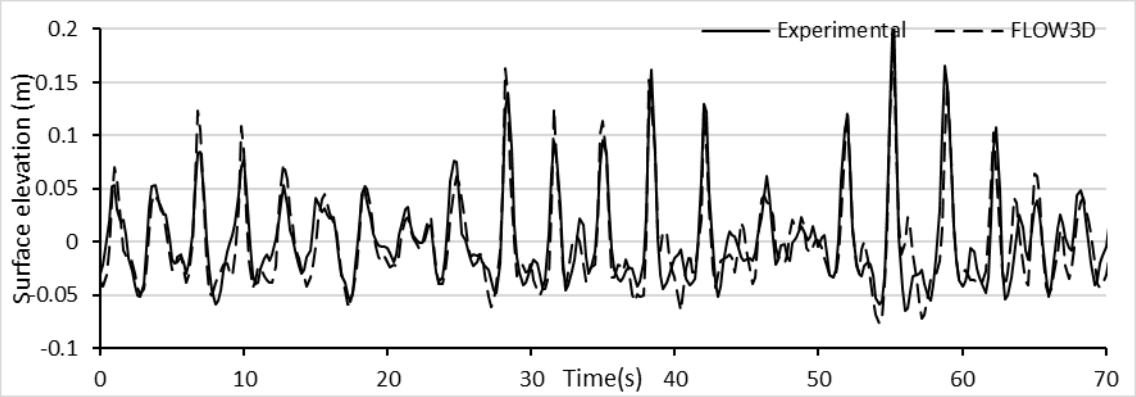

Figure 7.94 Experimental and numerical surface elevations for (IRW_H_s = 0.17 m, T_s = 3.1 s) at Probes P1 (a) and P2 (b) for the 3-Slope Proposition Design.

(a) Probe P1

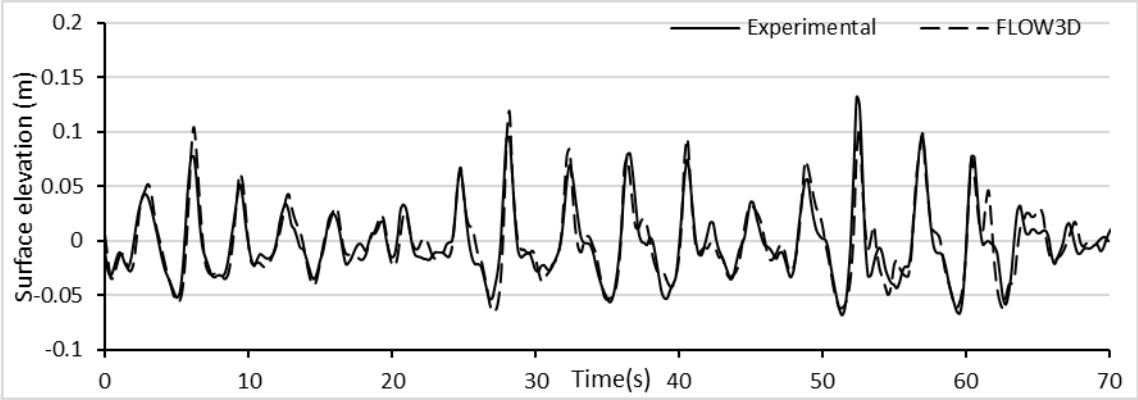

(b) Probe P2

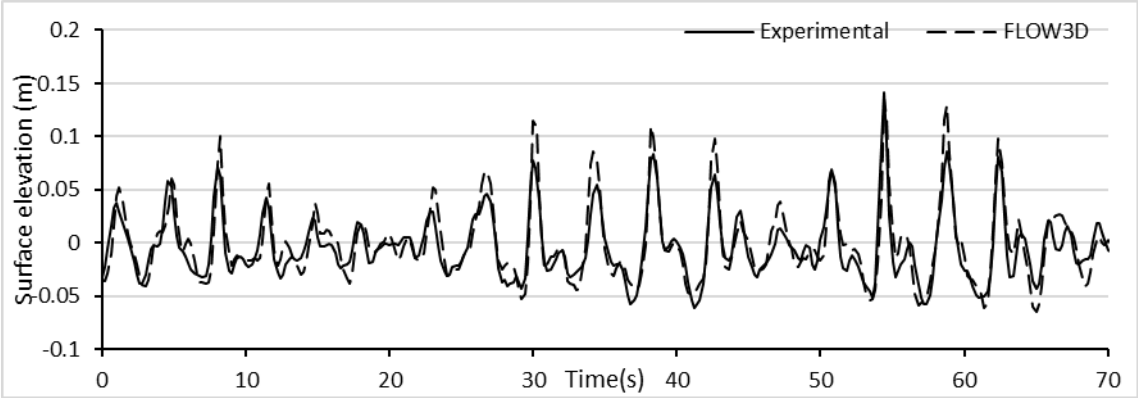

Figure 7.95 Experimental and numerical surface elevations for (IRW_H_s = 0.13 m, T_s = 3.6 s) at Probes P1 (a) and P2 (b) for the 3-Slope Proposition Design.

Table 7.13 Reflection coefficient of irregular waves of the 2-slopes proposition design.

		Experimental			**Numerical**		
H_s**(m)**	T_s**(s)**	E_I	E_R	C_r	E_I	E_R	C_r
0.25	**2**	0.2948	0.2752	0.0338	0.2877	0.2959	0.0141
0.22	**2.3**	0.2143	0.2307	0.0375	0.1603	0.1673	0.0216
0.20	**2.7**	0.1820	0.1945	0.0337	0.1479	0.1329	0.0520
0.17	**3.1**	0.1970	0.1834	0.0351	0.1318	0.1255	0.0241
0.13	**3.6**	0.0738	0.0679	0.0408	0.058	0.0645	0.0545

Figure 7.96 to Figure 7.100 depict the experimental and numerical surface elevations at probe P1 and P2 of the 2-slopes proposition design under non-breaking irregular wave conditions.

(a) Probe P1

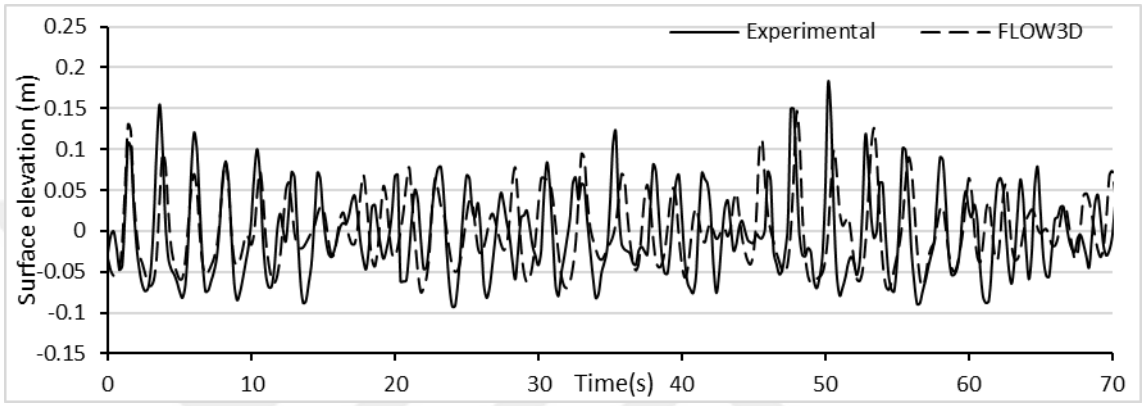

(b) Probe P2

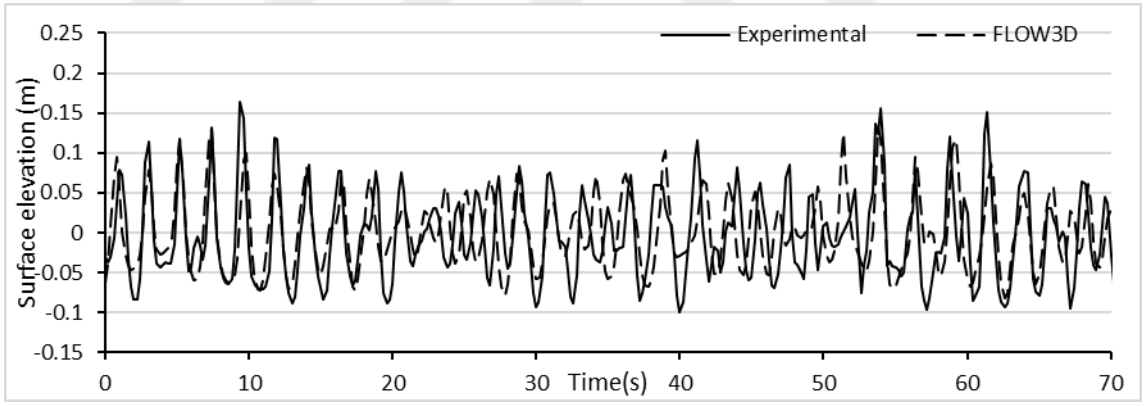

Figure 7.96 Experimental and numerical surface elevations for (IRW_H_s = 0.25 m, T_s = 2.0 s) at Probes P1 (a) and P2 (b) for the 2-Slope Proposition Design.

(a) Probe P1

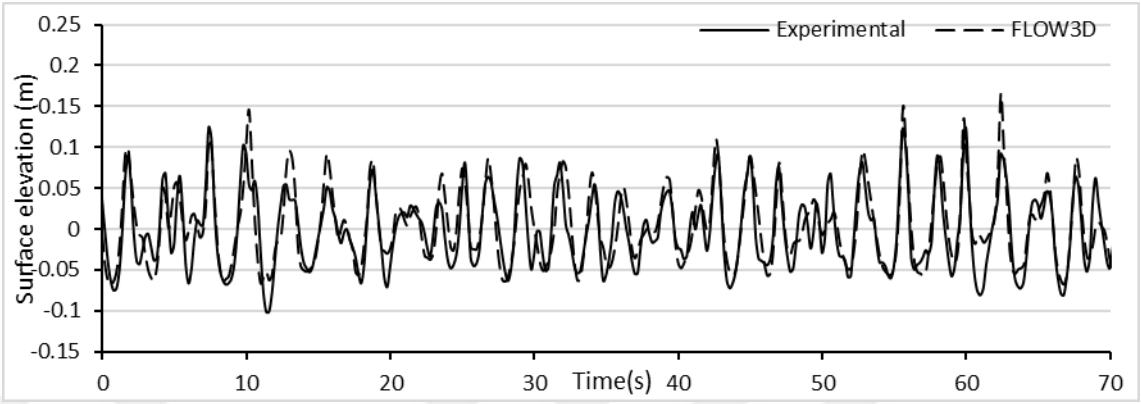

(b) Probe P2

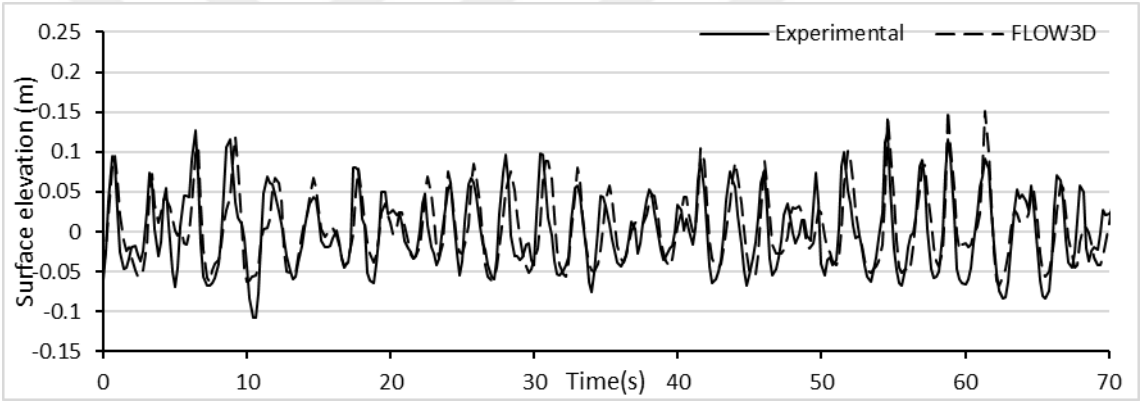

Figure 7.97 Experimental and numerical surface elevations for (IRW_H_s = 0.22 m, T_s = 2.3 s) at Probes P1 (a) and P2 (b) for the 2-Slope Proposition Design.

(a) Probe P1

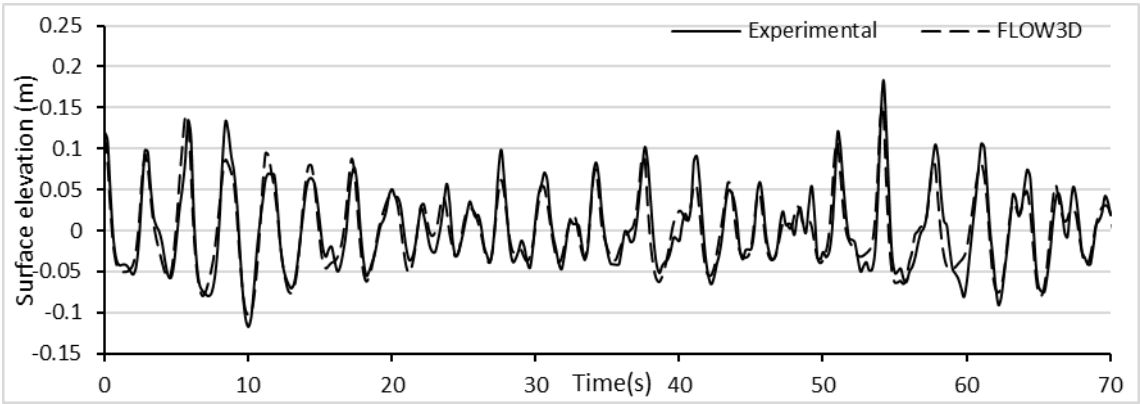

(b) Probe P2

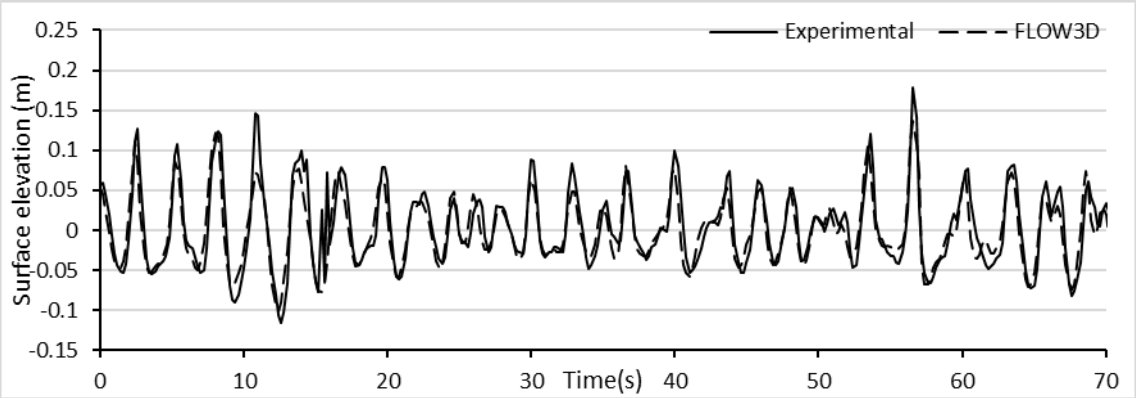

Figure 7.98 Experimental and numerical surface elevations for (IRW_H_s = 0.20 m, T_s = 2.7 s) at Probes P1 (a) and P2 (b) for the 2-Slope Proposition Design.

(a) Probe P1

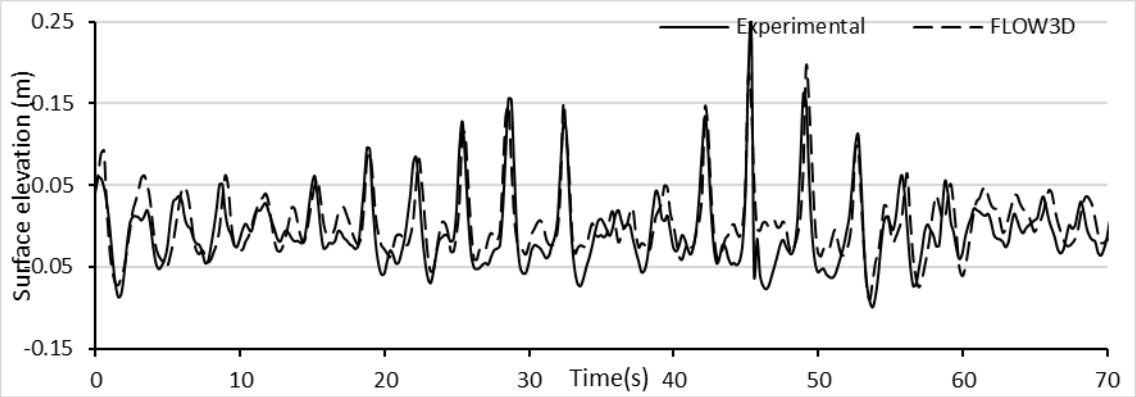

(b) Probe P2

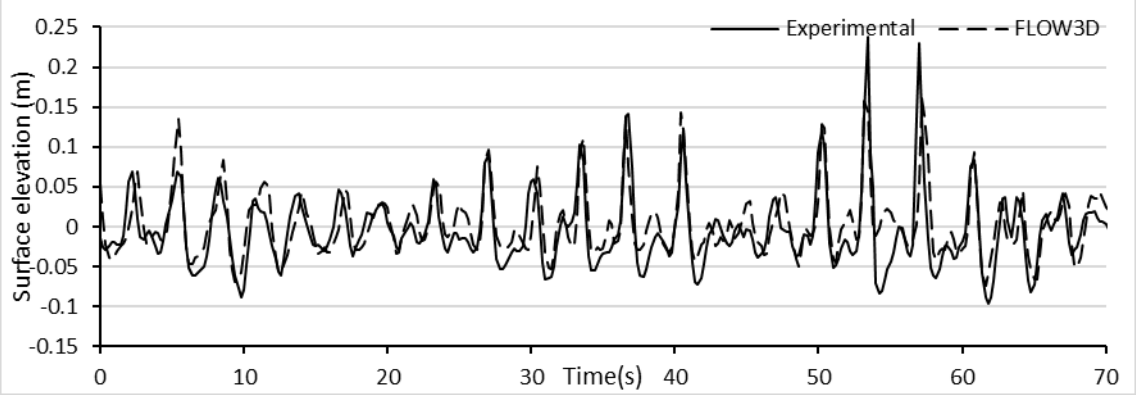

Figure 7.99 Experimental and numerical surface elevations for (IRW_H_s = 0.17 m, T_s = 3.1 s) at Probes P1 (a) and P2 (b) for the 2-Slope Proposition Design.

(a) Probe P1

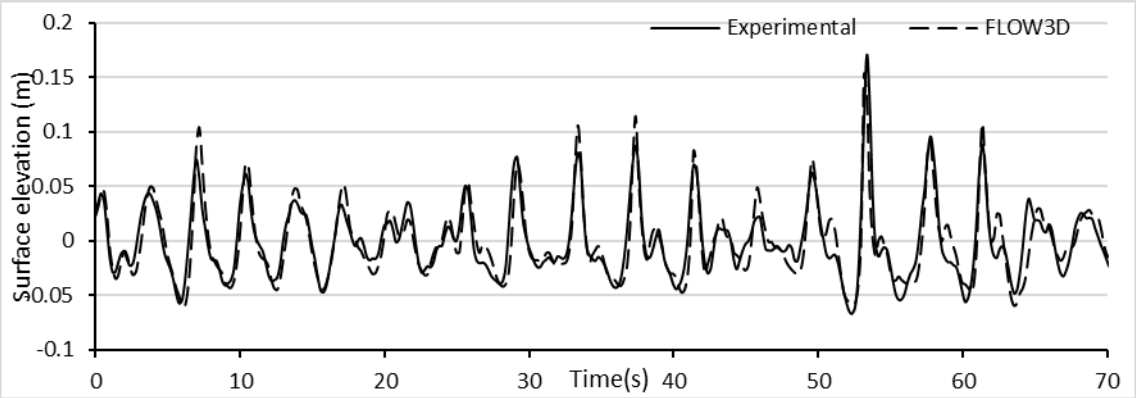

(b) Probe P2

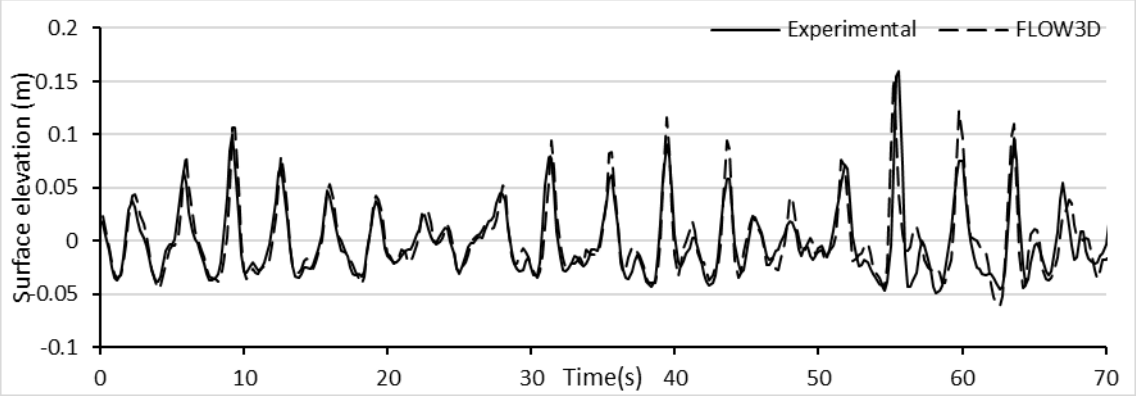

Figure 7.100 Experimental and numerical surface elevations for (IRW_H_s = 0.13 m, T_s = 3.6 s) at Probes P1 (a) and P2 (b) for the 2-Slope Proposition Design.

Table 7.14 Reflection coefficient of irregular waves of the parabolic proposition design.

		Experimental			**Numerical**		
H_s**(m)**	T_s**(s)**	E_I	E_R	C_r	E_I	E_R	C_r
0.25	**2**	0.3311	0.2937	0.0581	0.2299	0.2584	0.0601
0.22	**2.3**	0.2694	0.2811	0.0214	0.2394	0.2448	0.0112
0.20	**2.7**	0.2443	0.2593	0.0302	0.2568	0.2788	0.0419
0.17	**3.1**	0.2043	0.1862	0.0453	0.2656	0.2390	0.0513
0.13	**3.6**	0.1276	0.1122	0.0622	0.1423	0.1250	0.0627

Figure 7.101 to Figure 7.105 depict the experimental and numerical surface elevations at probe P1 and P2 of the parabolic proposition design under non-breaking irregular wave conditions.

(a) Probe P1

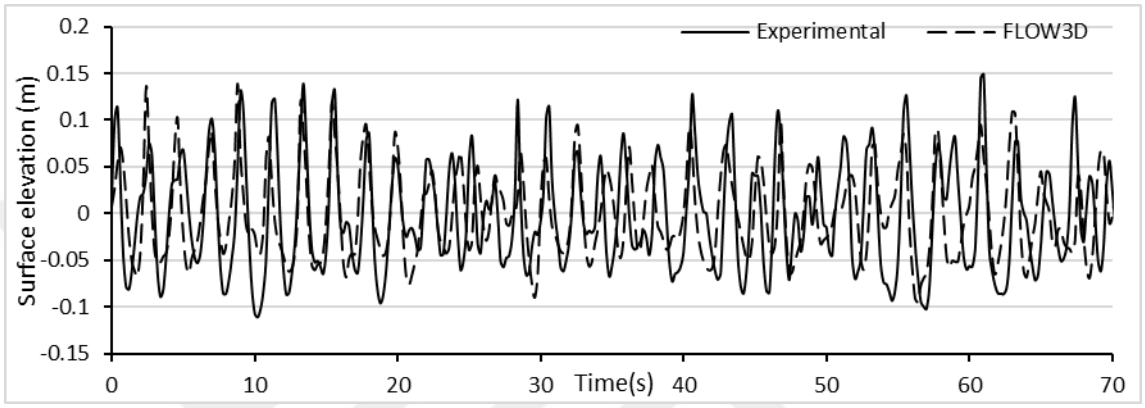

(b) Probe P2

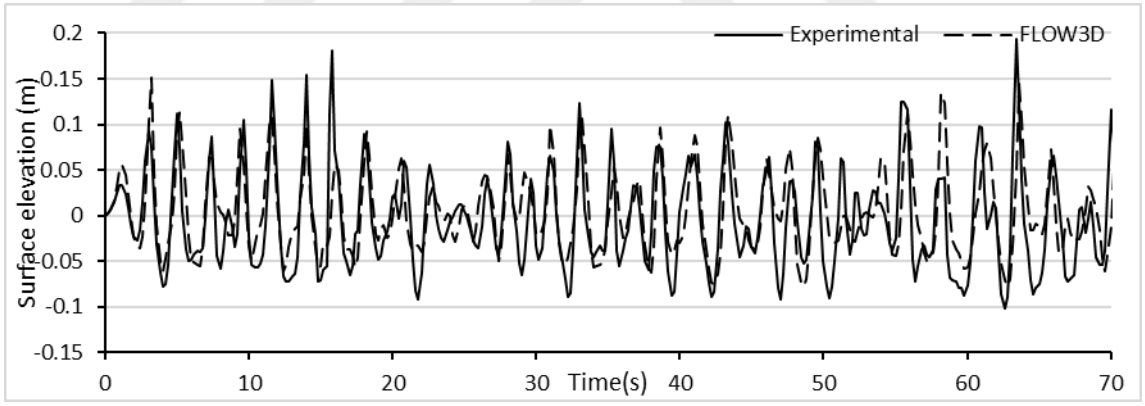

Figure 7.101 Experimental and numerical surface elevations for (IRW_H_s = 0.25 m, T_s = 2.0 s) at Probes P1 (a) and P2 (b) for the Parabolic Proposition Design.

(a) Probe P1

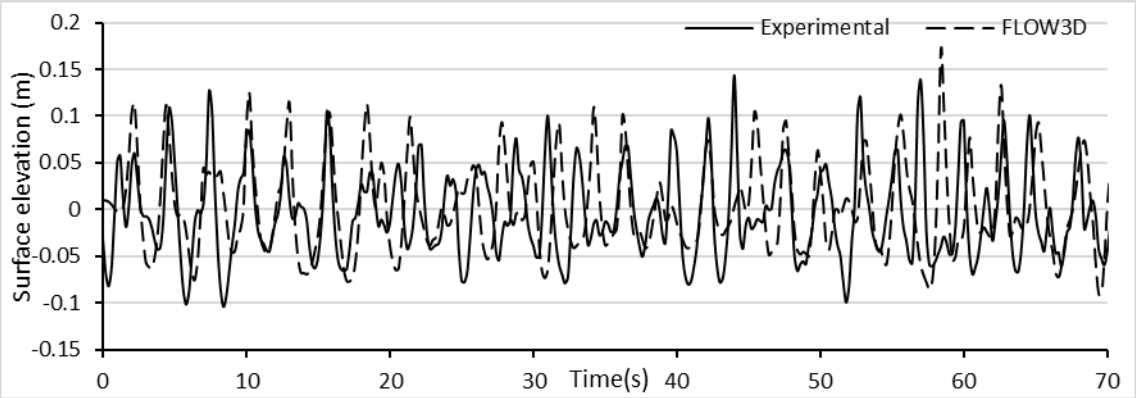

(b) Probe P2

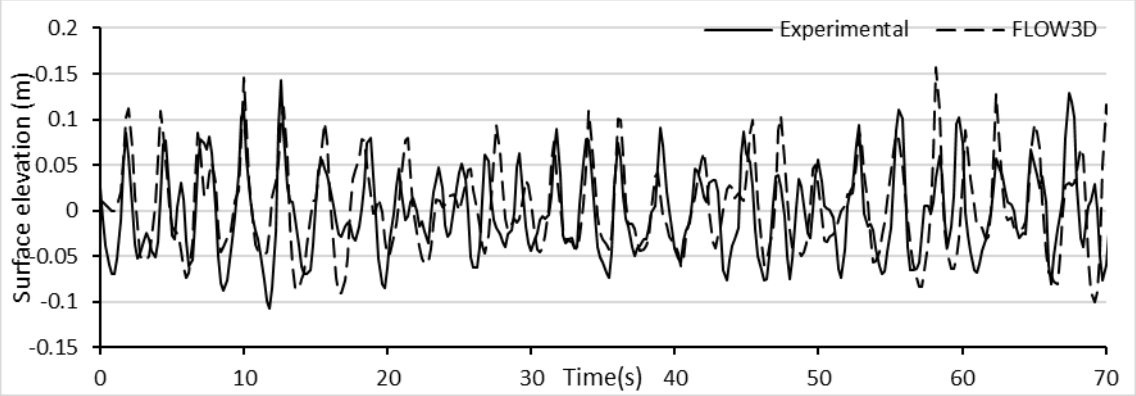

Figure 7.102 Experimental and numerical surface elevations for (IRW_H_s = 0.22 m, T_s = 2.3 s) at Probes P1 (a) and P2 (b) for the Parabolic Proposition Design.

(a) Probe P1

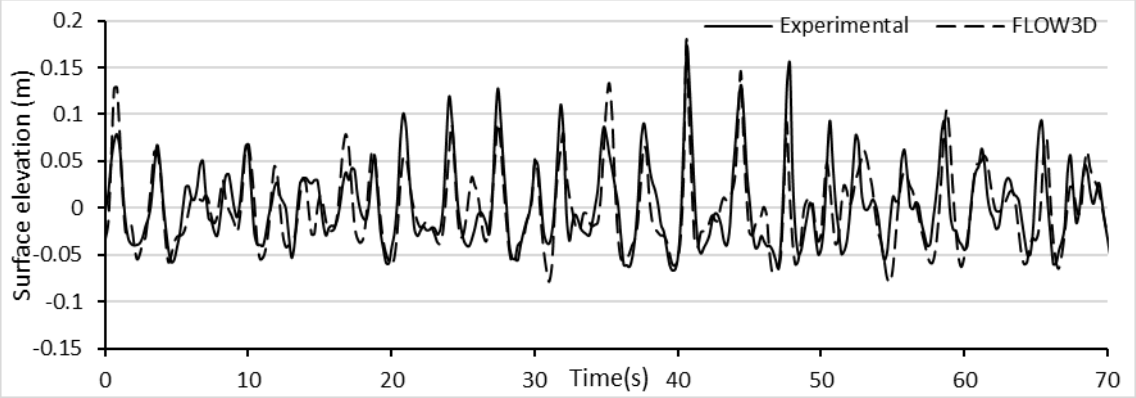

(b) Probe P2

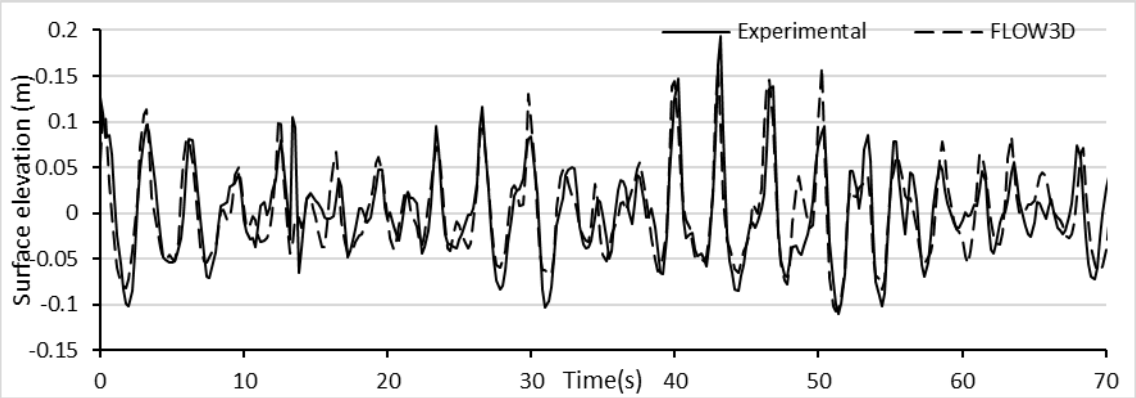

Figure 7.103 Experimental and numerical surface elevations for (IRW_H_s = 0.20 m, T_s = 2.7 s) at Probes P1 (a) and P2 (b) for the Parabolic Proposition Design.

(a) Probe P1

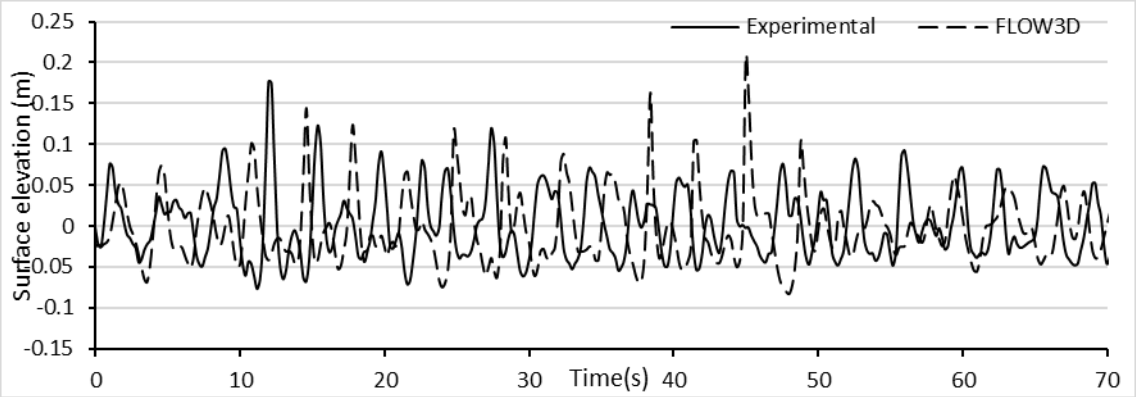

(b) Probe P2

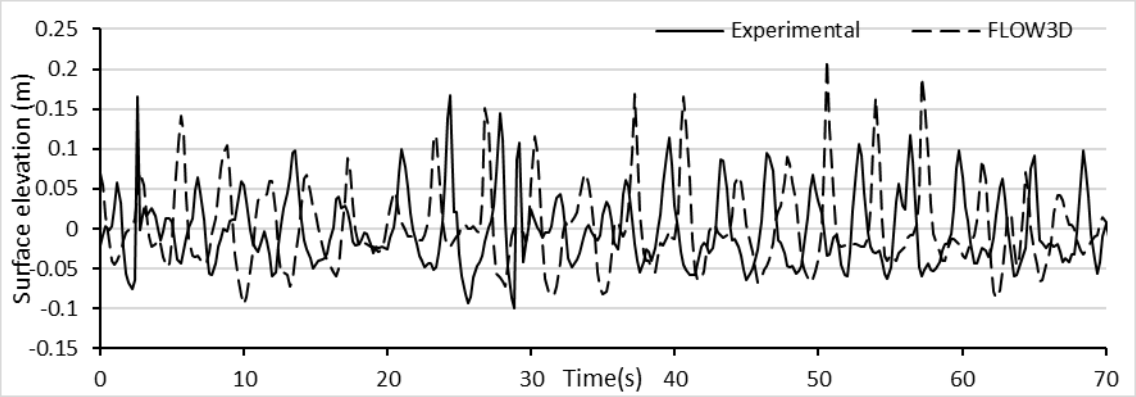

Figure 7.104 Experimental and numerical surface elevations for (IRW_H_s = 0.17 m, T_s = 3.1 s) at Probes P1 (a) and P2 (b) for the Parabolic Proposition Design.

(a) Probe P1

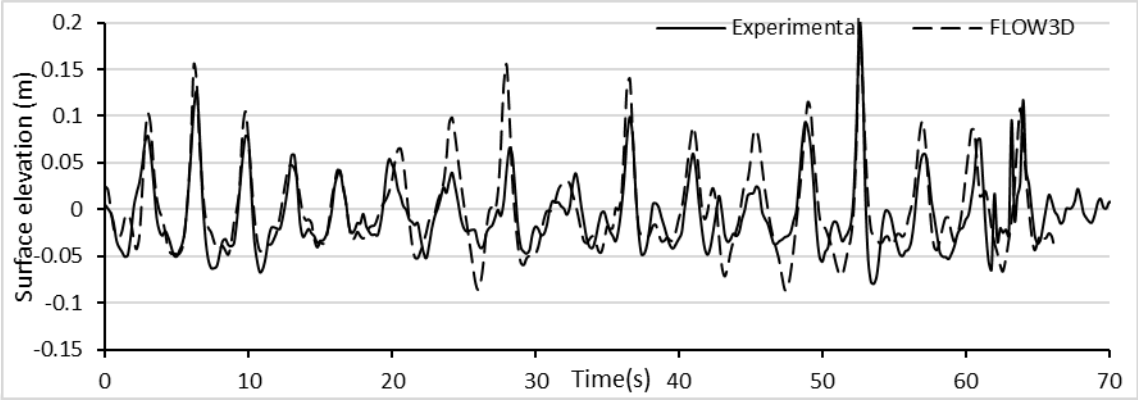

(b) Probe P2

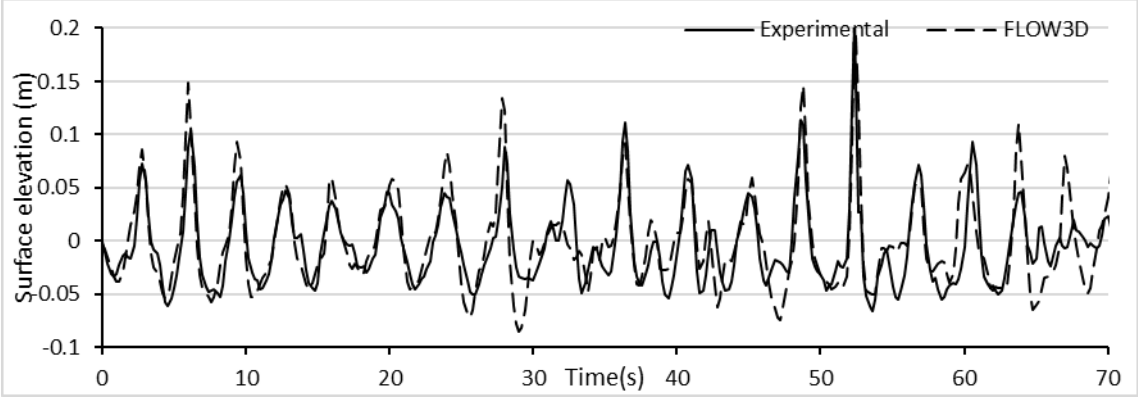

Figure 7.105 Experimental and numerical surface elevations for (IRW_H_s = 0.13 m, T_s = 3.6 s) at Probes P1 (a) and P2 (b) for the Parabolic Proposition Design.

Figure 7.106 to Figure 7.110 depict comparisons of the experimental and numerical power density spectrums to the target spectra in case of the selected 2-slopes proposal.

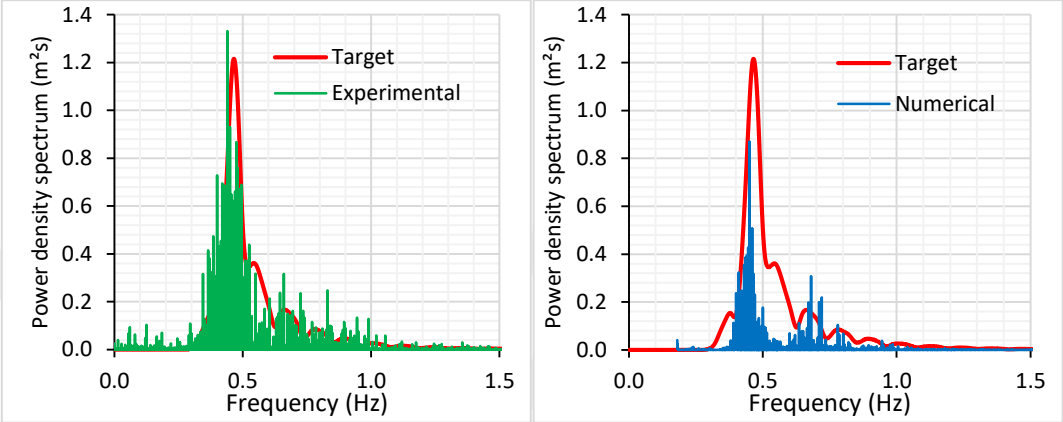

Figure 7.106 Experimental (left) and Numerical (right) power density spectrum of irregular wave with H_s=0.25 m, and T_s= 2.0 s, in case of 2-slopes proposal design.

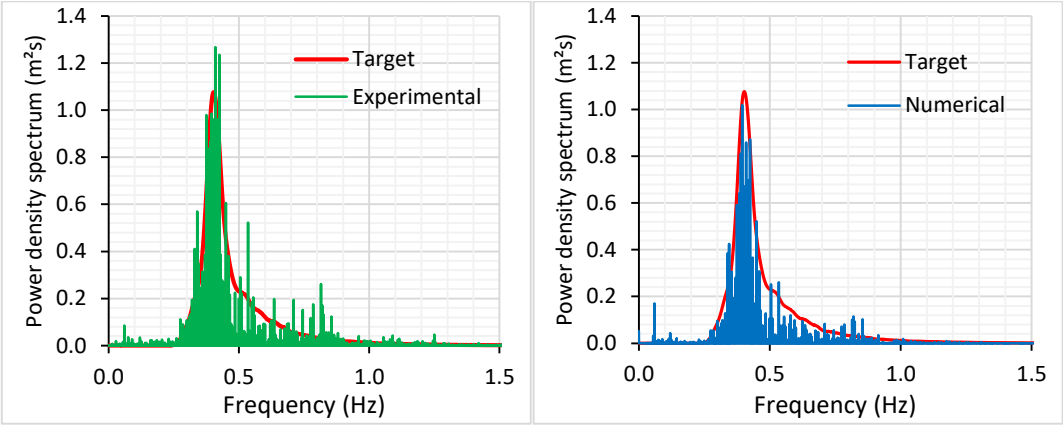

Figure 7.107 Experimental (left) and Numerical (right) power density spectrum of irregular wave with H_s=0.22 m, and T_s= 2.3 s, in case of 2-slopes proposal design.

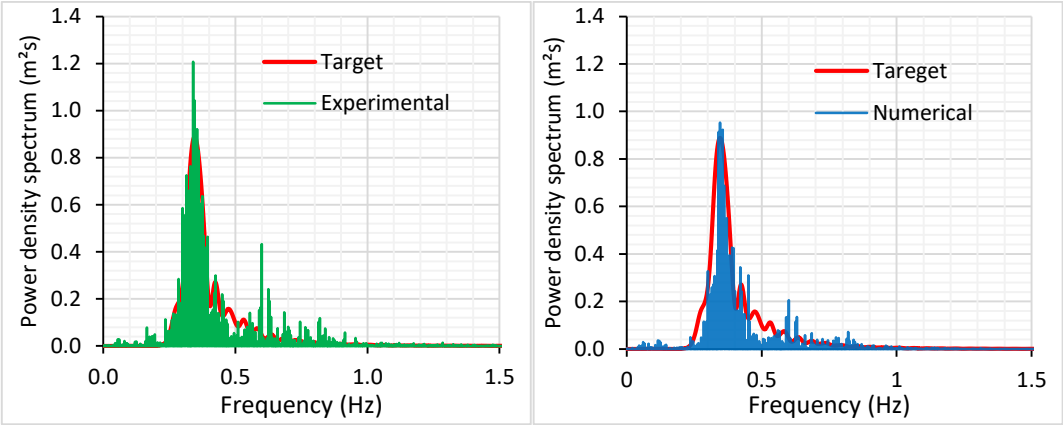

Figure 7.108 Experimental (left) and Numerical (right) power density spectrum of irregular wave with H_s=0.20 m, and T_s= 2.7 s, in case of 2-slopes proposal design.

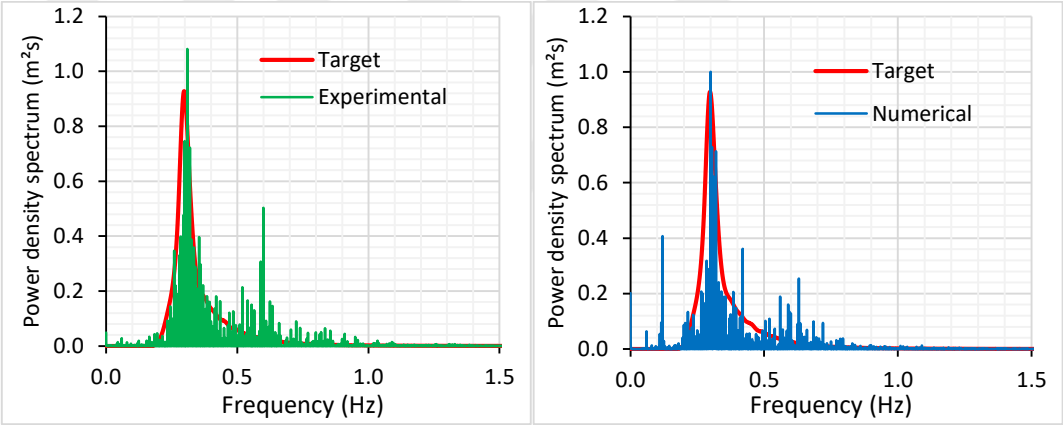

Figure 7.109 Experimental (left) and Numerical (right) power density spectrum of irregular wave with H_s=0.17 m, and T_s= 3.1 s, in case of 2-slopes proposal design.

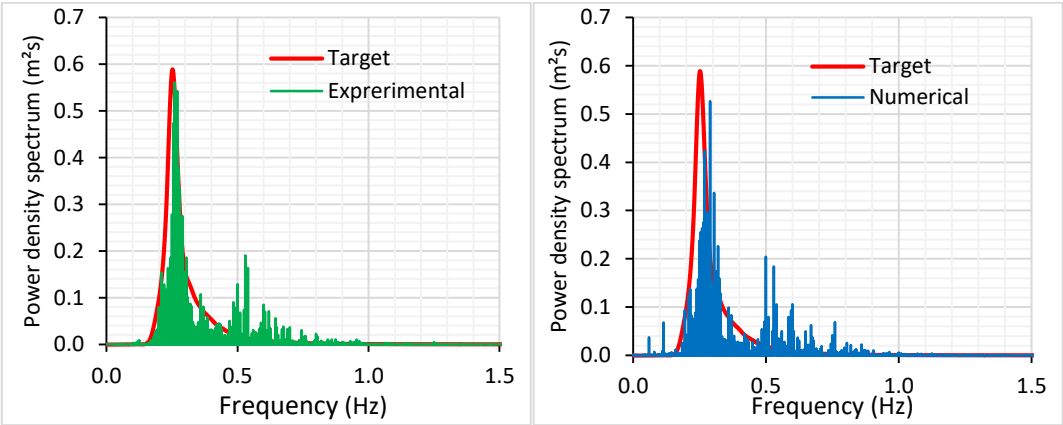

Figure 7.110 Experimental (left) and Numerical (right) power density spectrum of irregular wave with H_s=0.13 m, and T_s= 3.6 s, in case of 2-slopes proposal design.

Figure 7.111 to Figure 7.115 depict comparisons of the experimental and numerical power density spectrums to the target spectra in case of selected 3-slopes proposal.

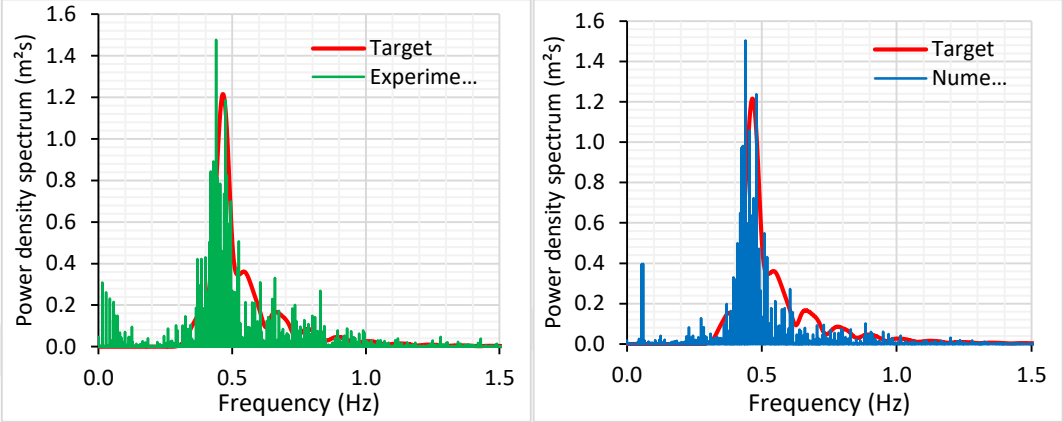

Figure 7.111 Experimental (left) and Numerical (right) power density spectrum of irregular wave with H_s=0.25 m, and T_s= 2.0 s, in case of 3-slopes proposal design .

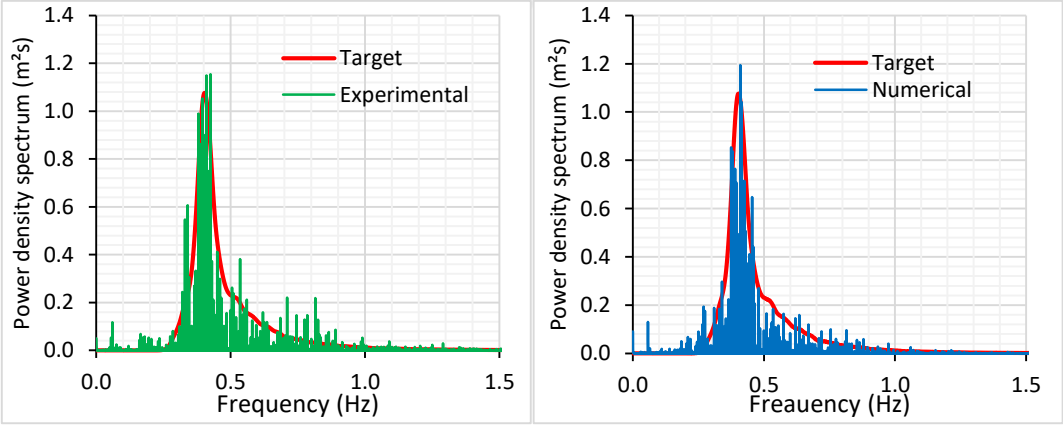

Figure 7.112 Experimental (left) and Numerical (right) power density spectrum of irregular wave with H_s=0.22 m, and T_s= 2.3s, in case of 3-slopes proposal design .

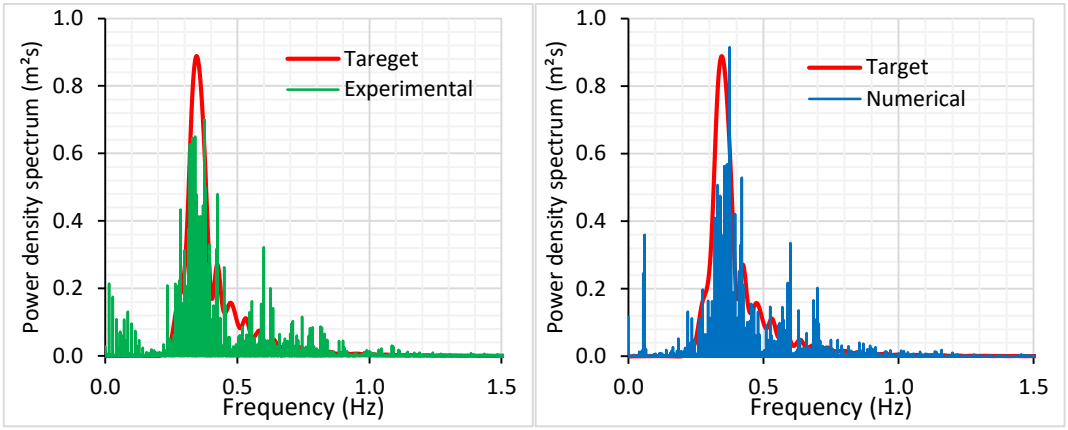

Figure 7.113 Experimental (left) and Numerical (right) power density spectrum of irregular wave with H_s=0.20 m, and T_s= 2.7 s, in case of 3-slopes proposal design.

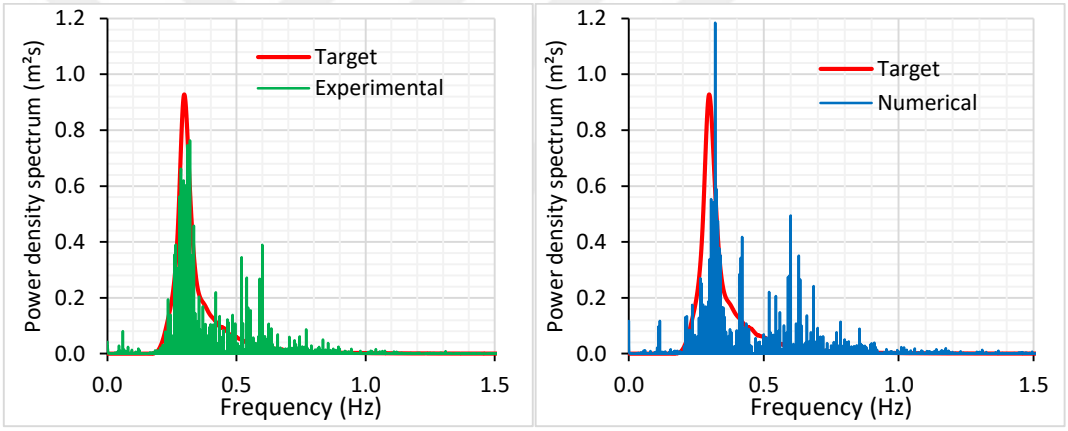

Figure 7.114 Experimental (left) and Numerical (right) power density spectrum of irregular wave with H_s=0.17 m, and T_s= 3.1 s, in case of 3-slopes proposal design.

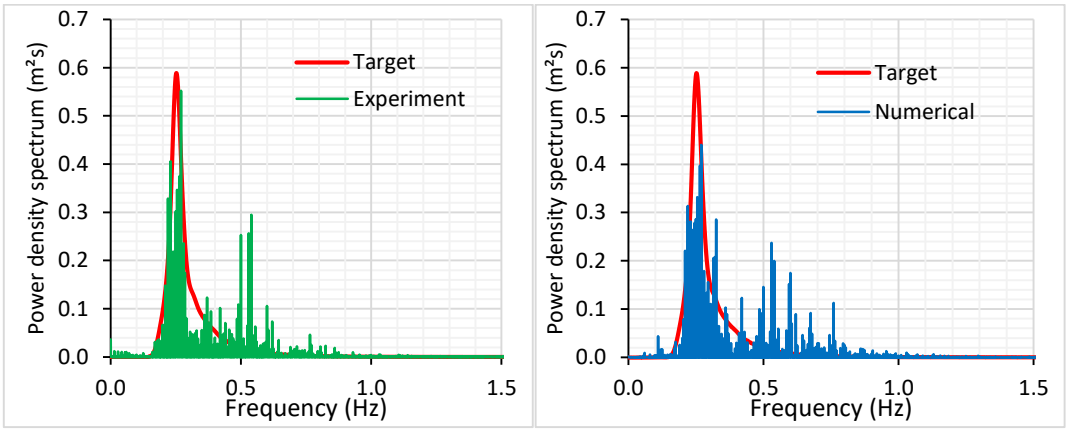

Figure 7.115 Experimental (left) and Numerical (right) power density spectrum of irregular wave with H_s=0.13 m, and T_s= 3.6 s, in case of 3-slopes proposal design.

Figure 7.116 to Figure 7.120 depict comparisons of the experimental and numerical power density spectrums to the target spectra in case of the selected parabolic proposal.

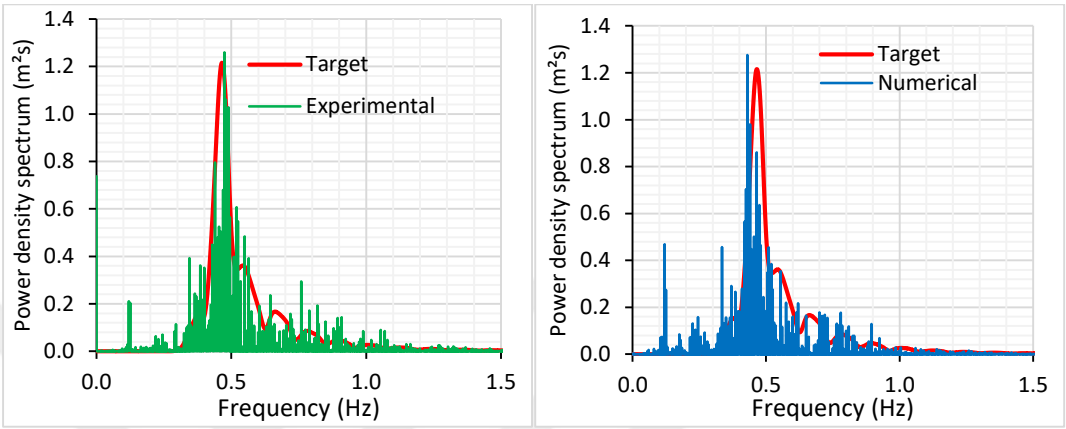

Figure 7.116 Experimental (left) and Numerical (right) power density spectrum of irregular wave with H_s=0.25 m, and T_s= 2.0 s, in case of parabolic proposal design.

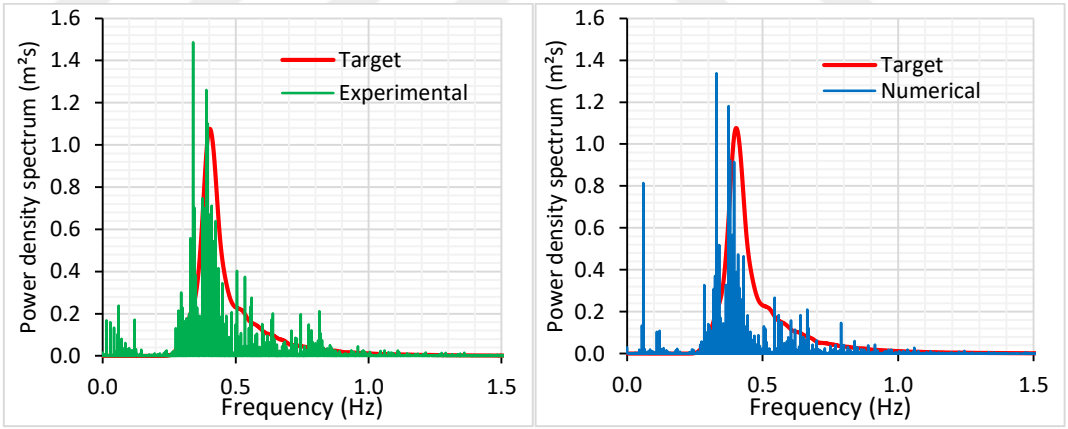

Figure 7.117 Experimental (left) and Numerical (right) power density spectrum of irregular wave with H_s=0.22 m, and T_s= 2.3 s, in case of parabolic proposal design.

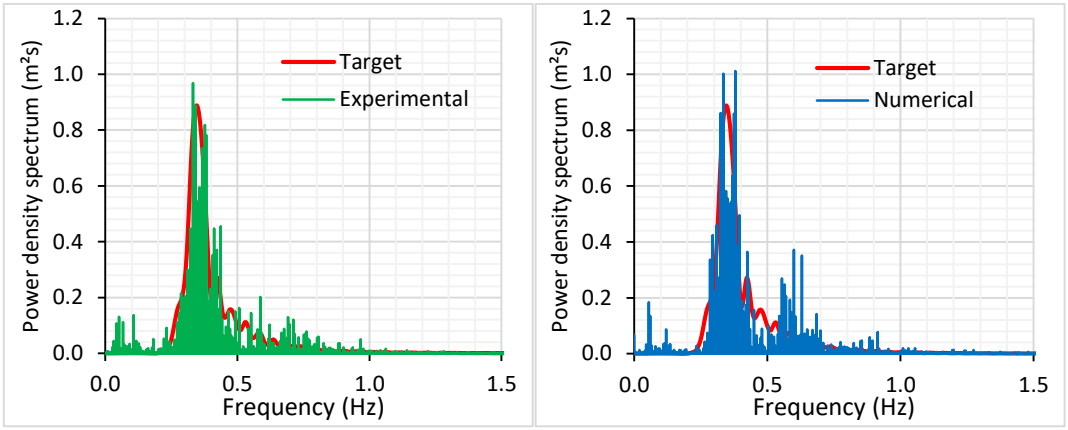

Figure 7.118 Experimental (left) and Numerical (right) power density spectrum of irregular wave with H_s=0.20 m, and T_s= 2.7 s, in case of parabolic proposal design.

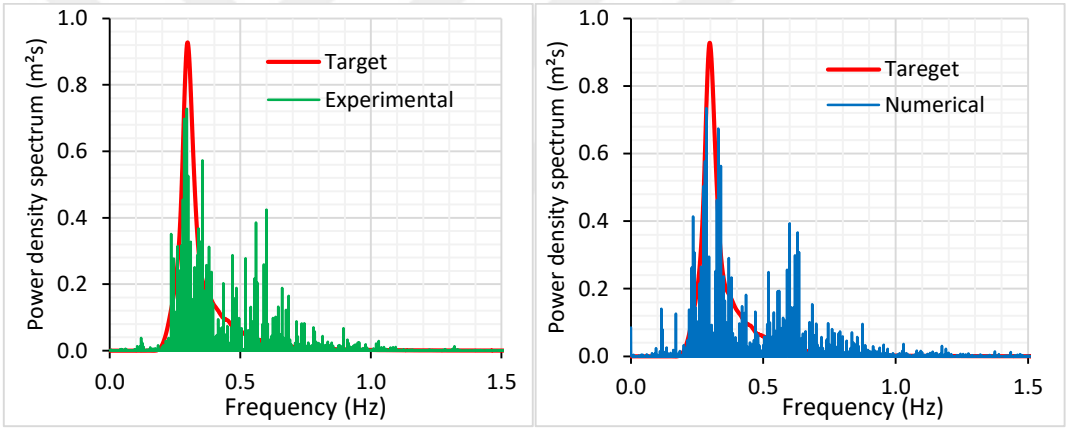

Figure 7.119 Experimental (left) and Numerical (right) power density spectrum of irregular wave with H_s=0.17 m, and T_s= 3.1 s, in case of parabolic proposal design.

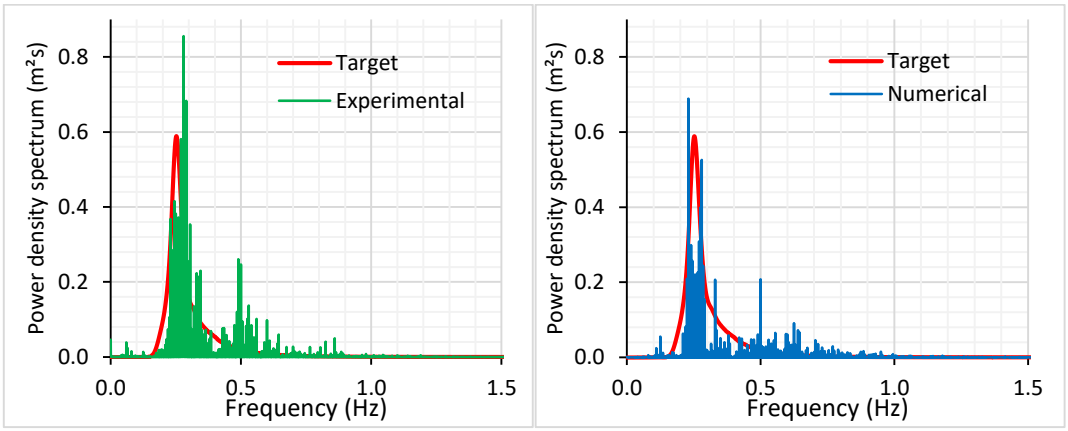

Figure 7.120 Experimental (left) and Numerical (right) power density spectrum of irregular wave with H_s=0.13 m, and T_s= 3.6 s, in case of parabolic proposal design.

The comparison between the numerical and experimental power density spectra of irregular waves for the three proposed designs reveals a generally good agreement between the simulated and experimental energy distributions, conforming to the target power density spectrum in most cases. In particular cases, numerical and experimental results showed discrepancies. Simulations of the 2-slope design with H_s= 0.25 m and T_s = 2 s, 3-slope design with H_s = 0.17 m and T_s = 3.1 s, and parabolic design with H_s = 0.13 m and T_s = 3.6 s demonstrated these deviations particularly clearly. Energy distributions are divergent from predictions.

CHAPTER EIGHT
CONCLUSIONS

The study aimed to evaluate the effectiveness of different designs of passive wave absorbers in a wave tank, with regular and irregular waves generated using a piston-type wave generator. In phase one of this study the FLOW 3D software used to simulate the behavior of these designs, and in the second phase the experiments perform for three selected passive wave absorbers with the low reflection coefficient.

The experiments study compared the performance of three different designs of passive wave absorbers, 2-slopes, 3slopes, and parabolic proposition design. The absorbers were placed at the end of the wave tank and were subjected to regular and irregular waves with different wave heights and frequencies. The wave height and frequency were adjusted using the piston-type wave generator, which simulates wave conditions by moving a piston to create waves of different heights and frequencies as discussed in section 1.

The effectiveness of the passive wave absorbers was evaluated based on their ability to reduce the reflection coefficient. The results of the study indicated that 2-slopes proposition and 3-slopes proposition design were significantly more effective in reducing wave amplitudes and improving wave damping compared to parabolic proposition in case of regular wave. Meanwhile, in the case of irregular waves, there was no significant difference in the reflection coefficient. Specifically, 2-slopes and 3-slopes propositions design having reflection coefficients spanning from 4% to 15%, while parabolic design with reflection coefficients within the range of 8% to 25% in case of regular waves.

The success of the 2-slopes and 3-slopes designs can be attributed to their specific design features. 2-slopes design had two inclined screen profiles and more simple geometric shape, which allowed for more effective wave energy dissipation. The 3-slopes design, on the other hand, had a more complex surface because it designed based on parabolic shape, which reduced wave reflections and increased wave absorption.

The findings of the study have important implications for the design and optimization of passive wave absorbers in wave tanks. The improvement of the successful designs can lead to better wave attenuation and enhanced performance of passive wave absorbers in wave tanks. Additionally, the study provides insights into the specific characteristics of successful designs that can inform the development of new and innovative passive wave absorber designs.

It is important to note that the study had some limitations. For example, the experiment study only tested three designs, and other possible designs (e.g. permeable screen profile) may perform differently under the same wave conditions. Moreover, the study only considered the performance of passive wave absorbers under regular and irregular waves, and the effectiveness of the absorbers may vary under other wave conditions, such as deep wave condition or breaking waves for example.

Further research is needed to improve waveform computation, control algorithms, and wave-generation precision by developing and testing the second order transfer function for a piston type irregular wave generator in the wave flume. More research is needed to investigate the specific characteristics of successful designs and to explore additional design options for optimizing the performance of passive wave absorbers under different wave conditions.

REFERENCES

AKTAŞ, K. (2020). *Wave generation and analysis in the laboratory wave channel to conduct experiments on the numerically modeled spar type floating wind turbine*. *Iyte University*.

Biesel, F., & Suquet, F. (1951). Les appareils générateurs de houle en laboratoire. *Houille Blanche*, *4*, 475–496. https://doi.org/10.1051/lhb/1951049

Blanche, L. H., & Fontanet, P. (1961). *par un batteur plan (2 ordre d ' approximation) Théorie de la génération de la houle cylindrique par un batteur plan*. *6368*, 2–31. https://doi.org/10.1051/lhb/1961020

Capitao, R., & Carvalho, M. M. de. (1993). *Separation of incident and reflected spectra in wave flumes*. *3*.

Chegini, V. (1995). *Design of upright perforated energy dissipators for use in wave basins Design of Upright Perforated Energy Dissipators for Use in Wave Basins*.

Chegini, V. (1993). *Experimental study of a permeable sloping wave absorber* . (Issue November 1993).

Coastal Engineering Research Center. (1984). *Shore protection manual us Army Corps of Engineers Glossary of Terms Appendix A*.

Coastal Engineering Research Center. (2006). CEM Coastal engineering manual. In *Department of the Army, US Army Corps of Engineers, Washington DC, USA* (Vol. 1100, Issue June, pp. 1–6). Springer-Verlag. https://doi.org/10.1007/BFb0042998

Daoud, B., & Kobus, J. M. (1995). Irregular wave generation method with given characteristics in experimental tanks. *Ocean Engineering*, *22*(4), 387–410. https://doi.org/10.1016/0029-8018(93)E0012-H

Dean, R. G., & Dalrymple, R. A. (1984). *Water wave mechanics for engineers and scientists*. https://doi.org/10.1029/eo066i024p00490-06

Draycott, S., Steynor, J., Davey, T., & Ingram, D. M. (2018). Isolating incident and reflected wave spectra in the presence of current. *Coastal Engineering Journal*, *60*(1), 39–50. https://doi.org/10.1080/05785634.2017.1418798

Eškinja, Z., Mišković, I., & Fabeković, Z. (2008). Software for wave generator control. *MIPRO 2008 - 31st International Convention Proceedings: Computers in Technical Systems and Intelligent Systems*, *3*(0), 65–69.

Eskinja, Z., Miskovic, I., & Androcec, V. (2008). Modular Wavemaker Design for Harbours and Ships Physical. *BroddGradnja*, *59*, 131–135.

Frigaard, P., & Andersen, T. L. (2010). Technical Background Material for the Wave Generation Software AwaSys 5. *DCE Technical Reports, No. 64*, 114.

Guillouzouic, B. (2014). Collation of Wave Simulation Methods. *MARINET Report*, 1–85.

Hodaei, S. M. R., Chamani, M. R., Moghim, M. N., Mansoorzadeh, S., & Kabiri-Samani, A. (2016). Experimental study on reflection coefficient of curved perforated plate. *Journal of Marine Science and Application*, *15*(4), 382–387. https://doi.org/10.1007/s11804-016-1383-5

Hughes, S. A. (1993). *Laboratory Wave Generation*. 333–457. https://doi.org/https://doi.org/10.1142/2154

Isaacson, B. M. (1992). *Measurement of regular wave reflection*. *117*(6), 553–569.

Jung, T. H., Lee, S. J., & Cho, Y. S. (2012). Characteristics of wave reflection for vertical and slit caissons with porous structures. *Journal of Applied Mathematics*, *2012*. https://doi.org/10.1155/2012/972650

Khalfin, I. S. (2007). Modeling and calculation of bed score around large-diameter vertical cylinder under wave action. *Water Resources*, *34*(1), 49–59. https://doi.org/10.1134/S0097807807010058

Kimura, A. (n.d.). *Decomposition of nonlinearly reflected irregular waves by the wave breaking and deformation*. 396–409.

Le Méhauté, B. (1972). Progressive wave absorber. *Journal of Hydraulic Research*, *10*(2), 153–169. https://doi.org/10.1080/00221687209500026

Lean, G. H. (1967). A simplified theory of permeable wave absorbers. *Journal of Hydraulic Research*, *5*(1), 15–30. https://doi.org/10.1080/00221686709500187

Lee, K.-H., Bae, J.-H., Kim, S.-G., & Kim, D.-S. (2017). Three-dimensional Simulation of Wave Reflection and Pressure Acting on Circular Perforated Caisson Breakwater by OLAFOAM. *Journal of Korean Society of Coastal and Ocean Engineers*, *29*(6), 286–304. https://doi.org/10.9765/kscoe.2017.29.6.286

Liu, Y., & Li, S. W. (2016). Resolution of incident and reflected components of nonlinear regular waves. *Coastal Engineering Journal*, *58*(3), 1–21. https://doi.org/10.1142/S0578563416500121

Liu, Y., Li, Y., & Teng, B. (2007). *Wave interaction with a perforated wall breakwater with a submerged horizontal porous plate*. *34*, 2364–2373. https://doi.org/10.1016/j.oceaneng.2007.05.002

Liu, Y., Cavalier, G., Pastor, J., Viera, R. J., Guillory, C., Judice, K., Guiberteau, K., & Kozman, T. A. (2012). Design and Construction of a Wave Generation System to Model Ocean Conditions in the Gulf of Mexico. *International Journal of Energy & Technology*, *4*(31), 1–7.

Madsen. (1971). On the Generation of Long Wave. *Journal Of Geophysical Research*, *76*(36).

Mansard, E. P. D. (1981). The measurement of incident and reflected spectra using a least squares method. *In: Proc. Seventeenth Coastal Engng. Conf., (Sydney, Australia: Mar. 23-28, 1980), 1, New Yo*, 154–172. https://doi.org/10.1061/9780872622647.008

McKee, R., Elsäßer, B., & Schmitt, P. (2018). Obtaining reflection coefficients from a single point velocity measurement. *Journal of Marine Science and Engineering*, *6*(2). https://doi.org/10.3390/jmse6020072

Mišković, I., Eškinja, Z., & Horvat, K. (2008). Wavemaker control system for irregular developed sea waves generation. *2008 Mediterranean Conference on Control and Automation - Conference Proceedings, MED'08*, 791–794. https://doi.org/10.1109/MED.2008.4602205

Mosquera, R., & Pedocchi, F. (2013). Decomposition of incident and reflected surface waves using an Ultrasonic Velocity Profiler. *Coastal Engineering*, *71*, 52–59. https://doi.org/10.1016/j.coastaleng.2012.08.002

Negm, A., & Nassar, K. (2016). Determination of Wave Reflection Formulae for Vertical and Sloped Seawalls Via Experimental Modelling. *Procedia Engineering*, *154*, 919–927. https://doi.org/10.1016/j.proeng.2016.07.502

Ouellet, Y., & Datta, I. (1986). A survey of wave absorbers Revue des amortisseurs à houle. *Journal of Hydraulic Research*, *24*(4), 265–280. https://doi.org/10.1080/00221688609499305

Rostaminia, M., Health, O., & Chegini, V. (2008). Study of Reflection and Transmission Coefficients of Waves From Perforated Plates and Introducing Dimensionless Parameter θ Study of Reflection and Transmission Coefficients of Waves from Perforated Plates and Introducing Dimensionless Parameter " θ ". *International Conference on Coastal and Port Engineering in Developing Countries (COPEDEC)*.

Schäffer, H. A., & Steenberg, C. M. (2003). Second-order wavemaker theory for multidirectional waves. *Ocean Engineering*, *30*(10), 1203–1231. https://doi.org/10.1016/S0029-8018(02)00100-2

Schäffer, H. A. (1996). Second-order wavemaker theory for irregular waves. *Ocean Engineering*, *23*(1), 47–88. https://doi.org/10.1016/0029-8018(95)00013-B

Schäffer, H. A. (1996). Second-order wavemaker theory for irregular waves. *Ocean Engineering*, *23*(1), 47–88. https://doi.org/10.1016/0029-8018(95)00013-B

Schmittner, C., Scharnke, J., Pauw, W., Van Den Berg, J., & Hennig, J. (2013). New methods and insights in advanced and realistic basin wave modelling. *Proceedings of the International Conference on Offshore Mechanics and Arctic Engineering - OMAE*, *5*(February). https://doi.org/10.1115/omae2013-11445

Sekiguchi, S. I., Miyabe, S., Yamamoto, Y., & Miwa, T. (2002). Development of a sloping-slit caisson breakwater. *Coastal Engineering Journal*, *44*(3), 203–215. https://doi.org/10.1142/S0578563402000548

Spanos, P. T. D. (1983). ARMA algorithms for ocean wave modeling. *Journal of Energy Resources Technology, Transactions of the ASME*, *105*(3), 300–309. https://doi.org/10.1115/1.3230919

Spinneken, J. (n.d.). *Wave Generation and Absorption using Force-feedback Control Imperial College London*.

Straub, L. G., Bowers, C. E., & Herbich, J. B. (2011). Laboratory Tests of Permeable Wave Absorbers. *Coastal Engineering Proceedings*, *1*(6), 44. https://doi.org/10.9753/icce.v6.44

Suh, K. D., Choi, J. C., Kim, B. H., Park, W. S., & Lee, K. S. (2001). Reflection of irregular waves from perforated-wall caisson breakwaters. *Coastal Engineering*, *44*(2), 141–151. https://doi.org/10.1016/S0378-3839(01)00028-X

Suh, K. D., Park, W. S., & Park, B. S. (2001). Separation of incident and reflected waves in wave-current flumes. *Coastal Engineering*, *43*(3–4), 149–159. https://doi.org/10.1016/S0378-3839(01)00011-4

Tiedeman, S. A., Allsop, W., Russo, V., & Brown, A. (2012). a Demountable Wave Absorber for Wave Flumes and Basins. *Coastal Engineering Proceedings*, *1*(33), 37. https://doi.org/10.9753/icce.v33.waves.37

Tiedeman, S., Allsop, W., Russo, V., & Brown, A. (2012). a demountable wave absorber for wave flumes and basins Simon Tiedeman 1, William Allsop 1 , Viviana Russo 2 and Andy Brown 1. *Coastal Engineering Proceedings*, *1*(33), 1–10.

Troch, P., & De Rouck, J. (1999). An active wave generating-absorbing boundary condition for VOF type numerical model. *Coastal Engineering*, *38*(4), 223–247. https://doi.org/10.1016/S0378-3839(99)00051-4

Twu, S., & Chieu, C. (2000). *A highly wave dissipation offshore breakwater*. *27*, 315–330.

Wang, D. xu, Sun, J. wen, Gui, J. song, Ma, Z., Ning, D. zhi, & Fang, K. zhao. (2019). A numerical piston-type wave-maker toolbox for the open-source library OpenFOAM. *Journal of Hydrodynamics*, *31*(4), 800–813. https://doi.org/10.1007/s42241-018-0116-4

Wu, J., Wan, Z., & Fang, Y. (1998). *Wave reflection by a vertical wall with a horizontal submerged porous plate*. *25*(9), 767–779.

Y.goda. (2000). *Random seas and design of maritime structure*. https://doi.org/10.1142/3587

Yoshimi Goda and Tasumasa Suzuki. (1976). Estimation of incident and reflected waves in regular wave experiments. *Ocean Engineering*. https://doi.org/10.1016/0029-8018(93)E0011-G

Zelt, J. A., Skjelbreia, J. E., & Wave Technologies. (1993). Estimating incident and reflected wave fields using an arbitrary number of wave gages. *Proceedings of the Coastal Engineering Conference*, *1*,777–788. https://doi.org/10.1061/9780872629332.058

Zhang, H. (2005). A deterministic combination of numerical and physical models for coastal waves. https://doi.org/https://doi.org/10.1016/j.coastaleng.2006.08.009

APPENDIX A

Photos from the experimental Study of the 2-slopes, 3slopes, and parabolic passive wave absorbers designs for wave reflection coefficient.



Figure A.1 The 2-slopes wave absorber proposition under test (RW_H= 0.25 m, T= 1.5 s).



Figure A.2 The 2-slopes wave absorber proposition under test (RW_H=0.25 m, T=2 s).



Figure A.3 The 2-slopes wave absorber proposition under test (RW_H=0.25 m, T=2.5 s).

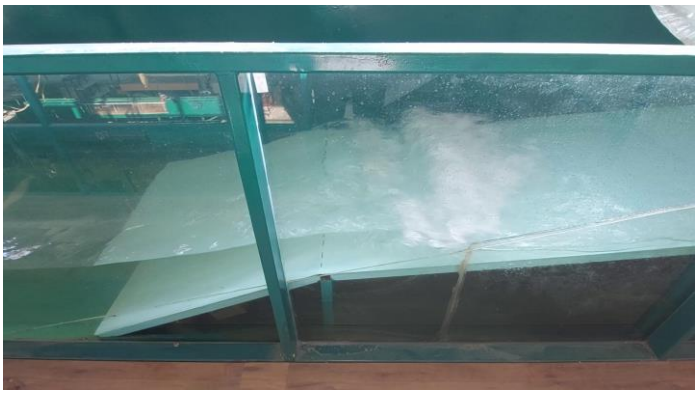

Figure A.4 The 2-slopes wave absorber proposition under test (RW_H=0.22 m, T=1.5 s).

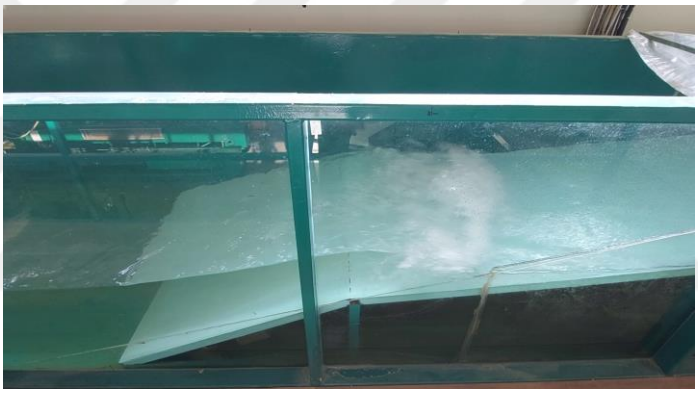

Figure A.5 The 2-slopes wave absorber proposition under test (RW_H=0.22 m, T=2 s).



Figure A.6 The 2-slopes wave absorber proposition under test (RW_H=0.22 m, T=2.5 s).



Figure A.7 The 2-slopes wave absorber proposition under test (RW_H=0.22 m, T=3 s).



Figure A.8 The 2-slopes wave absorber proposition under test (RW_H=0.2 m, T=1.5 s).



Figure A.9 The 2-slopes wave absorber proposition under test (RW_H=0.2 m, T=2 s).



Figure A.10 The 2-slopes wave absorber proposition under test (RW_H=0.2 m, T=2.7 s).



Figure A.11 The 2-slopes wave absorber proposition under test (RW_H=0.2 m, T=3 s).



Figure A.12 The 2-slopes wave absorber proposition under test (RW_H=0.17 m, T=1.5 s).



Figure A.13 The 2-slopes wave absorber proposition under test (RW_H=0.17 m, T=2 s).



Figure A.14 The 2-slopes wave absorber proposition under test (RW_H=0.17 m, T=2.5 s).



Figure A.15 The 2-slopes wave absorber proposition under test (RW_H=0.17 m, T=3.1 s).



Figure A.16 The 2-slopes wave absorber proposition under test (RW_H=0.17 m, T=3.5 s).



Figure A.17 The 2-slopes wave absorber proposition under test (RW_H=0.13 m_ T=1.5 s).



Figure A.18 The 2-slopes wave absorber proposition under test (RW_H=0.13 m, T=2 s).



Figure A.19 The 2-slopes wave absorber proposition under test (RW_H=0.13 m, T=2.5 s).



Figure A.20 The 2-slopes wave absorber proposition under test (RW_H=0.13 m, T=3 s).



Figure A.21 The 2-slopes wave absorber proposition under test (RW_H=0.13 m, T=3.6 s).



Figure A.22 The 3-slopes wave absorber proposition under test (RW_H=0.25 m, T=1.5 s).



Figure A.23 The 3-slopes wave absorber proposition under test (RW_H=0.25 m, T=2 s).



Figure A.24 The 3-slopes wave absorber proposition under test (RW_H=0.25 m, T=2.5 s).



Figure A.25 The 3-slopes wave absorber proposition under test (RW_H=0.22 m, T=1.5 s).



Figure A.26 The 3-slopes wave absorber proposition under test (RW_H=0.22 m, T=2 s).



Figure A.27 The 3-slopes wave absorber proposition under test (RW_H=0.22 m, T=2.3 s).



Figure A.28 The 3-slopes wave absorber proposition under test (RW_H=0.22 m, T=2.5 s).



Figure A.29 The 3-slopes wave absorber proposition under test (RW_H=0.22 m, T=3 s).



Figure A.30 The 3-slopes wave absorber proposition under test (RW_H=0.2 m, T=1.5 s).



Figure A.31 The 3-slopes wave absorber proposition under test (RW_H=0.2 m, T=2 s).



Figure A.32 The 3-slopes wave absorber proposition under test (RW_H=0.2 m, T=2.7 s).



Figure A.33 The 3-slopes wave absorber proposition under test (RW_H=0.2 m, T=3 s).



Figure A.34 The 3-slopes wave absorber proposition under test (RW_H=0.17 m, T=1.5 s).



Figure A.35 The 3-slopes wave absorber proposition under test (RW_H=0.17 m, T=2 s).



Figure A.36 The 3-slopes wave absorber proposition under test (RW_H=0.17 m, T=2.5 s).



Figure A.37 The 3-slopes wave absorber proposition under test (RW_H=0.17 m, T=3.1 s).



Figure A.38 The 3-slopes wave absorber proposition under test (RW_H=0.17 m, T=3.5 s).



Figure A.39 The 3-slopes wave absorber proposition under test (RW_H=0.13 m, T=1.5 s).



Figure A.40 The 3-slopes wave absorber proposition under test (RW_H=0.13 m, T=2 s).



Figure A.41 The 3-slopes wave absorber proposition under test (RW_H=0.13 m, T=2.5 s).



Figure A.42 The 3-slopes wave absorber proposition under test (RW_H=0.13 m, T=3 s).



Figure A.43 The 3-slopes wave absorber proposition under test (RW_H=0.13 m, T=3.5 s).



Figure A.44 The 3-slopes wave absorber proposition under test (RW_H=0.13 m, T=3.6 s).



Figure A.45 The parabolic wave absorber proposition under test (RW_H=0.25 m, T=1.5 s).



Figure A.46 The parabolic wave absorber proposition under test (RW_H=0.25 m, T=2 s).



Figure A.47 The parabolic wave absorber proposition under test (RW_H=0.25 m, T=2.5 s).



Figure A.48 The parabolic wave absorber proposition under test (RW_H=0.22 m, T=1.5 s).



Figure A.49 The parabolic wave absorber proposition under test (RW_H=0.22 m, T=2 s).



Figure A.50 The parabolic wave absorber proposition under test (RW_H=0.22 m, T=2.3 s).



Figure A.51 The parabolic wave absorber proposition under test (RW_H=0.22 m, T=2.5 s).



Figure A.52 The parabolic wave absorber proposition under test (RW_H=0.22 m, T=3 s).



Figure A.53 The parabolic wave absorber proposition under test (RW_H=0.2 m, T=1.5 s).



Figure A.54 The parabolic wave absorber proposition under test (RW_H=0.2 m, T=2 s).



Figure A.55 The parabolic wave absorber proposition under test (RW_H=0.2 m, T=2.7 s).



Figure A.56 The parabolic wave absorber proposition under test (RW_H=0.2 m, T=3 s).



Figure A.57 The parabolic wave absorber proposition under test (RW_H=0.17 m, T=1.5 s).



Figure A.58 The parabolic wave absorber proposition under test (RW_H=0.17 m, T=2 s).



Figure A.59 The parabolic wave absorber proposition under test (RW_H=0.17 m, T=2.5 s).



Figure A.60 The parabolic wave absorber proposition under test (RW_H=0.17 m, T=3.1 s).



Figure A.61 The parabolic wave absorber proposition under test (RW_H=0.17 m, T=3.5 s).



Figure A.62 The parabolic wave absorber proposition under test (RW_H=0.13 m, T=1.5 s).



Figure A.63 The parabolic wave absorber proposition under test (RW_H=0.13 m, T=2 s).



Figure A.64 The parabolic wave absorber proposition under test (RW_H=0.13 m, T=2.5 s).



Figure A.65 The parabolic wave absorber proposition under test (RW_H=0.13 m, T=3 s).



Figure A.66 The parabolic wave absorber proposition under test (RW_H=0.13 m, T=3.6 s).

APPENDIX B

Waves generation and wave absorbers modeling setup

1- Simulation Manager tab:

- Open simulation Manager tab and great new simulation (Figure B.1).



Figure B.1 The simulation manager tab .

2- The Model setup tab:

- Select the "General" sub-tab and specify the finish time. Next, define the number of fluids as one and choose the simulation units as SI with the temperature unit set to Celsius. Utilize the free surface interface. Leave all other settings at their default values (Figure B.2) .

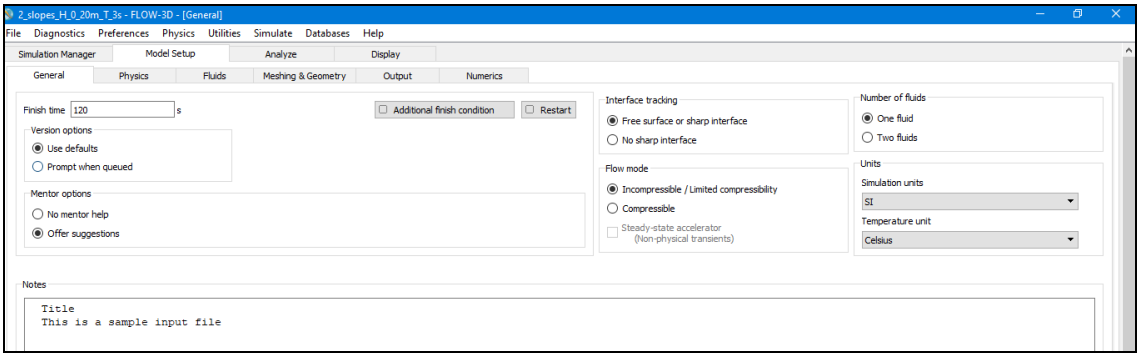

Figure B.2 The model setup tab and the general sub-tab .

- Move to the "Physics" sub-tab (Figure B.3). Firstly, select the gravity option and define gravity in the z-direction (Figure B.4). Secondly, open the "Viscosity and Turbulence" section and enable the "Viscous flow" option, specifying the RNG turbulence model (Figure B.5). Afterward, activate the "Density evaluation" and choose the second option (Figure B.6). Following this, select "Porous media" and configure it as "Darcian saturated drag (Figure B.7). Lastly, activate the "Moving and Sample Deformation Object (Figure B.8).

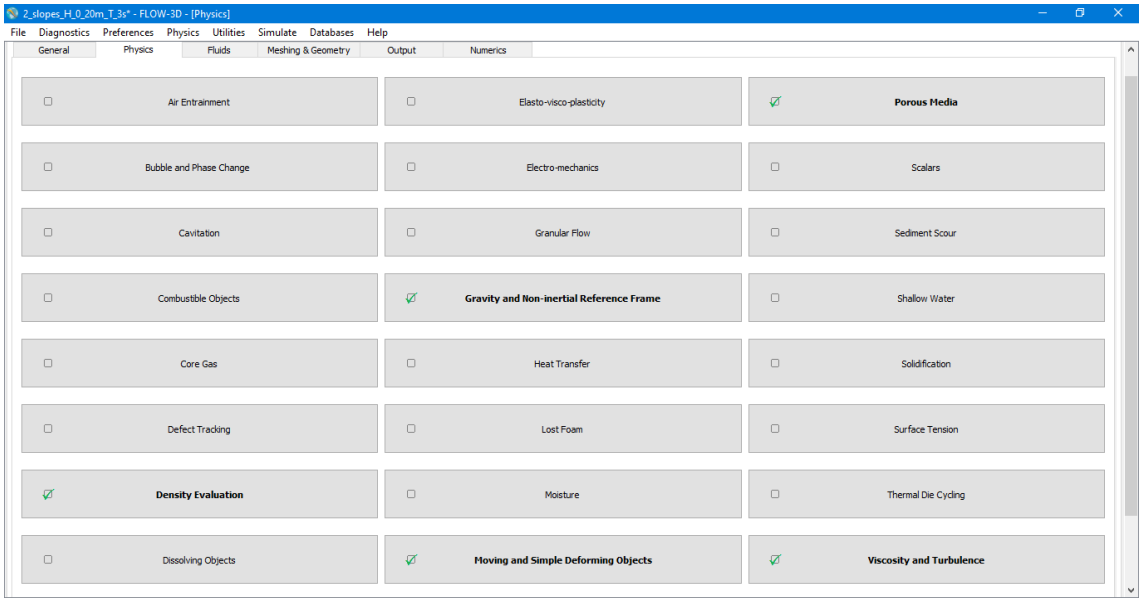

Figure B.3 The physics sub-tab .

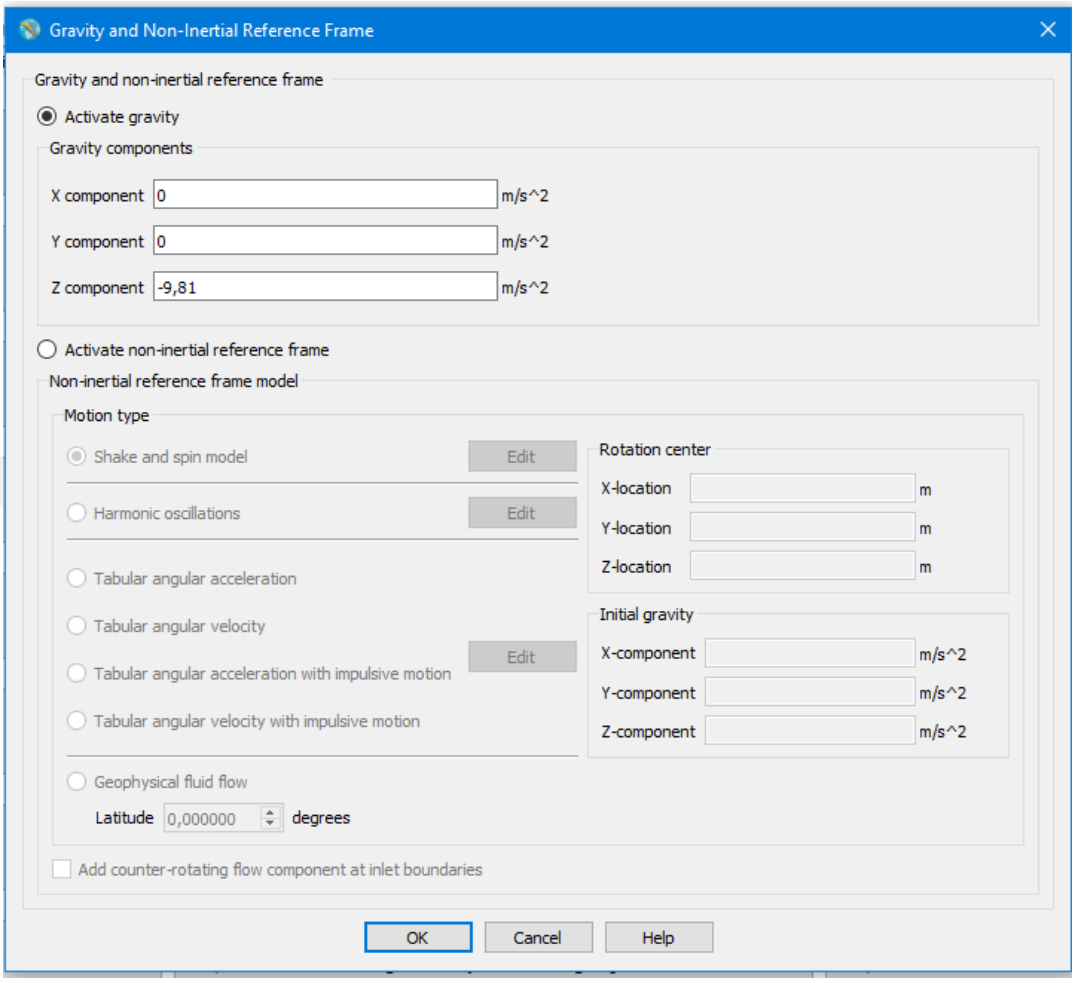

Figure B.4 The gravity and non-inertial reference frame window .

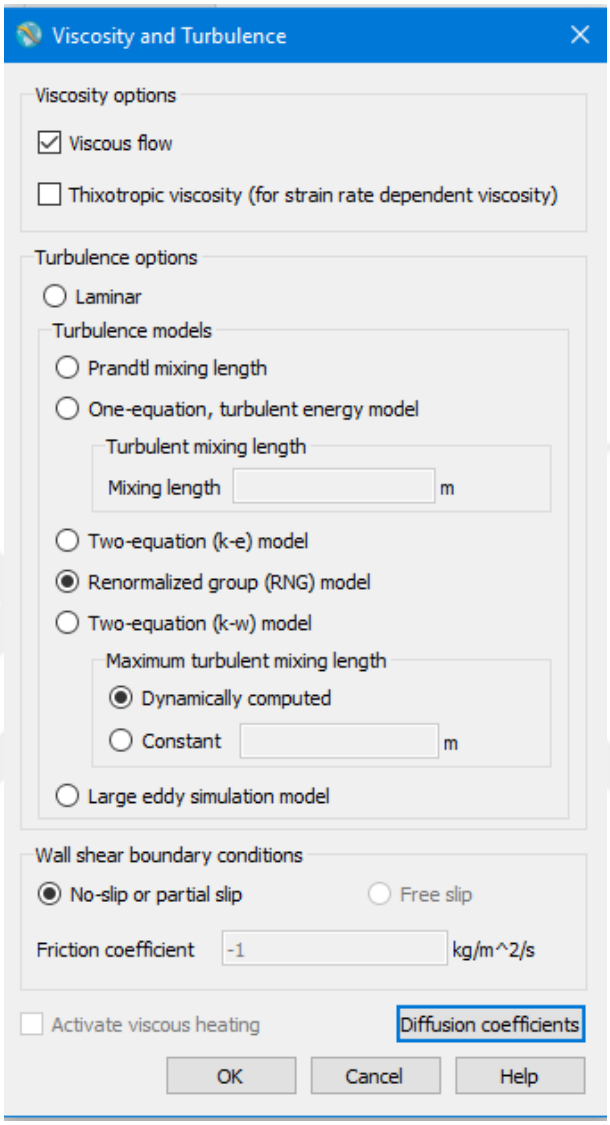

Figure B.5 The viscosity and turbulence window .

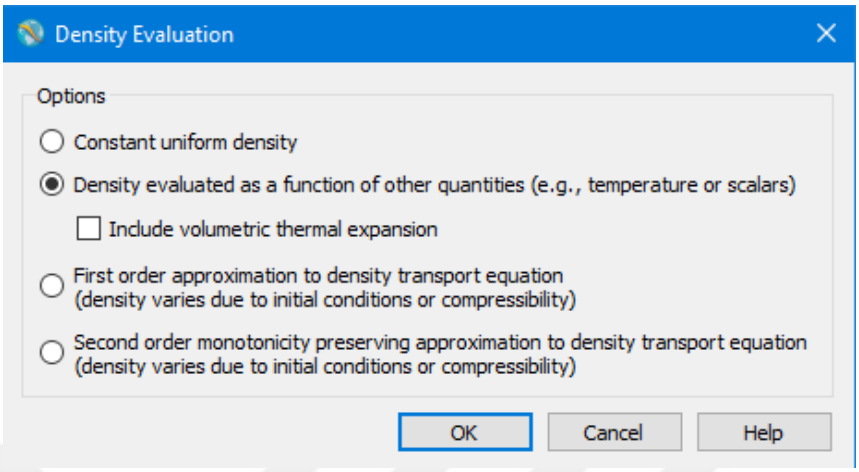

Figure B.6 The density evaluation window .

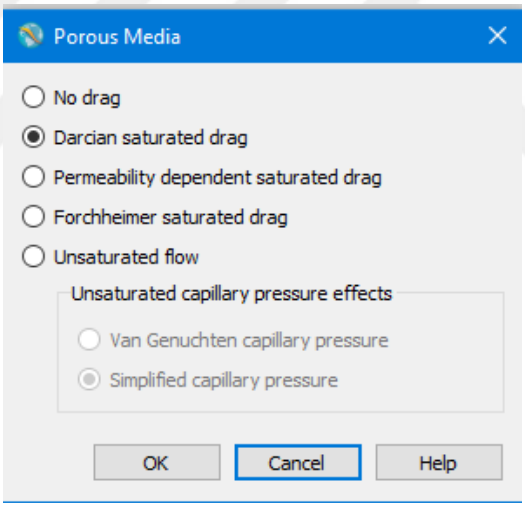

Figure B.7 The porous media window .

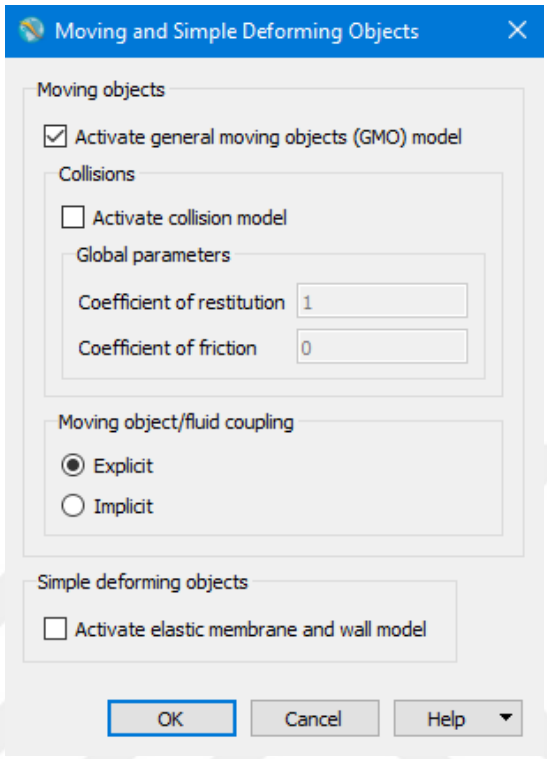

Figure B.8 The moving objects window .

- In Fluids tab (Figure B.9) load the fluid properties and define it as Water at 20 C.

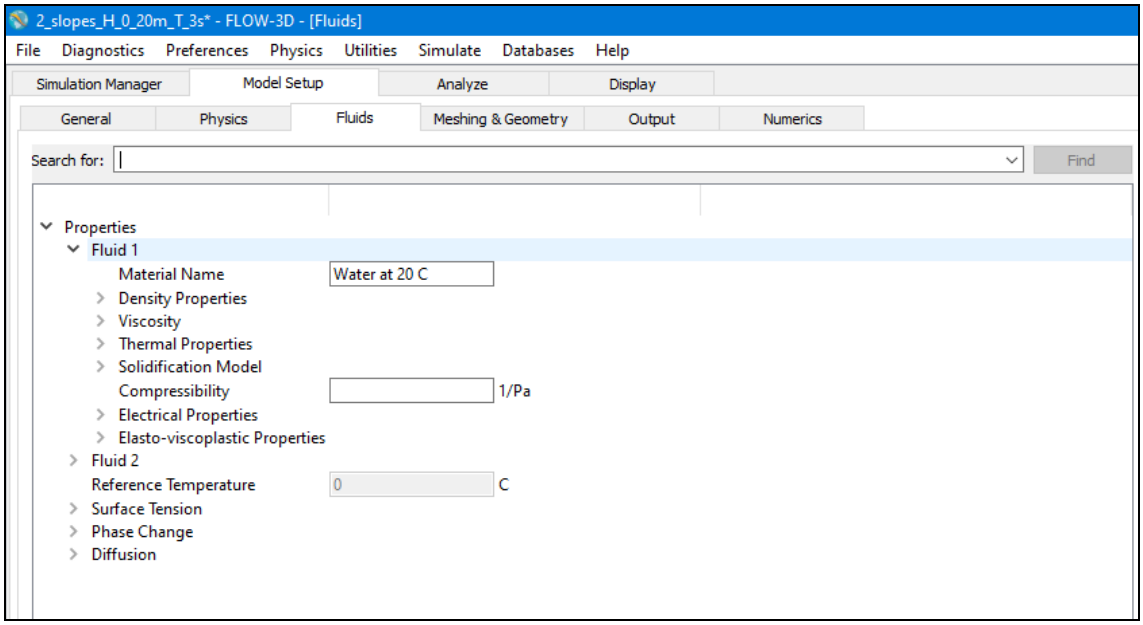

Figure B.9 The fluids sub-tab .

3- Meshing and Geometry:

- In the Geometry widget, import the STL file (Figure B.10).

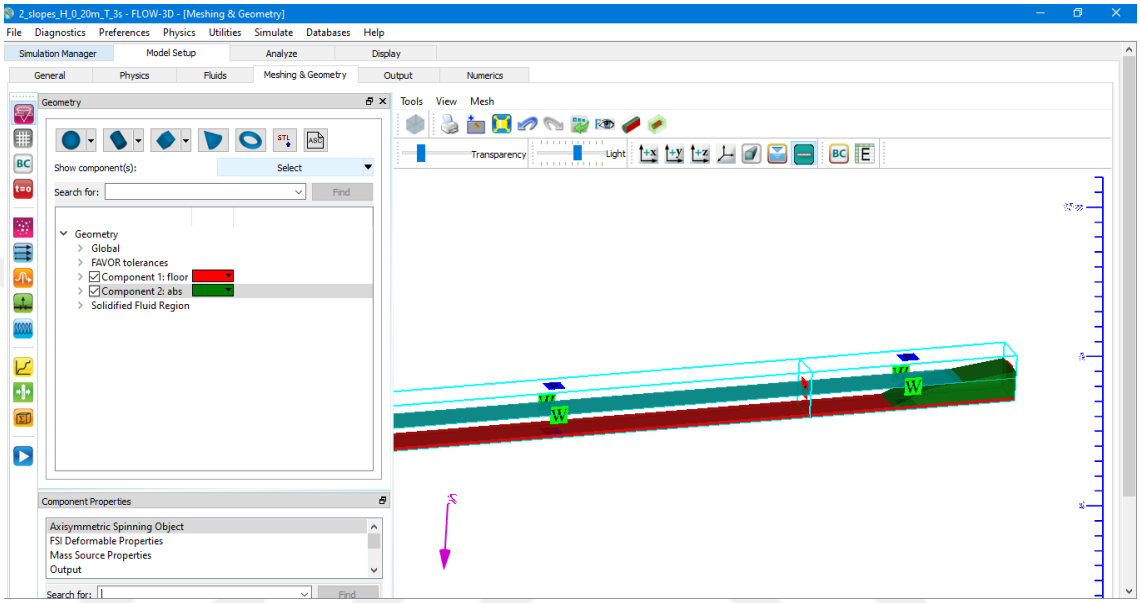

Figure B.10 The meshing and geometry sub-tab .

- Open the Mesh Operation widget and create a new mesh (Figure B.11). Afterward, enable the mesh gridlines to visualize the relative size of the mesh elements compared to the geometry. Finally, run the Simulation pre-check to verify the mesh quality and the maximum aspect ratio (Figure B.12).

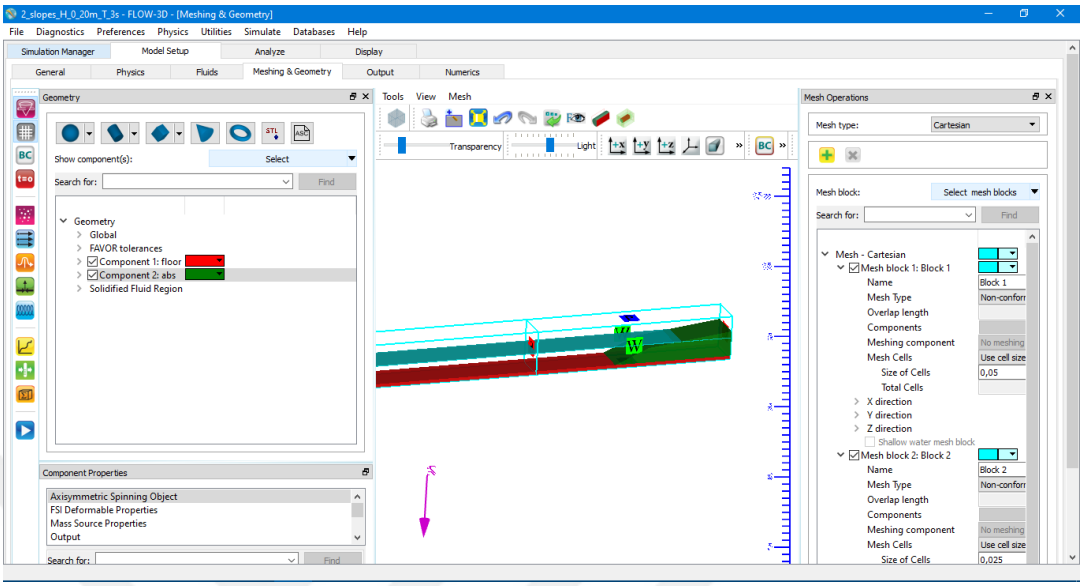

Figure B.11 The mesh operation widget .

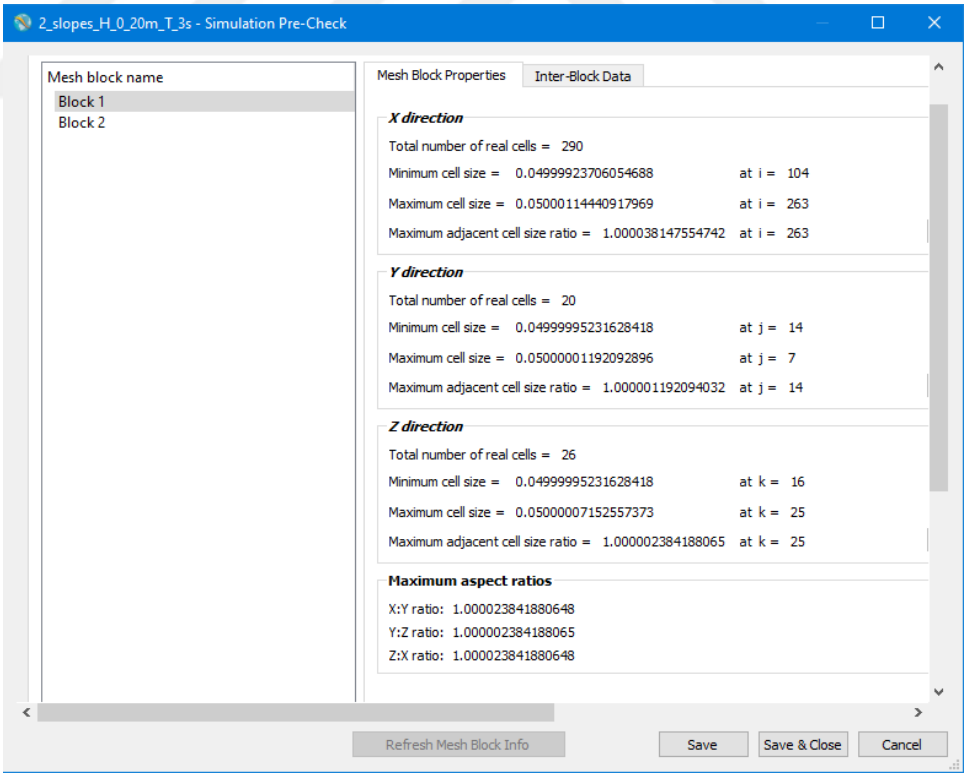

Figure B.12 The simulation pre-check window .

- Following that step, define the boundary conditions for each face of the mesh block as illustrated in the Figure B.13. A regular wave is defined as Stokes and cnoidal waves with given height, period, and mean fluid depth (Figure B.14).

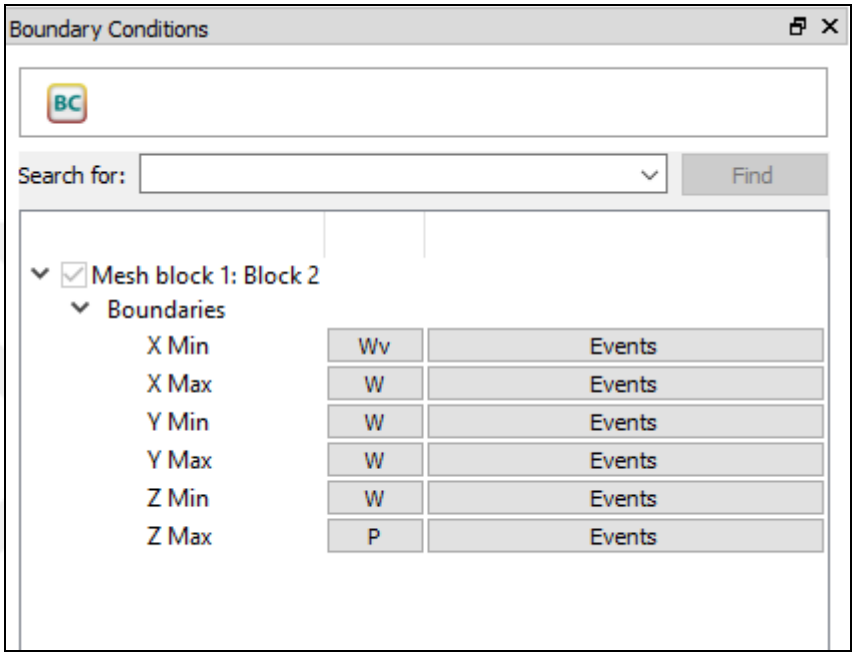

Figure B.13 The boundary condition widget .

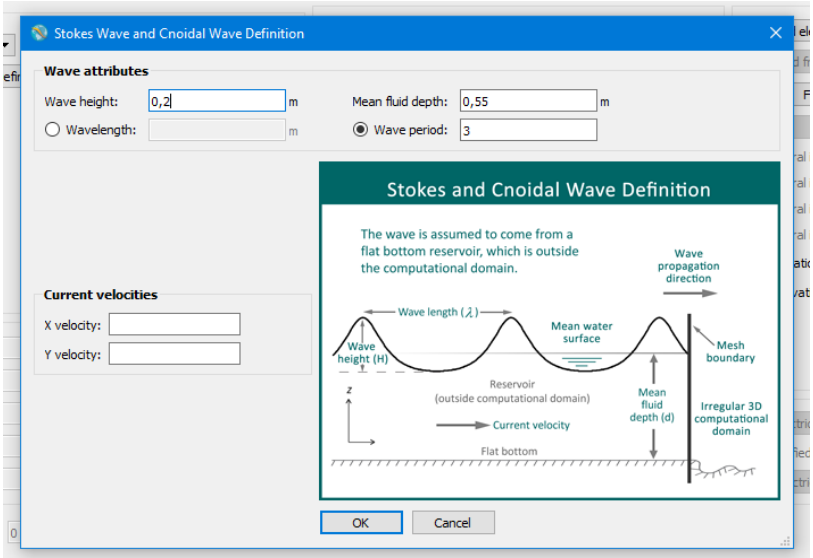

Figure B.14 The wave definition window .

- The initial fluid elevation set to 0.55 m (Figure B.15).

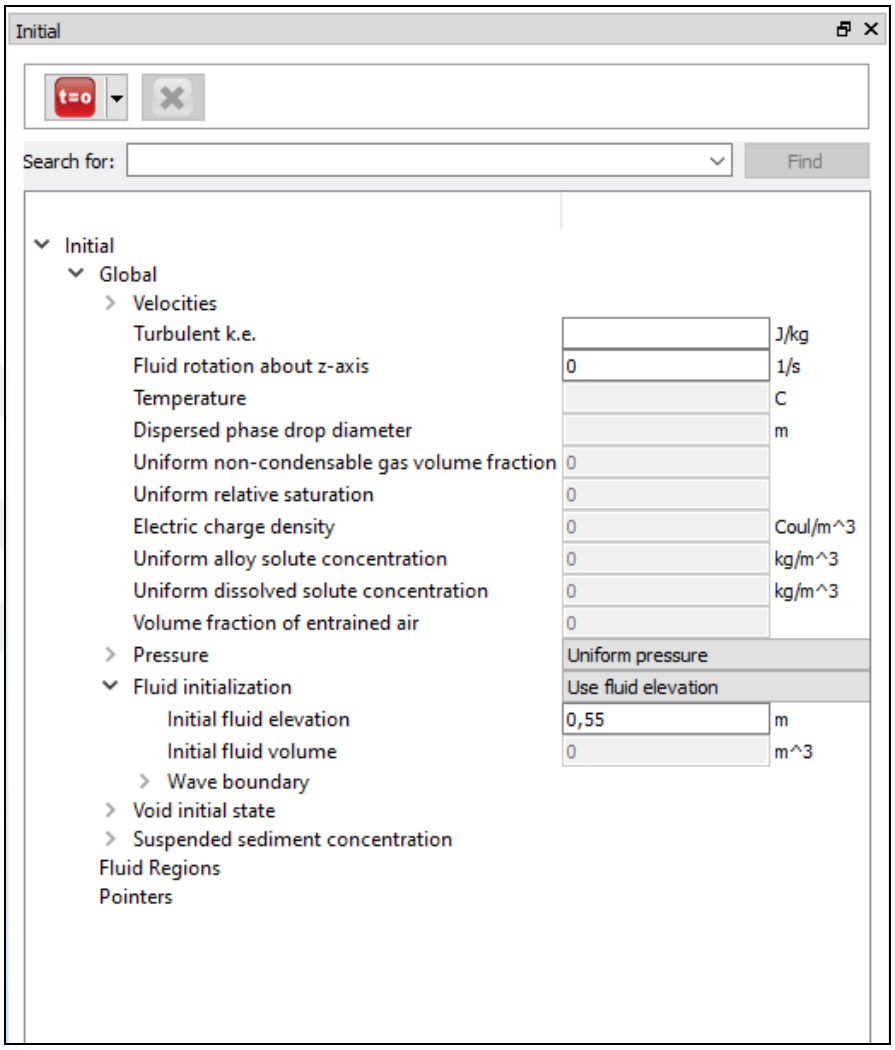

Figure B.15 The initial widget .

4- In the Output tab (Figure B.16), we specify the data that will be included in our results file. We select the 'Hydraulic data' option and set the data interval to 0.2 seconds.

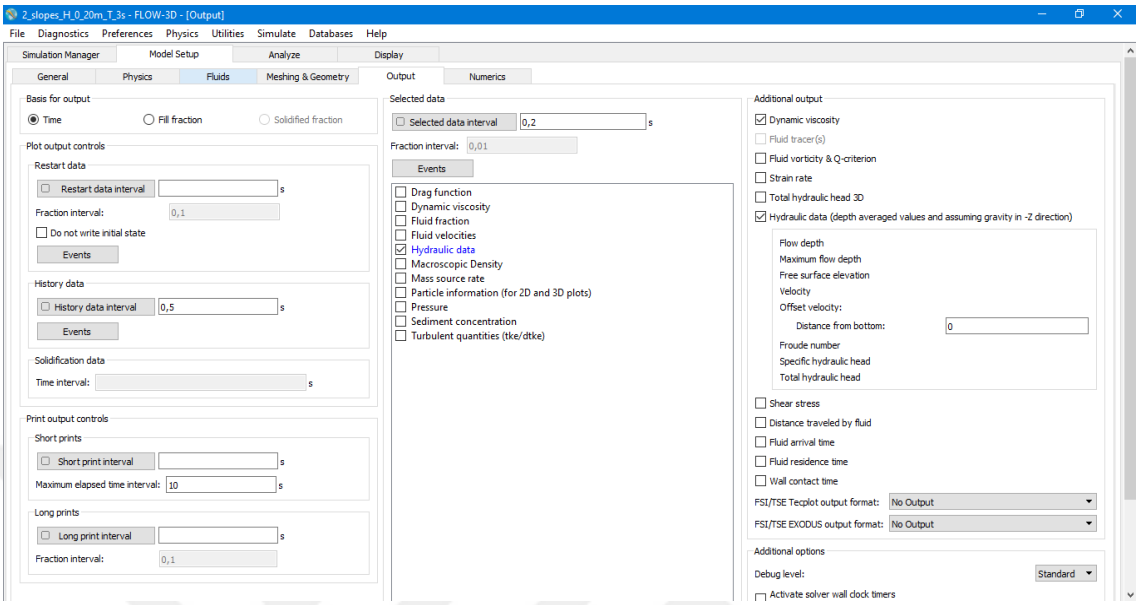

Figure B.16 The output sub-tab .

5- In the Numerical sub-tab (Figure B.17), the options are set to their default values.

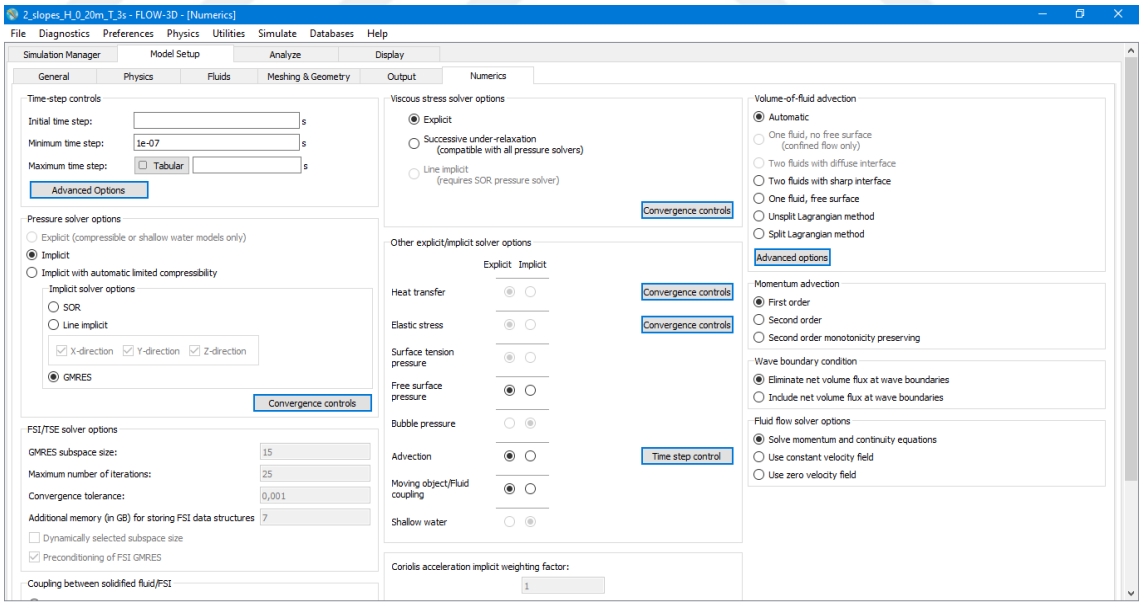

Figure B.17 The numerical sub-tab .